Pair creation in extreme light : highlights on vortex laser beam

Anthony Mercuri-Baron

École Doctorale Physique en Île-de-France - EDPIF

Laboratoire pour l'Utilisation des Lasers Intenses - LULI

THESE

pour obtenir le grade de

DOCTEUR DE SORBONNE UNIVERSITÉ

Discipline : Physique

Présentée et soutenue par :

Anthony MERCURI-BARON

le : 26 Janvier 2023

Pair creation in extreme light : highlights on vortex laser beams

Sous le direction de :

Mme Caterina RICONDA - Professeure, LULI, Sorbonne Université

Membres du jury :

Dr. Felix KARBSTEIN	Helmholtz Insitute, Jena	Rapporteur
Dr. Ben KING	University of Plymouth	Rapporteur
Pr. Richard TAIEB	Sorbonne Université	Président du jury
Dr. Thomas GRISMAYER	Técnico Lisboa (IST), GoLP	Examinateur
Dr. Rachel NUTER	CEA, CESTA	Examinatrice
Pr. Caterina RICONDA	LULI	Directrice de thèse
Dr. Mickael GRECH	LULI	Invité, co-encadrant

Abstract

Since the invention of the Chirped Pulse Amplification technique in the 80s, achievable laser intensities never stopped increasing. The upcoming facilities are expected to deliver several PW peak power on a focal spot of a few microns diameter. When particles interact with those extreme electromagnetic fields, nonlinear effects of a quantum nature can be dominant. The theory describing the phenomena is called strong-field quantum electrodynamics (SFQED), which evaluate in a non-perturbative way the interaction between particles and the strong background field. Among all of the new phenomena SFQED is predicting, two of them particularly attracted the interest of the community over the last decade. The first one, the nonlinear Compton scattering process, is the emission of a high energy gamma photon (from a hundred of MeV to tens of GeV) by an electron or a positron interacting with a strong background field. The second one, but not the least, is the nonlinear Breit-Wheeler (NBW) process. It consists in the creation of an electron-positron pair from the conversion of a high energy gamma photon interacting with the strong electromagnetic field.

The new ultra high intensities reached by the modern laser facilities open the way of prolific electron-positron pair production in the laboratory by the NBW process. The ultimate goal, although not achievable in the near future, would be the creation of an electron-positron pair plasma on earth. Indeed this plasma is of interest on a fundamental point of view as it has exotic properties. Moreover it is of interest fro astrophysical objects.

The red string guiding the present work is the optimisation of pair creation in ultra intense lasers. In order to do so we studied two promising physical configurations achievable in the future. The first one, called the shower, is the head-on collision of a high intensity laser pulse with a flash of high energy gamma photons. For this configuration, we built a semi-analytical model which is able to predict the amount of produced pairs, by taking into account all of the laser pulse spatio-temporal distribution. We confronted our prediction with three dimensional Particle-in-cell (PIC) simulations performed with the code SMILEI and found a very good agreement. In particular, to explore the general

reach of our model, we studied Laguerre-Gauss (LG) beams. These vortex beams recently attracted the attention of the high intensity community has they have interesting properties. For example they have a ring shape transverse intensity distribution, and they carry angular momentum. Even in those exotic beams our model performed very well compared to simulations. In particular it is shown that for this configuration in order to maximise pair production, one should not always try to reach the maximum intensity achievable by focalising the beam at the maximum. Furthermore general guidelines for the upcoming experiments are provided.

The second configuration explored consists in two counter streaming laser beams, with initial seeding electrons at the center. It was shown in the literature that under the right conditions, charges can be constantly reaccelerated, leading to constant emission of high energy photons, which are converted into pairs. An exponential growing phase of the number of pairs, called the avalanche, can then be reached. The present work extended the study of this configuration to LG beams. It is shown in PIC simulations that at the same peak intensity, LG beams can perform better than usual gaussian beams. The dynamics of pairs being of main importance there, we used an existing model on the dynamics of charges in strong field to qualitatively explain the difference of performance between the different field configurations explored. Finally is presented a newly built model which performs well at predicting the growth rate of the avalanche on ideal cases, with opens the perspective of an extension to the counter-streaming beams configuration.

Résumé

Depuis l'invention de la technique de Chirped Pulse Amplification, les intensités lasers atteignables n'ont cessé d'augmenter. Les futures installations devraient produire des puissances de plusieurs PW sur des tâches focales de quelques microns. Quand des particules interagissent avec ces champs extrêmes, des effets non-linéaires de nature quantique, décrits par l'électrodynamique quantique en champs forts (SFQED), peuvent devenir dominants. Parmis les prédictions de cette théorie, deux phénomènes on particulièrement attiré l'attention de la communauté ces dernières années. Le premier, la diffusion Compton non-linéaire, est l'émission d'un photon gamma de haute énergie (d'une centaine de MeV à des dizaines de GeV) par une charge interagissant avec le champ fort. Le second est le processus Breit-Wheeler non-linéaire (NBW), qui est la conversion d'un photon gamma de haute énergie en une paire électron positrons, lors de l'interaction avec un électromagnétique champ fort.

Grâces à ces processus, les installations multi-PW ouvrent la voie vers une production de paires électrons-positrons abondante en laboratoires. L'objectif ultime, bien qu'inaccessible dans les installations actuelles, est la création d'un plasma de paires électron-positron. Ce genre de plasma est intéressant fondamentalement pour ces propriétés exotiques, mais aussi car il est présent dans des environnements astrophysiques.

Le theme de cette thèse est l'optimisation de la production de paires dans les lasers ultra intenses. Pour cela deux configurations physiques prometteuses ont été étudiées. La première, appelée shower, est la collision frontale d'une impulsion laser haute intensité avec un flash de photons gamma de haute énergie. Un model semi-analytique a été développé pour cette configuration, prenant en compte la structure spatio-temporelle de l'impulsion laser, et permettant de prédire rapidement le nombre de paires produites. Ce modèle est en excellent accord avec des simulations Particle-in-cell (PIC) en trois dimensions réalisées avec le code SMILEI. Une étude systématique avec différentes configurations d'impulsions a été réalisée, en fixant l'énergie totale de l'impulsion pour se rapprocher des conditions expérimentales. Dans cette analyse, des faisceaux

Laguerre-Gauss (LG), ou faisceaux à vortex, ont été étudiés en raison de leurs propriétés intéressantes, comme leur distribution d'identité en forme d'anneau ou le fait qu'ils transportent un moment angulaire orbital. Cette étude a permis d'identifier la focalisation optimale pour la création de paires, qui selon l'énergie totale disponible n'est pas nécessairement la focalisation maximale. Ce travail dispense aussi des conseils généraux pour les futures expériences.

La seconde configuration étudiée est formée de deux faisceaux laser contre-propagatifs, avec des électrons placés initialement au plan focal. Dans ce cas une croissance exponentielle du nombre de paires (avalanche) peut-être obtenue, car les charges sont constamment réaccélérées et rayonnent des photons gamma, par la suite convertis en paires. Le présent travail réévalue les conditions de démarrage de la cascade dans une géométrie 3D réaliste pour les impulsions lasers, et étend l'étude aux faisceaux LG. Il est présenté une analyse semi-analytique de la dynamiques des particules sur les temps courts (petits comparés à la période laser) dans cette configurations de faisceaux contre-propagatifs. Il est montré qu'il y a de grandes différences qualitatives dans le déclenchement de l'avalanche suivant la configuration des champs. Le taux de croissance des paires obtenu de simulations PIC 3D confirme ces différences. De plus il est montré qu'à amplitudes maximum égales, les LG on un plus haut taux de croissances que les faisceaux gaussiens. L'analyse de la dynamique aux temps courts permet de proposer un nouveau modèle pour prédire le taux de croissance dans un cas idéal, avec le potentiel d'être étendu à des cas plus réalistes.

Contents

Introduction

Context

Light does not usually interact with itself. The fact that this text can be read properly, or that in our everyday life we are able to see distant objects, is because photons, carrying electromagnetic waves, most of the time cross each other without any consequences. This translates in classical electromagnetism, in the Maxwell's equations. In vacuum they are partial linear differential equations of the fields, from which the electromagnetic wave equation can be extracted, which is linear in the electromagnetic fields. Therefore, a linear combination of solutions of these equations can be added in order to obtain a new one. Hence the everyday experience with electromagnetic waves, mainly described by classical electromagnetism, results in the direct linear superposition of electromagnetic fields [Feynman et al., 2010], at the origin of some counter-intuitive phenomena like interference. However this changes when we need to take into account quantum electrodynamics (QED), describing the behaviour of charged particles and photons at the quantum level. In QED two photons can scatter through virtual particles. This collision can convert the two photons into an electron-positron pair, provided the total energy of the two photons in their center of mass frame is greater than the mass energy of the pair $2mc^2$, with m the mass of the electron or positron and c the speed of light. This is called the (linear) Breit-Wheeler process [Breit and Wheeler, 1934]. Observing this phenomenon is still one of the great challenges of experimental physics to date and some schemes have been proposed and investigated in the last decade [Thomas, 2014, Pike et al., 2014, Ribeyre et al., 2016].

However, light by light scattering has already been observed in the laboratory, through the nonlinear Breit-Wheeler (NBW) process. This was done in the seminal E-144 SLAC experiment [Burke et al., 1997], in which about a hundred pairs have been created by colliding over 22000 times a $\simeq 45\,\mathrm{Gev}$ electron beam, from a conventional accelerator, head-on with a high intensity laser ($\simeq 10^{18}\,\mathrm{W/cm^2}$). The laser particle interaction resulted in the emission of gamma photons, which in turn interacted with the laser. The NBW process

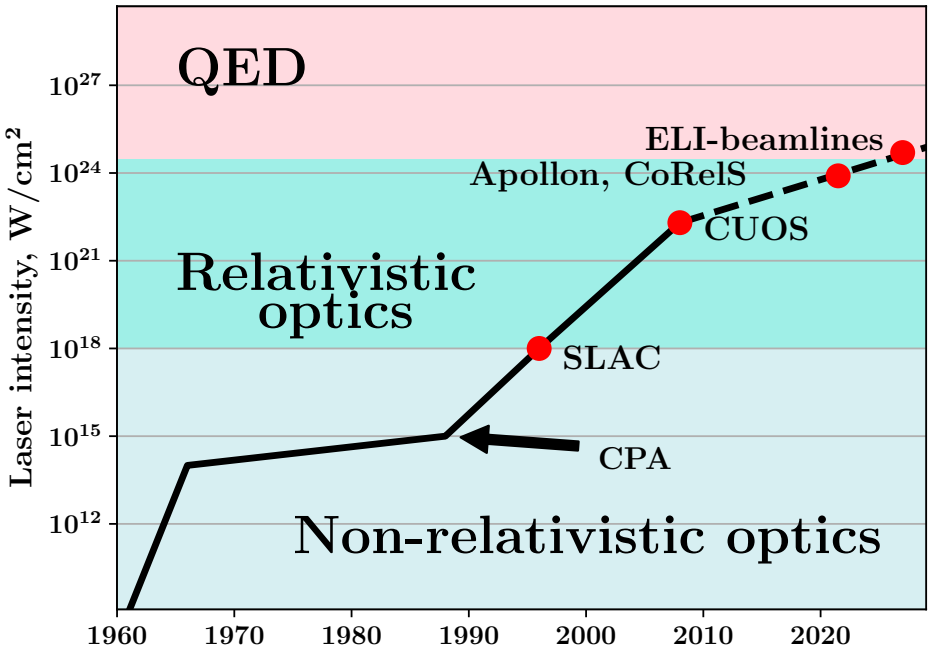

Figure 1: Schematic representation of the achievable maximum laser intensity over the last decades. The red dots are examples of the achieved or expected intensity for the corresponding facilities.

is the nonlinear version of the Breit-Wheeler pair creation mentioned above: instead of having two photons scattering, here one high energy gamma photons (with more than $2mc^2$) interacts with multiple usually optical photons of an intense background field and it is converted into a pair. This process is at the heart of the present work and is expected to open the way to abundant pair creation in the laboratory. The NBW process is present together with the nonlinear inverse Compton Scattering (NCS), the emission of a high energy gamma photon, from the interaction of an electron (or a positron) with an intense background electromagnetic field. In particular, the NCS process can be the source of gamma photons for the NBW process, as it was in the above mentioned SLAC experiment. The theoretical framework describing those processes is called Strong-field QED (SFQED), and contrary to usual perturbative QED, it takes into account the interaction of particles with a strong background electromagnetic field in a non-perturbative way. The reference field in this approach is the so-called Schwinger field $E_S = 1.3 \times 10^{18}$V/m. A constant electric field with this amplitude in vacuum will create electron-positron pairs via the Schwinger-Sautter mechanism [Sauter, 1931, Schwinger, 1951].

Since the invention of the Chirped Pulses Amplification technique in the 80s [Strickland and Mourou, 1985] the achievable laser intensities have constantly increased, as showed in fig. 1. The envisioned intensities for forthcom-

ing facilities such as Apollon [Cros et al., 2014], CoReLS [Nam et al., 2018], ELI[1], OMEGA-EP OPAL [Bromage et al., 2019], XCELS[2], and ZEUS[3], are $10^{22} - 10^{23}\,\mathrm{W/cm^2}$. Under these conditions much more prolific pair production than in the SLAC experiment is expected, dominated by NBW processes. The perspective of these high intensities renewed interest in SFQED in the last decade, not only in order to produce pairs but also in order to test theoretical and phenomenological predictions [Fedotov et al., 2022].

In parallel to the development of higher laser fields, laser plasma accelerations techniques improved over the last decades. High energy electrons, up to tens of GeV, play a crucial role in this scenario as they can be the source of high energy gamma photons, by the NCS process, needed to trigger the NBW effect. Since its conception [Tajima and Dawson, 1979] and demonstration, laser wakefield acceleration [Mangles et al., 2004, Geddes et al., 2004, Faure et al., 2004] has advanced to the point that electron beams of 8 GeV have been obtained [Gonsalves et al., 2019] and electron energies of 10 GeV are expected at Apollon [Cros et al., 2014] via this technique. Other promising methods for electron acceleration by laser-plasma interaction are also under investigation, such as surface plasma wave acceleration [Marini et al., 2021]. These can provide high-energy electron beams without the need to resort to standard accelerators. Indeed, the progress in this kind of acceleration schemes allows to envision the use of a fully optical scheme to produce pairs, by converting the laser-accelerated electrons into high energy gamma photons and then colliding them head-on with another high intensity laser beam. The laser required to produce the high energy electrons can be obtained either by splitting an intense laser beam or in facilities with multiple laser beams. Together with strategies to produce high energy electrons beams, several sources of high energy gamma photons for pair production have been proposed [Phuoc et al., 2012, Gong et al., 2017, Gonoskov et al., 2017, Capdessus et al., 2018, Blackburn and Marklund, 2018, Vranic et al., 2019, Magnusson et al., 2019, Zhu et al., 2020, Sampath et al., 2021].

In the last decade, various simulation campaigns have been conducted to help designing future experiments aiming to efficient pair production, an effort that was largely made possible and supported by Particle-in-Cell (PIC) simulations accounting for SFQED processes [Duclous et al., 2010a, Elkina et al., 2011, Arber et al., 2015, Gonoskov et al., 2015, Grismayer et al., 2016, Lobet et al., 2016]. The configuration discussed above, which is similar to the SLAC

[1] Extreme Light Infrastructure (ELI), https://eli-laser.eu.

[2] Exawatt Center for Extreme Light Studies (XCELS), http://www.xcels.iapras.ru.

[3] Zetawatt-Equivalent Ultrashort Pulse Laser System (ZEUS), https://zeus.engin.umich.edu.

experiment and involves the head-on collision of high energy particles with an ultra high intensity laser pulse, was studied extensively theoretically and via PIC simulations in [Blackburn et al., 2017, Vranic et al., 2018, Chen et al., 2018]. We will refer to the regime of pair production achievable within this configuration in upcoming facilities as *shower pair production*. On top of this, several other configurations have been considered. Electron-seeded electromagnetic/QED *self-sustained cascades* (a scenario in which particles are constantly re-accelerated by the field and an exponential growth of pairs can be reached) in the collision of two counter-propagating laser pulses, a setup originally proposed by Bell and Kirk [Bell and Kirk, 2008], have attracted particular attention [Elkina et al., 2011, Grismayer et al., 2016, Nerush et al., 2011b, Grismayer et al., 2017, Tamburini et al., 2017, Jirka et al., 2017] as such cascades were identified as a possible limitation on the attainable intensity of high power lasers [Fedotov et al., 2010]. Variations of this setup have been proposed, considering either the use of plasma channels [Zhu et al., 2019] or the collision of multiple laser pulses [Gelfer et al., 2015, Vranic et al., 2016, Gonoskov et al., 2017]. All these works considered multiple laser beams. Alternative schemes considered the direct irradiation of a solid target by a single, extremely intense laser pulse, a situation that leads to the production of dense pair plasmas [Ridgers et al., 2012]. In these cases, the solid target, an overdense plasma, acts as a mirror and pair production is efficiently achieved in the field of the incident and reflected laser light at the target front [Kostyukov and Nerush, 2016].

The present work focus on the theoretical and numerical study with PIC simulations (performed with the code Smilei [Derouillat et al., 2018]), of the shower configuration, and the self-sustained cascade with two counter-streaming laser beams mentioned above. In particular, special attention is given to the impact on the efficiency of pair production of the laser parameters, such as its spatio-temporal envelope, its maximum intensity and its field configuration. Optimisation of pair production is obtained through the understanding of the impact of each of these quantities. We have performed numerical studies for the two configurations, using vortex beams, more specifically Laguerre-Gauss (LG) beams, that have non-trivial field configurations. LG beams have recently attracted the interest of the ultra-high intensity laser-plasma community [Chen et al., 2018, Mendonça and Vieira, 2014, Nuter et al., 2020, Longman et al., 2020, Duff et al., 2020] for their ability to carry orbital angular momentum (OAM) [Allen, 1992]. These beams, that emerge as eigen-modes of the paraxial equation, have unique properties, such as a ring-shaped intensity distribution and the large OAM, that can influence the pairs

generation. The present work provides a numerical investigation along with simplified theoretical models to describe the the impact of using LG pulses on pair production.

Outline

Part 1

The theoretical background necessary to understand this thesis is introduced in the first part of this work. Rather than being an exhaustive and detailed explanation of the physical background, it simply aims at presenting in a synthetic way the physical concepts, tools and previous results needed for our study. References for a deeper understanding are provided. The conventions and notations used to describe the original results of parts two and three are also introduced.

Chapter 1

In chapter 1, the paraxial wave equation is derived from Maxwell's equations. This equation gives the theoretical framework for the description of the propagation of a laser beam, and allows to introduce the complex amplitude of the Laguerre-Gauss (LG) beams, of particular importance for this work. The properties of the LG beams are essential to understand the results presented in part two and three, especially in chapters 5 and 7.

Chapter 2

Chapter 2 presents the aspects of electrodynamics relevant to this work. After recalling the relativistic classical equations of motion of a charge in an electromagnetic field, the dynamics of a charge in a plane wave is briefly presented. To conclude the classical approach, and to introduce briefly the historical problem of charges interacting with self-emitted radiation, the Landau-Lifshitz [Landau and Lifshitz, 1980] classical radiation reaction force is presented. Strong-field quantum electrodynamics is then introduced. Some key concepts such as the Schwinger field are presented. We focus on the two phenomena which are of utmost importance for this work: Nonlinear Breit-Wheeler (NBW) and Nonlinear inverse Compton scattering (NCS). The first is the creation of an electron-positron pair by the interaction of a gamma photon with a strong electromagnetic field, and the second corresponds to the emission of a high energy gamma photon by the interaction of a charged particle with a strong

background field. The differential rates of these two quantum processes are presented, since they are at the basis of the results in part two and three.

Chapter 3

Chapter 3 presents the general structure and main concepts of the Particle-In-Cell (PIC) method for simulating plasmas at kinetic level. In particular we focus on the PIC code Smilei which has been used to perform all the simulations of the present work. After presenting the basics of the PIC method, a section is devoted to the algorithms used to include in the code quantum processes such as nonlinear Breit-Wheeler and nonlinear inverse Compton scattering considered in this study.

Part 2

In the second part, we present the first study performed during this thesis that led to the publication [Mercuri-Baron et al., 2021]. We focus on the study of nonlinear Breit-Wheeler pair production in the shower configuration, which is the head-on collision of an extremely intense laser (intensities in the range $10^{21} - 10^{25}\,\mathrm{W/cm^2}$) with a burst of gamma photons (with energies ranging from 100 MeV to few 10s of GeV). In contrast to previous works [Blackburn and Marklund, 2018], where the authors focused on the optimization of the photon source, we consider here the high-energy photon burst as given (only its energy will vary), and do not discuss its origin (various sources of high-energy photons have been proposed [Phuoc et al., 2012, Gong et al., 2017, Gonoskov et al., 2017, Capdessus et al., 2018, Blackburn and Marklund, 2018, Vranic et al., 2019, Magnusson et al., 2019, Zhu et al., 2020, Sampath et al., 2021]). Rather, we aim at optimizing the conditions of interaction with the colliding high-intensity laser. Motivated by experimental constraints, we investigate the optimal conditions for pair production varying the laser polarization, focusing, spatial or temporal profiles, always considering a fixed laser energy.

Chapter 4

In chapter 4, we describe a simple model for the prediction of pair production during the interaction of a gamma flash with a high intensity laser. Starting from the rate of the NBW process we develop a semi-analytical model based on the probability of pair creation. We first solve the problem for a plane wave, which is also used to benchmark the SFQED modules of Smilei. We then describe how to extend the model to finite laser pulses with a time envelope and a non trivial transverse intensity distribution. Along with a discussion

about the necessary approximations made to extend the model to this more realistic case, PIC simulations are performed to validate the model. This work provides the reader with a tool for the prediction of the number of pairs produced by the interaction of gamma photons with an intense laser pulse, for a broad range of conditions relevant to forthcoming experiments.

Chapter 5

In chapter 5, special attention is paid to the use of Laguerre-Gauss beams in the context of pair production. These beams have unique properties, that could have an impact on pair production. It was for instance demonstrated in [Chen et al., 2018] that the collision of an electron beam with a LG beam can lead to efficient production of gamma rays carrying large OAM, to enhanced secondary radiation emission and pair production. However, that study was performed at constant maximum intensity, so it is hard to distinguish the impact of the increased energy (up to 3× higher for the LG beam) from the role of the laser spatial profile itself. In this chapter, we first compare 3D PIC simulations (considering different laser beams with the same total pulse energy) to our model. We then compare two different regimes of intensities and discuss the impact of the spatial extent of the laser pulses on the efficiency of pair creation. From this study, we conclude that while using LG beams can be in principle favorable for pair creation, in some conditions an experimentally simpler but still effective alternative is the defocusing of a gaussian laser pulse. This knowledge allows us to give general guidelines for experiments in upcoming facilities.

Part 3

In part three we study a configuration of utmost importance for pair creation, a standing wave obtained from two counter-propagating laser pulses, with initial seeding electrons at focus. In this configuration, contrary to the shower configuration studied in part two, charged particles can be efficiently re-accelerated by the laser pulse, allowing them to keep emitting gamma photons. These gamma photons interact in turn with the strong laser field and can be converted into pairs. A phase of exponential growth in the number of pairs can thus be reached, called avalanche or (self-sustained) cascade.

Chapter 6

Chapter 6 presents the state of the art for the two beams configuration and the self-sustained cascade. First the ideal case of the cascade in a pure rotating

electric field is presented, along with PIC simulations to verify and discuss the analytical results. Next, we present a short review of the main ideas and results found in the literature for a more realistic configuration where a standing wave is generated by two crossing laser beams. We then discuss the role of the laser polarization, reminding that a rotating field can be obtained by considering counter-propagating circularly polarised gaussian laser pulses at their magnetic nodes. A presentation of a model of the short time dynamics of charges in strong fields [Mironov et al., 2021] follows. This allows to explain how the field structure can influence quantities relevant for the development of the avalanche and to identify the conditions for the onset of the self-sustained cascade. This model will be used extensively to discuss the results of chapter 7. Finally we summarize previous results about the dynamics of particles in standing waves, taking into account classical radiation reaction. This is important to understand the motion of the produced pairs from the location where they are generated to other positions, that correspond to attractors, as will be shown in chapter 7.

Chapter 7

In chapter 7 we present some original results obtained by investigating a configuration with two counter-streaming beams leading to a cascade. The study is based first on 3D PIC simulations of two colliding gaussian or LG beams. Fixing the maximum amplitude, as it is one of the critical parameter of the cascade growth rate, we explore different field configurations and combinations of polarisation, and compare the growth in number of pairs and their properties. Our results suggest that, at a given intensity, some LG beam configurations are more efficient in maximising the cascade growth rate than the reference case studied in the literature of two circularly polarised gaussian beams. To interpret this result, we compare the results of the simulations to the model for short time dynamics [Mironov et al., 2021] presented in the previous chapter and show that the relative efficiency of pair production of the simulations for the different cases is consistent with the model. Finally we derive quantitative predictions for the growth rate, still based on the short time dynamics. The estimated growth rate shows very good agreement with simulations for the ideal rotating electric field case for a wide range of parameters, and opens perspectives for the extension of the prediction to the more realistic case of two counter-streaming LG beams.

Part I

Theoretical background

Chapter 1

Modelling of electromagnetic fields and pulses

Contents

In this thesis we study the effect of arbitrary spatio-temporal configurations of laser pulses in strong-field processes, with a special focus on the use of Laguerre-Gauss (LG) beams. In this chapter their properties, their field structure, and the convention used are introduced. The LG beam unusual field structure and intensity distribution will be at the heart of this work, as we will see in chapters 4 and 5 where we consider a single LG pulse interacting with a photon flash, and in chapters 6 and 7 were we consider two counter-propagating LG laser pulses.

1.1 The Helmholtz equations and the paraxial equation

LG beams are a family of solution of the paraxial equation. As shown in the following, this equation is obtained from Maxwell's equations. Its derivation allows to introduce the conventions used in this work for classical electromagnetic fields.

In the following chapters we use either the 4-vector notation, (we use the $(+,-,-,-)$ signature for the Minkowski metric), or the electric and magnetic field vectors depending on which description is more suited. The electromagnetic field strength tensor is given by

$$F^{\mu}_{\ \nu} = \begin{pmatrix} 0 & E_x/c & E_y/c & E_z/c \\ E_x/c & 0 & B_z & -B_y \\ E_y/c & -B_z & 0 & B_x \\ E_z/c & B_y & -B_x & 0 \end{pmatrix} ; \tag{1.1}$$

and the 4-vector potential is

$$A^{\mu} = (V/c, \boldsymbol{A}) , \tag{1.2}$$

with V the usual scalar potential and $\boldsymbol{A}$ the usual vector potential. Maxwell's equations in vacuum, in the absence of charges, are

$$\partial_{\mu} F^{\mu}_{\ \nu} = 0 \tag{1.3}$$

$$\partial_{\mu} * F^{\mu}_{\ \nu} = 0 , \tag{1.4}$$

where

$$* F^{\mu\nu} = \frac{1}{2} \epsilon^{\mu\nu\delta\lambda} F_{\delta\lambda} , \tag{1.5}$$

with $\epsilon^{\mu\nu\delta\lambda}$ being the Levi-Civita tensor components. Corresponding, in the usual 3 vectors notations, to

$$\boldsymbol{\nabla} \cdot \boldsymbol{E} = 0 \tag{1.6}$$

$$\boldsymbol{\nabla} \times \boldsymbol{E} = -\frac{\partial \boldsymbol{B}}{\partial t} \tag{1.7}$$

$$\boldsymbol{\nabla} \cdot \boldsymbol{B} = 0 \tag{1.8}$$

$$\boldsymbol{\nabla} \times \boldsymbol{B} = \frac{1}{c^2} \frac{\partial \boldsymbol{E}}{\partial t} , \tag{1.9}$$

with fields linked to the potentials by

$$\boldsymbol{E} = -\boldsymbol{\nabla} V - \frac{\partial \boldsymbol{A}}{\partial t} \tag{1.10}$$

$$\boldsymbol{B} = \boldsymbol{\nabla} \times \boldsymbol{A} . \tag{1.11}$$

Maxwell's equations lead to the usual wave equation for the electric and

magnetic field in vacuum

$$\nabla^2 \boldsymbol{E} - \frac{1}{c^2}\frac{\partial^2 \boldsymbol{E}}{\partial t^2} = 0 \quad , \tag{1.12}$$

$$\nabla^2 \boldsymbol{B} - \frac{1}{c^2}\frac{\partial^2 \boldsymbol{B}}{\partial t^2} = 0 \quad . \tag{1.13}$$

Since we study wave solutions we switch to the complex notation, with ω being the angular frequency of the wave

$$\boldsymbol{E} = \Re\left[\boldsymbol{\mathcal{E}} e^{i\omega t}\right] , \tag{1.14}$$

$$\boldsymbol{B} = \Re\left[\boldsymbol{\mathcal{B}} e^{i\omega t}\right] , \tag{1.15}$$

with $\boldsymbol{\mathcal{E}}$ and $\boldsymbol{\mathcal{B}}$ being the complex envelope of the fields, which are independent of time. By inserting these into the wave equations, one obtains the vectorial Helmholtz equations

$$\boldsymbol{\nabla}^2 \boldsymbol{\mathcal{E}} + k^2 \boldsymbol{\mathcal{E}} = 0 \,, \tag{1.16}$$

$$\boldsymbol{\nabla}^2 \boldsymbol{\mathcal{B}} + k^2 \boldsymbol{\mathcal{B}} = 0 \,, \tag{1.17}$$

with k (being ω/c for plane waves) the angular wavenumber. Moreover, applying Eqs. (1.6) and (1.8) to $\boldsymbol{\mathcal{E}}$ and $\boldsymbol{\mathcal{B}}$ leads to

$$\boldsymbol{k} \cdot \boldsymbol{\mathcal{E}} = 0 \tag{1.18}$$

$$\boldsymbol{k} \cdot \boldsymbol{\mathcal{B}} = 0 \,, \tag{1.19}$$

which means that the vectors $\boldsymbol{\mathcal{E}}$ and $\boldsymbol{\mathcal{B}}$ are transverse. They can then be written as

$$\boldsymbol{\mathcal{E}} = \boldsymbol{\theta}_{\mathcal{E}} \mathcal{E} \tag{1.20}$$

$$\boldsymbol{\mathcal{B}} = \boldsymbol{\theta}_{\mathcal{B}} \mathcal{B} \tag{1.21}$$

with $\boldsymbol{\theta}_{\mathcal{E}}$ and $\boldsymbol{\theta}_{\mathcal{B}}$ being transverse vectors. Finally inserting these expressions into the vectorial Helmholtz equations results in the scalar Helmholtz equations

$$\nabla^2 \mathcal{E} + k^2 \mathcal{E} = 0 \,, \tag{1.22}$$

$$\nabla^2 \mathcal{B} + k^2 \mathcal{B} = 0 \,. \tag{1.23}$$

In order to obtain the paraxial approximation, one first has to chose a direction of propagation, let it be z here, and write $\mathcal{E}$ and $\mathcal{B}$ in the following form

$$\mathcal{E} = u_{\mathcal{E}} e^{-ikz}, \tag{1.24}$$
$$\mathcal{B} = u_{\mathcal{B}} e^{-ikz}. \tag{1.25}$$

Inserting the two previous forms in the scalar Helmholtz Eqs. (1.22) and (1.23) lead to the equations

$$\nabla_\perp^2 u_{\mathcal{E}} - 2ik\frac{\partial u_{\mathcal{E}}}{\partial z} + \frac{\partial^2 u_{\mathcal{E}}}{\partial z^2} = 0 \tag{1.26}$$
$$\nabla_\perp^2 u_{\mathcal{B}} - 2ik\frac{\partial u_{\mathcal{B}}}{\partial z} + \frac{\partial^2 u_{\mathcal{B}}}{\partial z^2} = 0 \tag{1.27}$$

where $\nabla_\perp^2$ is the transverse part of the Laplacian, in the (x, y) directions. The heart of the paraxial approximation is then to assume that the longitudinal variations of the field envelope are small compared to the transverse variation, and happen on a typical length larger than the wavelength $\lambda = 2\pi/k$. This allows to neglect the $\dfrac{\partial^2 u_{\mathcal{E},\mathcal{B}}}{\partial z^2}$ terms in the equations.

The most convenient way to solve this problem is not to solve the equation for the fields, but the one for the vector potential [M. Lax, 1975, Davis, 1979, Haus, 1984]. In the same way as the electric and magnetic fields, the scalar and vector potentials follow the wave equation in the Lorenz gauge

$$\boldsymbol{\nabla} \cdot \boldsymbol{A} + \frac{1}{c^2}\frac{\partial V}{\partial t} = 0. \tag{1.28}$$

One can use the complex notation for them too

$$V = \Re\left[\mathcal{V} e^{i\omega t}\right], \tag{1.29}$$
$$\boldsymbol{A} = \Re\left[\boldsymbol{\mathcal{A}} e^{i\omega t}\right]. \tag{1.30}$$

Using Eqs. (1.10) and (1.11) and going into the Lorenz gauge one can relate the potentials to the complex field envelopes by

$$\boldsymbol{\mathcal{E}} = -i\omega\left[\boldsymbol{A} + \frac{1}{k^2}\boldsymbol{\nabla}(\boldsymbol{\nabla} \cdot \boldsymbol{A})\right], \tag{1.31}$$
$$\boldsymbol{\mathcal{B}} = \boldsymbol{\nabla} \times \boldsymbol{A}. \tag{1.32}$$

Going back to the potential, since they follow the wave equations in the Lorenz gauge as the electromagnetic field, one can perform the same procedure to obtain the Helmholtz equation on the vector potential, to write it in the following

form

$$\boldsymbol{\mathcal{A}} = \boldsymbol{\theta}_{\mathcal{A}} u e^{-ikz}\,, \tag{1.33}$$

with $\boldsymbol{\theta}_{\mathcal{A}}$ being a transverse vector and u being the complex amplitude. The $\boldsymbol{\theta}_{\mathcal{A}}$ can be written $\boldsymbol{\theta}_{\mathcal{A}} = a\hat{\boldsymbol{x}} + b\hat{\boldsymbol{y}}$, with a and b two complex numbers such that $|a|^2 + |b|^2 = 1$. Those two complex numbers are related to the polarisation of the beam by the quantity

$$s = i(ab^* - ba^*)\,, \tag{1.34}$$

when $s = \pm 1$ the wave has a circular polarisation (CP) (left handed for $+1$, and right handed for -1), and when $s = 0$ the wave has a linear polarisation (LP). Furthermore, as it was done previously, by inserting this form of the potential vector into the vectorial Helmholtz equation, one obtains the following relation

$$\nabla_\perp^2 u - 2ik\frac{\partial u}{\partial z} + \frac{\partial^2 u}{\partial z^2} = 0 \tag{1.35}$$

which, after applying the paraxial approximation, leads to the paraxial wave equation

$$\nabla_\perp^2 u - 2ik\frac{\partial u}{\partial z} = 0\,. \tag{1.36}$$

Then once the equation on the complex amplitude u is solved, the complex envelope of the fields in the paraxial approximation can be obtained back by the following expressions

$$\boldsymbol{\mathcal{E}} = -i\omega\left[au\hat{\boldsymbol{x}} + bu\hat{\boldsymbol{y}} - \frac{i}{k}\left(a\frac{\partial u}{\partial x} + b\frac{\partial u}{\partial y}\right)\hat{\boldsymbol{z}}\right]e^{-ikz}\,, \tag{1.37}$$

$$\boldsymbol{\mathcal{B}} = -ik\left[-bu\hat{\boldsymbol{x}} + au\hat{\boldsymbol{y}} + \frac{i}{k}\left(b\frac{\partial u}{\partial x} - a\frac{\partial u}{\partial y}\right)\hat{\boldsymbol{z}}\right]e^{-ikz}\,. \tag{1.38}$$

1.2 Laguerre-Gauss beams

1.2.1 The gaussian beam

The most common and well known solution of the paraxial equation corresponds to gaussian beams. Its complex amplitude in cylindrical coordinates is given by [Siegman, 1986]

$$u(\rho, z) = \frac{E_0}{\omega}\frac{w_0}{w(z)}\exp\left[-\frac{\rho^2}{w^2(z)}\right]\exp\left[-i\frac{k\rho^2}{2R(z)} + i\psi(z)\right]. \tag{1.39}$$

In the above expression $\rho = \sqrt{x^2+y^2}$ and $w(z)$ is the radius at which the amplitude fall off by a factor $1/e$ at the position z on the axis of propagation, w_0 the so called waist being this radius at focus. Then $z_R = \pi w_0^2/\lambda$ is the Rayleigh length which characterises the divergence of the beam at $z = z_R$ one has the radius of the beam $w(z) = \sqrt{2}w_0$. The quantity $R(z) = z\left[1 + \left(\frac{z_R}{z}\right)^2\right]$ is the radius of curvature of the beam wavefront, $\psi(z) = \arctan(z/z_R)$ is called the Gouy phase, and finally E_0/ω is the maximum amplitude of the vector potential, with E_0 being the amplitude of the corresponding electric field.

Before continuing and introducing more complex beams let us make a small remark about notations. In this work strong fields will be discussed and used, the meaning of strong being defined in chapter 2. Usually in the high intensity laser community, one uses the normalised electric field amplitude

$$a_0 = \frac{eE_0}{mc\omega}\,, \tag{1.40}$$

m being the electron mass and E_0 the electric field amplitude. The quantity a_0 is sometimes referred to as the normalised vector potential. As one can see from (1.39) it is related to the vector potential amplitude by the constant e/mc. This parameter is especially used first when relativistic effects are important ($a_0 > 1$) and also when quantum processes are kicking in, as it is a Lorentz invariant. In the following, we will use either a_0 or E_0 depending on what is more convenient for the discussion.

1.2.2 Higher order solutions and LG beams

While solving the paraxial equation, one may want to look at solutions with cylindrical symmetry. If one assumes an azimuthal dependence of the complex amplitude in the form of $\exp(-i\ell\varphi)$, φ being the azimuthal angle in cylindrical coordinates, then it can be shown that any solutions of this type can be decomposed using a family of modes, which are called the Laguerre-Gauss (LG) modes [Siegman, 1986, Allen, 1992, Vallone, 2015]. This family of modes is indexed by two integers $p \geq 0$ and $\ell \in \mathbb{Z}$. The complex amplitude of a Laguerre-Gauss beam of order (p,ℓ) in cylindrical coordinates is given by

$$\begin{aligned} u_{p\ell}(\rho,\varphi,z) &= \frac{E_0}{\omega} C_{p\ell} \frac{w_0}{w(z)} \left(\frac{\sqrt{2}\rho}{w(z)}\right)^{|\ell|} L_p^{|\ell|}\left(\frac{2\rho^2}{w^2(z)}\right) \\ &\times \exp\left[-\frac{\rho^2}{w^2(z)}\right] \exp\left[+i\psi_{pl}(z) - i\ell\varphi - i\frac{k\rho^2}{2R(z)}\right], \\ &= \frac{E_0}{\omega} U_{p\ell}(\rho,z) \exp\left[i\Phi_{p\ell}(z)\right], \end{aligned} \tag{1.41}$$

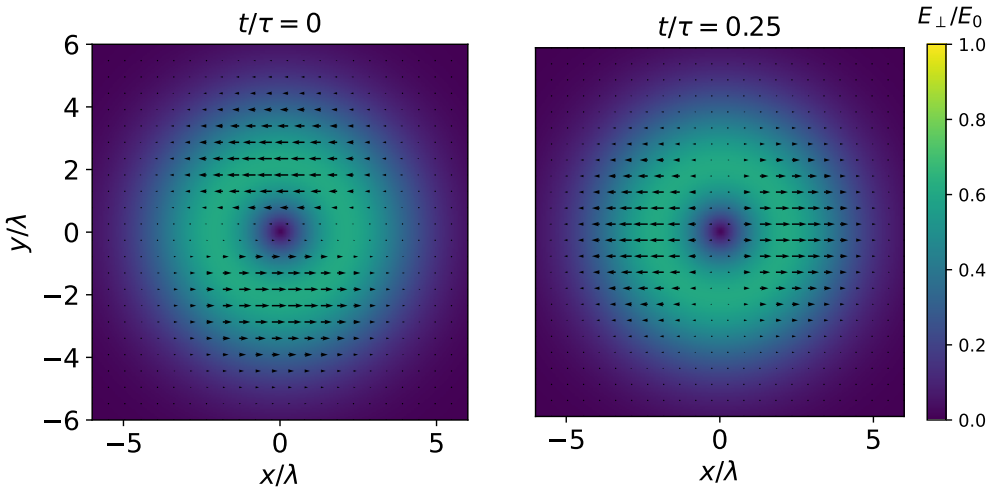

Figure 1.1: Transverse electric field (arrows) and maximum amplitude distribution (in colour) of a LP LG beam of order $(p;\ell) = (0;1)$, at focus for two different times. The laser period is τ and the laser reaches focus at $t = 0$. The waist is chosen to be $w_0 = 3\lambda$.

with $C_{p,\ell} = \sqrt{\dfrac{p!}{(p+|\ell|)!}}$ a normalizing factor, $\psi_{pl}(z) = (2p+\ell+1)\arctan(z/z_R)$ the generalized Gouy phase and $L_p^{|\ell|}(x)$ the the generalized Laguerre polynomials [M. Abramowitz, 1964]. The $L_p^{|\ell|}$ are polynomials of degree p, the first fews are given by

$$L_0^{|\ell|}(x) = 1\,, \tag{1.42}$$

$$L_1^{|\ell|}(x) = 1 + |\ell| - x\,, \tag{1.43}$$

$$L_2^{|\ell|}(x) = \frac{x^2}{2} - (2+|\ell|)x + \frac{3}{2}|\ell| + 1\,, \tag{1.44}$$

$$\dots$$

By looking at the complex amplitude (1.41), the two major differences with the Gaussian beam is the azimuthal dependence in the phase, and then the polynomial factor in the transverse amplitude distribution. Before seeing what it will imply on the amplitude distribution and phase structure of the beam, one should remark that $u_{0,0}$ is simply the usual complex amplitude of the gaussian beam, meaning that the gaussian beam is simply a special case of LG beams.

Let us now discuss general properties of this family of beams. First one can check that from (1.41) for all values of p and ℓ the beams have the same energy since

$$\int_0^{2\pi} \mathrm{d}\varphi \int_0^{+\infty} \rho \mathrm{d}\rho |u_{p\ell}(\rho,\varphi,z)|^2 = \frac{\pi}{2}\frac{E_0^2}{\omega^2}\,. \tag{1.45}$$

Next one can look at the field phase structure and the distribution of the

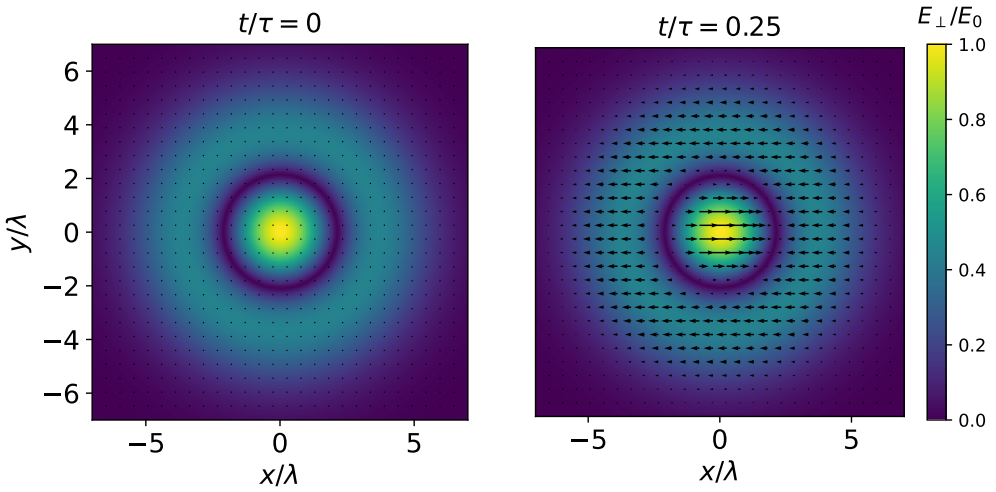

Figure 1.2: Transverse electric field (arrows) and maximum amplitude distribution (in colour) of a LP LG beam of order $(p;\ell) = (1;0)$, at focus for two different times. The laser period is τ and the laser reaches focus at $t = 0$. The waist is chosen to be $w_0 = 3\lambda$.

amplitude. The polynomial factor in (1.41) gives, for $\ell \neq 0$, a transverse intensity distribution in the form of concentric rings. The number of rings depends on the value of p (e.g. for $p = 0$, the field vanishes on the laser axis and the intensity distribution is made of one ring). In order to visualise it, let us take the example of a LP LG beam of order $(p;\ell) = (0;1)$, the linear polarisation corresponding to choosing $a = 1$ and $b = 0$ in (1.37). The obtained amplitude distribution is represented in color in fig. 1.1, and one indeed obtains a ring shape. The radius of the ring is increasing with ℓ, and one can show that the position of the maximum of the amplitude distribution for $p = 0$ is given by

$$\rho^{max}(z) = w(z)\sqrt{|\ell|/2}\,. \tag{1.46}$$

One can then understand the difference between the transverse size of an LG beam and a gaussian one, as for $(p;\ell \geq 2)$, the maximum of the fields is at a radius larger than the gaussian beam waist.

For $p > 0$ and $\ell = 0$, the amplitude distribution is composed of a disc with its maximum value at the center, which is encircled by concentric rings. Between each rings the amplitude goes to zero, and in fact for $p > 0$ $\ell = 0$, p is the number of rings or the number of zero between the center and the last ring. Again to illustrate this, the LP case $(p;\ell) = (1;1)$ is represented in fig. 1.2. In a similar way, for $p > 0$ and $\ell \neq 0$ the amplitude distribution is compose of $p+1$ concentric ring, like it is represented in fig. 1.3. Last we would like to point out the effect of p and ℓ on the value of the amplitude. Since all considered LG modes have the same energy, but their transverse size increases with the

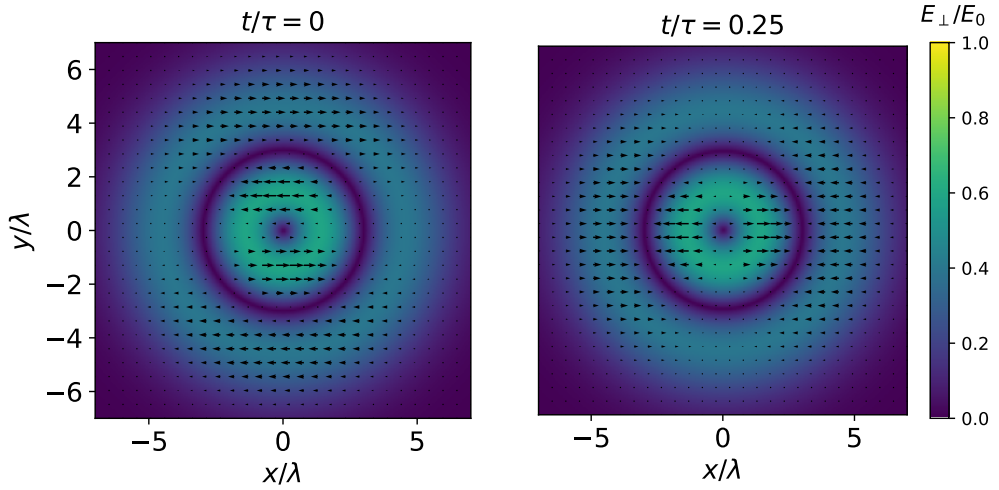

Figure 1.3: Transverse electric field (arrows) and maximum amplitude distribution (in colour) of a LP LG beam of order $(p;\ell) = (1;1)$, at two different times. The laser period is τ and the laser reaches focus at $t = 0$. The waist is chosen to be $w_0 = 3\lambda$.

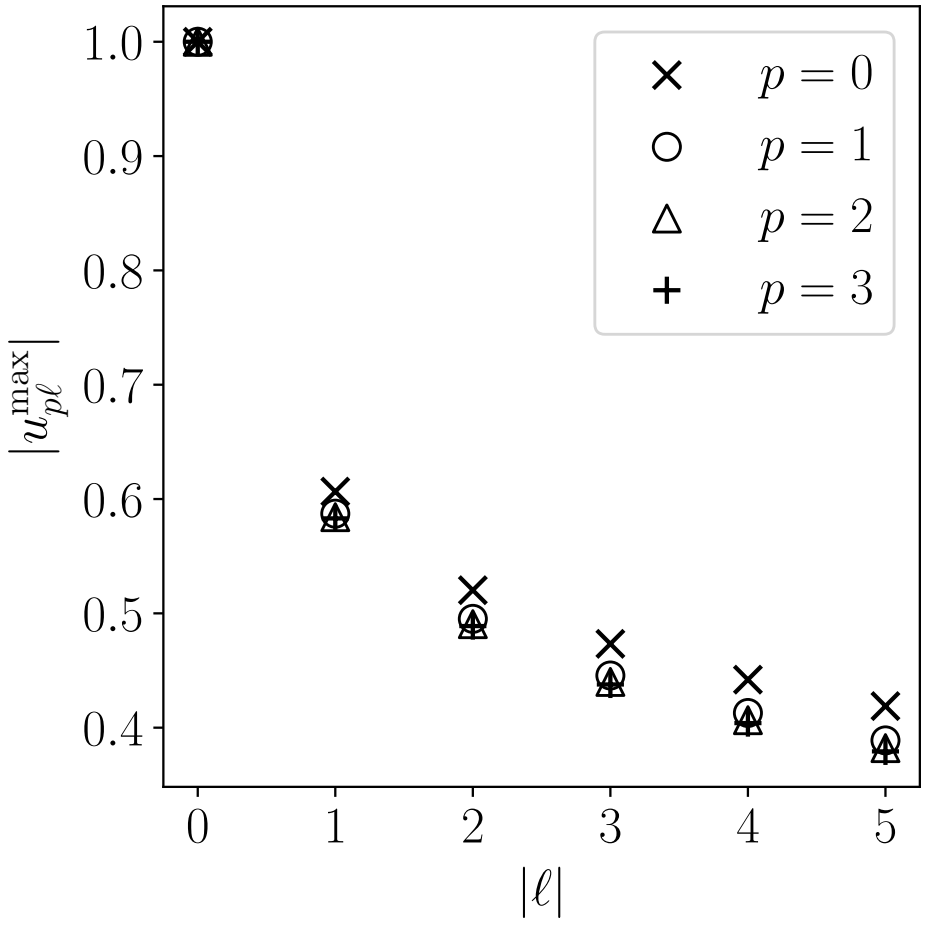

Figure 1.4: Maximum value of the complex amplitude of LP LG beams, normalised to the maximum value of the LP gaussian beam, as a function of the beam orders p and ℓ. All orders carry the same total energy.

order, the maximum amplitude has to decrease with the increase of the order. To be more precise the maximum value is slowly decreasing with p, and it is more influenced by ℓ. For $p = 0$ this value can be computed analytically and is given by

$$\frac{|u_{0\ell}(\rho^{\max}, \varphi, z)|}{E_0/\omega} = \frac{1}{\sqrt{1 + z^2/z_R^2}} \frac{|\ell|^{|\ell|/2}\, \mathrm{e}^{-|\ell|/2}}{\sqrt{|\ell|!}}\,. \tag{1.47}$$

For $p > 0$ however the value has to be computed numerically. The normalised maximum value of the amplitude is represented in fig. 1.4 for different values of $|\ell|$ and p. Finally one can show for $p = 0$ that

$$\frac{|u_{0\ell}(\rho^{\max}, \varphi, z)|}{E_0/\omega} \sim \frac{1}{\sqrt{1 + z^2/z_R^2}} |2\pi\ell|^{-1/4}\,,\ |\ell| \gg 1\,. \tag{1.48}$$

1.2.3 Phase structure and angular momentum

Let us look now in more details at the phase structure of the field. Since as previously mentioned,the increase of p adds rings in the amplitude distribution, we will look at the cases with $p = 0$ (only one ring) and and $\ell \neq 0$, the the generalization for the cases with $p > 0$ being straightforward. In this configuration, a LP LG beam has the following field structure. The transverse fields at focus consist in 2ℓ lobes rotating with time around the laser axis, as represented in fig. 1.1 for the $\ell = 1$ case. If $\ell > 0$ then the lobes are rotating counter-clockwise around the axis of propagation, if $\ell < 0$ then the rotation is clockwise. This behavior can also be seen in the wavefronts of the beam. For LG beams these are surfaces satisfying for a fixed time the equation

$$\frac{k\rho^2}{2R(z)} + kz + \ell\varphi = C \tag{1.49}$$

with C a constant.

One should remark that contrary to the gaussian beam (corresponding to $\ell = 0$), here the wavefronts depend on ℓ. This equation describes wavefronts with an helical shape, which are spiraling around the axis of propagation as it is pictured near focus in fig. 1.5. This has a strong consequence as the electric and magnetic fields lie into the surface of the wavefronts. It means that if the wavefronts are not orthogonal to the direction of propagation then there is a longitudinal component in the electromagnetic field as the projection of it onto the axis of propagation is not zero. This strongly impacts the linear and angular momentum of the field as it will be explained in the following.

In order to compute the field momentum one has to start from the well

Figure 1.5: Wavefront of and LP LG beam with $\ell = 1$ near focus. One can see it is a spiral rotating around the axis of propagation z.

known Poynting vector

$$\boldsymbol{\Pi} = \frac{\boldsymbol{E} \times \boldsymbol{B}}{\mu_0}\,, \tag{1.50}$$

where μ_0 is the magnetic permeability of vacuum. From there one can write the linear and angular momentum densities [Jackson, 1999]

$$\boldsymbol{p} = \frac{\boldsymbol{\Pi}}{c^2}\,, \tag{1.51}$$

$$\boldsymbol{j} = \boldsymbol{r} \times \frac{\boldsymbol{\Pi}}{c^2} = \boldsymbol{r} \times \boldsymbol{p}\,, \tag{1.52}$$

where $\boldsymbol{r}$ is the position. However one might be more interested in the average density over a wave period, which is

$$\langle \boldsymbol{p} \rangle = \frac{\epsilon_0}{2}(\boldsymbol{\mathcal{E}}^* \times \boldsymbol{\mathcal{B}} + \boldsymbol{\mathcal{E}} \times \boldsymbol{\mathcal{B}}^*), \tag{1.53}$$

$$\langle \boldsymbol{j} \rangle = \boldsymbol{r} \times \langle \boldsymbol{p} \rangle\,, \tag{1.54}$$

where ϵ_0 is the vacuum dielectric permittivity. It can already be seen from these relations that the component of the angular momentum along the direction of propagation $\langle j_z \rangle$ can only exist if $p_\varphi \neq 0$. In the paraxial approximation the linear momentum average density is related to the complex amplitude by [Allen, 1992]

$$\langle \boldsymbol{p} \rangle = \frac{\epsilon_0}{2}\left[i\omega\left(u^* \boldsymbol{\nabla} u - u \boldsymbol{\nabla} u^*\right) + \omega s \hat{\boldsymbol{z}} \times \boldsymbol{\nabla}|u^2| + 2k\omega|u|^2 \hat{\boldsymbol{z}}\right]\,, \tag{1.55}$$

with s defined as in (1.34). The total average momenta can then be obtained simply by using

$$\langle \boldsymbol{P} \rangle = \int \mathrm{d}^3x \langle \boldsymbol{p} \rangle\,, \tag{1.56}$$

$$\langle \boldsymbol{J} \rangle = \int \mathrm{d}^3x \langle \boldsymbol{j} \rangle\,. \tag{1.57}$$

Now let us look at the particular case of LG beams for which the computation of their angular momentum was first presented by [Allen, 1992]. The angular and linear momentum densities along the propagation direction are given by

$$\langle p_z \rangle = k\varepsilon_0\omega|u_{p\ell}|^2\,, \tag{1.58}$$

$$\langle j_z \rangle = \epsilon_0\omega\left(\ell|u_{p\ell}|^2 + \frac{s\rho}{2\omega}\frac{\partial|u_{p\ell}|^2}{\partial\rho}\right)\,. \tag{1.59}$$

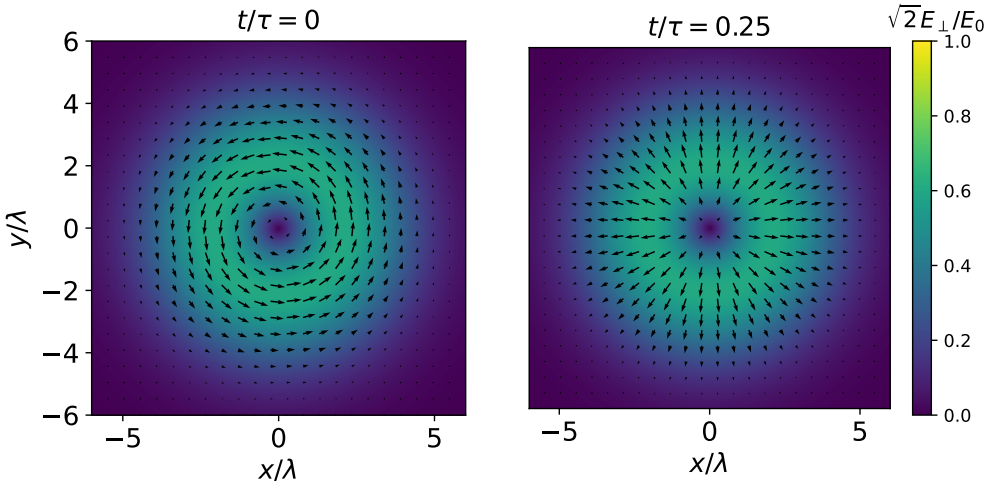

Figure 1.6: Transverse electric field (arrows) and maximum amplitude distribution (in colour) of a left handed CP LG beam of order $(p;\ell) = (0;1)$, at two different times. The waist is chosen to be $w_0 = 3\lambda$.

The angular momentum can then be split into two terms one proportional to ℓ and another one proportional to s related to the polarisation. In order to interpret the significance of those terms, one can compute the ratio between the flux of angular momentum and the flux of linear momentum along the propagation direction

$$\begin{aligned}\frac{\int_0^{2\pi}\mathrm{d}\varphi\int_0^{+\infty}\rho\mathrm{d}\rho\langle j_z\rangle}{\int_0^{2\pi}\mathrm{d}\varphi\int_0^{+\infty}\rho\mathrm{d}\rho\langle p_z\rangle} &= \frac{2\pi\epsilon_0\omega\left(\int_0^{+\infty}\mathrm{d}\rho\,\rho^2|u_{p\ell}|^2 + s\int_0^{+\infty}\mathrm{d}\rho\frac{\rho^2}{2}\frac{\partial|u_{p\ell}|^2}{\partial\rho}\right)}{2\pi k\omega\epsilon_0\int_0^{+\infty}\rho\mathrm{d}\rho|u_{p\ell}|^2}\,, \\ &= \frac{\ell-s}{k} = c\,\frac{\hbar(\ell-s)}{\hbar\omega}\,, \end{aligned} \tag{1.60}$$

where we used $k = \omega/c$ and multiply numerator and denominator by $\hbar$ in the last step. This can be interpreted as if each photon of energy $\hbar\omega$ has a total angular momentum of $\ell - s$. Then one can identify $\hbar\ell$ as an orbital angular momentum, and $-\hbar s$ as the spin part, as it is related to the field polarisation. To be clear, although the convention chosen here implies that $-s$ and not $+s$ is appearing in the angular momentum, one should recall that $s = -1$ is a right-handed circular polarisation, and so it is coherent to have a positive contribution to momentum from the spin along z in this case. One can check the rotation of the field on the figures of the two cases of CP LG in figs. 1.6 and 1.7. Although one is tempted to decompose total angular momentum in spin and orbital part, one should remember that in practice those terms are separately not gauge invariant and therefore not observable. However, it appears that in the paraxial conditions, these can be treated separately. In this work we will not discuss in details this subject. The interested reader

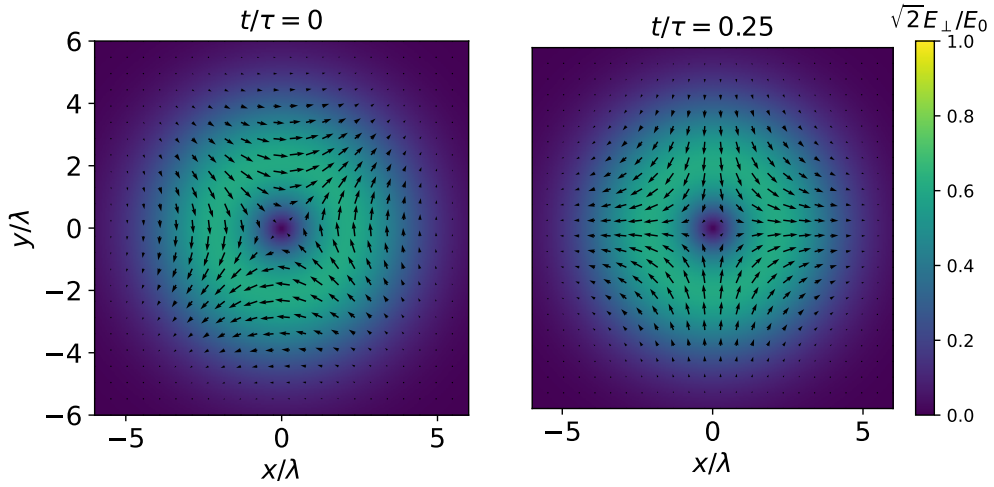

Figure 1.7: Transverse electric field (arrows) and maximum amplitude distribution (in colour) of a left handed CP LG beam of order $(p;\ell) = (0;-1)$, at two different times. The laser period is τ and the laser reaches focus at $t = 0$. The waist is chosen to be $w_0 = 3\lambda$.

are encouraged to check the following references on this topic [Barnett and Allen, 1994, Enk and Nienhuis, 1994, Barnett, 2010, Ornigotti and Aiello, 2014, Fernandez-Corbaton et al., 2014, Leader and Lorcé, 2014, Bliokh et al., 2014, Leader, 2018].

1.3 Conclusions

In this chapter we introduced the analytical framework to describe LG laser beams, and we discussed their properties. LG beams are a family of solutions of the paraxial wave equation, derived at the beginning of the chapter. The first section should provide the readers with the necessary information to retrieve the actual electromagnetic fields used in the next chapters starting from the complex amplitude of the LG modes. LG modes are characterised by two orders (p, ℓ). The order p is related to the number of rings in the transverse intensity distribution, which increases with p. This ring shape intensity could push particles toward the laser axis, where the field is zero, by ponderomotive effects, which can be interesting to trap particles. It has also been shown that LG beams carry orbital angular momentum, proportional to ℓ. In the rest of this work we will consider only $p = 0$ beams. Moreover LG beams can have different polarization, resulting in very diverse transverse electric field structures, from the rotating lobes of LP LG to the vortices, saddles and more complex structures of CP LG beams.

Chapter 2

Classical and strong-field quantum electrodynamics

Contents

In this chapter we will present the basics of classical electrodynamics (CED), and strong-field quantum electrodynamics (SFQED). This will allow to introduce the conventions and describe the classical radiation reaction approach. The basics of the SFQED approach that are required to understand the results of this thesis will be presented here, while the interested reader can find details on the derivations and an introduction in [Niel, 2021], where a more extended literature is also included. A modern review [Fedotov et al., 2022] is also covering all the recent work related to SFQED. The purpose of this chapter is to provide the reader with the key concepts behind the investigated phenomena.

2.1 Classical electrodynamics

2.1.1 Equations of motion for the fields and particles

Classical electrodynamics is a classical field theory which describes the classical relativistic behaviour of the electromagnetic field and charges. The fundamental object of the theory is its Lagrangian density, given by [Landau and Lifshitz, 1980]

$$\mathcal{L} = -\frac{1}{2}\rho_m \eta_{\mu\nu} u^\mu u^\nu - \frac{1}{4\mu_0} F^{\mu\nu} F_{\mu\nu} + J^\mu A_\mu \,, \tag{2.1}$$

where ρ_m is the mass per unit volume, which is expressed in the case of a single particle with a delta function such as $\rho_m = m\delta^3(\boldsymbol{x} - \boldsymbol{x}_{particle}(t))$ where $x_{particle}$ is the position of the particle, then u^μ is the 4-velocity 4-vector such that $u^\mu = \mathrm{d}x^\mu/\mathrm{d}\tau$ with τ the particle proper time, next μ_0 is the magnetic permeability of vacuum and $F^{\mu\nu} - \partial^\mu A^\nu = \partial^\nu A^\mu$, and is related to the usual electromagnetic field by Eq. (1.1). Finally $J^\mu = (\rho_e c, \boldsymbol{j}^\mu)$ is the 4-current 4-vector with ρ_e the charge per unit of volume and $\boldsymbol{j}_e$ the 3-vector current density.

The first term on the right hand side of Eq. (2.1) describes the dynamics of particles in vacuum, the second to electromagnetic field in vacuum and the last one to charges interacting with the electromagnetic field. Applying the Euler-Lagrange equations of motion (EOM) on A_μ on the second term alone brings back the Maxwell's equations of electromagnetism in vacuum (1.3) and (1.4). By adding the interaction term one then recovers the usual Maxwell's equations in the presence of charged particles

$$\partial_\mu F^{\mu\nu} = J^\nu \,, \tag{2.2}$$

$$\partial_\mu * F^{\mu\nu} = 0 \,. \tag{2.3}$$

Now on the side of particles, the EOM give for the case of a particle of 4-momentum p^μ of charge q

$$\frac{\mathrm{d}p^\mu}{\mathrm{d}\tau} = \frac{q}{m} F^\mu{}_\nu p^\nu \,. \tag{2.4}$$

When one separates the temporal and spatial components, using the electromagnetic fields and expressing the time in the laboratory frame, this gives

$$\frac{\mathrm{d}\gamma}{\mathrm{d}t} = \frac{q}{\gamma} \frac{\boldsymbol{E} \cdot \boldsymbol{p}}{m^2 c^2} \,, \tag{2.5}$$

$$\frac{\mathrm{d}\boldsymbol{p}}{\mathrm{d}t} = q\left(\boldsymbol{E} + \boldsymbol{v} \times \boldsymbol{B}\right) \,, \tag{2.6}$$

where $\boldsymbol{p} = \gamma m \boldsymbol{v}$ with γ the Lorentz factor of the particle. Now that we have obtained these equations, let us apply them to the case of a charge in the strong field of the plane wave, as it is relevant for the present work.

2.1.2 Trajectories of a charged particle in a plane wave

Let us consider a plane wave given by a transverse potential vector $\boldsymbol{A}$ such that the electric and magnetic field are given by

$$\boldsymbol{E} = -\frac{\partial \boldsymbol{A}}{\partial t}\,, \tag{2.7}$$
$$\boldsymbol{B} = \boldsymbol{\nabla} \times \boldsymbol{A}\,. \tag{2.8}$$

Let us assume the wave propagates along the z axis, then one can show [Landau and Lifshitz, 1980] for a particle initially at rest that

$$\boldsymbol{p}_\perp = -q\boldsymbol{A}\,, \tag{2.9}$$
$$\frac{p_z}{mc} = \frac{1}{2}\left(\frac{\boldsymbol{p}_\perp}{mc}\right)^2\,, \tag{2.10}$$
$$\gamma = 1 + \frac{p_z}{mc} = 1 + \frac{1}{2}\left(\frac{q\boldsymbol{A}}{mc}\right)^2\,, \tag{2.11}$$

where $\boldsymbol{p}_\perp$ is the momentum in the plane transverse to the direction of propagation of the wave.

Linearly polarised plane wave

If one assumes that the monochromatic plane wave is linearly polarised

$$\frac{q\boldsymbol{A}}{mc} = a\cos(\omega t - kz)\hat{\boldsymbol{y}}\,, \tag{2.12}$$

then it can be shown [Landau and Lifshitz, 1980, Mora, 2021] that for a particle initially at rest in $z = 0$

$$ky(t) = a\sin(\omega t)\,, \tag{2.13}$$
$$kz(t) = \frac{a^2}{8}\left[2\omega t + \sin(2\omega t)\right]\,, \tag{2.14}$$
$$v_{drift} = \frac{a^2/4}{1 + a^2/4}c\,, \tag{2.15}$$
$$\gamma_{drift} = 1 + a^2/2\,, \tag{2.16}$$

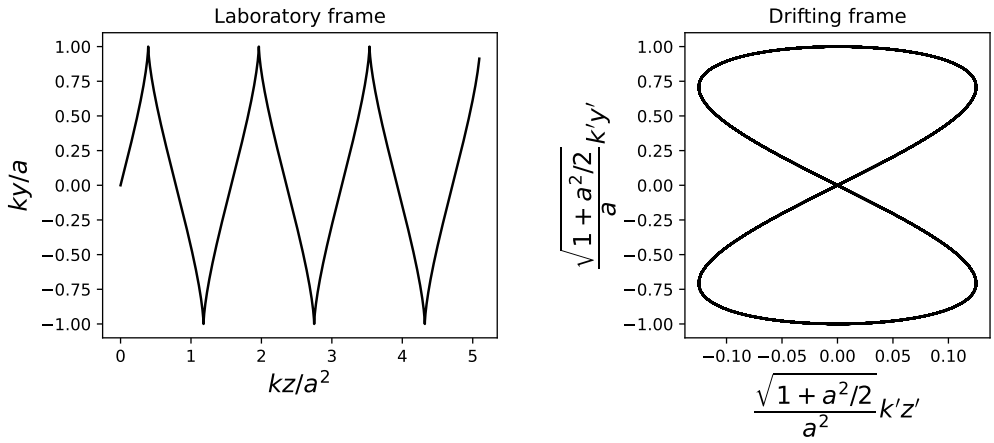

Figure 2.1: Trajectory of a positive charge in a LP plane wave in the laboratory frame (left) and the drifting frame (right). The particle is drifting in the propagation direction of the wave z with a Lorentz factor of $\gamma_{drift} = 1 + a^2/2$.

where $k = \omega/c$ is the wave number, and v_{drift} is the drifting speed of the particle along the propagation direction of the wave.

The trajectory of the particle is represented in fig. 2.1. Then one can move to the frame drifting at constant velocity v_{drift}. In this frame one has

$$k'y'(t') = \frac{a}{\sqrt{1+a^2/2}} \sin(\omega' t') \,, \tag{2.17}$$

$$k'z'(t') = \frac{a^2}{8(1+a^2/2)} \sin(2(\omega' t') \,, \tag{2.18}$$

$$\omega' = \frac{\omega}{\sqrt{1+a^2/2}} \,. \tag{2.19}$$

In this frame, the trajectory is an eight shape curve in the yz plane as represented in fig. 2.1.

Circularly polarised plane wave

Let us assume that the plane wave is circularly polarised, so that

$$\frac{q\boldsymbol{A}}{mc} = a\left[\cos(\omega t - kz)\hat{\boldsymbol{x}} + \sin(\omega t - kz)\hat{\boldsymbol{y}}\right] \,. \tag{2.20}$$

In this configuration, the trajectory is given by

$$
\begin{aligned}
kx(t) &= -a\cos(\omega t)\,, && (2.21)\\
ky(t) &= a\sin(\omega t)\,, && (2.22)\\
kz(t) &= \frac{a^2}{2}\omega t\,, && (2.23)\\
v_{drift} &= \frac{a^2/2}{1+a^2/2}\,c\,, && (2.24)\\
\gamma_{drift} &= 1+a^2/2\,. && (2.25)
\end{aligned}
$$

The trajectory in the laboratory frame is then an helix. As for the LP case, one can go to the drifting frame, where the trajectory this time is a circle in the transverse plane.

2.1.3 Classical radiation reaction

What is usually studied when first looking at CED is the trajectory of particles in a given imposed external field. However the moving charges might be radiating, therefore modifying the surrounding electromagnetic field that they are interacting with. Because of this, they experience experienced a back reaction. This becomes particularly important as the external field amplitude increases. In order to solve exactly the trajectory of a particle one should solve consistently the equations of motion with $F^{\mu\nu} = F^{\mu\nu}_{ext} + F^{\mu\nu}_{rad}$, where ext designates the imposed electromagnetic field and rad the field emitted by the moving charge. Of course the latter depends in a non trivial way on the first. The problem of taking into account the back reaction of the radiation on the particle, called radiation reaction, is an old and difficult problem of CED [Dirac, 1938, Jackson, 1999, Rohrlich, 2008]. Several equations of motion have been proposed to take into account this effect, starting from the Lorentz-Abraham-Dirac equation, which can lead to nonphysical solutions, to more recent developments [Di Piazza et al., 2011] including the fact that quantum effects may became important, especially at high field intensities [Niel et al., 2018a]. In this thesis, the RR approach will be used to understand some of the results of chapter 6. We will here briefly present the classical Landau and Lifshitz (LL) radiation reaction force [Landau and Lifshitz, 1980]. The equation of motion they derived for an electron reads

$$
\frac{\mathrm{d}p^\mu}{\mathrm{d}\tau} = -\frac{e}{mc}F^{\mu\nu}p_\nu + g^\mu\,, \qquad (2.26)
$$

where

$$g^{\mu} = -\frac{2}{3}\,\tau_e \left[\frac{e}{m^2 c}\partial_\eta F^{\mu\nu} p_\nu p^\eta + \frac{e^2}{m^2 c^2}\,F^{\mu\nu}F_{\eta\nu}p^\eta - \frac{e^2}{m^4 c^4}\,F^{\nu\eta}p_\eta F_{\nu\alpha}p^\alpha p^\mu\right], \tag{2.27}$$

where τ_e is the time for light to cross the classical radius of the electron $r_e = \dfrac{e^2}{4\pi\epsilon_0 m c^2}$. In the 3-vector notation this is written as

$$\begin{aligned}
mc^2\frac{\mathrm{d}\gamma}{\mathrm{d}t} &= -ec\boldsymbol{u}\cdot\boldsymbol{E} - \frac{2}{3}\,ec\tau_e\gamma\frac{\mathrm{d}\boldsymbol{E}}{\mathrm{d}t}\cdot\boldsymbol{u} \\
&+ \frac{2}{3}\,\frac{ec}{E_{cr}}\boldsymbol{E}\cdot(\boldsymbol{E}+\boldsymbol{u}\times c\boldsymbol{B}) \\
&- \frac{2}{3}\,\frac{ec}{E_{cr}}\gamma^2\left[(\boldsymbol{E}+\boldsymbol{u}\times c\boldsymbol{B})^2 - (\boldsymbol{u}\cdot\boldsymbol{E})^2\right], \qquad (2.28)\\
\frac{\mathrm{d}\boldsymbol{p}}{\mathrm{d}t} &= -e\,(\boldsymbol{E}+\boldsymbol{u}\times c\boldsymbol{B}) - \frac{2}{3}\,e\tau_e\gamma\left(\frac{\mathrm{d}\boldsymbol{E}}{\mathrm{d}t} + \boldsymbol{u}\times c\frac{d\boldsymbol{B}}{\mathrm{d}t}\right) \\
&+ \frac{2}{3}\,\frac{e}{E_{cr}}\left[(\boldsymbol{u}\cdot\boldsymbol{E})\boldsymbol{E} - c\boldsymbol{B}\times(\boldsymbol{E}+\boldsymbol{u}\times c\boldsymbol{B})\right] \\
&- \frac{2}{3}\,\frac{e}{E_{cr}}\gamma^2\left[(\boldsymbol{E}+\boldsymbol{u}\times c\boldsymbol{B})^2 - (\boldsymbol{u}\cdot\boldsymbol{E})^2\right]\boldsymbol{u}\,, \qquad (2.29)
\end{aligned}$$

where $E_{cr} = 4\pi\epsilon_0 m^2 c^4/e^3$ and $\boldsymbol{u} = \dfrac{\boldsymbol{p}}{\gamma m c}$. These equations, in the ultra-relativistic case $\gamma \gg 1$, reduce to

$$\begin{aligned}
mc^2\frac{\mathrm{d}\gamma}{\mathrm{d}t} &= -ec\boldsymbol{u}\cdot\boldsymbol{E} - \frac{2mc^2}{3\tau_e}\,\frac{\gamma^2}{E_{cr}^2}\left[(\boldsymbol{E}+\boldsymbol{u}\cdot c\boldsymbol{B})^2 - (\boldsymbol{u}\cdot\boldsymbol{E})^2\right], \qquad (2.30)\\
\frac{\mathrm{d}\boldsymbol{p}}{\mathrm{d}t} &= -e(\boldsymbol{E}+\boldsymbol{u}\times c\boldsymbol{B}) \\
&- \frac{2mc^2}{3\tau_e}\,\frac{\gamma^2}{E_{cr}^2}\left[(\boldsymbol{E}+\boldsymbol{u}\cdot c\boldsymbol{B})^2 - (\boldsymbol{u}\cdot\boldsymbol{E})^2\right]\frac{\boldsymbol{u}}{c\boldsymbol{u}^2}\,. \qquad (2.31)
\end{aligned}$$

The first term in the right hand side of the momentum equation is the usual Lorentz force, while the last term acts like a friction force parallel to $-\boldsymbol{u}$. Please note that this approach is not valid when quantum effects become important, which is usually the case when the field amplitude a_0 is above a few hundreds as it will be in the studied configurations of the present work. Indeed in the regime dominated by quantum effects the emission of radiation by a charge becomes a stochastic process, and not a continuous one as given by the LL description [Niel et al., 2018a]. In the next section we will describe briefly the main aspects of quantum electrodynamics in strong fields, we will introduce all quantities necessary to explain what is a strong field and when quantum effects become important in most of the cases encountered in this work.

2.2 Strong-field quantum electrodynamics (SFQED)

2.2.1 Relevant quantities and general context

Strong field quantum electrodynamics is a part of quantum electrodynamics (QED), which describes QED processes with the addition of a strong electromagnetic background field. In order to understand what is meant by strong, one should find a field of reference. This field is called the Schwinger field. QED predicts that having a constant electromagnetic field of this amplitude in vacuum creates electron-positron (e^- - e^+) pairs [Schwinger, 1951, Sauter, 1931]. The order of magnitude of this critical field can be obtained as follows. In quantum field theory, due to Heisenberg uncertainty relation $\Delta\varepsilon\Delta t \sim \hbar$, the quantum vacuum is boiling with fluctuations which are virtual pairs of particles and anti particles [Schwartz, 2014]. These particles do not satisfy the mass shell relation, which is the reason why they are called virtual, and one can picture them as popping out of vacuum and annihilating on short timescales given by Heisenberg relation. The typical length scale at which these fluctuations occur is called the Compton wavelength

$$\lambda_C = \frac{\hbar}{mc}\,, \tag{2.32}$$

where m is the mass of the particles. Here only electrons and positrons will be considered. This is usually done in SFQED works, since they are the leptons with the lightest mass and so they have the lowest critical field. Also, QED alone only describes photons, electrons and positrons. Then to estimate the Schwinger field, one should remark that, in order to get those pairs out of vacuum, the electric field needs to bring them on-shell, with at least an energy of mc^2, in a Compton wavelength. Then one obtains the magnitude of the electric Schwinger field

$$E_S = \frac{m^2c^3}{e\hbar} \simeq 1.3 \times 10^{18}\,\mathrm{V/m}\,. \tag{2.33}$$

Even though high intensity laser technologies achieved major progress over the last decades [Keller, 2003] this field is far from being reached in the laboratory frame.

However, there is still intense research to demonstrate SFQED processes in the laboratory, starting with the seminal SLAC experiment [Burke et al., 1997] where around a hundred pairs were produced, in the 22000 head-on collisions of a 46.6 GeV electrons beam with a high intensity laser beam of $10^{18}\mathrm{W/cm^2}$. To understand why, one needs to come back to basic properties

of special relativity. Indeed the electromagnetic field amplitude is a frame dependent quantity, as the fields are components of the electromagnetic field strength tensor, they are changed following Lorentz transformations. Roughly, if one imagines a head-on collision between a plane wave and an relativistic electron, the field amplitude is boosted by a factor γ_e, the Lorentz factor of the electron. For this reason SFQED processes are usually characterised by two Lorentz invariant parameters. The first one is the normalised field amplitude a_0 defined in (1.40). The other one is called the quantum parameter, which is given for an electron or a positron by [Ritus, 1979]

$$\chi_e = \frac{|F_\mu{}^\nu p_\nu|}{E_S mc}\,, \tag{2.34}$$

where $|B^\mu| = B^\mu B^\nu \eta_{\mu\nu} = (B^0)^2 - (B^1)^2 - (B^2)^2 - (B^3)^2$. This parameter is the norm of the contraction of the field strength tensor with the momentum of the particle, normalised to the Schwinger field. One can immediately see from its definition in Eq. (2.34) that this quantity is a Lorentz invariant. For ultra-relativistic particles and field less intense than the critical Schwinger field, which will be the main interest of this thesis, one has

$$\chi_e \underset{\gamma_e \gg 1}{\simeq} \frac{\gamma_e}{E_S} \|\boldsymbol{E}_\perp + \boldsymbol{v_e} \times \boldsymbol{B}_\perp\|\,, \tag{2.35}$$

where $\boldsymbol{E}_\perp$ and $\boldsymbol{B}_\perp$ designate the electric and magnetic fields transverse to the particle momentum, and $\boldsymbol{v}_e$ is its velocity. From this equation one can give a simple interpretation of the quantum parameter as the ratio of the magnitude of the electromagnetic field transverse to its motion and the Schwinger field. Therefore one can now understand that the threshold for strong-field quantum processes is achieved when the quantum parameter of a particle is close to one or above, simply because in the charge rest frame, this field amplitude reaches the critical Schwinger value.

A different form of χ_e can be obtained by using the equations of motion (2.4) and plug them in (2.34)

$$\chi_e = \sqrt{-\frac{\hbar^2}{m^4 c^6}\left(\frac{\mathrm{d}p^\mu}{\mathrm{d}\tau}\right)^2} \tag{2.36}$$

which means that the quantum parameter of a charge can also be interpreted as the ratio of the instantaneous proper acceleration compared to the acceleration caused by the Schwinger field.

The SFQED phenomena that we are mainly interested in, and that will be presented in the next sections, are the radiation of a high energy gamma photon

by a charge interacting with a strong background field, and the conversion of a high energy photon interacting with the background into an electron positron pair. It turns out that, for gamma photons one can defined useful quantities analogous to the lepton case, such as its normalised energy γ_γ and its quantum parameter

$$\gamma_\gamma = \frac{\varepsilon_\gamma}{mc^2}\,, \tag{2.37}$$

$$\chi_\gamma = \frac{\hbar|F^{\mu\nu}k_\nu|}{E_S mc}\,, \tag{2.38}$$

where ε_γ is the energy of the gamma photon and k^ν its 4 wave vector. In the same way as for the electron, a quantum parameter of order one and above characterises the threshold of SFQED effects for photons. Moreover for a photon one has the exact expression

$$\chi_\gamma = \frac{\gamma_\gamma \|\boldsymbol{E}_\perp + \boldsymbol{c}\times\boldsymbol{B}_\perp\|}{E_S} = \frac{\gamma_\gamma}{E_S}\sqrt{\left(\mathbf{E}+\mathbf{c}\times\mathbf{B}\right)^2 - \left(\mathbf{c}\cdot\mathbf{E}\right)^2/c^2} \tag{2.39}$$

which will be used extensively in part II.

Before moving to the two main processes that will be relevant to this work, some general remarks on SFQED will be made. Usually in perturbative quantum field theory and high energy physics, asymptotic states of particles after interaction are considered free. It means that particles interaction is generally studied within the interaction picture, where one supposes that initially and at the end of the interaction, particles do not interact and are free in vacuum. Then one can compute the cross section of the desired process, via a perturbative expansion. This is where the famous Feynman diagrams come into play. They are terms of a perturbative expansion, used to compute matrix elements, that can finally be translated into cross sections or decay rates of particles. Contrarily to this approach, when considering SFQED particles are not free after interaction. Instead of vacuum, one has this strong field, which can also be a plane wave, or a coherent state [Glauber, 1963, Fradkin et al., 1991, Harvey et al., 2009]. One possible scheme to investigate SFQED effects relies on the use of ultra high intensity lasers with optical frequencies. Those intense laser fields have a huge amount of soft photons, which have low energies compared to the gamma photons (which have energies above $2mc^2$). Because of this, the background field can be treated as a classical field on some aspects [Berestetskii et al., 1982, Niel, 2021]. Then SFQED can be used to describe the interactions of particles with this strong field in a non-perturbative way. To be precise, the interaction of charges together or with hard photons (high energy photons) is still treated perturbatively as in usual QED, but in

SFQED the interactions of particles with the background field are taken into account non-perturbatively, which makes nonlinear processes appearing. All of this procedure and theoretical framework is described in [Baier and Katkov, 1968, Ritus, 1979, Mitter, 1975, Baier et al., 1998, Di Piazza et al., 2012, Niel, 2021].

2.2.2 Nonlinear Breit-Wheeler process

The nonlinear Breit-Wheeler (NBW) process is the nonlinear version of the QED linear Breit-Wheeler process [Breit and Wheeler, 1934], which corresponds to the creation of an electron-positron pair from the collision of two high energy photons. The NBW process is the creation of an electron-positron pair by the conversion of a high energy gamma photon interacting with multiple photons of a strong field. It is represented by the diagram in fig. 2.2. The double line notation appearing for electrons and positrons is specific to SFQED. This double line represents the charge propagating in the strong field. The contribution of this double line would translate in the usual perturbative QED diagrams as the sum of all the diagrams of the charge interacting with n photons of the background strong field. The double line corresponds then to the sum of these diagrams from $n = 0$ to infinity. This means, as stated before, that the interaction between the charge and the background field is accounted for in a non-perturbative manner.

From this diagram, the differential probability of pair creation can be obtained after non trivial computations [Baier and Katkov, 1968, Ritus, 1979], using the Local Constant Field Approximation (LCFA) [Di Piazza, 2018, Ilderton et al., 2018], which supposes the typical length and time scales of the quantum process are small compared to the scales of variation of the background field. It is expressed as a function of the photon quantum parameter χ_γ and the quantum parameter χ_e of one of the charges (either the electron or the positron), from the Eqs. (2.38) and (2.34).

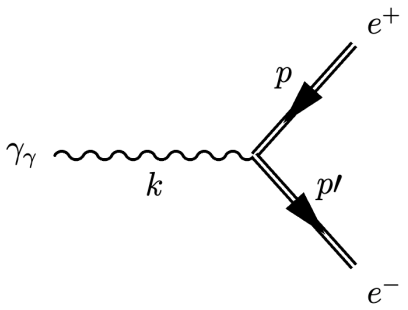

Figure 2.2: Strong field Feynman diagram of the nonlinear Breit-Wheeler process.

$$\frac{\mathrm{d}^2 N_{BW}}{\mathrm{d}t\mathrm{d}\chi_e} = \frac{2\alpha mc^2}{3\hbar}\frac{T_{BW}(\chi_\gamma,\chi_e)}{\chi_\gamma\gamma_\gamma} \equiv W_0\frac{T_{BW}(\chi_\gamma,\chi_e)}{\chi_\gamma\gamma_\gamma} \tag{2.40}$$

$$T_{BW}(\chi_\gamma,\chi_e) = \frac{\sqrt{3}}{2\pi}\left[-\int_\mu^{+\infty}\mathrm{d}x K_{5/3}(x) + \frac{3}{2}\chi_\gamma\mu K_{2/3}(\mu)\right] \tag{2.41}$$

with $\mu = \dfrac{2\chi_\gamma}{3(\chi_\gamma-\chi_e)\chi_e}$ and $K_n(x)$ the modified Bessel functions of second kind. In Eq. (2.40) $\dfrac{\mathrm{d}^2 N_{BW}}{\mathrm{d}t\mathrm{d}\chi_e}$ is the differential probability of pair production. The quantity W_0 has the dimension of a rate and its numerical value is $W_0 \simeq 3.78\times10^{18}\,\mathrm{s}^{-1}$.

In order to obtain the rate of pair creation, it is first useful to express Eq. (2.40) with laboratory frame quantities, i.e. using γ_e instead of χ_e, one obtains

$$\frac{\mathrm{d}^2 N_{BW}}{\mathrm{d}t\mathrm{d}\gamma_e}(\chi_\gamma,\gamma_\gamma,\gamma_e) = W_0\frac{\xi T_{BW}(\chi_\gamma,\xi)}{\gamma_\gamma\gamma_e} \tag{2.42}$$

using $\xi = \chi_e/\chi_\gamma = \gamma_e/\gamma_\gamma$ and $\mu = \dfrac{2}{3\chi_\gamma\xi(1-\xi)}$.

To obtain the rate of pair creation, one should now integrate 2.42 over all the possible values of γ_e, meaning from $\xi = 0$ to $\xi = 1$

$$\frac{\mathrm{d}N_{BW}}{\mathrm{d}t} \equiv W_{\mathrm{BW}}(\chi_\gamma,\gamma_\gamma) = W_0\frac{b_0(\chi_\gamma)}{\gamma_\gamma} \tag{2.43}$$

$$b_0(\chi_\gamma) = \frac{\sqrt{3}}{2\pi}\int_0^1 \frac{\mathrm{d}\xi}{\xi\,(1-\xi)}\left[\frac{2}{3\chi_\gamma}\frac{1-2\xi}{(1-\xi)}\mathrm{K}_{5/3}\,(\mu) + \mathrm{K}_{2/3}\,(\mu)\right]. \tag{2.44}$$

The expression of b_0 is obtained by integrating by part the first term in 2.41. One can see that the rate of pair production can be then separated into a function of the quantum parameter χ_γ and another one depending on the energy of the gamma photon. Moreover, as χ_γ behaves like the product of the field amplitude and gamma photon energy ε_γ, one can see that W_{BW} is not affected in the same way by the field amplitude and the gamma photon energy, owing to its γ_γ factor in the denominator. Hence changing χ_γ, by varying one of these two parameters, does not influence the rate of the process in the same way. This aspect will be discussed extensively in the next chapters.

Finally, the two asymptotic forms of the b_0 function are

$$b_0(\chi_\gamma) \sim c_1\,\chi_\gamma\,e^{-8/(3\chi_\gamma)} \quad \text{for} \quad \chi_\gamma \ll 1\,, \tag{2.45}$$

$$b_0(\chi_\gamma) \sim c_2\,\chi_\gamma^{2/3} \quad \text{for} \quad \chi_\gamma \gg 1\,, \tag{2.46}$$

with $c_1 = 9\sqrt{6}/64 \simeq 0.344$ and $c_2 = 3^{2/3}45\,\Gamma^4(2/3)/(56\pi^2) \simeq 0.569$ ($\Gamma(x)$

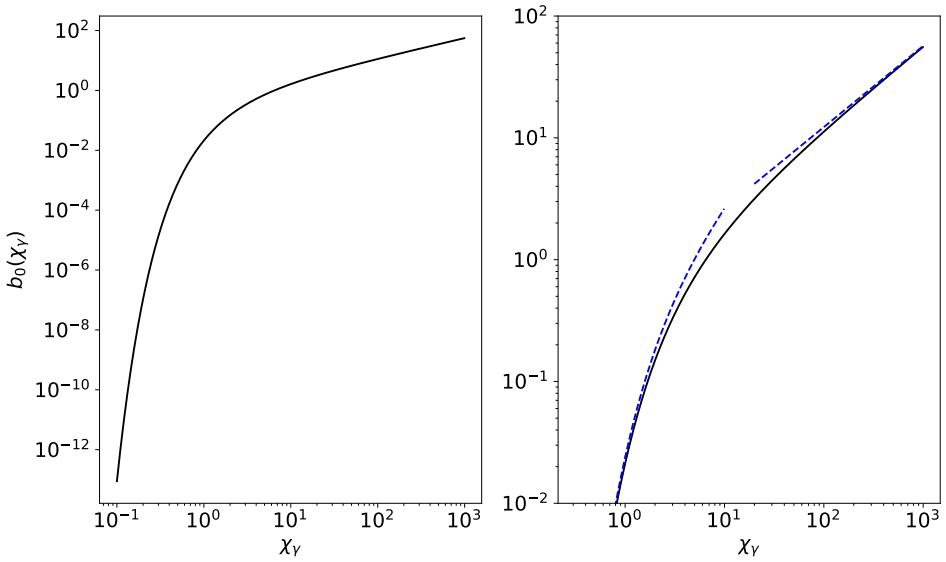

Figure 2.3: (a) Dependence of $b_0(\chi_\gamma)$ on the photon quantum parameter χ_γ as defined by Eq. (2.44). (b) Zoom on the region where $b_0 > 0.01$, the blue dashed lines are representing its asymptotic behaviour given by Eqs. (2.45) and (2.46)

denoting the Euler gamma function). The function b_0 is represented in fig. 2.3. It goes exponentially to 0 when $\chi_\gamma \ll 1$, which corresponds to the classical limit where indeed no pair creation takes place.

Finally, the b_0 function can be well approximated, within less than 1% of error for $\chi_\gamma \in [10^{-2}, 10^3]$ by

$$b_0(\chi_\gamma) \simeq 0.242 \, \frac{\mathrm{K}_{1/3}^2\big(4/(3\chi_\gamma)\big)}{1 - 0.172/(1 + 0.295\,\chi_\gamma^{2/3})} \,. \tag{2.47}$$

This equation gives the same behaviour at low and high χ as the two asymptotic limits of b_0 of Eqs. (2.45) and (2.46).

2.2.3 Nonlinear inverse Compton scattering

The Nonlinear inverse Compton scattering process is the emission of a high energy photon by a charge due to its interaction with several photons of a strong field. We chose here the charge to be an electron, but the reasoning would be the same for a positron. The strong field diagram representing the process at the first order is given in fig. 2.4.

Here again, using the LCFA, implying that the spatio-temporal variation of the field is much bigger than the emission time and length scale, one obtains [Baier and Katkov, 1968, Ritus, 1979, Seipt, 2012, Mackenroth, 2014] the differential probability of photon emission

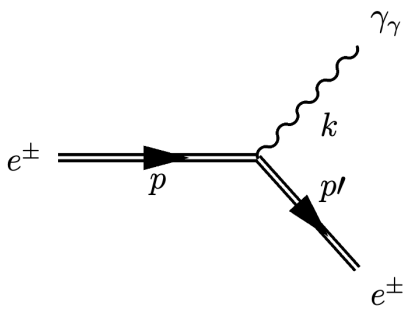

Figure 2.4: Strong field Feynman diagram of the nonlinear Compton scattering process.

$$\frac{\mathrm{d}^2 N_{CS}}{\mathrm{d}\tau \mathrm{d}\chi_\gamma} = \frac{2\alpha mc^2}{3\hbar}\frac{G(\chi_e,\chi_\gamma)}{\chi_\gamma} = W_0\frac{G(\chi_e,\chi_\gamma)}{\chi_\gamma} \tag{2.48}$$

$$G(\chi_e,\chi_\gamma) = \frac{\sqrt{3}}{2\pi}\frac{\chi_\gamma}{\chi_e}\left[\int_{\mu'}^{\infty}\mathrm{d}x K_{5/3}(x) + \frac{3}{2}\chi_\gamma\mu' K_{2/3}(\mu')\right] \tag{2.49}$$

where τ is the proper time of the electron, $\mu' = \dfrac{2\chi_\gamma}{3\chi_e(\chi_e-\chi_\gamma)}$ and $G(\chi_e,\chi_\gamma)$ the quantum emissivity. In Eq. (2.40) $\dfrac{\mathrm{d}^2 N_{BW}}{\mathrm{d}t\mathrm{d}\chi_e}$ is the differential probability of photon emission by the NCS process. As we did in the previous section, it is useful to express the differential probability with laboratory quantities by making the change of variable $\tau \to t$ and by using $\xi' = \chi_\gamma/\chi_e = \gamma_\gamma/\gamma_e; \mu' = \dfrac{2}{3\chi_e\xi'(1-\xi')}$. One obtains

$$\frac{\mathrm{d}^2 N_{CS}}{\mathrm{d}t\mathrm{d}\gamma_\gamma}(\chi_e,\gamma_\gamma,\gamma_e) = W_0\frac{\xi' G(\chi_e,\xi')}{\gamma_e\gamma_\gamma}\,. \tag{2.50}$$

One can obtain the rate of photon emission, by integrating Eq.(2.50) over all the possible values of γ_γ meaning from $\xi' = 0$ to 1

$$\frac{\mathrm{d}N_{CS}}{\mathrm{d}t} \equiv W_{\mathrm{CS}}(\gamma_e,\chi_e) = W_0\frac{c_0(\chi_e)}{\gamma_e} \tag{2.51}$$

$$c_0(\chi_e) = \frac{\sqrt{3}}{2\pi}\int_0^1 \frac{\mathrm{d}\xi'}{1-\xi'}\left[\mu' K_{5/3}(\mu') + \xi'^2 K_{2/3}(\mu')\right]\,, \tag{2.52}$$

where we obtain the expression of c_0 by integrating by part the first term of Eq. (2.49). The function c_0 has the following asymptotic behaviours

$$c_0(\chi_e) \sim \frac{5\sqrt{3}}{12}\chi_e \quad \text{for} \quad \chi_e \ll 1\,, \tag{2.53}$$

$$c_0(\chi_e) \sim 3^{2/3}\frac{7\,\Gamma(2/3)}{9}\chi_e^{2/3} \quad \text{for} \quad \chi_e \gg 1\,, \tag{2.54}$$

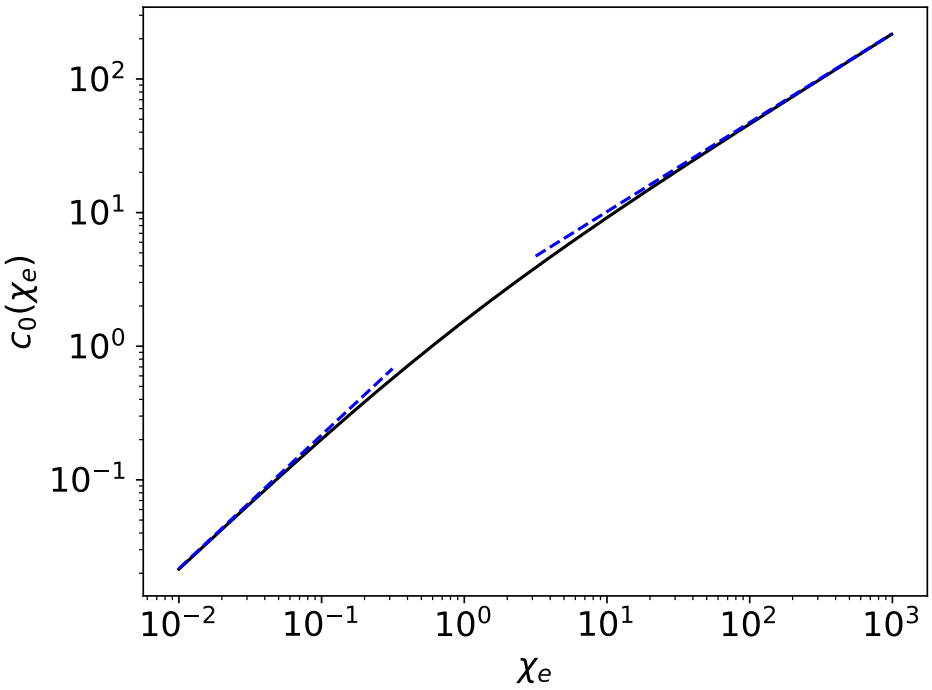

Figure 2.5: In black, the dependence of $c_0(\chi_e)$ on the electron quantum parameter χ_e as defined by Eq. (2.52). In dashed blue, the two asymptotes of c_0 defined in Eqs. (2.53) and (2.54).

with $3^{2/3}\dfrac{7\,\Gamma(2/3)}{9} \simeq 2.19$. This function and its asymptotic behaviours are represented in fig. 2.5.

2.3 Conclusions

In this chapter the fundamental equations and characteristic quantities of classical and strong-field electrodynamics necessary to understand the present work were summarised with particular attention to the Nonlinear Breit-Wheeler process and the nonlinear inverse Compton scattering. In particular, it was pointed out how, even though the critical Schwinger field is not reached in the laboratory with current laser technologies, pair creation and other strong field processes can still happen in current and upcoming laser facilities, by using ultra-relativistic seeding particles or photons. In the following we will use the concepts introduced here to model pair creation in the so-called shower configuration, where a beam of high gamma photons collides head-on with an high intensity laser pulse, mainly based on the NBW rate of Eq.(2.43). Intense photons production, based on nonlinear inverse Compton scattering will be instead important when considering the possibility of pair creation in the avalanche regime, discussed in Chaps. 6 and 7 for a configuration of two counter-propagating lasers.

Chapter 3

Numerical approach to simulate particle-field interaction: Particle-in-cell (PIC) codes

Contents

The Particle-in-cell (PIC) method, which was initially developed in fluid dynamics [Harlow, 1955], has become an essential tool in the simulation of plasma physics. This method, which is well suited for the kinetic description of collisionless plasmas, is used by the code Smilei [Derouillat et al., 2018], which has been used to perform all the simulations in this work. The PIC code, through the Maxwell-Vlasov model which will be detailed in the following, solves self-consistently the classical (relativistic) equations for the dynamics of the em fields and the charged particles composing the plasma. On top of simulating classical plasma dynamics, several physics module can be added to the PIC approach. In particular SFQED modules describing NBW and NCS

are implemented in SMILEI. In this chapter, we will present the basics of the PIC algorithm, and in particular of the SMILEI code.

3.1 The Maxwell-Vlasov model, normalised units and macro-particles

The Maxwell-Vlasov model consists first in Maxwell's equations

$$\boldsymbol{\nabla}\cdot\boldsymbol{E} = \rho/\epsilon_0\,, \tag{3.1}$$

$$\boldsymbol{\nabla}\cdot\boldsymbol{B} = 0\,, \tag{3.2}$$

$$\boldsymbol{\nabla}\times\boldsymbol{E} = -\partial_t\boldsymbol{B}\,, \tag{3.3}$$

$$\boldsymbol{\nabla}\times\boldsymbol{B} = \mu_0\boldsymbol{j} + \mu_0\epsilon_0\partial_t\boldsymbol{E}\,. \tag{3.4}$$

Then in the kinetic description of collisionless plasmas the different species of particles forming the plasma are characterised by a distribution function in phase space $f_s(\boldsymbol{x},\boldsymbol{p},t)$, with s denoting each species having a charge q_s and a mass m_s. The total charge and current densities are given by

$$\rho(t,\boldsymbol{x}) = \sum_s q_s \int \mathrm{d}^3p f_s(t,\boldsymbol{x},\boldsymbol{p})\ , \tag{3.5}$$

$$\boldsymbol{j}(t,\boldsymbol{x}) = \sum_s q_s \int \mathrm{d}^3p\, \boldsymbol{u} f_s(t,\boldsymbol{x},\boldsymbol{p})\ , \tag{3.6}$$

with $\boldsymbol{u} = \dfrac{\boldsymbol{p}}{m_s\gamma_s}$. The distribution of each species follows the Vlasov equation

$$\left(\partial_t + \frac{\boldsymbol{p}}{m_s\gamma_s}\cdot\boldsymbol{\nabla} + \boldsymbol{F}_L\cdot\boldsymbol{\nabla}_p\right) f_s = 0\,, \tag{3.7}$$

where $\gamma_s = \sqrt{1+(\boldsymbol{p}/m_sc)^2}$ is the Lorentz factor, $\boldsymbol{\nabla}_p$ is the gradient operator in momentum space, and $\boldsymbol{F}_L$ is the Lorentz force given by

$$\boldsymbol{F}_L = q_s(\boldsymbol{E} + \boldsymbol{u}\times\boldsymbol{B})\,. \tag{3.8}$$

The equations from (3.1) to (3.8) form the Maxwell-Vlasov model, which describes self-consistently the evolution of the electromagnetic field and the plasma. The fields affect the particles dynamics, their current and charge distribution, by the Lorentz force, and in turn this modification of the currents and charges distributions changes the electromagnetic fields.

The SMILEI code uses dimensionless variables normalised to specific reference quantities. The electron mass m, the elementary charge e and the speed

of light c provide the reference charge, mass and velocity. From them the reference energy mc^2 and momentum mc can be built. Now the main idea is that the code does not know the scale of the physical problem, the user can scale it back to the desired physical scale by providing the physical value of a reference quantity. In our case, we provide the reference laser frequency ω_r, which is usually the laser frequency. Then the results from the simulations can be put in the desired physical scale. Moreover this reference frequency can have a different role, as it is also used for physics modules which need to have the physical scale of the problem when the simulation is ran in order to work. It is the case for example of the ionisation or SFQED modules. Having set this reference frequency, now all needed referenced quantities can be built in the following way

$$
\begin{aligned}
T_r &= 1/\omega_r \quad \text{the reference time,} \\
L_r &= c/\omega_r \quad \text{the reference length,} \\
E_r &= mc\omega_r/e \quad \text{the reference electric field,} \\
B_r &= m\omega_r/e \quad \text{the reference magnetic field,} \\
n_r &= \epsilon_0 m\omega_r^2/e^2 \neq L_r^{-3} \quad \text{the reference particle density,} \\
J_r &= ceN_r \quad \text{the reference current density.}
\end{aligned}
$$

One can see that if ω_r is the laser frequency ω, as it is assumed from now on, the electric field normalised to its reference E/E_r is equal to the normalised field a_0 presented in (1.40) which is convenient. One should also note that N_r the reference number of particle density is not L_r^{-3}, in order to make the Vlasov equation simpler and written as Eq. (3.7) in normalised quantities. Finally the Maxwell's equations can be written as follows in normalised quantities

$$
\begin{aligned}
\boldsymbol{\nabla} \cdot \boldsymbol{E} &= \rho \,, && (3.9) \\
\boldsymbol{\nabla} \cdot \boldsymbol{B} &= 0 \,, && (3.10) \\
\boldsymbol{\nabla} \times \boldsymbol{E} &= -\partial_t \boldsymbol{B} \,, && (3.11) \\
\boldsymbol{\nabla} \times \boldsymbol{B} &= \boldsymbol{j} + \partial_t \boldsymbol{E} \,. && (3.12)
\end{aligned}
$$

Macro-particles

One of the main aspect of the PIC algorithm is the discretisation of the distribution function f_s. The distribution function is decomposed in the sum of

N_s macro-particles

$$f_s(\boldsymbol{x}, \boldsymbol{p}, t) = \sum_{p=1}^{N_s} \frac{w_p}{V_c} S(\boldsymbol{x} - \boldsymbol{x}_p(t)) \delta^3(\boldsymbol{p} - \boldsymbol{p}_p(t)) \,, \tag{3.13}$$

with $\boldsymbol{p}_p$ and $\boldsymbol{x}_p$ the momentum and position of the macro-particle and w_p its *weight*, which ponders the relative contribution of the particle to the distribution function. The quantity V_c is the hyper-volume of a cell, given by the spatial resolution of the simulation. The delta function is the usual Dirac's delta distribution. S is called the shape function and it describes how the properties (charge and current density) associated to the macro-particle are distributed around its position in space. The expression of the shape function depends on the spatial resolution of the simulation, and on order of the interpolation of the electromagnetic field at the macro-particle position (which will be discussed in the following). For instance at order one the shape function has the form

$$S(\boldsymbol{x}) = \begin{cases} 1 - |\frac{x}{\Delta x}|)(1 - |\frac{y}{\Delta y}|)(1 - |\frac{z}{\Delta z}|) \,, \text{ if } |x| < \Delta x \text{ and } |y| < \Delta y \text{ and } |z| < \Delta z \\ 0 \text{ otherwise} \end{cases}$$

with $\Delta x \,;\, \Delta y \,;\, \Delta z$ being the resolution in the three spatial directions. To understand why the shape function presented above is generally better than Dirac's delta function, it is worth noticing that one macro-particle in general describes many physical particles of the plasma. The interested reader will find more details in [Derouillat et al., 2018]

In PIC codes, the Vlasov equation (3.7) is integrated along the continuous trajectories of the macro particles, whereas the Maxwell's equations are solved on a discrete spatial grid. The size of the grid steps in each spatial direction is chosen by the user. Each element of this grid is called a cell, and the evolution in time of the macro-particle dynamics is described on these cells, giving the name *Particle-in-cell* to the method. It can be shown that the macro-particles follow the equations of motions, by inserting Eq. (3.13) into the Vlasov equation (3.7)

$$\frac{\mathrm{d}\boldsymbol{u}_p}{\mathrm{d}t} = \frac{q_s}{m_s} \left(\boldsymbol{E}_p + \boldsymbol{u}_p \times \boldsymbol{B}_p \right) \,, \tag{3.14}$$

with $\boldsymbol{u}_p = \boldsymbol{p}_p / (\gamma_p m_s)$, and where $\boldsymbol{E}_p$ and $\boldsymbol{B}_p$ are the interpolated (as described in the following section) fields at the macro-particle position. One now has all of the ingredients at hand needed to describe the core of the PIC algorithm, the PIC loop which will be presented in the next section.

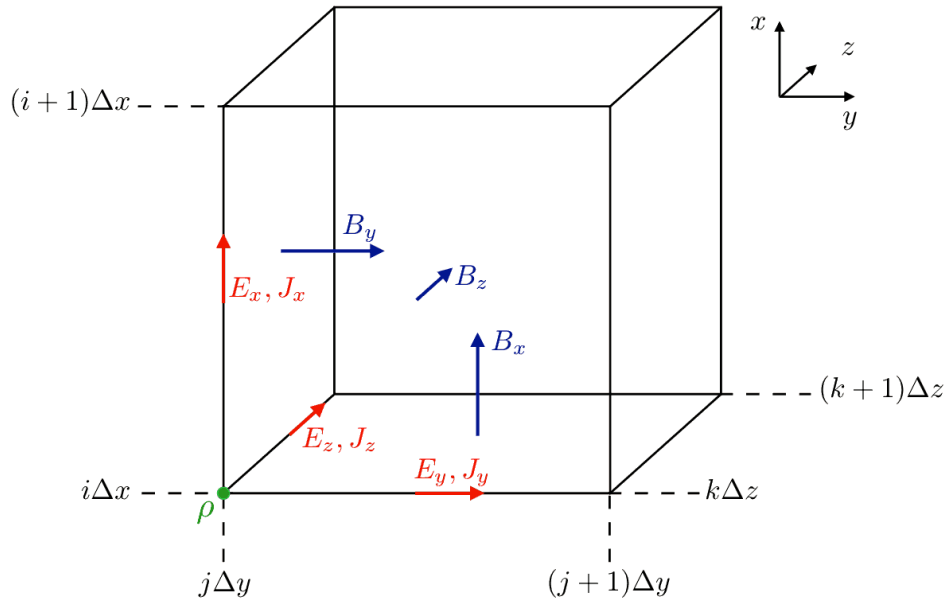

Figure 3.1: The staggered Yee grid in SMILEI as represented in [Derouillat et al., 2018], defined by the spatial resolutions $(\Delta x, \Delta y, \Delta z)$. The electric field as well as charge and current densities are defined at integer steps of the grid (i, j, k), whereas the magnetic field is defined at half integer steps.

3.2 The PIC loop

3.2.1 The field grid

In SMILEI the Maxwell equations are solved on a discrete grid by a refined version of the Finite Difference Time Domain method [Taflove et al., 2005, Nuter et al., 2014]. In this kind of method, the electromagnetic field is discretised onto a so-called staggered grid in space, like the Yee grid represented in fig. 3.1. This kind of grid allows the spatial centering of the discrete version of the curl operator used to solve Maxwell's equations. As shown in fig. 3.1, the electric field (as well the charge and current densities) is defined at integer steps i given by the spatial resolutions, while the magnetic field is solved at half integer steps $i+1/2$. The centering also needs to be done time-wise, and so the electric field is defined at integer time-steps n while the magnetic field is defined at half integer time-steps $n+1/2$. This centering is needed for the computation of the Lorentz force acting on particles, but also for the diagnostics.

A final remark about the grid and the discretisation in SMILEI and PIC codes in general is that the Yee grid may have one, two or three spatial dimensions. However the momentum space of macro particles, the fields and the current always have three dimensions in SMILEI. To denote it, sometimes we refer to a simulation as being 1D3V, or 3D3V for example, where ND identifies the number N of spatial dimension, and the 3V recalling that momentum space

has always three dimensions.

3.2.2 The initialisation of the simulation

The initialisation of the simulation is a three step process. First the code has to load the macro-particles. Especially the number of macro particles, speed, density and temperature of each species are specified in every cell by the user. Then the code creates uniformly or randomly spread macro-particles in each cell where the density is not zero, with a momentum distribution according to what the user has chosen, which can be a Maxwell-Jüttner distribution for example, with potentially a chosen average velocity and temperature. Then the weight of each particle, which was already introduced in Eq. (3.13), is computed

$$w_p = V_c \frac{n_s(\boldsymbol{x}_p, t=0)}{N_s(t=0)}\,, \tag{3.15}$$

with n_s the user specified density of the specie in the cell and N_s the number of macro-particles of the specie requested by the user in the cell.

The second step is the computation of the total charge and current densities on the grid. This is done by projecting the charge pondered by the weight and shape function of every macro-particle onto the grid

$$\rho_{\text{total}}(\boldsymbol{x}, t=0) = \sum_s \sum_p \frac{q_s w_p}{V_c} S(\boldsymbol{x} - \boldsymbol{x}_p(t=0))\,, \tag{3.16}$$

where s runs over the species and p runs over the macro-particles of a given species. Finally, the code has to compute the initial electromagnetic field from the charge and current distribution. In Smilei it is done by the conjugate gradient method [Press et al., 2007].

Since all of the initial conditions of the simulation are now known the algorithm can enter the PIC loop and find the numerical solution of the evolution in time of the Vlasov-Maxwell system of equations.

3.2.3 The loop

The heart of the PIC algorithm consists in a loop, which is performed for each time-step Δt. This loop can be decomposed in four tasks. First(i) the interpolation of the electromagnetic field from the grid at the macro-particle positions; (ii) the particle *pusher*, that computes their new velocities and positions due to the interaction with the electromagnetic fields; (iii) the projection of the new charge and current distributions on the grid; (iv) the computation of the new electromagnetic fields on the grid. After having performed these

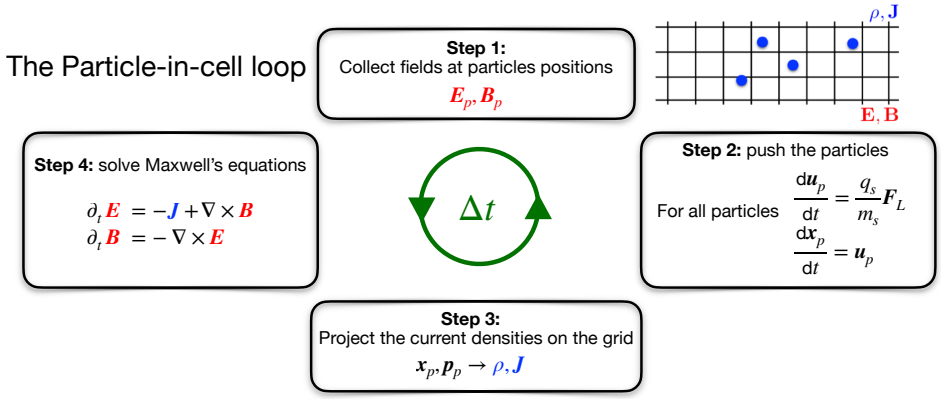

Figure 3.2: Schematic representation of the four steps of the PIC loop algorithm.

four steps the algorithm has gone from time-step n to time-step $n+1$ and the loop can start again. These four steps are schematically represented in fig. 3.2 and performed at each time-step Δt of the simulation. They will be described in more details in the following.

Fields interpolation

At the time-step n the particles positions and momentum are known and the fields $\boldsymbol{E}^{(n)}$ and $\boldsymbol{B}^{(n+1/2)}$ are known on the Yee grid. In order to see how the particles are impacted by the field, on first need to interpolate the field at the macro-particles position, since the fields are known on the grid and not everywhere in the cells. The interpolated fields are given by

$$\boldsymbol{E}_p^{(n)} = \frac{1}{V_c}\int \mathrm{d}^3x S(\boldsymbol{x} - \boldsymbol{x}_p^{(n)})\boldsymbol{E}^{(n)}(\boldsymbol{x})\,, \tag{3.17}$$

$$\boldsymbol{B}_p^{(n)} = \frac{1}{V_c}\int \mathrm{d}^3x S(\boldsymbol{x} - \boldsymbol{x}_p^{(n)})\boldsymbol{B}^{(n)}(\boldsymbol{x})\,, \tag{3.18}$$

where $\boldsymbol{B}^{(n)} = \frac{1}{2}\left(\boldsymbol{B}^{(n-1/2)} + \boldsymbol{B}^{(n+1/2)}\right)$ is the time centered magnetic field at time-step n, and $\boldsymbol{x}_p^{(n)}$ is the macro-particle position at time-step n.

Particles pusher

Having now the fields at particles' positions, one can compute the new position and momentum of each particle. It can be done using a second order leap-frog integrator such as the well-known Boris pusher [Boris, 1970]. The new

momentum and position are given by

$$\frac{\boldsymbol{p}_p^{(n+1/2)}}{m_s} = \boldsymbol{v}_p^{(n-1/2)} + \Delta t \frac{q_s}{m_s}\left[\boldsymbol{E}_p^{(n)} + \frac{\boldsymbol{v}_p^{(n-1/2)} + \boldsymbol{v}_p^{(n+1/2)}}{2} \times \boldsymbol{B}_p^{(n)}\right] \quad (3.19)$$

$$\boldsymbol{x}_p^{(n+1)} = \boldsymbol{x}_p^{(n)} + \Delta t \frac{\boldsymbol{p}_p^{(n+1/2)}}{m_s \gamma_p} \,. \quad (3.20)$$

Note that other schemes are available in Smilei such as the Vay pusher [Vay, 2008].

Charged density and current deposition

The new charge and current distribution projection on the grid, is performed by an algorithm proposed by [Esirkepov, 2001] which ensures charge conservation. The current densities along the spatial dimensions of the grid are computed from the charge flux crossing the cell border. The current on spatial dimensions that are not on the grid like in 1D3V or 2D3V simulations are computed by a projection.

As an example for a 2D3V simulations the contribution from a macro-particle to the current along x and y at position i, j in the grid are given by

$$(J_x)_{i+1/2,j}^{(n+1/2)} = (J_x)_{i-1/2,j}^{(n+1/2)} + \frac{q_s w_p}{V_c}\frac{\Delta x}{\Delta t}(W_x)_{i+1/2,j}^{(n+1/2)} \,, \quad (3.21)$$

$$(J_y)_{i,j+1/2}^{(n+1/2)} = (J_y)_{i,j-1/2}^{(n+1/2)} + \frac{q_s w_p}{V_c}\frac{\Delta y}{\Delta t}(W_y)_{i,j+1/2}^{(n+1/2)} \,, \quad (3.22)$$

with (W_x) and (W_y) given by the algorithm [Esirkepov, 2001] and computed with the particle present and past positions $x_p^{(n+1)}$ and $x_p^{(n+1)}$ respectively. Then the total current density along z and the total charge density, are given by the projection technique detailed in [Derouillat et al., 2018]

$$(J_z)_{i,j}^{(n+1/2)} = \sum_s \sum_p \frac{q_s w_p}{V_c} \boldsymbol{v}_p S(\boldsymbol{x}_{i,j} - \boldsymbol{x}_p) \quad (3.23)$$

$$\rho_{i,j}^{(n+1)} = \sum_s \sum_p \frac{q_s w_p}{V_c} S(\boldsymbol{x}_{i,j} - \boldsymbol{x}_p) \,. \quad (3.24)$$

Advancing electromagnetic field

Having the current at time-step $n + 1/2$ on the grid, the algorithm can now advance the electromagnetic field by solving the Maxwell equations. The code solves the Maxwell-Ampère equation, to have the advanced electric field on

the grid as

$$\boldsymbol{E}^{(n+1)} = \boldsymbol{E}^{(n)} + \Delta t \left[(\boldsymbol{\nabla} \times \boldsymbol{B})^{(n+1/2)} - \boldsymbol{J}^{(n+1/2)} \right] . \tag{3.25}$$

Next Maxwell-Faraday's equation is solved to obtain the advanced magnetic field.

$$\boldsymbol{B}^{(n+3/2)} = \boldsymbol{B}^{(n+1/2)} - \Delta t (\boldsymbol{\nabla} \times \boldsymbol{E})^{(n+1)} . \tag{3.26}$$

The reader interested in having more details about the computation of the discretised curl operator is encouraged to read [Derouillat et al., 2018]. The advanced field at the next time-step is completely determined by Eqs. (3.25) and (3.26). Indeed, it can be shown that Poisson's equation is verified at all time-steps if it is verified initially. Also the non diverging property of the initial magnetic field is maintained if Gauss's equation is verified initially.

This last step concludes the description of the PIC loop, which will be repeated at each time-step of the simulation until the end, and eventually solves self-consistently the Maxwell-Vlasov system. One part of the Smilei code is still lacking in our presentation in order to understand the simulations in this thesis, specifically the implementation of SFQED by complementary physics modules. These algorithms will be presented in the next section.

3.3 How to include quantum stochastic processes?

Having the main PIC loop, that allows us to classically simulate plasmas, one should now consider how to implement SFQED processes which are of interest in this work, namely high energy gamma emission by NCS and pair creation by NBW. Due to the stochastic nature of those processes, which are described by rates as discussed in section 2.2, what will be used is a Monte-Carlo procedure, as described in [Duclous et al., 2010b, Lobet, 2015, Lobet et al., 2016].

3.3.1 High energy photon emission

Let us first look at NCS. The emission of a high energy gamma photon through this process by an electron or a positron can be decomposed in the following steps.

A quantity called the optical depth δ_e is assigned to each macro-lepton and is set to zero at the beginning of the simulation. In order to identify the time of emission, we first draw random number $r_1 \in]0; 1]$ is drawn. Indeed the optical depth δ_e will evolve with time following the equation of the NCS (nonlinear

Compton scattering) rate from Eq. (2.51)

$$\frac{\mathrm{d}\delta_e}{\mathrm{d}t} = \frac{\mathrm{d}N_{CS}(\chi_e, \gamma_e)}{\mathrm{d}t}\,, \tag{3.27}$$

as the charge interacts with the field. When $\delta_e \geq \delta_f = -\log(r_1)$ emission occurs. Note that for the sake of performance, the integral of Eq. (2.51) is not computed every time, but it has been tabulated.

Third, at the time-step of emission one needs to compute the quantum parameter of the emitted gamma photon χ_γ. To do this, one needs to invert the cumulative distributive function

$$\mathcal{P}_e(\chi_e, \chi_\gamma) = \frac{\int_0^{\chi_\gamma} \mathrm{d}\chi G(\chi_e, \chi/\chi_e)/\chi}{\int_0^{\chi_e} \mathrm{d}\chi G(\chi_e, \chi/\chi_e)/\chi}\,. \tag{3.28}$$

The determination of χ_γ is done by drawing a random number $r_2 \in [0;1]$ and finding numerically the χ_γ that satisfies $r_2 = \mathcal{P}_e^{-1}(\chi_e, \chi_\gamma)$. The energy of the emitted gamma photon is then given by $\varepsilon_\gamma = \gamma_\gamma mc^2 = mc^2\gamma_e \dfrac{\chi_\gamma}{\chi_e}$.

Finally one has to take into account the back reaction onto the emitting charge by updating its momentum. This is done using momentum conservation, and by assuming that the photon is emitted in the direction of the charge momentum, which is a reasonable assumption for $\gamma_e \gg 1$. The variation of momentum of the charge is then

$$\Delta \boldsymbol{p_e} = -\frac{\varepsilon_\gamma}{c}\frac{\boldsymbol{p}_e}{\|\boldsymbol{p}_e\|}\,. \tag{3.29}$$

The radiation recoil experienced by the charge from the emission of the gamma photon is then taken into account discretely. This procedure does not conserve exactly the energy, but the error tends to zero when the electron energy increases [Lobet, 2015].

After this procedure, the algorithm might have to create or not a macro-photon. This is determined in practice by an energy threshold above which the code creates a macro-photon with the same statistical weight as the macro-charge that emitted it. In this work the threshold is fixed to $2mc^2$ as we are interested in gamma photons able to create pairs. These gamma photons do not interact with the classical field or other particles, unless other physical modules are added, like the NBW module which will be presented in the following section.

As a final remark, in this work we consider field intensities at which the radiation processes happen predominantly in the quantum regime. Hence a fully stochastic treatment is well suited for our study. Nevertheless, the description

of radiation emission with frequencies above the PIC grid resolution, is still an active area of research, in particular the transition between the classical and quantum treatment [Niel et al., 2018a].

3.3.2 Pair creation by nonlinear Breit-Wheeler

In this section, we use the same approach described in the previous one to present the implementation of NBW module in SMILEI.

Each macro-photon has an optical depth δ_γ, and it is converted into a pair when $\delta_\gamma = \delta_f = -\log(r_3)$ with $r_3 \in]0;1]$ a random number. In this case the time evolution of the optical depth is given by the NBW rate Eq. (2.43)

$$\frac{\mathrm{d}\delta_\gamma}{\mathrm{d}t} = \frac{\mathrm{d}N_{BW}(\chi_\gamma, \gamma_e)}{\mathrm{d}t}\,. \tag{3.30}$$

As for NCS, the rate is tabulated to speed up the numerical computation. Then, at the time of pair creation, one needs to compute the quantum parameter of the electron(analogously for the positron). This is done by inverting the cumulative distribution function

$$\mathcal{P}_\gamma(\chi_\gamma, \chi_{e^-}) = \frac{\int_0^{\chi_{e^-}} \mathrm{d}\chi T_{BW}(\chi_\gamma, \chi/\chi_\gamma)/\chi}{\int_0^{\chi_\gamma} \mathrm{d}\chi T_{BW}(\chi_\gamma, \chi/\chi_\gamma)/\chi}\,, \tag{3.31}$$

where χ_{e^-} is the quantum parameter of the produced electron and T_{BW} is defined in Eq. (2.41). As it was explained before for NCS, χ_{e^-} is found by numerically solving $\mathcal{P}_\gamma^{-1}(\chi_\gamma, \chi_{e^-}) = r_4$ with $r_4 \in [0;1]$ a random number. Knowing the quantum parameter of the electron, the one of the positron can be computed as $\chi_{e^+} = \chi_\gamma - \chi_{e^-}$.

Since the gamma photon is destroyed in the process, all the momentum and energy are transferred to the pair into the pair. The energy of the electron is given by

$$\varepsilon_{e^-} = mc^2 \left[1 + (\gamma_\gamma - 2)\frac{\chi_{e^-}}{\chi_\gamma}\right]\,. \tag{3.32}$$

The pair is then created at the position of the macro-photon with the same total momentum. The same weight as the macro-photon is assigned to each charge of pair and then the macro-photon is destroyed.

3.4 Conclusions

In this chapter we presented the basics of the PIC algorithm and the code Smilei. We explained how the PIC loop self-consistently solves the equations of the kinetic description of the plasma, i.e. the Maxwell-Vlasov model. We

also presented how SFQED stochastic processes can be included in the classical PIC code, by taking the example of NBW and NCS implementation which are relevant to the present work. PIC simulations with the additional MC modules for SFQED will be used extensively in parts two and three.

Part II

Theory and simulation of gamma photon conversion into electron-positron pairs

Chapter 4

Model of primary gamma photons conversion into pairs

Contents

In this chapter we present original results on the conversion of gamma photons into electron-positron pairs by intense laser pulses. The final aim is to study the complex interaction of an LG laser pulse with a flash of high energy gamma photons in order to optimise electron positron pair production. In order to do so one first needs to develop a model to study the impact of the different parameters characterizing the laser beam on pair production. In this chapter we will detail our approach for the development of such a model, by

starting from the simple case of a single gamma photon in a plane wave, and by including progressively more complex spatio-temporal time dependence for the field. These results are published in [Mercuri-Baron et al., 2021].

4.1 Decay probability of a high energy gamma photon: the building block of the model

In order to develop a model capable of predicting the amount of produced pairs one should start from the most basic block of the problem, the rate of the NBW process defined in Eq.(2.43)

$$W_{\mathrm{BW}}(\chi_\gamma, \gamma_\gamma) = W_0 \frac{b_0(\chi_\gamma)}{\gamma_\gamma}\,, \tag{4.1}$$

which depends on the normalised energy of the gamma photon γ_γ (2.37) and its quantum parameter (2.39)

$$\chi_\gamma = \frac{\gamma_\gamma \|\boldsymbol{E}_\perp + \boldsymbol{c} \times \boldsymbol{B}_\perp\|}{E_S} = \frac{\gamma_\gamma}{E_S}\sqrt{\left(\mathbf{E} + \mathbf{c} \times \mathbf{B}\right)^2 - \left(\mathbf{c} \cdot \mathbf{E}\right)^2/c^2}\,. \tag{4.2}$$

Since the electromagnetic field varies with time, $\chi_\gamma(t)$ is in general a function of time and of the photon energy. If the electromagnetic field and the trajectory of the gamma photon crossing the field are known, the decay rate is known. However in order to predict the amount of pair created through this interaction, we need the probability for a given gamma photon to be converted after a given time t of interaction. To obtain this, one can consider a set of gamma photons, all seeing the same electromagnetic field, and write the differential equation ruling the evolution of their number

$$\frac{\mathrm{d}N_\gamma(t)}{\mathrm{d}t} = -W_{\mathrm{BW}}(t) N_\gamma(t)\,. \tag{4.3}$$

This equation takes into account the production of primary pairs, i.e. the one coming form the conversion of the initial gamma photons flash. It however neglects the possibility of having secondary pairs. Indeed, when gamma photons are converted in pairs, the latter could be re-accelerated by the field and emit more gamma photons. However in this chapter we will limit our study to the soft shower regime, in which the soft shower is defined by the fact that secondary pairs are negligible in number compared to the primary pairs. The validity of this hypothesis will be verified by PIC simulations in chapter 5 for the range of parameters of interest.

Equation (4.3) describes how the number of gamma photons decreases with time due to their conversion into pairs. Since the rate is time dependent, one can write the general form of the number of gamma photons as a function of time as

$$N_\gamma(t) = N_0 \exp\left[-\int_{t_0}^{t} W_{\mathrm{BW}}(t')\mathrm{d}t'\right] \tag{4.4}$$

where t_0 is the initial time and N_0 the number of gamma photons at $t = t_0$. Since this takes into account only the conversion of gamma photons, for a large number of gamma photons the proportion of remaining photons, $N_\gamma(t)/N_0$, goes as the probability $\overline{P}(t_0, \Delta t)$ of a gamma photon to not be converted into a time interval Δt

$$\overline{P}(t_0, \Delta t) = N_\gamma(t)/N_0 = \exp\left[-\int_{t_0}^{t_0+\Delta t} W_{\mathrm{BW}}(t')\mathrm{d}t'\right] . \tag{4.5}$$

Then the probability of a photon to be converted in Δt is

$$P(t_0, \Delta t) = 1 - \overline{P}(t_0, \Delta t) = 1 - \exp\left[-\int_{t_0}^{t_0+\Delta t} W_{\mathrm{BW}}(t')\mathrm{d}t'\right] , \tag{4.6}$$

which is the probability of a pair to be formed by converting a gamma photon during the time interval Δt. Equation (4.6) allows to express the probability to create a pair as a function of the integral of the rate over time. This integral cannot be computed analytically in general. This is possible in the special case of the head-on collision of a gamma photon with a CP plane wave (PW) with constant amplitude. In this case the rate of pair production is a constant and Eq. (4.3) can be solved analytically. In a regime in which pair creation is weak one can consider small rates and relatively short times and approximate the integral of the rate by $W_{\mathrm{BW}}\Delta t$, i.e. a constant rate (given by asymptotic developments) times the duration of the interaction. Considering this quantity small and developing the exponential leads to $P(t_0, \Delta t) \sim W_{\mathrm{BW}}\Delta t$. However this is valid only for short duration of the interaction and small rate of pair production, and it fails when one has substantial pair production [Di Piazza et al., 2010, Meuren et al., 2015, Tamburini and Meuren, 2021, Podszus and Di Piazza, 2021], i.e. when one has $P(t_0, \Delta t) \sim 1$. In this small rate approximation the nonlinear growth and the saturation of probability with time will be missed. In this work we look at physical situations with substantial pair creation. We then need to consider the full probability of pair creation. In order for the model to estimate pair creation in this situation, the evaluation of the integral of the rate is needed. This will be discussed in the following section.

4.2 Probability of pair creation in a plane wave

4.2.1 Quantum parameter of a gamma photon in a plane wave

In order to evaluate the integral of Eq.(4.6), and discuss in detail its time dependence, let us consider the head-on collision of a high energy gamma photon with a plane wave. In the following the collision will always be head-on unless stated otherwise. In particular, the generalisation of the approach to an arbitrary angle of collision will be discussed in Sec. 4.2.2. Let us take the electric field of a plane wave propagating along z

$$\boldsymbol{E}(z,t) = \frac{E_0}{\sqrt{1+\sigma^2}} \left[\sin(\omega t - kz)\,\hat{\boldsymbol{x}} + \sigma\cos(\omega t - kz)\,\hat{\boldsymbol{y}}\right] , \tag{4.7}$$

where σ is its polarisation, and the factor $1/\sqrt{1+\sigma^2}$ is chosen so that *waves with every possible polarisation carry the same energy density*. This choice is motivated by the fact that when we consider more realistic configurations, we will work at fixed total laser energy. Considering a gamma photon with velocity $-c\hat{\boldsymbol{z}}$ (head-on collision), and using Eq. (2.39) one can show that, the quantum parameter of the gamma photon in is

$$\chi_\gamma(t) = \chi_0\,\Psi_\sigma(2\omega t) \quad \text{with} \quad \Psi_\sigma(\varphi) = \sqrt{\frac{\sin^2\varphi + \sigma^2\cos^2\varphi}{1+\sigma^2}} , \tag{4.8}$$

with

$$\chi_0 = 2\,\gamma_\gamma\,\frac{E_0}{E_S} \simeq 0.801 \left(\frac{\hbar\omega_\gamma}{1\,\text{GeV}}\right)\sqrt{\frac{I_0}{10^{22}\ \text{W/cm}^2}} . \tag{4.9}$$

Note that the quantum parameter takes the following simple forms for LP and CP PW

$$\chi_\gamma(t) = \frac{\chi_0}{\sqrt{2}} \quad \text{for } \sigma = \pm 1 , \tag{4.10}$$

$$\chi_\gamma(t) = \chi_0 |\sin(2\omega t)| \quad \text{for } \sigma = 0 , \tag{4.11}$$

where one can see that for the CP case the rate is constant over time.

Several remarks can be made here. First the quantum parameter is a product of a constant and the function Ψ, whose time dependence is related to the polarisation. The maximum value of χ_γ is

$$\chi_m = \frac{\chi_0}{\sqrt{1+\sigma^2}} , \tag{4.12}$$

and only for the LP case ($\sigma = 0$) this coincides with χ_0.

Secondly, the quantity $\Psi_\sigma(2\omega t)$ is a periodic function with period $\tau/4$ (τ being the period of the plane wave) for all polarisations. This is intuitively understandable by looking at the LP case. The quantum parameter depends on the absolute value of the field and, since the gamma photon and the PW collide head-on, the time for a photon to cross a peak of the field is a quarter of a period. This periodicity is a useful property of the quantum parameter, since before conversion into a pair the energy of the gamma photon does not vary with time, and the time dependence of the rate corresponds to the one of the quantum parameter. Therefore, if the latter is periodic, the value of the integral of the rate at any time equal to a multiple of quarter of periods, is known once we have the value of the integral over $\tau/4$.

4.2.2 Decay probability of a photon crossing half a period of the field

Taking advantage of the properties discussed in the previous section we can compute the probability P_m of the high-energy photon to decay into a pair during the interval of time $\tau/4$, that will become the basic element of our model. Let us then consider a time t_m at which the high-energy photon *sees* a local maximum of the background electric field, and compute the probability P_m for the high-energy photon to decay into an electron-positron pair in between the times $t_0 = t_m - \tau/8$ and $t_0 + \tau/4 = t_m + \tau/8$:

$$P_m = P(t_0, \tau/4) = 1 - \exp\left(-R_m \frac{\tau}{4}\right) \tag{4.13}$$

$$R_m \frac{\tau}{4} = \frac{W_0}{2\omega\gamma_\gamma} \int_0^\pi b_0\big(\chi_0 \Psi_\sigma(\varphi)\big)\, d\varphi \tag{4.14}$$

where $R_m\tau/4$ is the time-integrate rate and R_m denotes the average rate. The variable φ is the phase of the field, it goes from 0 to π as one local maximum of the field amplitude is explored.

The dimensionless quantity $W_0/(2\omega\gamma_\gamma)$ in Eq. (4.13) is of order 1 for optical background fields (with micrometric wavelength λ) and GeV-level high-energy photons:

$$\frac{W_0}{2\omega\gamma_\gamma} = \frac{\alpha}{3} \frac{m_e c^2}{\hbar\omega} \frac{m_e c^2}{\hbar\omega_\gamma} \simeq 0.512 \left(\frac{\lambda}{1\,\mu\mathrm{m}}\right) \left(\frac{1\,\mathrm{GeV}}{\hbar\omega_\gamma}\right) . \tag{4.15}$$

The probability P_m, that measures the contribution of a single field maxi-

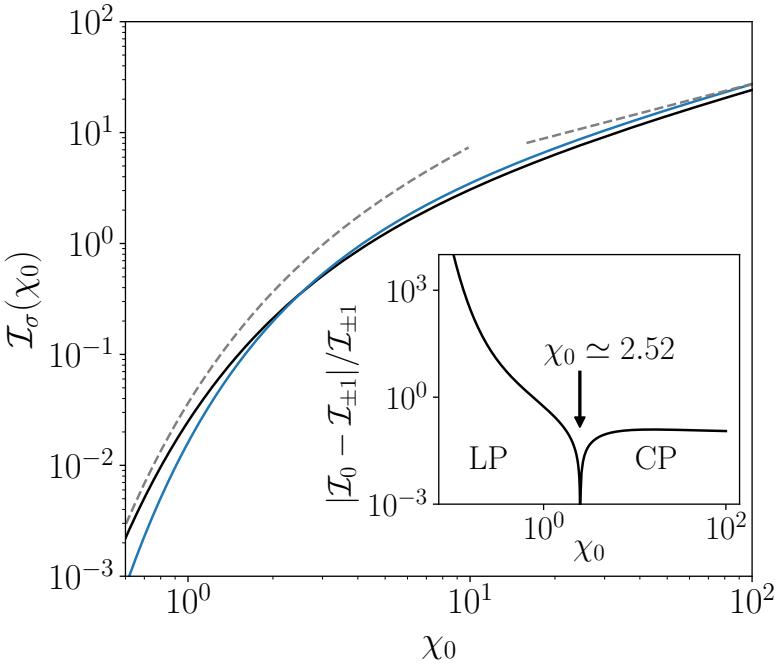

Figure 4.1: Dependence of $\mathcal{I}_\sigma(\chi_0)$ [Eq. (4.16)] on the maximum photon quantum parameter χ_0 [as defined by Eq. (4.9)], for a linearly polarized (LP) background field ($\sigma = 0$, black line) and a circularly polarized (CP) background field ($\sigma = \pm 1$, blue line). Dashed lines show the asymptotic behavior given by Eqs. (4.20) and (4.21) for the LP case. The inset highlights the values of χ_0 for which LP ($\chi_0 < 2.52$) or CP ($\chi_0 > 2.52$) gives higher pair production probability and the relative difference of $\mathcal{I}_\sigma$ (in absolute value) between the two cases.

mum, depends on the integral quantity

$$\mathcal{I}_\sigma(\chi_0) = \int_0^\pi b_0\big(\chi_0 \Psi_\sigma(\varphi)\big)\, d\varphi\,, \tag{4.16}$$

which, for a given polarization σ, is a function of χ_0 only as shown in fig. 4.1 for LP (black line) and CP (blue line).

This integral is the building block of our model and, as we will show, it can be used to compute the pair creation probability in an arbitrary configuration. It can be calculated analytically with very good approximation, as shown in the following, or numerically in order to have the exact solution.

The details of the analytical approximated form that we derived for $\mathcal{I}_\sigma$ are given in the Appendix A.1, where we generalize the approach proposed in [Blackburn et al., 2017] to arbitrary σ and χ. With this approach we obtain:

$$\mathcal{I}_\sigma(\chi_0) \quad \simeq \quad \pi\, b_0(\chi_m)\, \min\big\{F\big(s_\sigma(\chi_m)\big), f(\sigma)\big\} \tag{4.17}$$

$$\text{with} \quad \begin{cases} F(s) = \sqrt{2/\pi}\, s\, \mathrm{erf}\big(\pi\sqrt{2}/(4s)\big) \\ f(\sigma) = \frac{1}{\pi}\int_0^\pi \big[\sin^2\varphi + \sigma^2\cos^2\varphi\big]^{1/3} d\varphi \end{cases} \tag{4.18}$$

where χ_m is defined in Eq. (4.12) and $\mathrm{erf}(x) = \frac{2}{\sqrt{\pi}}\int_0^x e^{-t^2}dt$ is the error function. The function $F(s)$ emerges from the saddle point approximation used to compute the integral when the main contribution over a half period comes from the vicinity of the field maximum. The function varies slowly with s, as $F(s) \simeq \frac{2}{\sqrt{\pi}}s$ for $s \ll 1$ and $F(s) \to 1$ for $s \to +\infty$. In Eq. (4.17), $F(s)$ takes for argument $s_\sigma(\chi_m)$, with

$$s_\sigma(\chi) = \sqrt{\frac{3}{2}}\frac{c(\chi)}{\sqrt{1-\sigma^2}} \quad \text{and} \quad c(\chi) = \sqrt{\frac{2\, b_0(\chi)}{3\chi\, b_0'(\chi)}}\,, \tag{4.19}$$

where $b_0'(\chi)$ denotes the derivative of $b_0(\chi)$ and $c(\chi)$ is a slowly varying function of χ, as $c(\chi) \simeq \sqrt{\chi}/2$ for $\chi \ll 1$ and $c(\chi) \to 1$ for $\chi \to +\infty$.

Equation (4.17) is exact for CP background fields ($\sigma = \pm 1$) for which $s_{\pm1}(\chi_m) \to +\infty$, so that $\mathcal{I}_{\pm1}(\chi_0) = \pi\, b_0\big(\chi_0/\sqrt{2}\big)$. Moreover it allows to recover the asymptotic behavior of Eq. (4.16) in the limiting cases of small and large quantum parameter χ_0:

$$\mathcal{I}_\sigma(\chi_0) \xrightarrow{\chi_0 \ll 1} \begin{cases} c_3\, \frac{\chi_0^{3/2}}{(1-\sigma^2)^{1/2}(1+\sigma^2)^{1/4}} \exp\left(-\frac{8\sqrt{1+\sigma^2}}{3\chi_0}\right) & \text{if } \chi_0 \ll 1-\sigma^2 \\ c_4\, \chi_0\, \exp(-\frac{8\sqrt{2}}{3\chi_0}) & \text{otherwise} \end{cases} \tag{4.20}$$

$$\mathcal{I}_\sigma(\chi_0) \xrightarrow{\chi_0 \gg 1} c_5\, \frac{f(\sigma)}{(1+\sigma^2)^{1/3}}\, \chi_0^{2/3}\,, \tag{4.21}$$

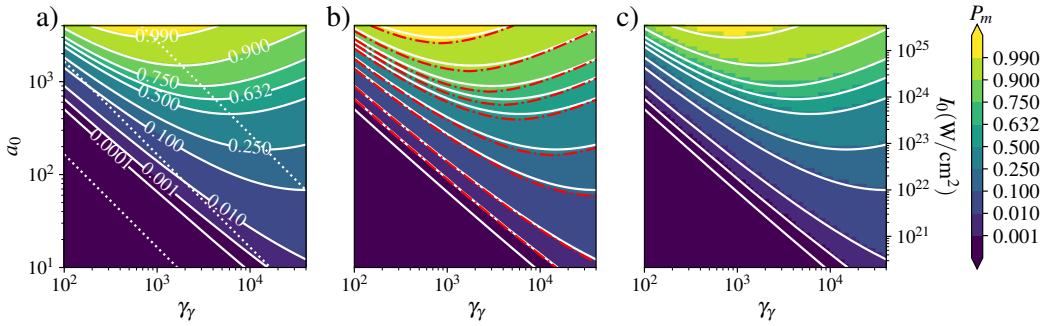

Figure 4.2: Probability P_m for a high-energy photon to decay into an electron-positron pair after crossing half-a-wavelength of a LP background field of wavelength $\lambda = 0.8$ μm, as a function of the photon energy $\gamma_\gamma = \hbar\omega_\gamma/(m_e c^2)$ and background field amplitude a_0: (a) integrating numerically Eq. (4.13), (b) computed using the approximate expression Eq. (4.17), (c) extracted from one-dimensional PIC simulations. In all three panels, the solid white lines report the isocontours of the first panel. In panel b), the isocontours obtained from Eq. (4.17) are shown in red dot-dashed lines. White dotted lines correspond to constant values of $\chi_0 = 0.1, 1, 16.5$ from bottom left to top right corners.

where we used Eqs. (2.45) and (2.46), and $c_3 = 27\sqrt{\pi/2}/64 \simeq 0.529$, $c_4 = 9\sqrt{3}\pi/64 \simeq 0.765$ and $c_5 = 3^{2/3}45\Gamma^4(2/3)/(56\pi) \simeq 1.789$.

Dependence of P_m on the field amplitude and the gamma photon energy

A consequence of the result shown in fig. 4.1 is that if we consider the interaction of a gamma flash with a ultra-high intensity laser the use of CP does not provide significant advantages, also given the experimental challenge of producing circularly polarised high intensity beam. The role of the polarisation will be discussed in more details in Sec. 4.3.2, while in this section we focus on the LP case, as the CP case is easier and can be treated with the same procedure

The impact of the gamma photon energy γ_γ and the background field amplitude a_0 (or equivalently intensity I_0) on pair production is summarized in Fig. 4.2. We consider here a given background field wavelength $\lambda = 0.8\,\mu$m). Figure 4.2 shows the probability P_m for a high-energy photon to decay in a pair after crossing half a wavelength of a LP background field: (a) integrating numerically Eq. (4.13) which provides an *exact* value of P_m; (b) using the approximate but fully analytical expression given by Eq. (4.17); (c) extracted from 1D PIC simulations of the interaction of a flash of high-energy photons colliding head-on with a plane wave (details are given in A.2).

Let us first discuss panel (a) where, in addition to the probability isocontours (solid white lines), the dotted white lines represent the contours of

constant quantum parameter, for $\chi_0 = 0.1$, 1 and 16.5. As $\chi_0 \propto \gamma_\gamma\, a_0$, these are straight lines with a $-45°$ slope.

In the limit $\chi_0 \ll 1$, i.e. the bottom-left of Fig. 4.2, P_m assumes very small values. In this limit, the time-integrated rate $R_m\tau/4$ scales as $\gamma_\gamma^{-1}\chi_0^{3/2}\exp[-8/(3\chi_0)]$ [Eq. (4.20)] and the exponential term, depending only on χ_0, gives the dominant contribution to P_m. As a result, the isocontours of P_m (solid white lines) behave as nearly straight lines, roughly parallel to the contours of constant χ_0. We wish to stress however that the dependence on γ_γ^{-1} cannot be fully ignored: the isocontours of P_m are less steep than the isocontours of χ_0 which indicates that P_m increases faster with a_0 than with γ_γ. In this range of small χ_0, for which probability and time-integrated rate are equivalent, the importance of increasing a_0 to improve pair production was already pointed out in [Blackburn et al., 2017]. However, the probability variation with both a_0 and γ_γ needs to be examined in more details at higher χ_0.

Indeed, the dependence with γ_γ^{-1} plays a more important role as χ_0 increases so that χ_0 can not be considered as the only relevant parameter in order to optimize the pair production rate. This is clearly seen by considering the isocontours of P_m in (a_0,γ_γ)-plane, Fig. 4.2(a): the isocontour slope becomes shallow and eventually changes sign. Thus, for any value of P_m, a minimum field strength a_0 is needed in order to obtain the desired level of probability. A corollary is that, at constant a_0, increasing γ_γ increases the probability P_m up to a maximum value, beyond which a further increase of γ_γ would only decrease P_m. The minimum of each isocontour can thus be found by solving $\partial P_m/\partial\gamma_\gamma = 0$, which one can recast in the form

$$\frac{\mathrm{d}\mathcal{I}_\sigma}{\mathrm{d}\chi_0} - \frac{\mathcal{I}_\sigma(\chi_0)}{\chi_0} = 0\,. \tag{4.22}$$

Interestingly, this equation involves only χ_0 so that the minima of the probability isocontours lie on a straight line of constant χ_0. This *a priori* surprising result can be better understood noting that both a_0 and P_m are Lorentz invariants, the minimum value of a_0 to reach a given probability P_m can depend only on the Lorentz invariant involving the photon energy, i.e. χ_0. Solving numerically Eq. (4.22) for $\sigma = 0$ (LP case), we obtain[1] $\chi_0 \simeq 16.5$, which is reported by a dotted line in Fig. 4.2.

Let us now consider panels (b) and (c) of Fig. 4.2. The probability P_m computed from Eq. (4.17) is plotted in panel (b) with the corresponding isocontours (red dashed lines). The white lines are the isocontours of the probability cal-

[1]Solving Eq. (4.22) for arbitrary values of $\sigma \in [-1, 1]$ leads to χ_0 in between 16.5 and 17.2, and corresponding values of $I_\sigma(\chi_0)$ in between 5.3 and 6.0.

culated numerically (as in panel (a)) and show an excellent agreement between the two approaches. This validates the approximate form, Eq. (4.17), which has the advantage to be completely analytical and can now be used to get quick yet precise estimates of the probability P_m. Finally, panel (c) reports the probability extracted from 1D PIC simulations of the head-on collision of a flash of high-energy photons with a laser beam. The probability was extracted from the depletion of high-energy photons after crossing half a laser wavelength. Here again, a very good agreement is observed with the isocontours (white lines) obtained from the *exact* integration shown in panel (a). This last panel thus provides a cross-benchmark of our model and the Monte-Carlo module for nonlinear Breit-Wheeler pair production implemented in our PIC code Smilei .

Gamma flash-laser interaction with an arbitrary collision angle

Before moving on to the generalisation of the model to pulses with a time envelope, we briefly discuss how the angle between the gamma flash and the laser pulse affects the probability of pair creation.

The first difference between head-on collision and the general case is the time for a gamma photon to cross a period of the PW. Let us consider a gamma photon with velocity $\boldsymbol{c} = c\hat{\boldsymbol{u}}$ with $\hat{\boldsymbol{u}}$ a unit vector pointing in an arbitrary direction. Let us denote θ the angle between the momentum of the gamma photon and the direction of propagation of the PW such that $\hat{\boldsymbol{u}} \cdot \hat{\boldsymbol{z}} = \cos(\theta)$.

The length of the PW crossed by the gamma photon is given by

$$\Delta z(t) = z_\gamma(t) - z_{PW}(t) = c\hat{\boldsymbol{u}} \cdot \hat{\boldsymbol{z}} t - ct = c(1 - \cos(\theta))t \,. \tag{4.23}$$

Then the time t_λ for a photon to cross a period of the wave is such that $\Delta z(t) = -\lambda$ and so

$$t_\lambda = \frac{\lambda}{c(1 - \cos(\theta))} = \frac{\tau}{1 - \cos(\theta)} \,. \tag{4.24}$$

As expected, for $\theta = \pi$ (which corresponds to head-on collision) we retrieve the time $t_\lambda = \tau/2$. Instead for $\theta \to 0$ the time $t_\lambda \to +\infty$: the gamma photon is co-propagating with the wave and is experiencing a constant field. The quantum parameter of such a gamma photon propagating into the plane wave Eq. (4.7) is given by using Eq. (2.39)

$$\chi_\gamma(t) = \frac{\chi_0}{2} \| \sigma \cos(\omega' t)(\hat{\boldsymbol{y}} - (\hat{\boldsymbol{u}} \cdot \hat{\boldsymbol{y}})\hat{\boldsymbol{u}} - \hat{\boldsymbol{u}} \times \hat{\boldsymbol{y}}) + \sin(\omega' t)(\hat{\boldsymbol{x}} - (\hat{\boldsymbol{u}} \cdot \hat{\boldsymbol{x}})\hat{\boldsymbol{u}} + \hat{\boldsymbol{u}} \times \hat{\boldsymbol{y}}) \| \,, \tag{4.25}$$

where

$$\omega' = \frac{\tau}{t_\lambda}\omega\,. \tag{4.26}$$

The frequency modification is related to the direction of propagation of the photon. The frequency is double for head-on collision and tends to zero for the co-propagation. Let us look in more detail at the expression of the quantum parameter for the case of a LP PW ($\sigma = 0$)

$$\chi_\gamma(t) = |\sin(\omega' t)|\|\hat{\boldsymbol{x}} - (\hat{\boldsymbol{u}}\cdot\hat{\boldsymbol{x}})\hat{\boldsymbol{u}} + \hat{\boldsymbol{u}}\times\hat{\boldsymbol{y}}\|\,. \tag{4.27}$$

The quantum parameter is now $t_\lambda/2$ periodic, as indeed $t_\lambda/2$ is the time for a photon to cross a peak of the field of the plane wave. Moreover there is a geometric factor depending on the relative orientation of the propagation direction of the gamma photon and the PW. This factor is equal to 2 for $\hat{\boldsymbol{u}} = -\hat{\boldsymbol{z}}$ (head-on case), and 1 for $\hat{\boldsymbol{u}} = \hat{\boldsymbol{y}}$ (perpendicular propagation). More generally this factor tends to zero when the gamma photon is co-propagating with the wave, and is maximum for head-on collision. The derivation of the probabilities and computation of the integral can be made in the same way as for the head-on collision, using instead the Eq. (4.27) for the quantum parameter time dependence . In the rest of this work we will focus on the head-on case because it maximises the quantum parameter, but the generalisation to arbitrary angles of collision can be easily performed.

4.3 Probability of pair creation in laser pulses with a time envelope

4.3.1 Total decay probability in a finite pulse

Having computed the elementary probability P_m of conversion of gamma photons into pairs during one PW peak, we will show in this section how to use this basic block to compute the total probability of pair creation after the head-on interaction with a finite pulse. In particular, we will present the analytical model to take into account the temporal envelop of the pulse.

As will be further discussed in the following, considering parameters typical of the upcoming generation of laser facilities, the probability for a high-energy photon to decay into a pair after crossing a single half-wavelength of the background field is in general small compared to 1. This is however not the case when considering the cumulative effect of crossing several wavelengths.

Let us denote as $t_0 = 0$ the time at which the photon starts to interact with

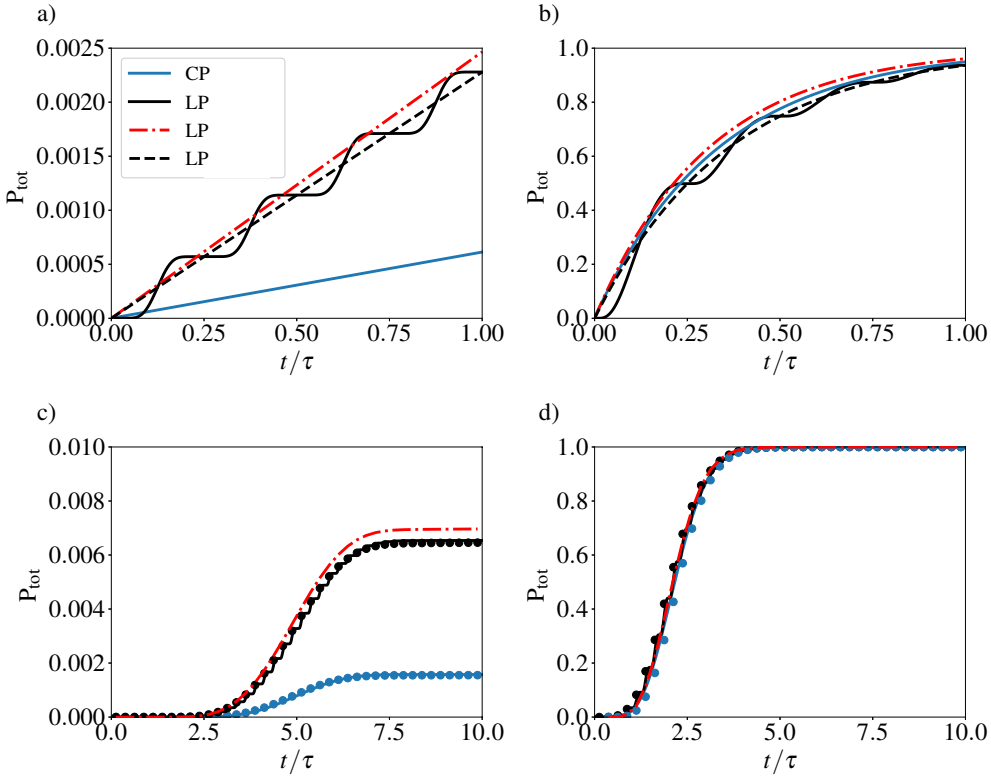

Figure 4.3: Temporal evolution of the probability for a high-energy photon with normalized energy $\gamma_\gamma = \hbar\omega_\gamma/(m_e c^2) = 10^3$ to decay into an electron-positron pair while interacting with a plane wave background field in head-on collision. Considering a constant background field envelop with (a) $a_0 \simeq 82$ corresponding to $\chi_0 = 0.5$ and (b) $a_0 \simeq 660$ corresponding to $\chi_0 = 4$. Considering a background field with $\sin^2$ temporal profile with maximum field amplitude (c) $a_0 \simeq 82$ corresponding to $\chi_0 = 0.5$, (d) $a_0 \simeq 660$ corresponding to $\chi_0 = 4$. Solid lines correspond to the *exact* probability obtained by integrating numerically Eq. (4.6), dashed lines and dots to the theoretical prediction obtained from Eq. (4.29), for LP ($\sigma = 0$, black) and CP ($\sigma = \pm 1$, blue) cases. The red dash-dotted lines correspond to the theoretical prediction from Eq. (4.29) using the approximation of Eq. (4.17) for LP.

the background field [2]. The probability for a high-energy photon to decay into a pair after $t = n\tau/4$ of interaction with the background field (or, equivalently, after crossing n local maxima of the field amplitude) $P_{\rm tot}(t = n\tau/4)$, can be derived from the number N_γ of photons surviving after a time t:

$$N_\gamma(t = n\tau/4) = N_0 \prod_{m=1}^{n} \overline{P}_m \quad \text{with} \quad \overline{P}_m = 1 - P_m = \exp(-R_m\tau/4)\,. \tag{4.28}$$

Here we have used m as a running index for compactness, and P_m [given by Eq. (4.13)] and $\overline{P}_m$ denote the probabilities for the photon to decay and *not to* decay, respectively, during the $m^{\rm th}$ interval. We can then write the total probability of producing a pair as

$$P_{\rm tot}(t = n\tau/4) = 1 - \prod_{m=1}^{n} \overline{P}_m = 1 - \exp\left(-R\,t\right) \quad \text{with} \quad R = \frac{1}{n}\sum_{m=1}^{n} R_m\,, \tag{4.29}$$

R denoting the average pair production rate.

Let us note that this formula is exact at $t = n\tau/4$ with $n \in \mathbb{N}$, and – as shown in figure 4.3 and discussed below – can also be used with good approximation at all times $t \gg \tau/4$. Moreover, in the case of a monochromatic plane wave (no temporal envelop), the average pair production rate simply reduces to $R = R_m$. When dealing with a pulse with a finite temporal envelop, however, equation (4.29) needs to be computed combining the contribution of successive $(\tau/4)$-long intervals, using the local maximum of the background field strength for each time interval. This approach gives very good results even considering ultra-short, few cycles laser pulses. To confirm this, Figure 4.3 shows the temporal evolution of the decay probability for a high-energy photon with $\gamma_\gamma = 10^3$ colliding head-on with different background fields. In panels (a) and (b), the high-energy photon interacts with a background field with constant amplitude $a_0 \simeq 82$ [$\chi_0 = 0.5$, Fig. 4.3(a)] and $a_0 \simeq 660$ [$\chi_0 = 4$, Fig. 4.3(b)]. The interaction lasts for a time τ, i.e. the photon explores two wavelengths of the background field. In panels (c) and (d), the high-energy photon interacts with a background field with a $\sin^2$ temporal profile in intensity, a full-width-half-maximum (FWHM) of 5τ, and maximum field strength $a_0 \simeq 82$ and $a_0 \simeq 660$, respectively.

In all panels, the solid lines denote the *exact* probability computed by numerically integrating Eq. (4.6), considering either LP (black lines) or CP (blue lines) background field. We can see that, for $\chi_0 = 0.5$, CP produces less

[2] Throughout this chapter and the next one, we consider background fields with a finite (e.g. $\sin^2$) temporal profile so that this time t_0 is uniquely defined.

pairs than LP, while for $\chi_0 = 4$ CP is slightly more efficient [the difference between the two polarisations will be discussed in details in the next section 4.3.2]. These probabilities are compared against the prediction of Eq. (4.29), computed using either the numerically evaluated $\mathcal{I}_\sigma(\chi_0)$ [dashed lines in panels (a) and (b), dots in panels (c) and (d)] or the approximation given by Eq. (4.17) to compute R_m (red dot-dashed lines, only computed for LP as it is exact for CP). Note that here and in the following, whenever Eq. (4.17) is used, the approximation of Eq. (2.47), which is an improved version of the Erber approximation, is exploited.

Panels (a) and (b) show an excellent agreement between the exact computations (solid lines) and Eq. (4.29) (dashed lines), both using the numerically integrated values of $\mathcal{I}_\sigma(\chi_0)$. A remarkably good agreement is also found when considering the fully analytical approximation of Eq. (4.17) for $\mathcal{I}_\sigma(\chi_0)$ (red dot-dashed lines). The probability is slightly overestimated in this case, as expected for $\chi_0 \sim 1$ for which Eq. (4.17) shows the greatest departure from the exact expression of $\mathcal{I}_\sigma(\chi_0)$.

Similarly, an excellent agreement between all three approaches is found in panels (c) and (d) considering a short (5τ FWHM in intensity) background field. In this case the value of R_m in each $\tau/4$ interval is computed by taking the value of $\mathcal{I}_\sigma$ given by the local maximum of the field, i.e. the time variation of the envelope is considered slow during $\tau/4$. The validity of this assumption is confirmed by PIC simulations discussed in the following chapter. In particular, Figure 4.3 shows that the approach leading to the derivation of Eq. (4.29), which consists in treating the cumulative contributions of successive maxima of the background field, remains a very good approach even for ultra-short, few cycle, background fields.

Last, we note that the results of 1D PIC simulations performed with SMILEI (see A.2 for details) are not distinguishable from the *exact* computations (solid lines) for all reported cases, and are therefore not shown in Fig. 4.3.

4.3.2 Impact of the electromagnetic field polarisation

The asymptotic behavior provided by Eqs. (4.20) and (4.21) allows to obtain some interesting insights into the importance of the electromagnetic field polarization on pair production.

We recall that, motivated by experimental constraints, we compare LP and CP at fixed energy: this condition implies that the CP beam has a lower maximum amplitude. Because of this, for $\chi_0 \ll 1$, equation (4.20) shows that any departure from the LP case leads to a tremendous decrease of $\mathcal{I}_\sigma(\chi_0)$.

Indeed the exponential cut-off of the pair production rate is strongly affected by the decrease of χ_m with $|\sigma|$ as shown in Eq. (4.12). In contrast, for $\chi_0 \gg 1$, $f(\sigma)/(1+\sigma^2)^{1/3}$ is an increasing function of $|\sigma|$: the reduction of the field peak amplitude is compensated by the fact that the absolute value of the amplitude is not time dependent [see Eq.(4.10)]. Hence, in this range, increasing the background field ellipticity increases the pair production rate. However, the rate increase from the LP to the CP case is small (less than 12%) so that considering CP for boosting pair production results in a marginal improvement[3].

The differences between the LP and CP cases are evidenced in the inset in Fig. 4.1(b), where $\mathcal{I}_0(\chi_0)$ is found to be orders of magnitude larger than $\mathcal{I}_{\pm1}(\chi_0)$ for $\chi_0 \ll 1$ while $\mathcal{I}_{\pm1}(\chi_0)$ is only about 10% larger than $\mathcal{I}_0(\chi_0)$ for $\chi_0 \gg 1$. Similar conclusions can be drawn from Fig. 4.3. For small values of the photon parameter, $\chi_0 = 0.5$ (left panels), the pair production probability is significantly larger considering a LP background field than a CP one. For the higher value of $\chi_0 = 4$ (right panels), CP increases, but only marginally, pair production.

4.3.3 Threshold for abundant probability of pair creation

Our model can be used to predict the efficiency of pair production for a given set of laser and high-energy photon parameters. In the case of large secondary pair production, our prediction will underestimate the number of pairs as our analysis is limited to the soft-shower regime. Most of the photons crossing the laser will be converted in pairs over a time Δt if the quantity $R\Delta t$ in Eq. (4.29) becomes of order 1, for which[4] $P_{\rm tot}(\Delta t) \geq 0.63$. In fig. 4.4, we highlight in yellow the region in the (a_0, γ_γ) plane where the probability for a high-energy photon to decay into a pair after interacting with a single maximum (half-wavelength) of the laser pulse $P_{\rm tot}(\tau/4)$ is equal or larger than 0.63 (the pulse duration is here $\tau/2$, but the time required for the photon to explore half the laser wavelength is $\Delta t = \tau/4$). The condition $P_{\rm tot}(\Delta t) = 0.63$ is also shown for pulses with a step-like time profile (solid lines) and duration $5\,\tau$ (green, $\Delta t = 2.5\tau$) or $100\,\tau$ (blue, $\Delta t = 50\tau$), and pulses with a $\sin^2$ intensity time profile with FWHM 5τ (green dashed line, $\Delta t = 5\tau$) and $100\,\tau$ (blue dashed line, $\Delta t = 100\tau$). Note that both step-like and $\sin^2$ time profiles correspond to laser pulses with the same energy and peak power, and lead to similar requirements to reach $P_{\rm tot} \simeq 0.63$. Comparing the blue and green

[3]Moreover, in practice, implementing CP on multi-petawatt facilities would lead to a decrease of the delivered laser pulse energy.

[4]Note that in this limit, the probability cannot be assimilated to the time-integrated rate, as in the case of very weak pair production.

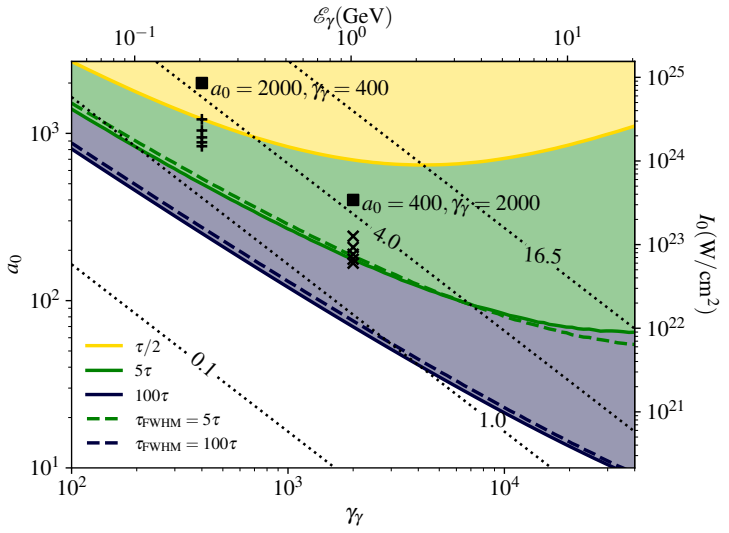

Figure 4.4: Position in the (γ_γ, a_0)-plane [equivalently in the $(\mathcal{E}_\gamma, I_0)$-plane] at which $R\Delta t = 1$ [$P_{\rm tot}(\Delta t) \simeq 0.63$] for the interaction with a single maximum of the incoming pulse (half-wavelength, i.e. pulse duration equal to $\tau/2$) for which the interaction lasts for $\Delta t = \tau/4$ (yellow line) and for the interaction with pulses with a step-like time profile (solid lines) of duration 5τ (green) and 100τ (blue), and pulses with a $\sin^2$ time envelope with FWHM of 5τ (green dashed line) and 100τ (blue dashed line). The color-shaded areas above the plain lines correspond to $R\Delta t > 1$ (considering the step-like time profiles). The dotted black lines correspond to constant $\chi_0 = 0.1\,, 1\,, 4\,, 16.5\,$. The symbols highlight the parameters of the simulations discussed in chapter 5

lines, we see that at constant γ_γ a longer pulse satisfies the condition of efficient conversion for a lower value of a_0. Hence, even though the condition $R\,\tau/4 = 1$ (yellow solid line) is quite stringent and achieving a high probability level over a time interval $\tau/4$ can be difficult, the condition $R\,\Delta t \gtrsim 1$ is significantly relaxed considering longer interaction time. Indeed, significant (order 1) pair production probability is expected on forthcoming multi-PW laser facilities (see Sec. 5.4 for details).

Let us also note that, when $R\,\tau/4 \geq 1$ (yellow area), more than 63% of conversion is achieved after crossing a single wavelength of the background field, and more than 99% of the incident gamma photons are converted into pairs in less than 3 periods. This gives a very robust condition for abundant pair creation, and it determines a limit above which is not useful to further increase the laser amplitude to increase the number of primary pairs. As we will show in the following, this condition ($R\,\tau/4 \geq 1$) can also be invoked to find the optimal laser transverse shape and focal spot for a given laser energy. The squares and crosses in Fig. 4.4 indicate the peak value of a_0 and γ_γ used in 3D PIC simulations discussed in detail in the next chapter for a $\sin^2$ pulse of fixed duration ($\tau_{\rm FWHM} = 5\tau$). The simulations are performed by varying

the peak intensity at constant energy, starting form the largest value (squares) and decreasing it (crosses). Indeed as we will see the two sets show a different behaviour depending on whether the two reference simulations (squares) lie in the yellow or green region of Fig. 4.4. The different sets of simulations correspond to the same values of χ_0, as visible explicitly for the squares, but lie in different regions of equiprobability.

As a final remark, we point out that the probabilities considered so far are computed considering a high energy gamma flash, with all photons having the same energy value. Generalizing our results to a given photon energy distributions is however straightforward as there is no coherence effects between the high-energy photons. In practice, we expect the high-energy photon beam to have a broad energy spectrum or at least a finite energy width (see e.g. Refs. [Gonoskov et al., 2017, Niel et al., 2018b, Blackburn and Marklund, 2018, Phuoc et al., 2012, Gong et al., 2017, Capdessus et al., 2018, Vranic et al., 2019, Magnusson et al., 2019, Zhu et al., 2020, Sampath et al., 2021]). The total probabilities can thus be computed independently for all relevant high-energy photon energies with $P_{\text{tot}}(\gamma_\gamma)$ a function of γ_γ. Then, to compute the total number N_{pair} of produced pairs, one only needs to integrate over the whole high-energy photon spectrum: $N_{\text{pair}} = \int d\gamma_\gamma \, P_{\text{tot}}(\gamma_\gamma) \; dN_\gamma/d\gamma_\gamma$, where $dN_\gamma/d\gamma_\gamma$ denotes the high-energy photon energy distribution.

4.4 Probabilitiy of pair creation in laser pulses with transverse spatial profile

In this Section we generalize the model developed in Sec. 4.3 to accurately describe pair production in complex, spatially structured laser beams. We consider a high energy gamma photon flash with a transverse size larger than the transverse spatial extension of the laser pulse. The interested reader could also check [Óscar Amaro and Vranic, 2021] where different geometries of the seeding particle beam are considered.

Since we deal with high-energy photons colliding head-on with a strong background field, we can consider that the photon momentum is unchanged as the photon crosses the background field, until it decays. Thus its trajectory is a straight line and the field seen by the photon along its trajectory is known and depends only on the photon initial position (x_0, y_0) in the plane transverse to the direction of propagation of the laser beams. For analytical tractability, we consider all photons to be propagating exactly in the z-direction. It follows that the quantum parameter of any photon is known throughout the photon

interaction with the background field, and for a given background field, is determined uniquely by the photon initial position (x_0, y_0). As a result, the total probability $P_{\rm tot}$ for any photon to decay into a pair after interacting with the laser pulse is also determined by the photon initial position, and the total number of produced pairs at the end of the interaction between the flash of high-energy photons (with density n_γ and longitudinal width L_γ) simply reads

$$N_{pair} = n_\gamma L_\gamma \, \sigma_{\rm tot} \quad \text{with} \quad \sigma_{\rm tot} = \int dx_0 \, dy_0 \, P_{\rm tot}(x_0, y_0) \, . \tag{4.30}$$

A key quantity to model pair production is thus the *total cross-section* $\sigma_{\rm tot}$, here defined as the integral of the total probability over the transverse plane.

Notice that, as discussed in the last paragraph of Sec. 4.3, for a given gamma photon energy spectrum, $\sigma_{\rm tot}$ can be considered a function of γ_γ, and the total number of produced pairs can be computed integrating over the incident high-energy photon spectrum. Moreover, equation (4.30) can be easily generalised to account for a transverse profile of the incident high-energy photon beam. In particular, in the limit where this beam is much narrower than the laser beam, equation (4.30) reduces to $\sigma_{\rm tot} \simeq S_\gamma \, P_{\rm tot}$, where S_γ is the transverse area of the high-energy photon beam, and $P_{\rm tot}$ is computed at the (transverse) location of the high-energy photon beam.

To compute the total probability at any position (x_0, y_0) we use Eq. (4.29) and proceed as described in section 4.3, reconstructing the total probability from successive time intervals of duration $\tau/4$. Gamma photons at different positions in the transverse plane explore different field peak amplitude, and probe a different field structure both in time and space, in particular if we consider arbitrary Laguerre-Gauss pulses described in Chapter 1.

For simplicity, we consider the field transverse distribution at focus, taking the absolute value of the field complex amplitude at $z = 0$. This approach, which neglects the effects of diffraction, is justified whenever the duration of the interaction ($\sim \tau_{FWHM}$) does not exceed the time z_R/c for light to cross the laser pulse Rayleigh length. As shown in the following, this approximation proves satisfactory considering typical ultra-short (Ti:Sapphire) light pulses. The validity and generalisation of this approach will be discussed in Sec.5.5.

The probability map for $P_{\rm tot}$ computed over the whole interaction time in the transverse focal plane by considering the model above is shown in Fig. 4.5(a) for the case of a LG beam with $\ell = 5$, $p = 0$ and $a_0 = 2000$ colliding with a flash of photons with energy $\gamma_\gamma = 400$ (corresponding to $\chi_0 = 4.85$). Note that the beam amplitude averaged over a period is the required quantity to obtain the map presented in Fig. 4.5(a) , while the details of the phase

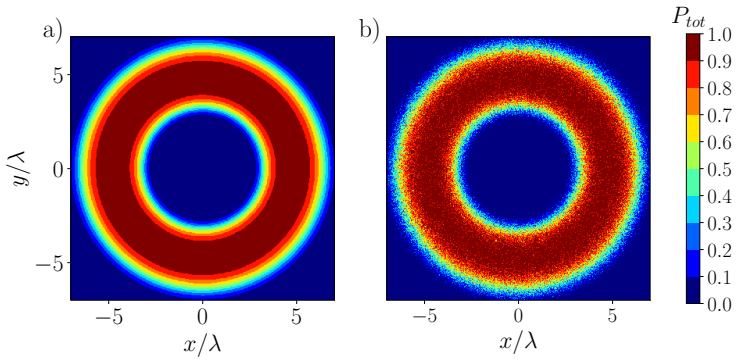

Figure 4.5: Probability map for a photon with energy $\gamma_\gamma = 400$ to produce a pair during the interaction with the LG_{05} beam with FWHM of 5τ and maximum amplitude of the reference Gaussian beam equal to $a_0 = 2000$, corresponding to $\chi_0 \simeq 4.85$. a) Analytical prediction from Eq. (4.29). b) Numerical results from the 3D PIC simulation.

structure can be neglected. This will be discussed further in Chap.5

Integrating over the transverse plane the Ptot shown in Fig. 4.5(a) provides the total cross-section $\sigma_{\rm tot} \simeq 91.4\,\lambda^2$. To verify the validity of the approximations used in the model (that neglects phase dependence and diffraction effects), we show in Fig. 4.5(b) the probability map extracted from a 3D PIC simulation, where those effects are intrinsically taken into account. The probability is extracted at the end of the interaction and defined as the ratio of the density of the remaining photon over the initial one. A thorough comparison between the model and PIC simulations is presented in the next Chap.5. Here we just point out that an excellent agreement is found with the theoretical prediction of panel (a). The cross-section measured in the Pic simulation is $\sigma_{\rm tot} \simeq 91.0\,\lambda^2$, confirming the predictive capability of our simple model for the case of spatially structured beams. The parameters of the simulations are detailed in the next chapter 5).

4.5 Conclusions

Let us summarize the results of this chapter. We considered a configuration in which gamma photons are converted in pairs by colliding with an electromagnetic wave n the soft shower limit, i.e. secondary gamma photons emitted by pairs are neglected. We derived the general form of the probability for gamma photon conversion into pairs in an arbitrary electromagnetic field (4.6). The key element to compute the probability.

First we considered head-on collision of the photons with a plane wave of arbitrary polarization and we evaluate this integral. We then provide an analytical approximated form that compare well with the numerical results.

For the specific case of a LP plane wave we also verified that in a broad range of field intensity and photon energy, the elementary probability of pair production after the interaction with a single peak of the PW (P_m) obtained by these techniques are in excellent agreements among themselves and with the results of a series of 1D PIC simulations. This allowed us to both validate the model and benchmark the Monte-Carlo module of Smilei. We also showed that in the soft-shower configuration considering CP does not increase significantly pair production with respect to the use of LP pulses.

We then generalised the model using P_m to evaluate the probability of pair creation in a finite pulse with a temporal envelope. The comparison of the analytical or semi-analytical results and the 1D PIC simulations in the finite pulse gives very good agreement.

Finally we further generalised our model to take into account the spatial intensity distribution of the laser pulse in the transverse direction. We tested for a given configuration that the model agrees well with the associated 3D PIC simulation. In the next chapter we will extend this comparison to different configurations, showing that the model predictions allow to give guidelines for optimising pair production in forthcoming experimental facilities.

Chapter 5

Soft showers by Laguerre-Gauss beams colliding with a gamma flash

Contents

In this chapter we further test the model discussed in Chap. 4 in a broad range of laser and gamma photons parameters. In the following we will present in detail the comparison of the model prediction and 3D PIC simulations of LG and Gaussian beams interacting with a gamma flash, considering two different intensity regimes. Our results confirm that the model introduced in the previous chapter allows to take into account not only Gaussian beams but also the complex LG beam structure. We then use these results to predict what can be expected in near future experiments.

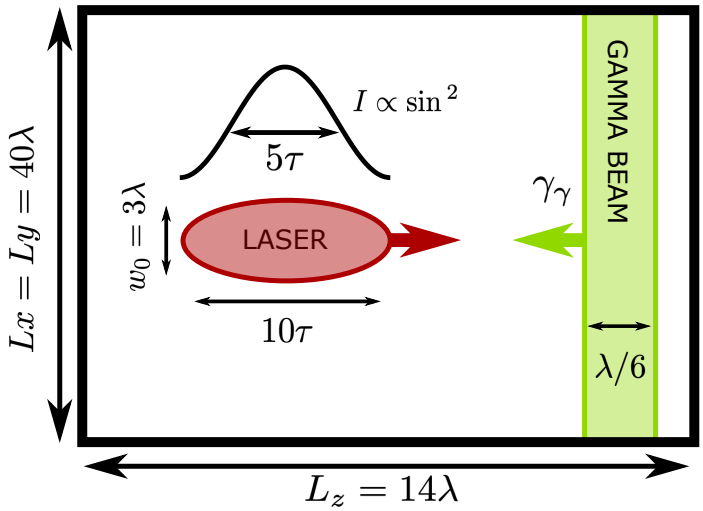

Figure 5.1: Typical set-up of the 3D PIC simulations, with λ and τ the laser wavelength and the optical cycle, respectively.

5.1 Setup of the simulations

The 3D PIC simulations are performed with the open-source code Smilei [Derouillat et al., 2018], considering the setup schematically represented in Fig. 5.1. For each simulation the volume is given by $40\lambda \times 40\lambda \times 14\lambda$ (in the x, y and z directions, respectively) with spatial resolution $\lambda/24$ and temporal resolution at 95% of the CFL condition [Nuter et al., 2014].

An intense laser pulse (with wavelength $\lambda = 0.8\,\mu$m) is injected from the left boundary $z = -5\lambda$ using the method presented in Ref. [Pérez and Grech, 2019] that allows the Maxwell-consistent injection of an electromagnetic wave with an arbitrary spatio-temporal profile. Here, this method is used to inject the laser pulse by prescribing its spatio-temporal profile in its focal plane [i.e. the (x, y)-plane at $z = 0$], as given by the complex amplitude Eq.(1.41) at $z = 0$, multiplied by a temporal envelope so that the laser pulse has a $\sin^2$ temporal profile in intensity with $\tau_{\mathrm{FWHM}} = 5\,\tau$, and total duration of $10\,\tau$. The laser beam collides head-on with a counter-propagating flash of high-energy photons with a finite longitudinal extension $L_\gamma = \lambda/6$, transverse extension equal to the simulation box, and a density n_γ equal to the critical density $n_c = \epsilon_0 m_e \omega^2/e^2$. The duration of the simulation is longer than the overlapping time of the two light beams, but short enough that none of the photons or secondary particles escape from the simulation box. All results presented hereafter have been extracted at the end of the simulations.

In Secs. 5.2, we discuss the results of the following two series of simulations: the first one with $a_0 = 2000$ and $\gamma_\gamma = 400$, the second with $a_0 = 400$ and $\gamma_\gamma = 2000$, both series corresponding to a reference quantum parameter $\chi_0 \simeq$

$6\times10^{-6}\,a_0\,\gamma_\gamma \sim 4.85$ (for $\lambda = 0.8\,\mu$m). For each series, we varied the transverse spatial profile of the high-intensity laser pulse at fixed energy, in order to study the impact of the spatio-temporal field profile. Different LG beams are considered (where we only vary ℓ, but keep $p = 0$) and extended gaussian (EG) beams . For each LG beam (i.e. each value of $|\ell|$), we define the associated EG beam as the Gaussian beam that has the same maximum field amplitude and carries the same total energy. As $u_{p\ell}^{\max}$ decreases with $|\ell|$ [Eq. (1.47)] and the energy is kept constant, the waist of the EG beams increases with respect to the fundamental Gaussian (equivalent to LG_{00}) as $w_\ell = w_0\sqrt{|\ell|!}\,\mathrm{e}^{|\ell|/2}|\ell|^{-|\ell|/2} \geq w_0$.

Within each series, a_0 refers to the maximum field amplitude of the reference Gaussian beam (for which we consider $w_0 = 3\lambda$). Notice however that the actual peak intensity decreases since the transverse surface increases and we keep the same laser pulse energy (equal to $\simeq 10\,$kJ for $a_0 = 2000$ and $\simeq 410\,$J for $a_0 = 400$). The photon flash surface energy density $m_e c^2\,\gamma_\gamma n_\gamma d$ is $\simeq 5\,\mathrm{mJ}/\lambda^2$ for the first series (with $\gamma_\gamma = 400$) and $\simeq 25\,\mathrm{mJ}/\lambda^2$ for the second one ($\gamma_\gamma = 2000$).

As highlighted in fig. 4.4 where the reference Gaussian cases are indicated by squares, the first series of simulations allows us to explore the physics in the regime of high pair production probability after a single $\tau/4$ interval (i.e. for this case $R_m\tau/4 > 1$ is in the yellow region). On the contrary, with the second series we investigate a regime where efficient pair production is achieved thanks to the cumulative effects of several wavelength (i.e. $R_m\tau/4 < 1$, but the reference Gaussian case is above the green line the figure).

5.2 Efficiency of pair creation for various peak amplitude at constant pulse energy

In this section we analyse systematically the interaction of the gamma flash with LG beams having the same energy and time duration, but different maximum amplitudes. The PIC simulations are compared with our model. In fig. 5.2 we show the value of the quantum parameter experienced by the photons of energy $\gamma_\gamma = 400$ for four different LP LG beams of order $l = 0, 1, 2, 3$ at focus. Analogous to the field structure, the quantum parameter for $l \neq 0$ consists in lobes, , rotating around the axis of propagation. As discussed in Sec.4.4, in order to take into account in our model the spatial distribution, we compute the probability over an interval of duration $\tau/4$ and we consider the field that corresponds to the average intensity distribution, that is without the effect of the LG phase evolution. This gives an excellent approximation

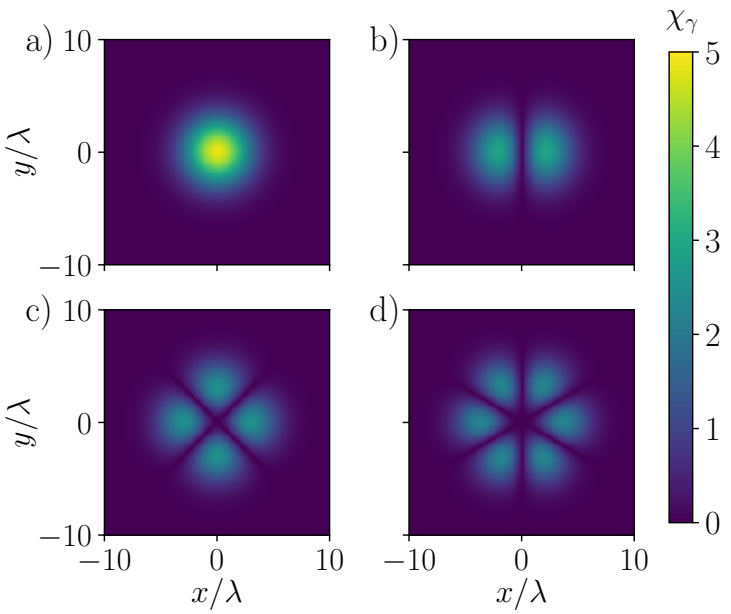

Figure 5.2: Photon quantum parameter χ_γ in the head-on collision of photons of energy $\gamma_\gamma = 400$ with a LP LG beam at focus [i.e. $z = 0$ in Eq. (1.41)] with $a_0 = 2000$, $p = 0$ and a) $\ell = 0$, b) $\ell = 1$, c) $\ell = 2$, d) $\ell = 3$.

because each of these structures moves to the position of the consecutive one in precisely half a period, and the photon crosses it in $\tau/4$.

5.2.1 Simulations in the regime of high pair production probability ($R_m\tau/4 > 1$)

In order to investigate the dependence of the number of produced pairs on the laser structure, we present first a study in the regime satisfying $R_m\tau/4 > 1$ for the reference Gaussian beam, in which we expect efficient pair production. We remind that we consider here photons with normalized energy $\gamma_\gamma = 400$ and a reference Gaussian beam with maximum amplitude $a_0 = 2000$, leading to $\chi_0 \simeq 4.85$ (all other parameters have been specified in Sec. 5.1).

To test the validity of our analytical predictions and model, that do not include secondary pairs, we performed simulations (hereafter referred to as *frozen cases*) in which the produced pairs are prevented to further radiate. The same simulations are also performed including the full system dynamics (hereafter referred to as *full cases*), that is the pairs produced by the gamma flash laser interaction can at their turn interact with the laser fields and potentially radiate and produce secondary pairs. This two sets of simulations confirm that in all the cases considered we are in the soft-shower regime, and the number of produced pairs predicted by the model is representative of the expected realistic results, with a small discrepancy when the full dynamics are

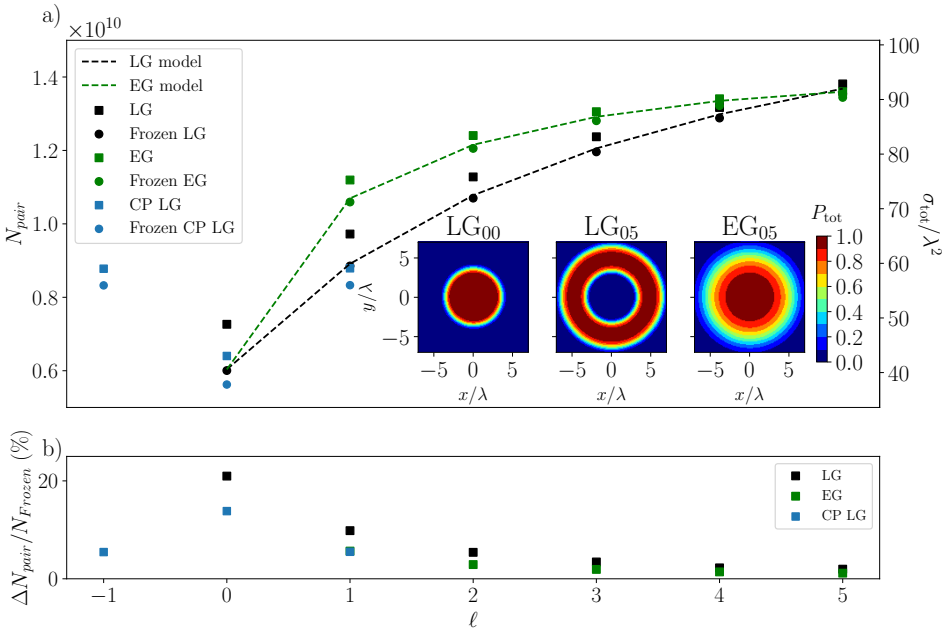

Figure 5.3: a) Number of produced pairs, and corresponding cross section $\sigma_{\text{tot}}/\lambda^2$ after the interaction of gamma photons with energy $\gamma_\gamma = 400$ and a counter-propagating LG with $p = 0$, $\ell \in [\![-1, 5]\!]$ and $a_0 = 2000$ [CP (blue), LP (black)], and the corresponding LP EG (green). Frozen simulations (dots), full simulations (squares) and theoretical predictions from Eq. (4.30) (dashed lines). The insets show the probability map for the LG$_{00}$, LG$_{05}$ and EG$_{05}$ cases. b) Relative difference in the number of produced pairs between the frozen and full simulation results.

included.

Figure 5.3(a) shows the number of produced pairs at the end of the interaction for all the tested cases, LP LG (in black), CP LG (blue) and EG (green), dots refer to the frozen simulations and squares to the full ones. Considering a LP LG laser beam, pair production efficiency increases with ℓ. This means that for the high value of a_0 considered here, it is preferable to increase ℓ, even if it decreases the maximum amplitude [as shown in fig. 1.4], as it increases the characteristic transverse size of the beam, and so the interaction area where the probability is high [see inset in fig. 5.3(a)]. The EG beams (which have by construction the same maximum amplitude of the LG beams but Gaussian profile) are more efficient than the corresponding LG, up to to $\ell = 4$, as they have a larger region with substantial probability in their probability maps. However, a slightly greater number of pairs are produced in the simulation with LG$_{05}$ than EG$_{05}$ beam. This because the maximum field amplitude has dropped substantially and a large part of the interaction region in the EG case has low probability of pair production [see inset in fig. 5.3(a)]. Predictions form our model discussed in Sec. 4.4 and based on Eq. (4.30), shown in dashed lines, are in very good agreement with both EG and LG simulations.

Based on the prediction from fig. 4.1, for the considered $\chi_0 \simeq 4.85$ we would expect at first look a higher efficiency in the CP case than with LP, contrary to what is obtained from PIC simulations [blue symbols in fig. 5.3(a)]. However, given the spatial structure of the laser field in the transverse plane, in a large part of the interaction region the quantum number is $\chi < 2.5$, i.e. the value above which CP should be favoured based on the analysis shown in fig. 4.1(b) obtained within the plane wave approximation. Hence, the slightly higher number of pairs produced in the CP case with respect to LP in the region where $\chi > 2.5$, cannot compensate the higher efficiency of LP in the region of $\chi < 2.5$. Note that the results using a CP beam are independent from the sign of ℓ (i.e from the total angular momentum). This suggests that the total angular momentum of the laser has no effect on the number of pair produced. Note however that we do not account for the spin polarization effects. Since we are focusing on the soft shower regime where there are few secondary pairs, the dynamics of the pairs affected by spin effects is expected to play a minor role for pair production in our case. Nevertheless, in other configurations spin effects can impact the created pairs and gamma photons dynamics as shown in Refs. [Chen et al., 2019, Seipt and King, 2020].

For completeness, we compare the results of the frozen cases with simulations reproducing the full dynamics of the system [squares in Fig. 5.3(a)]. As highlighted in Fig. 5.3(b), the difference in the produced number of pairs is always below 25% of its value in the frozen case, and it decreases with $|\ell|$. This confirms that the majority of pairs comes from the conversion of primary gamma photons and not from subsequent radiation, as expected for a soft-shower. In this regime, our model, which accurately captures the physics of pair production for the frozen simulations (dashed lines), can be therefore used to predict pair production in realistic conditions.

5.2.2 Simulations in the regime of moderate pair production probability ($R_m\tau/4 < 1$)

In this second series of simulations we explore the regime of $R_m\tau/4 < 1$, maintaining the same maximum χ_0 as in the previous section by exchanging the values of field amplitude (now equal to $a_0 = 400$) and photons energy (now equal to $\gamma_\gamma = 2000$). Note that considering a laser duration ($\tau_{\mathrm{FWHM}} = 5\tau$), we still expect efficient pair production (the reference plane wave simulation lies above the green dashed line in fig. 4.4). This can be seen in the inset of fig. 5.4(a) for the Gaussian case LG_{00} where a significant region exhibits a probability of order 1.

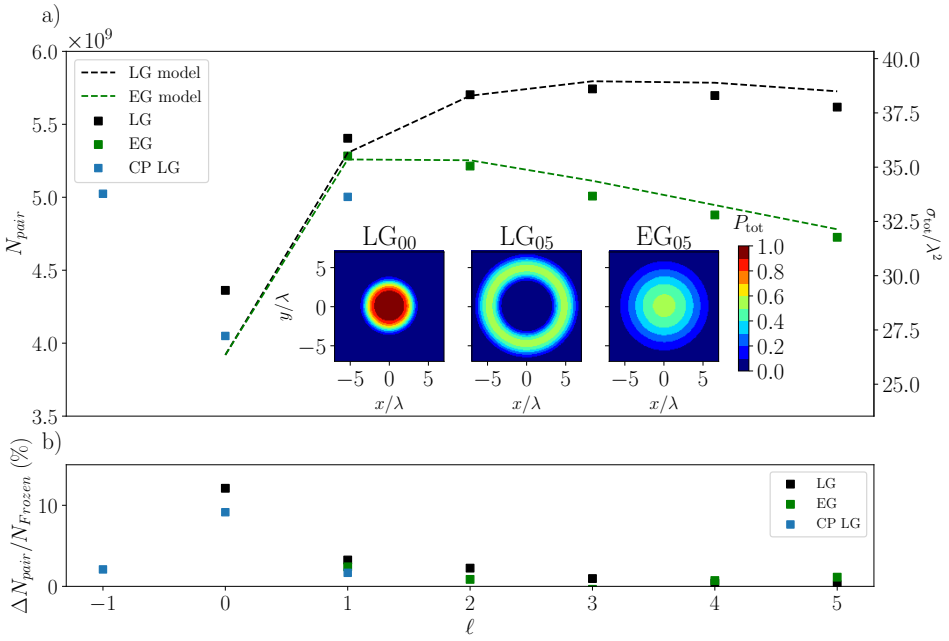

Figure 5.4: a) Number of produced pairs and corresponding cross section $\sigma_{\text{tot}}/\lambda^2$, after the interaction of gamma photons of energy $\gamma_\gamma = 2000$ with a counter-propagating LG beam with $p = 0$, $\ell \in [\![-1, 5]\!]$ and $a_0 = 400$ [CP (blue) and LP (black)], and the corresponding LP EG (green). Full simulations (squares) and theoretical predictions from Eq. (4.30) (dashed lines). The insets show the probability map for the LG$_{00}$, LG$_{05}$ and EG$_{05}$ cases. b) Relative difference in the number of produced pairs between the frozen and full simulation results. The frozen cases are not shown in panel (a) as the difference with the full ones is always below 15%.

As fig. 5.4 shows, for the simulations with LG beams the number of produced pairs is optimized for $\ell = 3$. The increase for $|\ell| \leq 3$ can be explained as in the previous section by geometrical considerations, i.e. the area with the field being large enough to reach P_{tot} of order one is getting wider with $|\ell|$. In the contrary for $|\ell| > 3$, the laser field amplitude becomes too low and having a laser beam with a larger transverse extension does not improve pair production. This means that at low intensity the effect the effect of decreasing P_{tot} on pair production is more important than (and hence is not compensated by) the increase in transverse size of the laser beam.

Moreover, in this regime, all LG beams perform better than the corresponding EG, given that the region with high probability (even though smaller than in the previous section) is larger for the LG beams than EG ones, as shown in the inset of fig. 5.4 for $\ell = 5$. A similar behaviour as the one discussed in the previous section is observed for the CP simulations and the same explanation is valid here. Last but not least, our model reproduce with high accuracy the observed number of pairs in this case as well.

5.3 Energy angular distribution and phase space of the created pairs

The energy-angular distribution of the produced pairs in the $z - x$ plane (i.e the plane formed by the laser propagation direction $\hat{\mathbf{z}}$ and the polarization direction $\hat{\mathbf{x}}$ for the LP case) recorded at the end of the interaction is shown in fig. 5.5 considering the reference LP and CP Gaussian beams. The top row gives the positron distribution in $\theta = \arctan(p_x/p_z)$ and in energy for the LP beams and the bottom one for the CP beams. The insets show the energy spectra of particles moving in the positive (same as the laser, black line) and negative (same as the gamma flash, red line) z-direction.

At high a_0 (panels a and c) the produced pairs, initially generated with momentum in the negative z-direction, are predominantly moving in the same direction as the laser (corresponding to $\theta = 0°$) within a cone of aperture 40°, meaning that they have been slowed down and then pushed by the laser. They reach a maximum energy of $\simeq 10^4\, m_e c^2$ for the LP case and $\simeq 8 \times 10^3\, m_e c^2$ for the CP case, consistent with the decrease of the peak field amplitude in CP with respect to LP at constant laser energy.

The spatial distribution is drastically modified when considering $a_0 = 400$. Even if there still is a substantial amount of pairs propagating in the laser direction, the majority of them keep their original direction, along the initial

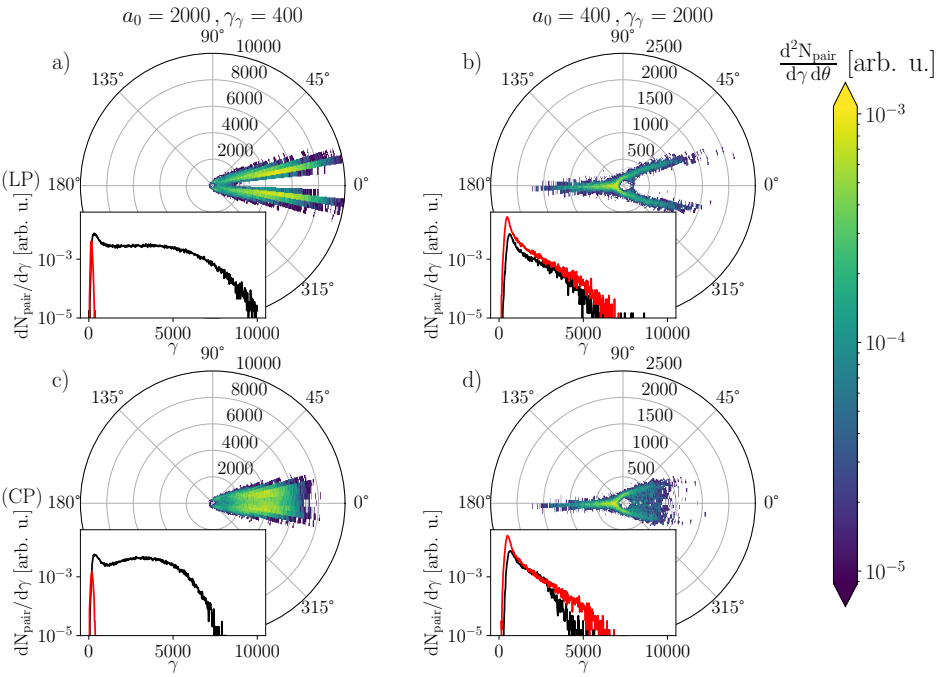

Figure 5.5: Positron distribution as a function of the Lorentz factor γ (equiv. normalized energy) and the angle $\theta = \arctan(p_x/p_z)$ for the first simulation series (left column) and for the second one (right column); LP (CP) in the top (bottom) row. The insets show the energy spectra for positrons propagating in the positive (black line) and in the negative (red line) directions.

gamma photons propagation axis and anti-parallel to the laser pulse one. For these pairs the maximum energy is independent from the polarization, as shown in fig. 5.5(b)-(d), contrarily to the pairs that are slowed down and pushed by the laser (right side of the quadrants or black line in the insets).

We can complement these results with the positrons phase spaces, that give more insights on the spatial distribution of the created pairs.

Let us consider first the phase space of the LP gaussian beam with $a_0 = 2000$ and $\gamma_\gamma = 400$, shown in fig. 5.6, where the weight, proportional to the number of particles, is given by the colour-scale. On the top left panel we have the (z, p_z) phase space, where the positive z-axis corresponds to the laser propagation direction. At the end of the simulation the majority of the particles have $p_z > 0$, i.e. they are pushed by the laser and they co-propagate with it, consistent with what was shown in the previous section. The vertical stripes at fixed values of z are separated by $\lambda/2$. This is due to the fact that in a LP plane wave pairs are predominantly created near the maxima of the field, and this signature persists over time. These stripes are also visible on the bottom left panel, in the (z, p_x) phase space, where they correspond to positive and negative values of the transverse momentum, $p_x > 0$ and $p_x < 0$, x being the direction of polarization of the electric field. This is due to the fact that E_x is

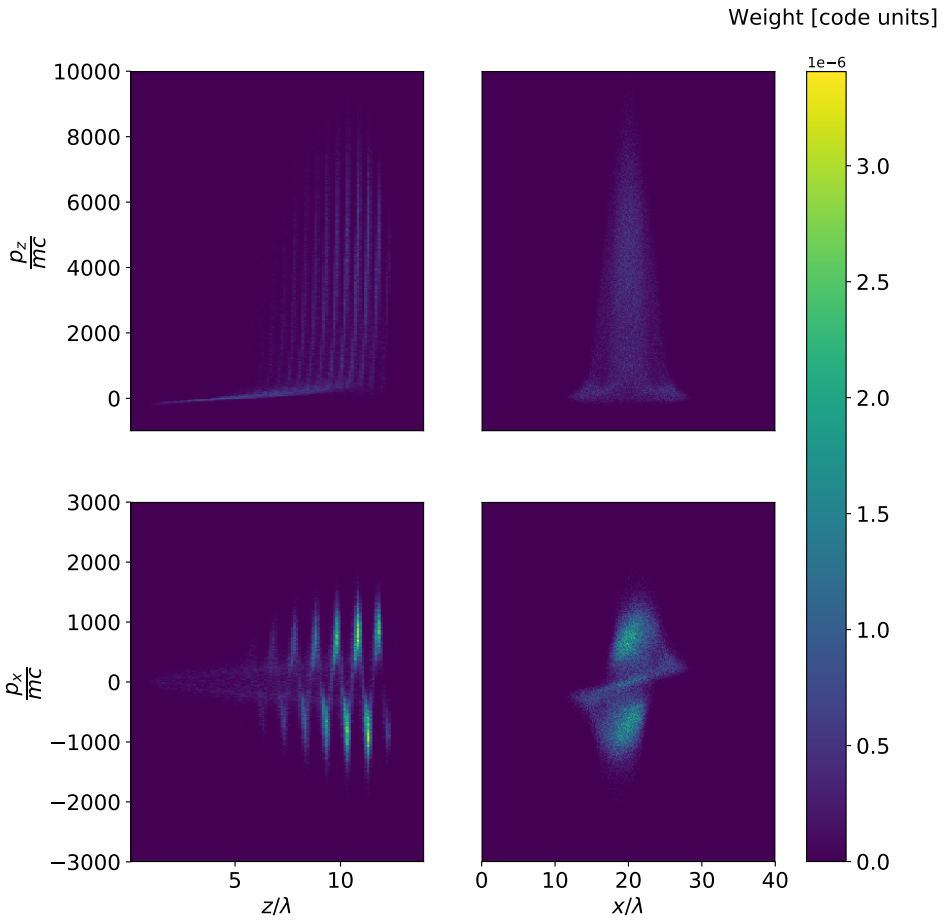

Figure 5.6: Phase space of the created positrons at the end of the simulation, for a LP gaussian beam with $a_0 = 2000$ and $\gamma_\gamma = 400$. The axis of propagation of the beam is z and the beam is polarised along x.

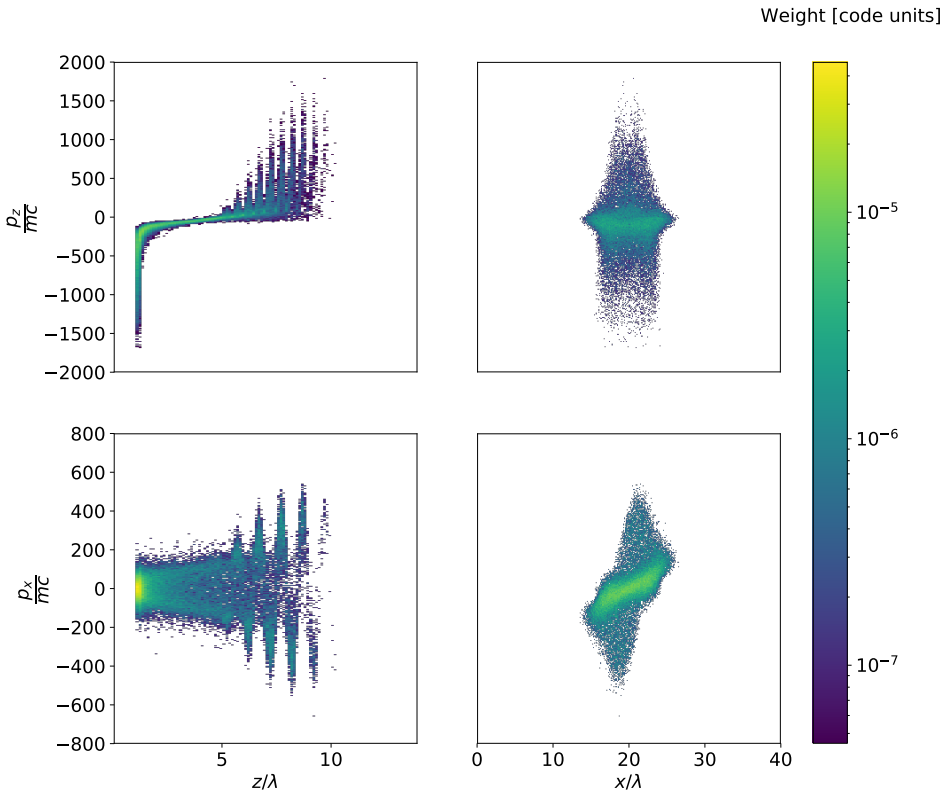

Figure 5.7: Phase space of the created positrons at the end of the simulation, for a LP gaussian beam with $a_0 = 400$ and $\gamma_\gamma = 2000$. The axis of propagation of the beam is z and the beam is polarised along x. Please note that here the scale is logarithmic contrary to other figures in order to see better the distribution.

changing sign over $\lambda/2$ and particles acquire opposite transverse momentum. Considering the (x, p_z) phase space shown in the top right panel, we can see that the particles having the highest longitudinal momentum are the ones at the center of the pulse. This is consistent with the fact that the pairs created at the maximum of the laser intensity are produced at early times and are therefore accelerated for a longer time by the laser.

Let us now consider the phase space of the LP Gaussian beam with the same peak value of the quantum parameter, but reversed values of a_0 and γ_γ ($a_0 = 400$ and $\gamma_\gamma = 2000$), shown in fig. 5.7. One can see that the laser has a weak influence on the particles and the majority of them are propagating in the direction of their initial momentum (negative z), as visible in the (z, p_z) top left panel.

We next consider the CP gaussian case $a_0 = 2000$ and $\gamma_\gamma = 400$, reported in fig. 5.8. Some differences are visible with respect to the LP case with the same initial conditions (fig. 5.6) in the (z, p_z) phase space. Since the total field amplitude is constant in the CP case, the stripes seen with LP are not produced here. The majority of pairs still propagate with the laser beam but the phase

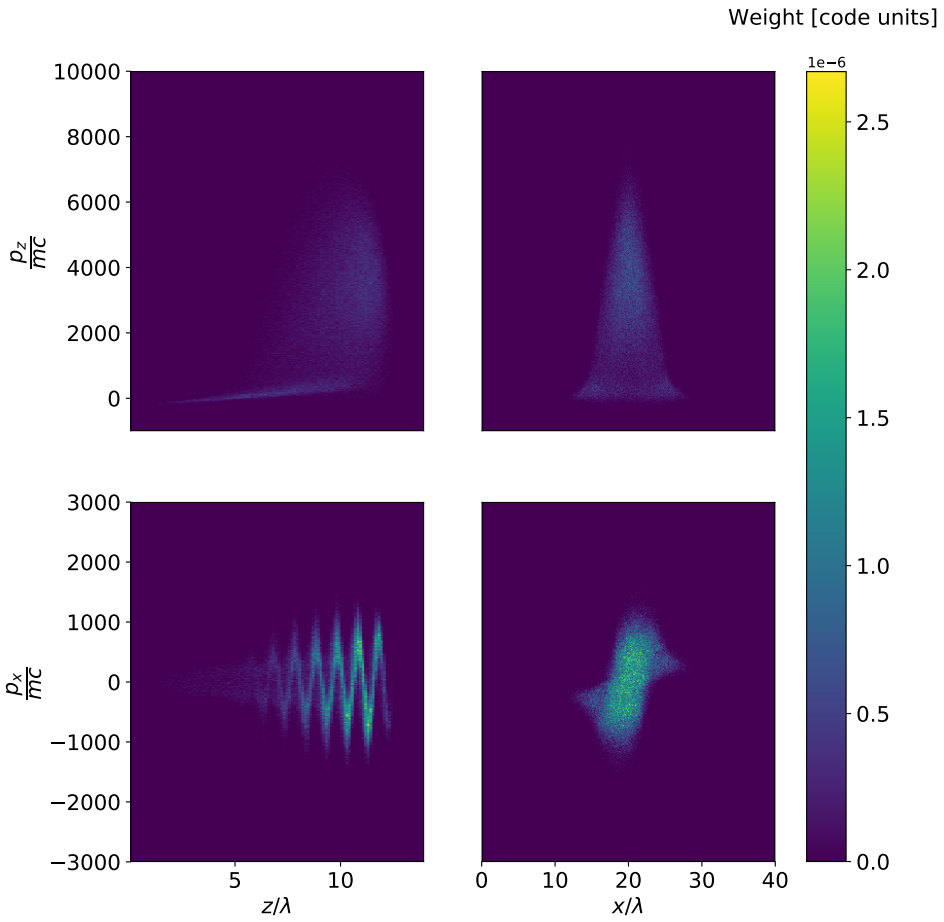

Figure 5.8: Phase space of the created positrons at the end of the simulation, for a CP gaussian beam with $a_0 = 2000/\sqrt{2}$ and $\gamma_\gamma = 400$. The axis of propagation of the beam is z.

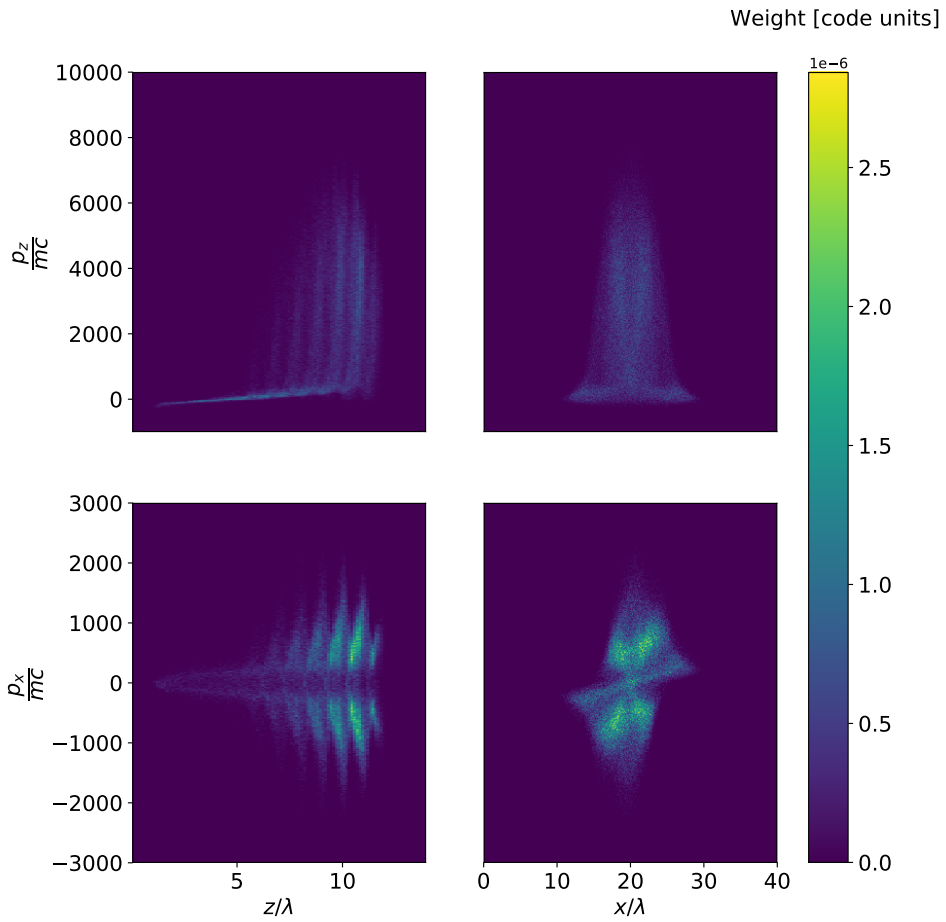

Figure 5.9: Phase space of the created positrons at the end of the simulation, for a LP LG beam with $\ell = 1$, $a_0 = 2000$ and $\gamma_\gamma = 400$. The axis of propagation of the beam is z and the beam is polarised along x.

space is homogeneous, and the peak amplitude of the momentum is smaller than in the LP case, since the laser peak amplitude is smaller by a factor $\sqrt{2}$. In the (z, p_x) phase space now a continuous line appears, oscillating between negative and positive values of p_x. In fact, since the particles are created continuously along the propagation axis, the pairs phase space (z, p_x, p_y) is an helix turning around z, as the particles follows the rotation of the field along z. The structure in the (x, p_z) space, is similar to the LP gaussian case, while the (x, p_x) phase space consists in one homogeneous spot going from negative to positive values of p_x, which is different the two spots of the bottom right panel of fig. 5.6.

The phase space of the CP Gaussian beam with the same peak value of the quantum parameter, but reversed values of a_0 and γ_γ ($a_0 = 400$ and $\gamma_\gamma = 2000$) is very similar to the LP Gaussian case, and does not bring additional information. For this reason, it is not shown here.

Finally we show the results of the simulation performed with the LP LG

beam with the highest amplitude, i.e. $l = 1$. The phase space reflects the phase structure of the LP LG beam, for which the two lobes (fig. 1.1) have opposite signs of the field components. This results in pairs co-propagating with the laser that are divided into two groups with opposite sign of the transverse momentum, as visible in the (z, p_x) space, bottom left panel. Vertical stripes similar to the LP Gaussian case, but wider, are present around fixed values of z. Looking at the phase spaces in the transverse x-direction both (x, p_z) and (x, p_x), the ring shape of the laser intensity can be retrieved, as the spots of fig. 5.6 are in this case divided into conic shapes.

An important feature of this configuration, is that particles are present also at the center of the transverse plane, where the field amplitude vanishes, with a positive longitudinal momentum $p_z > 0$. This suggests that the ponderomotive push of the laser towards the center of the pulse can help confining pairs. This should be however confirmed by simulations studying the evolution on longer timescales, that are left for future research.

This study, supported by complementary simulations (not shown), suggests that for $a_0 \gtrsim \gamma_\gamma$ most of the created particles propagates along the laser direction, while for smaller values of the laser maximum amplitude, a large fraction of pairs keeps their original propagation direction. A complete characterisation of the pairs spectrum and directionality is beyond the scope of this work, and will be investigated in more details in the future, as it can give important information for the planning of upcoming experimental campaigns.

5.4 What can be expected from upcoming facilities?

The model developed in this work allows to predict the pair production capability of upcoming facilities. In fig. 5.10, we discuss the pair production maximum probability and total cross-section as a function of the photon energy and laser amplitude. The considered parameter range is relevant to ultrashort Ti:Sapphire ($\lambda = 0.8$ μm) lasers, where studies of high-field physics and QED are already planned [Lee et al., 2018, Meuren et al., 2020, Zhang et al., 2020, Grech et al., 2021]. Two types of facilities can be distinguished. First, the Apollon[1], CoReLS[2] and ZEUS[3] facilities (shown in black in fig. 5.10)

[1]The Apollon, located on the *Plateau de Saclay*, south of Paris, France, started operating at the PW-level [Cros et al., 2014, Papadopoulos et al., 2016]; see also the Apollon website.

[2]CoReLS, in Gwanju, South Korea, is operating at up to 4PW [Nam et al., 2018]; see also the CoReLS website.

[3]A 3PW laser facility being built at the University of Michigan; see the ZEUS website.

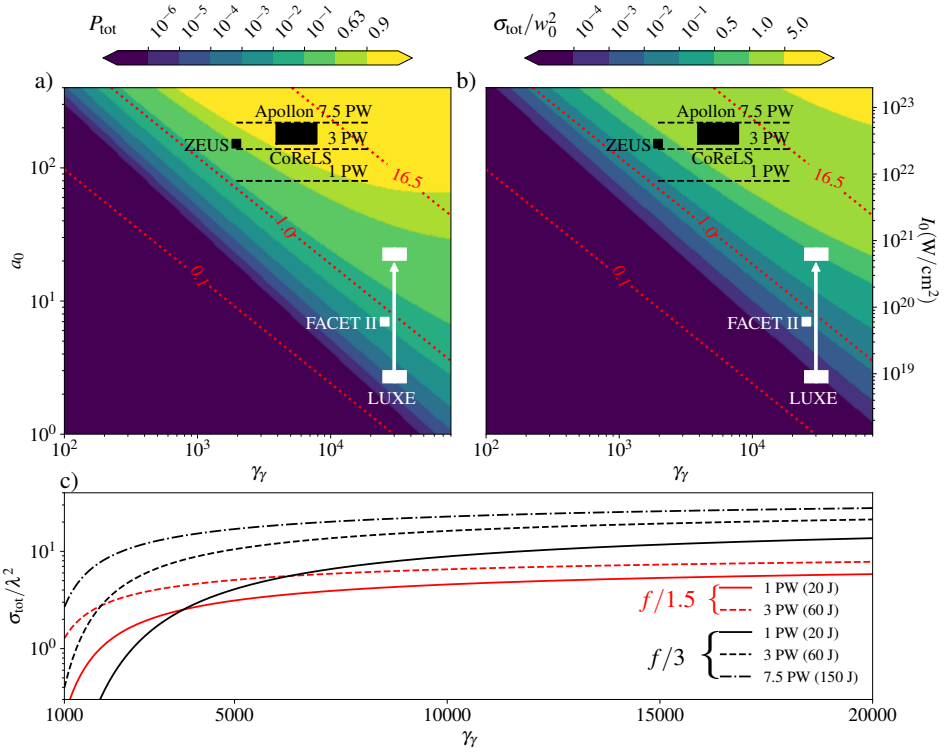

Figure 5.10: Model predictions considering a laser pulse with $\sin^2$ time-envelope in intensity ($\tau_{\rm FWHM} = 25\,$fs) and $\lambda = 0.8\,\mu$m. (a) Maximum pair production probability from Eq. (4.29). (b) Total cross section normalised to w_0^2 using the model discussed in Sec. 4.4. In both panels (a) and (b) the red lines denote contours of constant $\chi_0 = 0.1\,,\,1\,,\,16.5$. The regimes accessible with current and upcoming facilities are also reported. c) Total cross section normalised to λ^2 as a function of γ_γ computed for the Apollon facility operating at 1 PW (solid lines), 3 PW (dashed lines) and 7.5 PW (dash-dotted line) and with focusing aperture $f/3$ (black lines) and $f/1.5$ (red lines). In this last panel, at a given power, the laser energy is the same for the different focusing aperture f/N.

are designed to deliver multiple light beams with duration in between 15 and 30 fs (FWHM) and peak power from 1 to 10 PW. Second, the FACET-II[4] and planned LUXE[5] experiments will couple conventional electron accelerators with high-intensity (100 TW-class) ultra-short laser pulses (in white in fig. 5.10).

In fig. 5.10(a,b) the accessible a_0 and typical γ_γ envisioned with these facilities (following the reference articles) are reported. For Apollon only, we computed a_0 considering a 20 fs light pulse delivering 20, 60 and 150 J on target, corresponding to peak power of 1, 3 and 7.5 PW, respectively. The reported value of a_0 is then computed for a LP Gaussian beam with focusing aperture $f/3$ (where the beam waist for a focusing aperture f/N is $w_0 \simeq 0.90\, N\lambda \simeq 2.2\ \mu$m), using

$$a_0 \simeq \frac{151}{N}\sqrt{\frac{\mathcal{E}_{\rm laser}}{10\,\rm J}}\sqrt{\frac{25\,\rm fs}{\tau_{\rm FWHM}}} \simeq \frac{239}{N}\sqrt{\frac{P_{\rm laser}}{1\,\rm PW}}\,. \tag{5.1}$$

Note in addition that, as most of these facilities will operate in the $\chi_0 \gtrsim 1$ regime, we consider a photon energy equal to the one of the electrons of the beam either expected from laser-driven wakefield acceleration (for Apollon, CoReLS and ZEUS) or emerging from the linear accelerators (for FACET-II and LUXE). In the case of a broad (e.g. synchrotron-like) energy distribution for the high-energy photon source, the expected number of produced pairs can be computed integrating the reported values of $P_{\rm tot}$ or $\sigma_{\rm tot}$, defined in Eq. (4.30), over the full high-energy photon spectrum. As detailed below, this integration can be carried out in two rough but straightforward ways depending on the kind of facility (multi-PW or laser combined with a conventional accelerator) that is considered.

Let us now focus on panel (a), which shows the maximum total decay probability [from Eq. (4.29)] for a photon with energy γ_γ colliding head-on with a LP Gaussian laser pulse with maximum field strength a_0 and duration $\tau_{\rm FWHM} = 25$ fs (typical for the facilities listed above). This panel suggests the strategy to optimize pair production depending on the type of facility.

First, despite the extremely high electron beam energies, facilities such as LUXE and FACET-II (in white in fig. 5.10) offer the possibility to probe the regime of moderate quantum parameter ($\chi_0 \lesssim 1$) for which pair production may be observed ($P_{\rm tot} \simeq 10^{-2}$) but will not be abundant. This limit might be overcome by increasing the laser power up to few 100's of TW (300 TW are

[4] FACET-II is planned at SLAC National Accelerator Facility [Yakimenko et al., 2019]; see also the FACET-II website.

[5] LUXE is an experiment proposed at the European XFEL [Abramowicz et al., 2019] [Abramowicz et al., 2021]; see also the LUXE experiment website.

envisioned at LUXE), which allows to enter the quantum regime ($\chi_0 > 1$) and increase $P_{\rm tot}$ to values exceeding 0.1. On these facilities however, because $P_{\rm tot}$ will not assume large values, increasing a_0 (e.g. by focusing the laser pulse as much as technically possible) is one of the most promising path to achieve abundant pair production.

In contrast, provided that multi-GeV electron beams can be obtained from laser wakefield acceleration, abundant pair production ($P_{\rm tot} \gtrsim 0.63$) is expected on all multi-PW laser facilities with the focalisation technique already in place (typically an aperture in between $f/3$ and $f/4$ was considered in fig. 5.10).

Similar conclusions can be drawn from panel (b) where we examine in more details the influence of the laser pulse spatial profile, by looking at the total cross-section[6] $\sigma_{\rm tot}$ [as defined by Eq. (4.30)] normalized to w_0^2, considering a Gaussian laser beam with the same temporal properties as in panel (a).

For the FACET-II and LUXE facilities, the total cross-section assumes very small values but increases fast as a_0 is increased: e.g. for LUXE, $\sigma_{\rm tot}$ increases by 3 orders of magnitude increasing a_0 by a factor 10. Clearly, operating at large field strength will be a bottleneck for achieving abundant pair production on these facilities.

In contrast, in the range of parameters covered by multi-PW facilities, the dependence of $\sigma_{\rm tot}$ with a_0 is much weaker. As in addition, $\sigma_{\rm tot} \simeq w_0^2$ (consistent with $P_{\rm tot} \simeq 1$ at the center of the beam), it becomes interesting for these facilities to increase the laser transverse size rather than opt for tight focusing.

Let us then discuss in more details the impact of focusing for the three upgrades of the Apollon facility (at 1, 3 and 7.5 PW). In panel (c), we present the total cross section (in units of λ^{-2}) as a function of γ_γ, considering either the standard $f/3$ aperture (black lines) or the more challenging $f/1.5$ aperture (red lines). For each laser power, a tighter focusing reduces the beam waist but increases the maximum a_0.

In all cases, the cross section is rapidly increasing with the photon energy for $\gamma_\gamma \lesssim 2\times10^3$ ($\simeq 1$ GeV). It is almost flat as γ_γ reaches 5×10^3 ($\simeq 2.5$ GeV), which suggests that it is not worth increasing the photon energy above this value in forthcoming experiments to optimize pair production in the soft-shower regime.

As shown in panel (c), for a given laser power the cross section for $f/1.5$ is larger than for $f/3$ only for small values of γ_γ, while the opposite behaviour is observed at large γ_γ (of the order of a few GeV). This means that such tight focus, which is technologically very challenging, is not necessary for pair

[6] Since the Gaussian field profiles depend on the transverse coordinate through the ratio ρ/w_0 [Eq. (1.41)], $\sigma_{\rm tot}/w_0^2$ is independent of w_0.

creation in forthcoming experiments on Apollon.

As a last remark, for the facility LUXE at the right bottom corner of fig. 5.10, the LCFA approximation, mentioned in 2.2 does not hold [Lv et al., 2021] due to the lower laser intensity of the facility. It first means that the number of produced pairs will vary from the model prediction, although it is still expected that the probability of pair creation will be low compared to other experiments. Secondly, the spectra of gamma photons and pairs will differ from what is given in 2.2. Experiments which aims at studying these aspects should go beyond the LCFA approximation, as it is studied in recent work such as [Ilderton et al., 2019, Gelfer et al., 2022].

5.5 Generalisations and limits of the model

To test the final predictions of the previous section summarized in fig. 5.10c) fot the Apollon facility, the Apollon facility, we have performed complementary 3D PIC simulations of the 3 PW case with $f/3$ and $f/1.5$ ($a_0 = 138.8$ and 276.7, respectively) interacting with a gamma flash with energy $\gamma_\gamma = 10^4$. These simulations give $\sigma_{\rm tot} \simeq 26.8\,\lambda^2$ for $f/3$, which is indeed larger than the value $\sigma_{\rm tot} \simeq 19.5\,\lambda^2$ obtained for the tight-focusing $f/1.5$ case. This is consistent with our reduced model predictions, but the values are noticeably above its predictions, which are $\sigma_{\rm tot} \simeq 16.2\,\lambda^2$ for $f/3$ and $\sigma_{\rm tot} \simeq 6.5\,\lambda^2$ for $f/1.5$ [as given by Fig. 5.10(c)].

One of the reason of the discrepancy is that our calculations are performed at focus, neglecting diffraction effects. While this was a good approximation for the parameters considered earlier (see Sec. 5.1), it is not correct when considering tightly focused intense background fields, or very long laser pulses, with an interaction region larger than the Rayleigh length. The model can be easily generalized to include diffraction. The probability is computed, following the model presented in Sec. 4.4, by adding the contribution of each peak of the field, taking into account temporal envelope as explained in Sec. 4.3, and considering the transverse distribution of the focus as explained in Sec. 4.4. To take into account diffraction, we evaluate the contribution of each peak of the field, by taking into account that the size of the transverse distribution of the laser changes with time. This is done by producing a probability map like the one in fig. 4.5 for each peak contribution, instead of doing that for the whole interaction, in order to take into account the change of the transverse field distribution over the pulse propagation axis. Then one should combine the contribution of each peak as it was discussed before.

This improves our predictions to $\sigma_{\rm tot} \simeq 22.2\,\lambda^2$ for $f/3$ and $\sigma_{\rm tot} \simeq 9.8\,\lambda^2$

for $f/1.5$. These values are now significantly closer to our 3D PIC simulation results, and are also in excellent agreement (within 1%) with additional 3D PIC simulations in which secondary pair production is not accounted (frozen case). Secondary pairs, responsible for a further increase of about 20% for the $f/3$ case and by a factor $\times 2$ for the tightly-focused $f/1.5$ case, are not included in the model and are the source of the remaining discrepancy. This suggests that for the highest peak intensity considered here we are at the limit of the soft-shower regime and the model should be considered as providing a lower bound estimate for pair production.

Let us briefly comment on how the effect of a broad energy spectrum and transverse extension of the high-energy photon beam can be accounted for depending on the type of facility considered.

In the case of FACET-II and LUXE facilities, both $P_{\rm tot}$ and $\sigma_{\rm tot}$ are steep functions of γ_γ, e.g. increasing by several (more than 4) orders of magnitude for the FACET-II configuration as γ_γ is increased from 5×10^3 to 3×10^4. One can thus expect that, for these facilities, only the photons with the highest energy contribute to pair production. The total number of produced pairs can then be estimated considering only the photons with the highest energy [maximum γ_γ as reported on panels (a) and (b)]. If the high-energy photon beam is much narrower that the laser beam, the total number of produced pair can be computed from the number of photons and $P_{\rm tot}$ evaluated at the maximum γ_γ. If instead the high-energy photon beam has a large transverse distribution, the final number of pairs can be calculated by taking the high-energy photon surface density and $\sigma_{\rm tot}$ computed at the maximum γ_γ.

For the multi-PW laser facilities, and large background field strength a_0, we have seen that both $P_{\rm tot}$ and $\sigma_{\rm tot}$ [for the latest, see e.g. panel (c) for the Apollon facility] reach a plateau above a minimum value of the photon energy [e.g. $\gamma_\gamma \simeq 5\times10^3$ in the case of panel (c) discussed above]. Hence, pair production will follow primarily from the decay of the high-energy photons in this plateau. A simple estimate of the number of produced pairs will then be obtained from either the number of all photons in the plateau region and a typical value of $P_{\rm tot}$ (if the photon beam transverse size is small with respect to the laser beam waist) or from their surface density and $\sigma_{\rm tot}$ obtained for this energy range (if the photon beam transverse size is large).

Finally let us summarise how the model can be adapted to many situations, as long as the soft shower hypothesis is valid. The important aspect is the knowledge of the field amplitude that the gamma photons experience during the interaction. Then one can simplify the problem by considering the

consecutive contribution of each peak of the field amplitude (intervals of duration $tau/4$). We can finally combine those contribution to obtain the value of the cross section. The various changes, in the gamma flash distributions, laser transverse profile and time envelope should be taken into account in the computation of the probability for each laser peak. This is simple if one assumes that locally the laser fields looks like a plane wave, e.g. for finite laser pulse the field amplitude would correspond to the value given by the temporal envelop. The model can then be adapted to various situations, narrow gamma flash, or long gamma beams and non uniform transverse distribution of the gamma flash for example. The procedure would essentially be the same.

5.6 Conclusions

Let us now conclude on the work presented in this chapter. In summary, we have presented a systematic study of nonlinear Breit-Wheeler pair production in the head-on collision of high-energy gamma photons with an ultra-high intensity laser beam. Combining analytical modeling and PIC simulations embarking the relevant QED modules, we have evaluated the impact on the efficiency of pair production of the laser spatio-temporal profile [comparing e.g. Gaussian with different focal spots and Laguerre-Gaussian (LG) pulses] and parameters such as polarization, intensity and duration. Motivated by experimental constraints, we have considered fixed laser energies while changing these parameters.

We have explored laser field strength and photon energy parameter ranges relevant to currently and/or upcoming high-power laser facilities, focusing in particular on ultra-short Ti:Sapphire laser facilities. A reduced model was proposed that allows to describe pair production in the regime of soft-shower, where secondary pair production can be neglected. This model, that would in principle allow to predict a minimum number of produced pairs, is found to agree remarkably well with 3D PIC simulations over a broad range of parameters, highlighting the importance of the soft-shower regime for experiments on the forthcoming laser facilities.

The model also allows to distinguish two regimes of interaction depending on whether the probability for a photon to decay into a pair as it crosses a single half-wavelength of the laser pulse is large (of order 1) or not. The two regimes are not however fully determined by the photon maximum quantum parameter χ_0, so that the laser field strength parameter a_0 and photon energy γ_γ do not play a symmetric role in the system dynamics. This was confirmed in 3D PIC simulations where the two regimes were investigated at $\chi_0 = 4.85$

considering laser beams with complex spatio-temporal profiles, LG beams in particular, and different polarizations. It was found that, for a fixed laser energy, using circular polarization or LG does not improve significantly pair production. As they are also quite difficult to produce experimentally, their effect on pair production is too marginal to be interesting for applications. It was found however that, in the regime of high pair production probability, it can be preferable not to focus much the laser beam (keeping the same total energy with lower peak intensity) and maintain a Gaussian shape in order to maximise the area with high-enough fields for efficient pair production.

These findings help to draw guidelines for future experiments on ultra-high intensity facilities. We show in particular that the path to abundant pair production is different whether one considers 100 TW-class or multi-PW laser systems. In particular, for facilities such as FACET-II or LUXE, 10 to 100 TW-class lasers will be coupled to ultra-relativistic 10-20 GeV electron beams emerging from conventional electron accelerators. On these facilities, pair production will develop in the low probability regime and operating in a tightly-focused configuration to access the highest possible laser field strength will be a major experimental challenge. In contrast, using multiple laser beam multi-PW facilities will operate in the regime of high pair production probability. In this regime, the pair production efficiency (measured in our work in terms of a total cross section) depends more strongly on the laser pulse transverse size than on its maximal field strength so that operating with standard (not too tight) focusing aperture increases the number of produced pairs. Interestingly, producing high-energy photons (or electrons, e.g. through laser wakefield acceleration) of a few (~ 5) GeV shall be enough for these facilities as higher energies do no help increase significantly the pair production efficiency in this high probability regime.

To conclude, this work provides a deeper understanding of the optimal conditions for pair production in upcoming experimental campaigns exploring nonlinear Breit-Wheeler pair production. We focused here on pair production seeded by high-energy photons, but it will be interesting for future works to investigate the differences with the case in which ultra-relativistic electrons are used to seed the pair production process.

Part III

Self-sustained cascades or avalanches

Chapter 6

State of the art of numerical and theoretical studies of QED cascades

Contents

In this work we focused so far on physical configurations in which one can neglect the production of secondary pairs. This is especially true in the conditions envisioned in upcoming facilities, and in the configuration studied in the previous Chap. 5. Indeed, after the conversion of photons into pairs, the latter either cross the short pulses or co-propagate with it without further major production of gamma photons, as shown in the previous Chap. 5. Since one of the ultimate purpose of pair creation in a laboratory is the production of a pair plasma, one would like to maximise the number of produced pairs.

In this chapter we introduce a regime of pair creation called QED avalanche, or self-sustained cascade, in which secondary pairs are of major importance. Indeed as suggested initially by [Bell and Kirk, 2008], in certain fields configurations, pairs are constantly being re-accelerated between each emission of hard gamma photons. In this situation the initial seeding particles first emit hard gamma photons by the NCS process and the emitted gamma ray is then converted by the NBW process. The newly generated particles are in turn accelerated and emit hard gamma photons, repeating the cycle. As a result, this constant re-acceleration, coupled with the conversion of gamma photons into pairs by the strong field, leads to a phase of exponential growth of the number of pairs, called the self-sustained cascade or avalanche. If the right conditions are met, this regime can therefore be more suitable for efficient pair creation than the previously presented shower regime.

However understanding and modeling this regime is more difficult than the previously discussed shower regime. Indeed one has now to take into account the dynamics of the particles in the strong field, which is a complex task in the quantum-dominated regime. A first approach (discussed in 6.3) considers that the field is high enough that particles become ultra-relativistic on time scales shorter than the temporal variation of the field. If one also assumes that the field is slowly varying compared to the timescale of quantum process, then the dynamics of ultra-relativistic particles is determined by the classical trajectory, punctuated by strong gamma photon emission events.

In the following we present the state of the art of some previously studied configurations and we introduce the relevant quantities and aspects important for the study of the cascade. This gives us the foundation to understand the results of the next chapter, in which we discuss simulation results and theoretical models of the avalanche in configurations considering two counter-streaming LG pulses.

6.1 Cascade generation in a purely electric rotating field

When trying to induced a QED avalanche, one ideal case is the configuration with a pure rotating electric field. As it is shown in the following, one can easily compute the classical trajectories (without radiation reaction) in this configuration. A charged particle interacting with this field performs circular motion, coupled with a drift, the latter depending on the initial momentum. The drift, for a particle initially at rest, is along the direction orthogonal

to the initial direction of the electric field. This trajectory is precisely the reason making this configuration interesting. Indeed, as shown in chapter 4, the quantum parameter of a gamma photon is larger if the angle between its momentum and the field is large, and χ_γ when the two vectors are co-linear. This is true also for electrons and positrons. In the pure rotating field, studied in [Nerush et al., 2011a,Elkina et al., 2011], particles following classical trajectories have a substantial angle between their momentum and the electric field. Moreover particles initially at rest accelerate during their interaction with this field and their quantum parameter increases, so that cascades could be triggered. We now recall some of the established results obtained in this configuration, and verify them with our own PIC simulations.

6.1.1 Particles dynamics

Let us assume a given rotating electric field

$$\boldsymbol{E} = E_0 \cos(\omega t)\hat{\boldsymbol{x}} + E_0 \sin(\omega t)\hat{\boldsymbol{y}}\,. \tag{6.1}$$

In the case of strong field, one can assume that the particle dynamics is classical and governed by the Lorentz force only between two quantum emissions of hard photons. In the field given above, the classical (relativistic) equations of motion give the following momentum for an electron or positron of charge $q = \pm e$

$$p_x(t) = p_x(0) + \frac{qE_0}{\omega}\sin(\omega t) \tag{6.2}$$

$$p_y(t) = p_y(0) + \frac{qE_0}{\omega}(1 - \cos(\omega t))\,. \tag{6.3}$$

We can see that there is a drift orthogonal to the initial electric field direction, the y direction in our case, unless it is compensated by the initial momentum. The drift momentum has an amplitude $\frac{\boldsymbol{p}_{drift}}{mc} = a_0$ for a particle initially at rest. The two components of the momentum and the drift are represented in figure 6.1.

Assuming the charge initially at rest $\boldsymbol{p}(0) = 0$, using the mass shell relation $\varepsilon_e^2 = m^2c^4 + p^2c^2$ and Eq. (2.39), one obtains the energy and quantum parameter of the charge [Elkina et al., 2011]

$$\varepsilon_e(t) = mc^2\sqrt{1 + 4a_0^2\sin^2(\omega t/2)}\,, \tag{6.4}$$

$$\chi_e(t) = \frac{E_0}{E_S}\sqrt{1 + 4a_0^2\sin^4(\omega t/2)}\,. \tag{6.5}$$

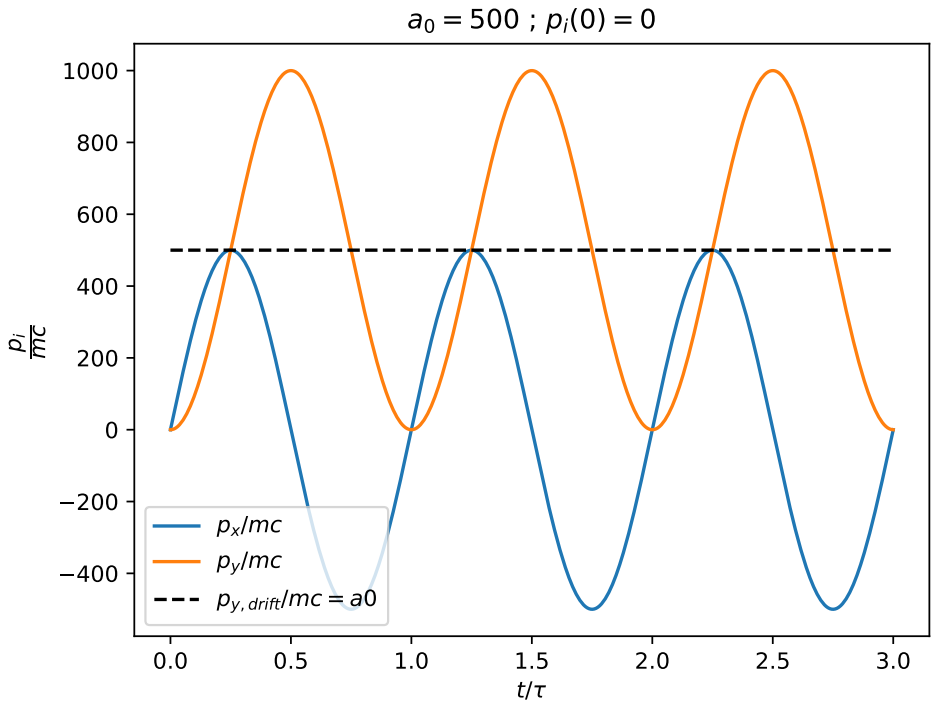

Figure 6.1: Representation of the classical components of the momentum as a function of time, for a positron initially at rest in a rotating electric field. The drift momentum, orthogonal to the initial direction of the electric field, is represented in dashed black. The field amplitude is $a_0 = 500$.

The evolution in time of the Lorentz factor and quantum parameter of an electron (or positron) following the equations above are represented in Fig. 6.2. The quantum parameter is strictly positive, meaning that a charge at rest in this field has a non zero quantum parameter at all times. This is due to the time component of the four momentum of the particle in Eq. (2.34) which is larger than $mc > 0$. The minimum value of the quantum parameter is E_0/E_S, the ratio of the electric field amplitude to the Schwinger field. This ratio, is small compared to 1 in the regime we are interested in. The dominant contribution to χ_e comes from the term with the factor a_0^2 in the square root of Eq. (6.5), that becomes important for $a_0 \gg 1$ and allows to reach χ_e values of order 1 and above. Indeed, from Eq. (6.5), $\chi_e \geq 1$ gives

$$a_0 \geq \sqrt{\frac{eE_S}{2mc\omega}}\,. \tag{6.6}$$

This corresponds to $a_0 \geq 400$ for a rotating frequency ω corresponding for a laser to a wavelength $\lambda = 0.8\mu$m.

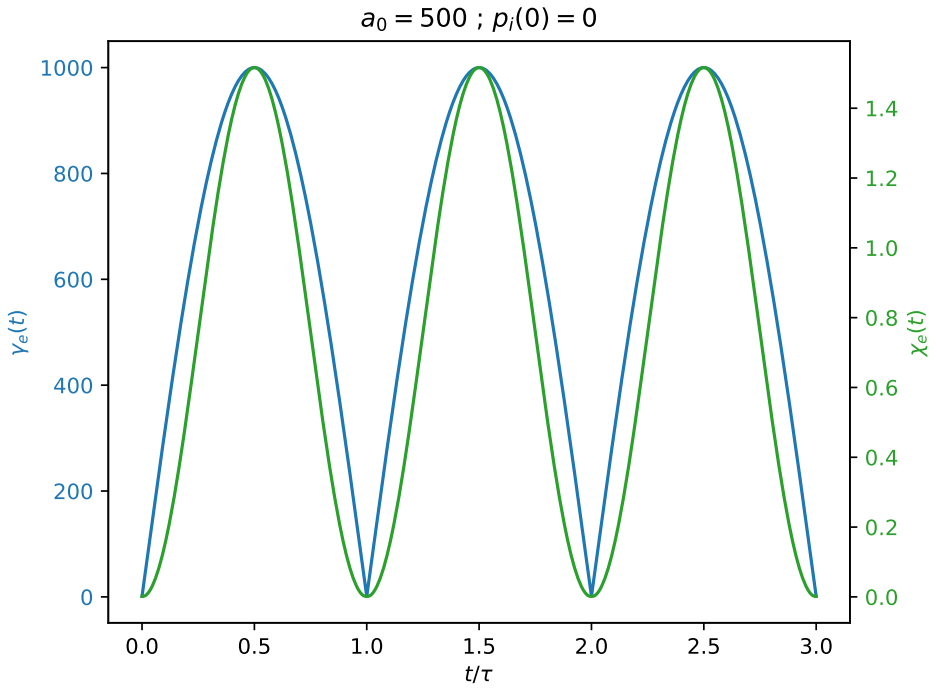

Figure 6.2: Representation of the Lorentz factor γ_e and quantum parameter χ_e of a positron initially at rest in a rotating electric field, following a classical trajectory. The field amplitude is $a_0 = 500$.

6.1.2 Pair creation in the quasi steady state regime

Let us now look at pair creation in this rotating electric field. The number of gamma photons and pairs follow the differential equations

$$\frac{\mathrm{d}N_\gamma}{\mathrm{d}t} = -W_p N_\gamma + 2W_\gamma N_p \,, \tag{6.7}$$

$$\frac{\mathrm{d}N_p}{\mathrm{d}t} = W_p N_\gamma \,. \tag{6.8}$$

Within the assumption of a quasi steady state, meaning that the shape of the pair and gamma photon distribution functions does not change with time, the gamma photons and pairs are created at constant rates W_γ and W_p, respectively. The equations can then be solved in a matrix form

$$\frac{\mathrm{d}\boldsymbol{N}}{\mathrm{d}t} = M\boldsymbol{N} \tag{6.9}$$

$$\boldsymbol{N} = \begin{pmatrix} N_\gamma \\ N_p \end{pmatrix} \; ; \quad M = \begin{pmatrix} -W_p & 2W_\gamma \\ W_p & 0 \end{pmatrix} . \tag{6.10}$$

This system of differential equations can be solved by diagonalising the matrix

M, whose eigenvalues are

$$\lambda_{\pm} = \frac{W_p}{2}\left(-1 \pm \sqrt{1 + \frac{8W_\gamma}{W_p}}\right), \tag{6.11}$$

with the corresponding eigenvectors

$$v_{\pm} = \begin{pmatrix} \frac{\lambda_{\pm}}{W_p} \equiv \Lambda_{\pm} \\ 1 \end{pmatrix}. \tag{6.12}$$

The matrix M can be written in the form QDQ^{-1} with D a diagonal matrix, and the solution of the differential equation is

$$\boldsymbol{N}(t) = Q \exp(tD) Q^{-1} \boldsymbol{N_0} \tag{6.13}$$

with

$$D = \begin{pmatrix} \lambda_+ & 0 \\ 0 & \lambda_- \end{pmatrix}; \boldsymbol{N}_0 = \begin{pmatrix} N_{\gamma 0} \\ N_{p0} \end{pmatrix} \tag{6.14}$$

$$Q = \begin{pmatrix} \Lambda_+ & \Lambda_- \\ 1 & 1 \end{pmatrix}; Q^{-1} = \frac{2}{\sqrt{1 + \frac{8W_\gamma}{W_p}}} \begin{pmatrix} 1 & -\Lambda_- \\ -1 & \Lambda_+ \end{pmatrix} \tag{6.15}$$

where $\boldsymbol{N}_0$ represents the initial conditions. Here the initial conditions should already satisfy the hypothesis of a steady state since we used it to solve the equations. From Eqs. (6.13),(6.14) and (6.15) we can deduce the growth rate of the number of pair. Using Eq. (6.13), we can express the number of pairs as

$$N_p(t) = \frac{2}{\sqrt{1 + \frac{8W_\gamma}{W_p}}} \left[e^{t\lambda_+}(N_{\gamma 0} - N_{p0}\Lambda_-) + e^{t\lambda_-}(N_{p0}\Lambda_+ - N_{\gamma 0})\right]. \tag{6.16}$$

Since $\lambda_+ > 0$ and $\lambda_- < 0$, the growth rate, is equal to λ_+. Note that the growth rate depends only on the rate of pair production and not on the initial number of particles, consistent with the hypothesis of a steady state. This value is in agreement with what was obtained in [Grismayer et al., 2017].

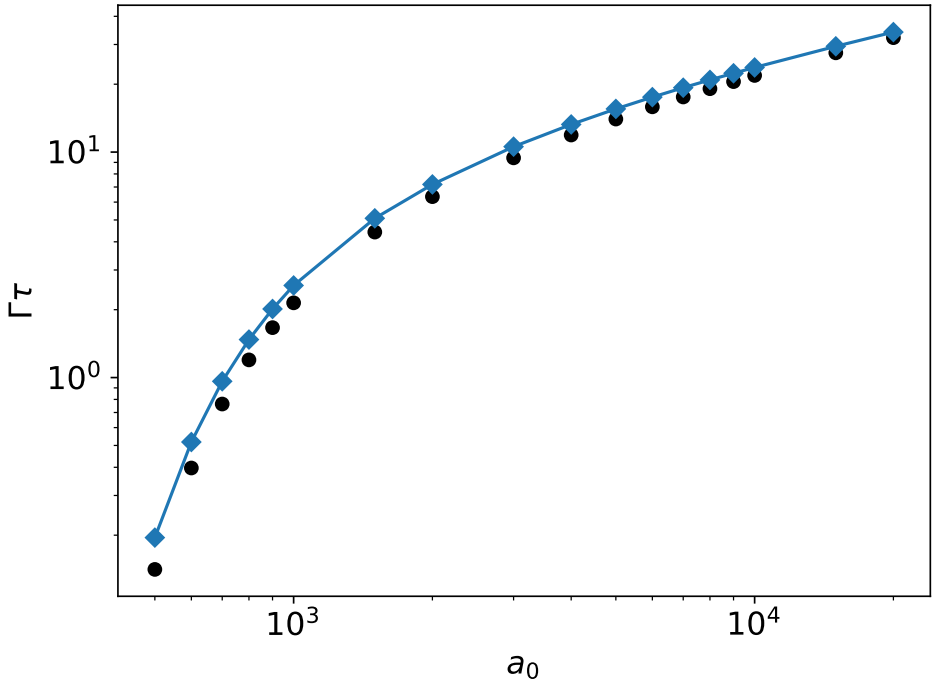

Figure 6.3: Growth rate Γ, normalised to the rotating frequency of the field $1/\tau$, of the cascade obtained from 1D3V PIC simulations of pure rotating electric field as a function of a_0 (black dots). These values are directly extracted from the number of particles as a function of time. Theoretically predicted λ_+ (blue line) given by equation (6.11), using the rates extracted from the particle distributions in the PIC simulations.

6.1.3 Validation of theoretical growth rate via PIC simulations

We compare the growth rate calculated in the previous section with the values extracted from 1D3V PIC simulations including the relevant Monte-Carlo modules. This is shown in fig. 6.3 as a function of the field strength a_0. In the simulations, we place the test particles, meaning that they do not depose current and charge densities and do not affect the external field, initially at rest in the rotating electric field of Eq. (6.1). When a steady state is reached we extract the corresponding growth rate from a fit of the evolution in time of the number of particles (black dots). We compare this value to the rate obtained from λ_+ (Eq. (6.11)), computed by extracting from the simulations the rates W_γ and W_p from the particles distributions in χ and γ (blue line). The two approaches are in good agreement, although the theoretical calculation slightly overestimates the growth rate, especially at low intensities. This is due to the fact that we use Eq. (2.51) for the rate of emission of gamma photons, which includes the emission of photons with energies smaller than $2mc^2$. These photons weakly contribute to pair production due to the strong cut off at low photon quantum parameter of the NBW rate (Eq. (2.45)). As a result the growth rate is overestimated by considering photons that do not participate to the process. To correct this we could integrate Eq. (2.52) from $\gamma_\gamma = 2$ to $\gamma_\gamma = \gamma_e$ instead of integrating from $\xi' = 0$ to $\xi' = 1$. However, having an integration range dependent on γ_e would be computationally more expensive as the intergral will be over (χ_e, γ_e). Hence, for the purpose of this chapter, the expression obtained in Eq. (2.51) will be sufficient.

Another important point is to verify that a quasi steady state is reached in the PIC simulations. To do that, we show in Figs. 6.4 and 6.5 the evolution in time of the χ and γ of positrons and gamma photons, averaged over the particle distributions. After an initial transient, which shorten as a_0 increases, the average values of the particles and photons Lorentz factor and their quantum parameter become constant.

In Figs. 6.6 and 6.7, we show the evolution in time of the standard deviations for these quantities, which are given by

$$\sigma_{\chi_e} = \sqrt{\frac{\int \mathrm{d}\chi_e (\chi_e - \langle\chi_e\rangle)^2 w(\chi_e)}{\int \mathrm{d}\chi_e w(\chi_e)}}, \tag{6.17}$$

with $w(\chi_e)$ the sum of the weights of all pairs having the quantum parameter χ_e. The standard deviations rapidly reach a constant value, confirming that a quasi steady state regime is indeed reached.

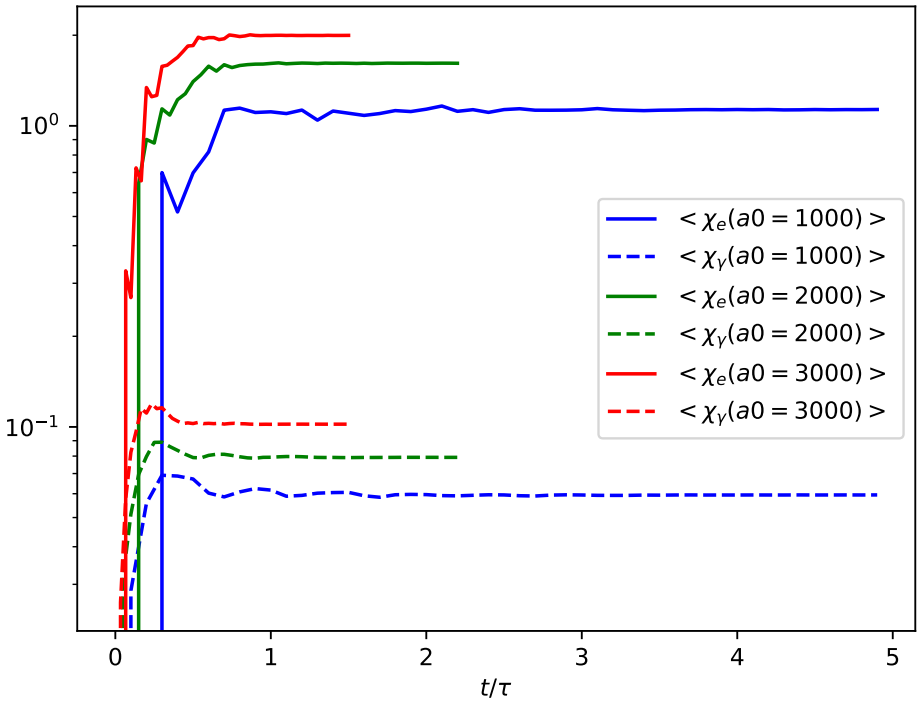

Figure 6.4: Average quantum parameter of particles as a function of time in a rotating electric field, for different field amplitudes.

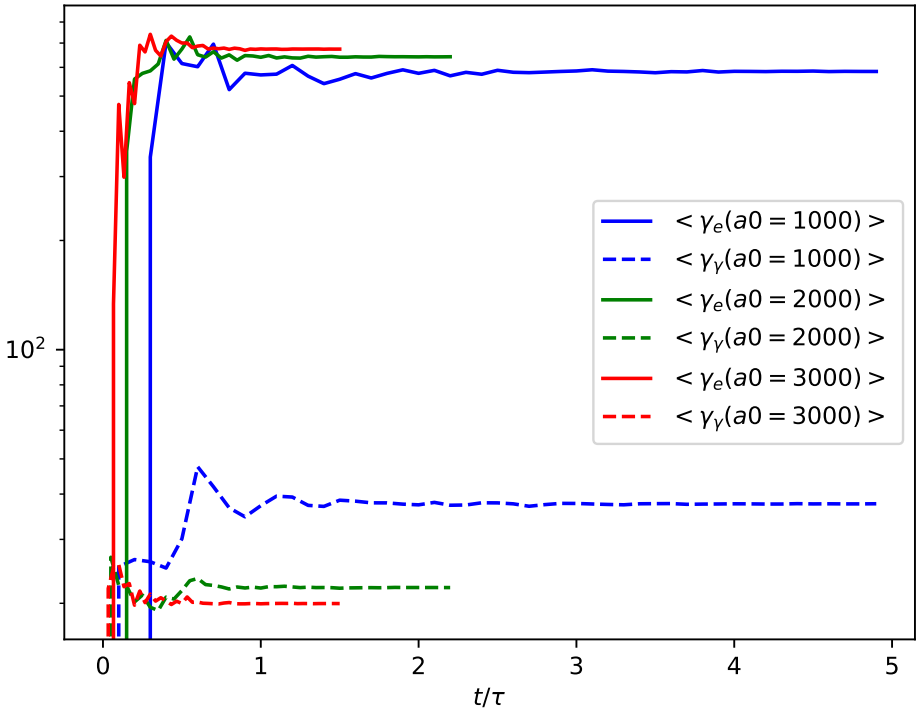

Figure 6.5: Average γ factor of particles as a function of time in a rotating electric field, for different field amplitudes.

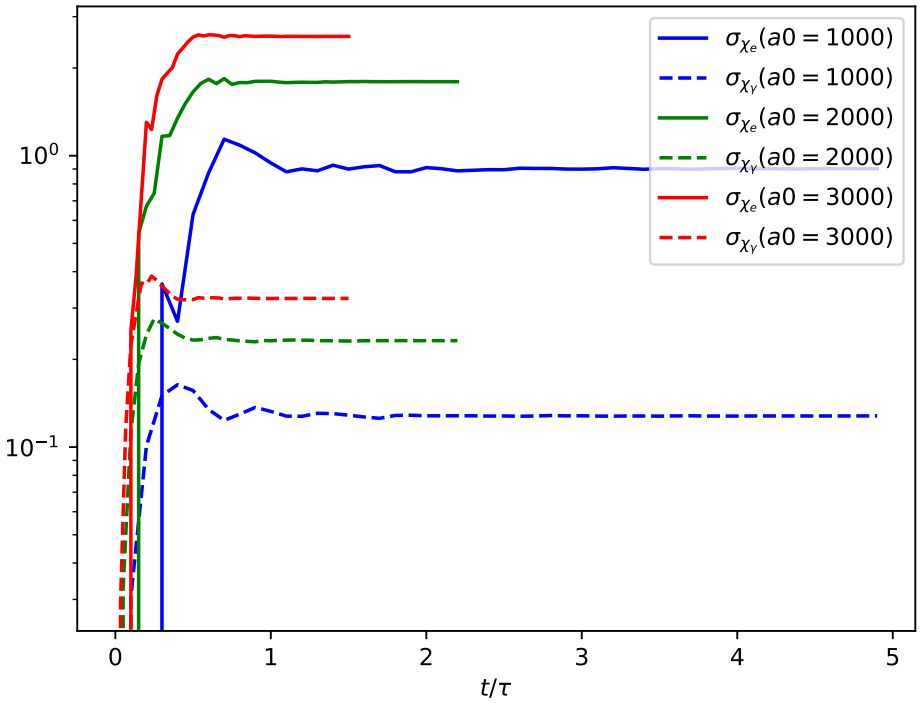

Figure 6.6: Standard deviation of the quantum parameter of particles as a function of time in a rotating electric field, for different field amplitudes.

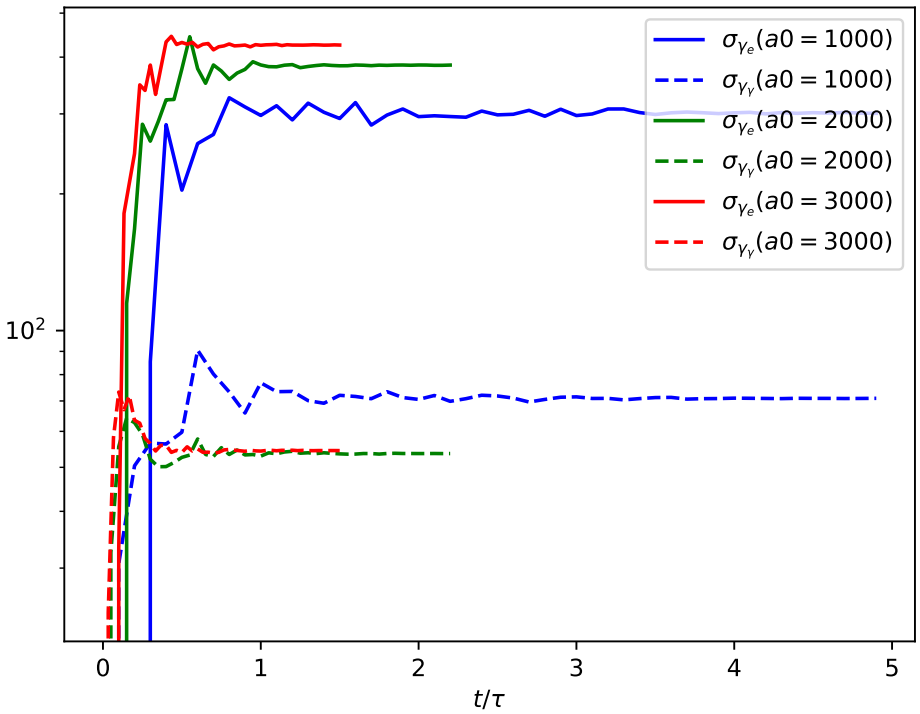

Figure 6.7: Standard deviation of the γ factor of particles as a function of time in a rotating electric field, for different field amplitudes.

As expected the average value and standard deviation of the quantum parameter of the particles and photons increase with the field amplitude a_0, see figures 6.4 and 6.6. This is also true for the particles Lorentz factor and the energy standard deviation. On contrary, the average value of the photon energy and its standard deviation decrease with a_0, see figures 6.5 and 6.7. Overall however the rate of pair production increases, since we see in Eq. (2.43) that increasing χ_γ and decreasing γ_γ results in a higher rate.

6.2 Avalanches in the two counter-streaming lasers configuration

As it was shown in the previous section, the ideal configuration of a pure rotating electric field can in theory leads to a self-sustained cascade and potentially to abundant pair creation. This prediction, together with the recent increase of attainable laser intensities, led Kirk and Bell to first investigate pair creation in two counter-streaming laser pulses [Bell and Kirk, 2008]. On can in principle create a pure rotating electric field configuration with two waves of opposite circular polarisations. Indeed, considering two counter-streaming PW of opposite circular polarisations, the electromagnetic field corresponds to a pure rotating electric field at the magnetic field nodes. In a more realistic scenario, we can envision the use of two gaussian pulses of opposite CP laser pulses, to produce a standing wave (this will be discussed further in Sec. 7.1.1). Contrary to the ideal PW case, the rotating electric field created by the two gaussian pulses has a finite extent in the transverse plane. Moreover, for realistic and focused laser pulses, longitudinal electromagnetic field components may exist on the magnetic field nodes. We stress here that even for the two plane waves, the electric field is purely rotating only at the magnetic nodes, which means that in practice particles will never experienced the fields of the ideal case presented in the previous Sec. 6.1.

However, this setup is the closest one to the ideal rotating case that has been proposed to date, and as therefore attracted much interest of the strong-field community over the last decade as testified by several publications [Kirk et al., 2009,Elkina et al., 2011,Nerush et al., 2011a,Bashmakov et al., 2014,Grismayer et al., 2016,Jirka et al., 2016,Grismayer et al., 2017,Tamburini et al., 2017,Jirka et al., 2017,Slade-Lowther et al., 2019]. After showing by numerical simulations the feasibility of the avalanche in the two lasers configuration, the efficiency of the cascade became the main focus. Depending if one measures efficiency of the avalanche in terms of pair density, total number of particles or the growth

rate, one may pursue different strategies to optimize the process. Indeed, several parameters can play a role in the cascade development, e.g. the wave polarisation, or the characteristics of the seeding particles. In this thesis, and especially in the following sections and chapters, we refer to the efficiency considering it proportional to the growth rate or the number of produced pairs.

In order to study the impact of laser polarisations, a first work comparing numerically and theoretically configurations with CP and LP at fixed total pulse energy has been performed by [Nerush et al., 2011a]. This suggests that, for the parameters explored, CP is the optimal choice, as it has been confirmed, in more recent works, such as [Grismayer et al., 2017], focusing on the study of the cascade growth rate. However, the latter work highlight a potential issue with the seeding particles in the CP configuration, as they can be pushed away from the interaction region of strong fields before the onset of the cascade. This is shown to be more problematic for the CP configuration than in the LP case. The LP configuration has been investigated in a work by [Jirka et al., 2017] which considers intensities below $10^{24}\mathrm{W/cm}^2$, and suggests that in this regime, LP produces higher number of particles than CP. This is believed to be owing to two reasons: first, at the same energy the LP case has higher field amplitude and so particles can more easily reach a value of the quantum parameter close to 1. We showed Sec. 2.2 that this argument is consistent with the fact that the rate of pair creation increases strongly with the quantum parameter in the range of $\chi \ll 1$, and so a difference in the field amplitude, even of a factor $1/\sqrt{2}$, could play a big role. The second reason is the presence of the so-called *attractors* in the phase space of particles. As it will be detailed in section 6.4, in a standing wave configuration particles are pushed away from the magnetic field nodes, where the electric field is at its maximum, towards the electric field nodes. In the CP case, particles get trapped in these attractors, i.e. at the electric field nodes, after one or a few laser periods. Hence, the particles are not efficiently re-accelerated since they do not experience strong electric fields. Then, the advantage of the LP configuration is that due to the field strength vanishing regularly, particles spread more in the phase space and can be re-injected into regions where their quantum parameter increases again. They can then contribute to the avalanche development. However, at intensity higher than $10^{24}\mathrm{W/cm}^2$, the attractors do not impact the dynamics of the particles enough to make the cascade in the LP configuration growing faster than in the CP case, as shown numerically by [Grismayer et al., 2017].

Another aspect that deserved discussions, is the impact of the transverse size of the laser beams, which was investigated in [Jirka et al., 2016]. Indeed to reach QED-relevant regime in near future facilities, one may want to increase

the field intensity as much as possible by focusing the laser. However the work of [Jirka et al., 2016] showed that the strong ponderomotive force of a tightly focused gaussian beam might push transversally the charged particles out of the interaction region. In these conditions, a cascade cannot be self sustained, or produces at best a drastically reduced number of pairs.

Finally a point that can be important in the case of an avalanche sustained for long times, is the effect of the produced pairs (potentially a pair plasma) on the laser field. This aspect has not been not explored in this thesis, however several studies are reported in [Fedotov et al., 2010, Grismayer et al., 2016, Slade-Lowther et al., 2019]. Since this effect can be responsible for a decrease of the growth rate of the cascade with time.

In this work we will study the cascades induced in two counter streaming gaussian and LG pulses. As shown by the short review of this section, many field characteristics, other than the laser amplitude, can be of strong relevance, e.g. the laser polarisation. To the author knowledge, no work has been performed at this time in the configuration using two counter-streaming LG beams, whose properties can be investigated to identify which field topology is more efficient to trigger a cascade. The interest toward these particular beams is motivated by the ring shape of their intensity distribution in the transverse plane, which could in principle help trapping pairs close to the laser propagation axis and enhance the cascade growth rate. This idea has to be numerically tested and the results of a series of 3D3V PIC simulations will be presented in the last chapter of this manuscript.

Before moving to it, in the next section we present some recent works, detailing a model to describe how the quantum parameter and the energy of charges grow in the presence of strong fields on short timescales. These results will be used in Chap. 7 to interpret the numerical results and compare the efficiency different field configurations, so as infer the parameters determining the efficiency of the avalanche.

6.3 Field invariants and particle dynamics in a strong field

6.3.1 Model for short time dynamics

We here present some aspects of the dynamics of a charged particle in a strong field following the discussion of [Mironov et al., 2021]. The focus is on the condition to have efficient particle acceleration in order for the charged particle keep emitting hard gamma photons. This study allows to understand which

field configuration is suitable for a renewal of the particle energy and its quantum parameter between hard photon emissions, beyond the purely rotating field case.

Let us consider a strong field with electromagnetic field tensor $F^{\mu\nu}$, and characteristic frequency ω. The motion of a charged particle in a strong field, in the quantum dominated regime, is complex. A first approach to describe the particle dynamics would be to consider that field is high enough so that particles become ultra-relativistic on time-scales shorter than the one of the field variation. If one assumes that the field is slowly varying compared to the timescale of quantum process for ultra-relativistic particles, then the dynamics is given by the classical trajectory, interrupted by gamma photon emissions. Let us consider a strong field with characteristic frequency ω, described by the electromagnetic field tensor $F^{\mu\nu}$. The classical equation of motion for a particle with charge q in this field is,

$$\frac{\mathrm{d}p^\mu}{\mathrm{d}\tau} = \frac{q}{m} F^\mu_{\ \nu}(x(\tau))p^\nu \,. \tag{6.18}$$

One way to ensure a cascade is to have strong gamma emission on timescales shorter than the field period, and consider the dynamics of the charged particles for $\omega t \ll 1$. In order to do so we can expand the momentum, position and field tensor in powers of the normalised time ωt,

$$p(\tau) = p_{(1)} + p_{(2)} + \dots \,, \text{ with } \quad p_{(n)} = \mathcal{O}((\omega t)^n) \,, \tag{6.19}$$

$$x(\tau) = x_{(1)} + x_{(2)} + \dots \,, \text{ with } \quad x_{(n)} = \mathcal{O}((\omega t)^n) \,. \tag{6.20}$$

We chose the initial conditions $x_{(i)}(0) = 0$, $p_{(i>1)}(0) = 0$ such that $p(0) = p_{(1)}(0)$ is the particle initial momentum. The mass shell relation $p^2 = m^2c^2$ then implies (by squaring Eq. (6.19) and evaluating order by order) that

$$(p_{(1)})^2 = m^2c^2 \,, \tag{6.21}$$

$$p_{(1)}p_{(2)} = 0 \,, \tag{6.22}$$

$$(p_{(2)})^2 + 2p_{(1)}p_{(3)} = 0 \quad \dots \tag{6.23}$$

Similarly the field tensor can be expanded to give

$$F^\mu_{\ \nu} = F^\mu_{\ \nu(0)} + F^\mu_{\ \nu(1)} + \dots \,, \text{ with } \quad F^\mu_{\ \nu(n)} = \mathcal{O}((\omega t)^n) \,. \tag{6.24}$$

The first non zero contribution of the field is the value at the origin given by $F^\mu_{\ \nu(0)} = F^\mu_{\ \nu}(x(0) = 0)$ which is a constant term. The following orders in the

field tensor are given by

$$F^{\mu}_{\ \nu(1)} = F^{\mu}_{\ \nu,\sigma(0)} x^{\sigma}_{(1)} \tag{6.25}$$

$$F^{\mu}_{\ \nu(2)} = \frac{1}{2} F^{\mu}_{\ \nu,\sigma\rho(1)} x^{\sigma}_{(1)} x^{\rho}_{(1)} + F^{\mu}_{\ \nu,\sigma(0)} x^{\sigma}_{(2)} \,, \tag{6.26}$$

where the indexes after the comma indicate a derivative, such as

$$F^{\mu}_{\ \nu,\sigma} = \frac{\partial F^{\mu}_{\ \nu}}{\partial x^{\sigma}} = \partial_{\sigma} F^{\mu}_{\ \nu} \,. \tag{6.27}$$

From now on and until the end of this chapter we will use the matrix notation F for the field tensor, and x and p will designate 4-vectors unless specified otherwise. At first order, the equation of motion of a charge $q = \pm e$ is

$$\frac{\mathrm{d}p_{(1)}}{\mathrm{d}\tau} = \frac{q}{m} F_{(0)} p_{(1)} \,. \tag{6.28}$$

This is the equation of motion of a particle in a constant electromagnetic field. An elegant approach to solve this equation in the general case is given by [Taub, 1948]. Since $F_{(0)}$ can be viewed as a matrix, the equation above can be solved using its eigenvectors u_k and eigenvalues α_k satisfying $F_{(0)} u_k = \dfrac{\alpha_k}{c} u_k$. The momentum on short timescales is then given by

$$p_{(1)}(\tau) \underset{\omega t \ll 1}{\simeq} \exp\left(\frac{q F_{(0)} \tau}{m}\right) p(0) = \sum_{k=0}^{3} C_k \exp\left(\frac{q \alpha_k \tau}{mc}\right) u_k \,, \tag{6.29}$$

where the C_k are defined by the initial conditions, such that $\sum_{k=0}^{3} C_k u_k = p(0)$. The eigenvalues of $F_{(0)}$ will be expressed using the following Lorentz invariants

$$\mathcal{F} = -\frac{c^2}{4} F^{\mu\nu} F_{\mu\nu} = (\boldsymbol{E}^2 - c^2 \boldsymbol{B}^2)/2 \,, \tag{6.30}$$

$$\mathcal{G} = -\frac{c}{4} * F^{\mu\nu} F_{\mu\nu} = c \boldsymbol{B} \cdot \boldsymbol{E} \,. \tag{6.31}$$

The eigenvalues are then given by

$$\alpha_{k=1,\ldots,4} = (\epsilon, -\epsilon, i\eta, -i\eta) \tag{6.32}$$

with

$$\epsilon = \sqrt{\sqrt{\mathcal{F}^2 + \mathcal{G}^2} + \mathcal{F}} \tag{6.33}$$

$$\eta = \sqrt{\sqrt{\mathcal{F}^2 + \mathcal{G}^2} - \mathcal{F}} \,. \tag{6.34}$$

Since $\epsilon > 0$, the main contribution to $p_{(1)}$ for $\tau \gg \dfrac{mc}{e\epsilon}$ (i.e. after a particle

initially at rest becomes ultra-relativistic) comes from the eigenvalue ϵ due to the exponential factor Eq. (6.29). So on short timescales one has

$$p_{(1)}(\tau) \underset{\omega t \ll 1}{\simeq} C_1 \exp\left(\frac{q\epsilon\tau}{mc}\right) u_1 \,, \tag{6.35}$$

which can be integrated to obtain the position

$$x_{(1)}(\tau) \underset{\omega t \ll 1}{\simeq} C_1 \frac{c}{e\epsilon} \exp\left(\frac{q\epsilon\tau}{mc}\right) u_1 \,. \tag{6.36}$$

By choosing the normalisation of the time component $u_1^0 = 1$ (see [Mironov et al., 2021]) we see that, since by construction $x^0 = ct$, we have

$$ct = x^0 \simeq x^0_{(1)} \simeq C_1 \frac{c}{e\epsilon} \exp\left(\frac{q\epsilon\tau}{mc}\right) \,, \tag{6.37}$$

such that

$$\exp\left(\frac{q\epsilon\tau}{mc}\right) \simeq e\epsilon t / C_1 \,. \tag{6.38}$$

After injecting this relation in Eq. (6.29), one finally obtains the energy grows

$$\frac{\varepsilon(t)}{mc^2} = \frac{p^0(t)}{mc} \underset{\omega t \ll 1}{\simeq} \frac{e\epsilon t}{mc} \,. \tag{6.39}$$

To derive the expression of the quantum parameter, one needs to go to the next two orders, balancing those terms in a matrix form gives

$$\frac{\mathrm{d}p_{(2)}}{\mathrm{d}\tau} - \frac{q}{m} F_{(0)} p_{(2)} = \frac{q}{m} F_{(1)} p_{(1)} \,, \tag{6.40}$$

$$\frac{\mathrm{d}p_{(3)}}{\mathrm{d}\tau} - \frac{q}{m} F_{(0)} p_{(3)} = \frac{q}{m} \left(F_{(1)} p_{(2)} + F_{(2)} p_{(1)}\right) \tag{6.41}$$

Let us look at the second order in Eq. (6.40) first. One can simplify the differential equation by making the following approximation. Since $F_{(1)}p_{(1)}$ and $F_{(0)}p_{(2)}$ are of order $\omega^2 t^2$ and so they are proportional to $\exp\left(\frac{2q\epsilon\tau}{mc}\right)$ since, as we showed above one has approximately $t \propto \exp\left(\frac{2q\epsilon\tau}{mc}\right)$. This leads to $p_{(2)} \propto \exp\left(\frac{2q\epsilon\tau}{mc}\right)$ and so

$$\frac{\mathrm{d}p_{(2)}}{\mathrm{d}\tau} \simeq \frac{2e\epsilon}{mc} p_{(2)} \,. \tag{6.42}$$

This approximation is valid as long as the expression $p_{(1)}$ is valid, meaning that we are in the ultra-relativistic regime and we consider only short timescales $\omega t \ll 1$. Then plugging back this result into Eq. (6.40), we can express $p_{(2)}$ as

$$p_{(2)} \simeq \left(2\frac{\epsilon}{c}\mathbb{I} - F_{(0)}\right)^{-1} F^{(1)} p^{(1)} \,, \tag{6.43}$$

with $\mathbb{I}$ the 4×4 identity matrix.

Now to derive the expression of χ_e, one should first write it in the following form

$$\chi_e^2 = -\frac{\hbar^2}{m^2c^6}\left(\frac{\mathrm{d}p}{\mathrm{d}\tau}\right)^2 . \tag{6.44}$$

Then we have up to order $(\omega t)^4$

$$\begin{aligned}\chi_e^2 \simeq & -\frac{\hbar^2}{m^2c^6}\left[\left(\frac{\mathrm{d}p_{(1)}}{\mathrm{d}\tau}\right)^2 + 2\frac{\mathrm{d}p_{(1)}}{\mathrm{d}\tau}\frac{\mathrm{d}p_{(2)}}{\mathrm{d}\tau}\right] \\ & -\frac{\hbar^2}{m^2c^6}\left[\left(\frac{\mathrm{d}p_{(2)}}{\mathrm{d}\tau}\right)^2 + 2\frac{\mathrm{d}p_{(1)}}{\mathrm{d}\tau}\frac{\mathrm{d}p_{(3)}}{\mathrm{d}\tau}\right] .\end{aligned} \tag{6.45}$$

In order to evaluate this expression, we need to express it in terms of $F_{(0)}$; $F_{(1)}$; $p_{(1)}$ and $x_{(1)}$, all known quantities. Here we simplify the expression, within the same approximation as in (6.42), and so we have for $p_{(n)}$

$$\frac{\mathrm{d}p_{(n)}}{\mathrm{d}\tau} \simeq n\frac{e\epsilon}{mc}p_{(n)} , \tag{6.46}$$

which allows to replace the derivatives with functions proportional to the momentum in Eq. (6.45). Note that the $p_{(1)}p_{(2)}$ term cancels due to Eq. (6.22). Now we can evaluate the last term of Eq. (6.45). his can be expressed as a function of $p_{(2)}$ using the relations in Eq. (6.46) and Eq.(6.23). We then we use the expression in Eq. (6.43) to obtain

$$-\frac{e^2\epsilon^2}{m^6c^8}(p_{(2)})^2 \simeq -\frac{\hbar^2}{m^2c^6}\left[\left(\frac{\mathrm{d}p_{(2)}}{\mathrm{d}\tau}\right)^2 + 2\frac{\mathrm{d}p_{(1)}}{\mathrm{d}\tau}\frac{\mathrm{d}p_{(3)}}{\mathrm{d}\tau}\right] \tag{6.47}$$

$$-\frac{e^2\epsilon^2}{m^6c^8}(p_{(2)})^2 = \frac{e^2\epsilon^2}{m^6c^8}p_{(1)}F_{(1)}(4\epsilon^2\mathbb{I} - (F_{(0)})^2)^{-1}F_{(1)}p_{(1)} . \tag{6.48}$$

Finally, as $F_{(1)}$ is determined by $F_{(0)}$ and $x_{(1)}$ one obtains that the quantum parameter behaves as

$$\chi_e^2(t) \underset{\omega t\ll 1}{\simeq} \chi_e^2(0) + \left(\frac{e^2\hbar\epsilon^2\omega_{\text{eff}}}{m^3c^4}\right)^2 t^4 \tag{6.49}$$

with

$$\omega_{\text{eff}}^2 = F_{\mu\nu,\sigma(0)}u_1^\mu u_1^\sigma (J^{-1})^\nu{}_\lambda F^\lambda{}_{\kappa,\rho(0)}u_1^\rho u_1^\kappa \tag{6.50}$$

$$J = \left(2\frac{\epsilon}{c}\mathbb{I} - F_{(0)}\right)^2 . \tag{6.51}$$

As we will see in further examples, ω_{eff} is an effective frequency that depends on the field and its derivatives, but not on its global amplitude. It therefore

encodes the contribution of the geometry of the fields that the charge experiences along its trajectory. in which the charge is evolving. Equation (6.49) shows that χ_e grows with ϵ^2 the invariant defined in Eq. (6.33). It is therefore needed to use electric type fields $\mathcal{F} > 0$, since on the contrary ϵ vanishes for magnetic type $\mathcal{F} < 0$ configurations. This needed condition can be reached in a purely rotating field, or near the nodes of the magnetic field in a standing wave.

6.3.2 Example of a purely rotating electric field

We want here to compare the exact solution find in Sec.6.1 for the case of a rotating electric field with the model presented in the previous section. Considering the expression for the χ_e derived in Eq.(6.5), and expanding it for $\omega t \ll 1$, one gets

$$\chi_e^2 \simeq \frac{e^2\hbar^2 E_0^2}{m^4c^6} + \frac{1}{4}\frac{e^4\hbar^2 E_0^4}{m^6c^8}\omega^2 t^4 + \mathcal{O}((\omega t)^5)\,. \tag{6.52}$$

If we use Eq. (6.49), we obtain the same results since in this case $\omega_{\text{eff}} = \omega/2$ and $\epsilon = E_0$ for the rotating field case (see Eq. (6.1)). We conclude that in this case the approach derived in [Mironov et al., 2021] is consistent with the development of the exact expression of the quantum parameter χ_e. This means that the approximation made in the model detailled in Sec.6.3 are well justified and the leading behaviour of the short time dynamics is properly captured. We will then use this model in configurations with more complex fields, i.e. considering LG laser pulses, in the following chapter.

6.4 Attractors in a standing wave

As mentioned before, one of the most promising configuration for an avalanche is the setup with two counter-streaming beams. This allows to create a standing wave where we can identify regions with two different types of field. Close to the magnetic field nodes, the electric field is large, and one expect pairs to be efficiently re-accelerated. If instead we consider the region near the nodes of the electric field, the magnetic field is dominant and it does not provide contribution to the energy increase of the pairs.. By studying the dynamics of the charges in those two regions we can understand how particles can move from one region to another and the conditions required for the onset of the cascade. In particular for certain field configurations, attractors can be present in phase space as shown numerically and theoretically by [Esirkepov et al., 2014, Lehmann and Spatschek, 2012, Gong et al., 2016, Kirk, 2016, King and

Hu, 2016]. In these cases the understanding of their impact on the particle dynamics is essential. The derivation we are going to present is detailed in [Gong et al., 2016].

Considering two counter-streaming beams with circular polarization with opposite helicity, a transverse rotating electric field is produced at the magnetic nodes of the resulting standing wave. This allows us to use the analytical results presented in Sec. 6.1. For two counter-propagating circularly polarised plane waves, the respective electromagnetic fields are given by

$$\boldsymbol{E}_1 = \frac{E_0}{2}\left[\sin(\omega t - kz)\hat{\boldsymbol{x}} + \sigma_1 \cos(\omega t - kz)\hat{\boldsymbol{y}}\right] \tag{6.53}$$

$$\boldsymbol{E}_2 = \frac{E_0}{2}\left[-\sin(\omega t + kz + \Delta\phi)\hat{\boldsymbol{x}} + \sigma_2 \cos(\omega t + kz + \Delta\phi)\hat{\boldsymbol{y}}\right] \tag{6.54}$$

$$\boldsymbol{B}_1 = \frac{E_0}{2c}\left[-\sigma_1 \cos(\omega t - kz)\hat{\boldsymbol{x}} + \sin(\omega t - kz)\hat{\boldsymbol{y}}\right] \tag{6.55}$$

$$\boldsymbol{B}_2 = \frac{E_0}{2c}\left[\sigma_2 \cos(\omega t + kz + \Delta\phi)\hat{\boldsymbol{x}} + \sin(\omega t + kz + \Delta\phi)\hat{\boldsymbol{y}}\right] , \tag{6.56}$$

where $\Delta\phi$ is the dephasing between the two waves. If we assume opposite circular polarisation $\sigma_2 = -\sigma_1$ the total field is given by

$$\begin{aligned}\boldsymbol{E} &= E_0\left[-\sin\left(kz + \frac{\Delta\phi}{2}\right)\cos\left(\omega t + \frac{\Delta\phi}{2}\right)\hat{\boldsymbol{x}}\right. \\ &+ \left.\sigma_1 \sin\left(kz + \frac{\Delta\phi}{2}\right)\sin\left(\omega t + \frac{\Delta\phi}{2}\right)\hat{\boldsymbol{y}}\right] , \qquad (6.57)\\ \boldsymbol{B} &= \frac{E_0}{c}\left[-\sigma_1 \cos\left(kz + \frac{\Delta\phi}{2}\right)\cos\left(\omega t + \frac{\Delta\phi}{2}\right)\hat{\boldsymbol{x}}\right. \\ &+ \left.\cos\left(kz + \frac{\Delta\phi}{2}\right)\sin\left(\omega t + \frac{\Delta\phi}{2}\right)\hat{\boldsymbol{y}}\right] . \qquad (6.58)\end{aligned}$$

If we choose $\sigma_1 = 1$ for simplicity and $\Delta\phi = \pi$ to have a maximum of the electric field at $z = 0$ the field reads

$$\boldsymbol{E} = E_0\left[\cos(kz)\sin(\omega t)\hat{\boldsymbol{x}} + \cos(kz)\cos(\omega t)\hat{\boldsymbol{y}}\right] \tag{6.59}$$

$$\boldsymbol{B} = -\frac{E_0}{c}\left[\sin(kz)\sin(\omega t)\hat{\boldsymbol{x}} + \sin(kz)\cos(\omega t)\hat{\boldsymbol{y}}\right] . \tag{6.60}$$

This field derives from the vector potential

$$\boldsymbol{A} = \frac{E_0}{\omega}\left[-\cos(kz)\cos(\omega t)\hat{\boldsymbol{x}} + \cos(kz)\sin(\omega t)\hat{\boldsymbol{y}}\right] . \tag{6.61}$$

The transverse components of the momentum can be easily solved

$$p_x = \frac{qE_0}{\omega}\cos(kz)\sin(\omega t) + p_x(0) - \frac{qE_0}{\omega} \tag{6.62}$$

$$p_y = -\frac{qE_0}{\omega}\cos(kz)\sin(\omega t) + p_y(0)\,. \tag{6.63}$$

Let us choose for simplicity $p_y(0) = 0$ and $p_x(0) = \dfrac{qE_0}{\omega}$, so that there is no drift. Then the energy of the particle is given by

$$\gamma = \frac{\varepsilon}{mc^2} = \sqrt{1 + \left(\frac{p}{mc}\right)^2} \tag{6.64}$$

and from above one obtains

$$\gamma = \sqrt{1 + \left(\frac{p_z}{mc}\right)^2 + a_0^2\cos^2(kz)}\,. \tag{6.65}$$

We now want to look at the (z, p_z) phase space. We are interested in possible fixed points in the (z, p_z) phase space. In order to do so we should look at the derivatives of z and p_z with respect to time, which are given by Hamilton equations

$$\frac{\mathrm{d}z}{\mathrm{d}t} = mc^2\frac{\partial\gamma}{\partial p_z}\,;\ \frac{\mathrm{d}p_z}{\mathrm{d}t} = -mc^2\frac{\partial\gamma}{\partial z}\,. \tag{6.66}$$

We then look for z^* and $p_z^*$where both the derivatives above are equal to zero. First we have that $(\partial\gamma/\partial p_z)_{|(z^*,p_z^*)} = 0$ only if $p_z^* = 0$. Then one has

$$\frac{\partial\gamma}{\partial z} = \frac{a_0^2 k\sin(kz)\cos(kz)}{\gamma}\,, \tag{6.67}$$

which means that $kz^* \equiv 0\,[\pi/2]$. Since the problem is periodic, we can restrain ourselves to the analysis of one wavelength. Note that $kz^* = 0\,;\,\pi$ correspond to the nodes of the magnetic field and $kz^* = \pi/2\,;\,3\pi/2$ to the nodes of the electric field. To study the behaviour of particles around those points, to infer the stability of the fixed points in the phase space, one should consider small perturbations around the fixed points following the discussion of [Jordan and Smith, 2007, Hirsch et al., 2012]. In order to do so, one should compute the following Jacobian matrix

$$J = \begin{pmatrix} \dfrac{\partial}{\partial z}\dfrac{\mathrm{d}z}{\mathrm{d}t} & \dfrac{\partial}{\partial p_z}\dfrac{\mathrm{d}z}{\mathrm{d}t} \\ \dfrac{\partial}{\partial z}\dfrac{\mathrm{d}p_z}{\mathrm{d}t} & \dfrac{\partial}{\partial p_z}\dfrac{\mathrm{d}p_z}{\mathrm{d}t} \end{pmatrix}_{|(z^*,p_z^*)} = mc^2 \begin{pmatrix} 0 & \dfrac{1}{m^2c^2\gamma} \\ \dfrac{a_0^2k^2\cos(2kz)}{\gamma} & 0 \end{pmatrix}_{|(z^*,p_z^*)}\,. \tag{6.68}$$

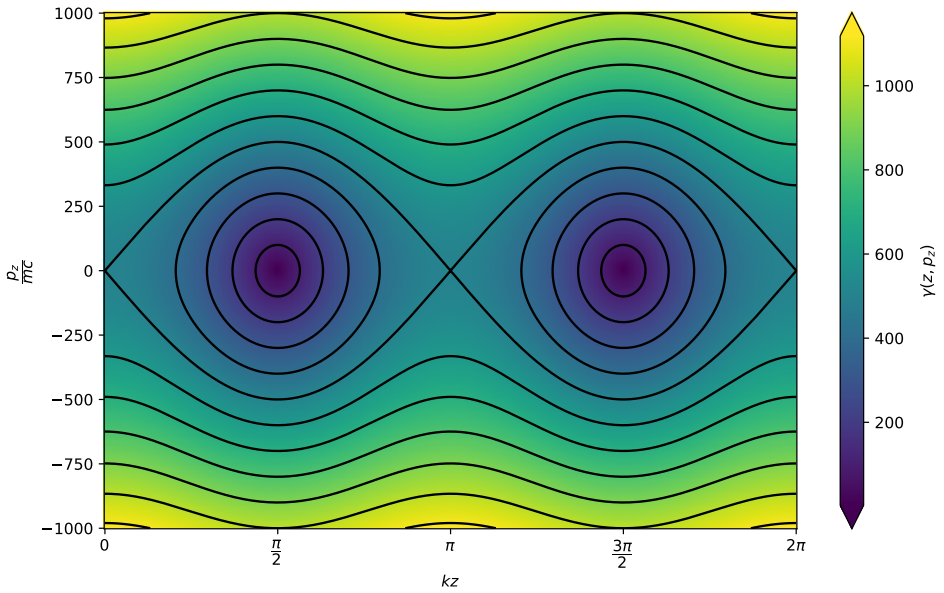

Figure 6.8: Map of the Lorentz factor gamma in the phase space $(kz, \frac{p_z}{mc})$ for $a_0 = 500.$ of electrons experiencing the fields of counter-streaming CP PW with opposite helicity. Radiation reaction is not taken into account here.

On the one hand for magnetic nodes $kz^* = 0; \pi$, one has $Tr(J) = 0$, $det(J) < 0$ which shows that these are unstable *saddle-points*. On the other hand for $kz^* = \pi/2; 3\pi/2$, $Tr(J) = 0$, $det(J) > 0$ which corresponds to *centers*. The phase space (z, p_z) is represented in fig. 6.8, where the colour map corresponds to the Lorentz factor. As expected, at the centers, i.e. the nodes of the electric field, particles have the lowest energy. On the other side, unstable saddle points on the magnetic nodes correspond to maxima of the particles energy.

In the following, we discuss what happens when radiation reaction is taken into account through the Landau-Lifshitz radiation friction force [Landau and Lifshitz, 1980] as shown in [Gong et al., 2016]. In the present case, only the terms proportional to γ^2 are considered in the radiation friction, since we consider relativistic particles. The force is then approximated by Eq. (2.31)

$$\boldsymbol{F}_{LL} = -\frac{2r_e e^2}{3mc^2}\gamma^2 \left[(\boldsymbol{E} + \boldsymbol{v} \times \boldsymbol{B})^2 - \left(\frac{\boldsymbol{v}.\boldsymbol{E}}{c} \right)^2 \right] \frac{\boldsymbol{v}}{c} . \tag{6.69}$$

In this case, following the same approach presented above, the Jacobian matrix with radiation reaction reads

$$J = mc^2 \begin{pmatrix} 0 & \frac{1}{m^2c^2\gamma} \\ \frac{a_0^2 k^2 \cos(2kz)}{\gamma} & -\frac{r_e e^2}{6m^3c^5} E_0^2 \gamma \end{pmatrix}_{|(z^*, p_z^*)} \tag{6.70}$$

With this new expression of the Jacobian taking into account radiation reaction, one can compute the trace and the determinant at the fixed points, i.e. the electric field nodes $kz^* = \frac{\pi}{2}\,;\,\frac{3\pi}{2}$ and $p_z^* = 0$. In those phase-space positions $\gamma = \sqrt{1+a_0^2}$ and $Tr(J) = -\frac{r_e e^2}{6m^2c^3}E_0^2\gamma = -\frac{r_e\omega^2}{6c}a_0^2\sqrt{1+a_0^2}$ which is negative and the determinant is takes positive values. This means that the fixed points at electric nodes are spiral sink attractors [Jordan and Smith, 2007, Hirsch et al., 2012]. So particles initially near them in the phase space start to spiral around them and lose momentum due too the radiation reaction. On the contrary, for the fixed points at the magnetic nodes $kz^* = 0\,;\pi$, the determinant is $\det(J) < 0$. So these fixed points are saddle points, which push away particles from them. In conclusion we have found that particles are pushed away from the magnetic nodes and spiral around the electric nodes.

Before concluding, note that it has been shown numerically by [Gonoskov et al., 2014], that at very high a_0 (above 10^4), particles can be trapped at the magnetic field nodes, through a process called *anomalous radiative trapping*. As we will not go to such high intensities in the following chapter, it will not be discussed here.

6.5 Conclusions

The main notions and the state of the art of the strong field community understanding of the avalanche regime have been presented in this Chapter. In the next one we will use and generalize these notions to present original results in this regime. The well known model for the purely rotating electric field configuration have been introduced in this chapter. The growth rate of the avalanche in the quasi steady state has been re-derived, and compared with PIC simulations for this idealised rotating field configuration. More specifically we verified that the growth depends on the field intensity, as predicted by analytical models. This motivates our choice to compare simulations at same peak laser intensity, contrarily to the comparison at fixed laser energy of Chap.5. The rotating field model has proved useful since a number of analytical results can be obtained, to infer the conditions leading to an avalanche. This field configuration can be locally produced at the magnetic nodes of the standing wave produced by two counter-streaming waves with opposite circular polarisation. A brief presentation of previous results obtained in this condition has been provided. Several numerical studies focused on the less idealized 3D configurations in which for instance ponderomotive effects can not be neglected and depend on the polarization.

In the last section of this chapter, an analysis of the so-called *attractors* has been presented. In specific configuration such as the standing wave presented here, these attractors make particles migrate to electric field nodes. In this analysis (classical) radiation reaction is taken into account, and we showed that this could have an important impact on the cascade development and its growth rate.

All the concepts introduced up to here are used to understand the particle dynamics and cascade development in the configuration investigated int the next chapter.

Chapter 7

QED cascades in the collision of two counter-propagating beams

Contents

As mentioned in the previous chapter, one of the promising configurations to produce a self-sustained cascade relies on the use of two counter-streaming beams. Indeed by producing a standing wave, choosing accurately the beam polarisation, one can locally create a rotating electric field, which is one of the simplest configurations to induce an avalanche. This physical setup is schematically represented in fig. 7.1. In this chapter using two LG beams,

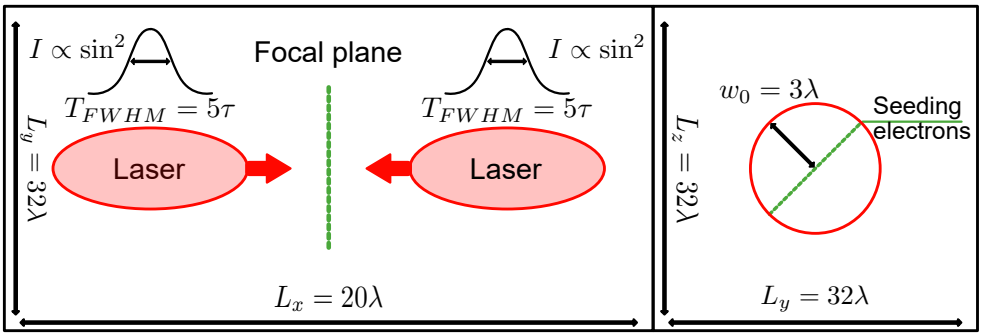

Figure 7.1: Physical setup and parameters of the 3D PIC simulations with two counter-streaming laser beams. The cascade is seeded with electrons initially at rest in the focal plane. The left panel shows the geometry in the x (longitudinal) direction and along y (transverse direction), whereas the right panel shows the schematically the properties of the set-up in the focal plane.

we first describe the variety of field configurations that can be obtained at a magnetic node. We then explore how the field configuration affects the onset of the avalanche and its growth rate. In order to do so, first we present 3D PIC simulations comparing the different configurations at the same total peak intensity. We then discuss the growth rates and the created pairs properties, such as their distribution in space, their quantum parameter and energy. Finally we present how the short time dynamics model presented in Sec. 6.3 can be used to obtain insights for the interpretation of the simulations results, since it allows to estimate the evolution of the quantum parameter and of the Lorentz factor of charges with time in an intense field. First we use the model to verify that the efficiency of different field configurations is consistent with the particles short time dynamics. Then, we exploit this model to derive an expression for the growth rate of the cascade for the pure rotating field configurations. This is in very good agreement with the numerical results and hence opens encouraging perspectives for future predictions of the growth rate in the two counter-streaming beams in more general configurations.

7.1 Physical setup and field structure of two counter-streaming beams

7.1.1 Field of two counter-steaming LG beams

In chapter 1 we have presented the properties of LG beams. In this section we detail the field structures that can be produced by two counter-streaming LG beams, creating a standing wave. The diversity of structures that can be obtained is wider than the one with a single beam. We focus in this chapter

on cases with $p = 0$.

Let us first look at the field of a standing wave produced by the superposition of two plane waves, in order to present the conventions that will be used

$$\boldsymbol{E}_1 = \frac{E_0}{\sqrt{1+\sigma_1^2}} [\sin(\omega t - kz)\hat{\boldsymbol{x}} + \sigma_1 \cos(\omega t - kz)\hat{\boldsymbol{y}}] \tag{7.1}$$

$$\boldsymbol{E}_2 = \frac{E_0}{\sqrt{1+\sigma_2^2}} [-\sin(\omega t + kz + \Delta\phi)\hat{\boldsymbol{x}} + \sigma_2 \cos(\omega t + kz + \Delta\phi)\hat{\boldsymbol{y}}] \tag{7.2}$$

$$\boldsymbol{B}_1 = \frac{E_0}{\sqrt{1+\sigma_1^2}\, c} [-\sigma_1 \cos(\omega t - kz)\hat{\boldsymbol{x}} + \sin(\omega t - kz)\hat{\boldsymbol{y}}] \tag{7.3}$$

$$\boldsymbol{B}_2 = \frac{E_0}{\sqrt{1+\sigma_2^2}\, c} [\sigma_2 \cos(\omega t + kz + \Delta\phi)\hat{\boldsymbol{x}} + \sin(\omega t + kz + \Delta\phi)\hat{\boldsymbol{y}}] \ , \tag{7.4}$$

where $\sigma_{1,2}$ are the beam polarisations and $\Delta\phi$ is the dephasing between the two waves. We define the polarization with respect to the corresponding laser propagation direction. In practise, this means that for $\sigma_1 = +1$ the field is left-handed around the z axis, and for $\sigma_2 = +1$ the field is left-handed around the $-z$ axis, so it is right-handed around the positive z direction. If one considers opposite circular polarisations, $\sigma = (\sigma_1; \sigma_2) = (\pm 1; \mp 1)$, then the field can be rewritten as

$$\begin{aligned} \boldsymbol{E} &= \frac{2E_0}{\sqrt{2}} \left[-\sin\left(kz + \frac{\Delta\phi}{2}\right) \cos\left(\omega t + \frac{\Delta\phi}{2}\right) \hat{\boldsymbol{x}} \right. \\ &+ \left. \sigma_1 \sin\left(kz + \frac{\Delta\phi}{2}\right) \sin\left(\omega t + \frac{\Delta\phi}{2}\right) \hat{\boldsymbol{y}} \right] , \end{aligned} \tag{7.5}$$

$$\begin{aligned} \boldsymbol{B} &= 2\frac{E_0}{\sqrt{2}\, c} \left[-\sigma_1 \cos\left(kz + \frac{\Delta\phi}{2}\right) \cos\left(\omega t + \frac{\Delta\phi}{2}\right) \hat{\boldsymbol{x}} \right. \\ &+ \left. \cos\left(kz + \frac{\Delta\phi}{2}\right) \sin\left(\omega t + \frac{\Delta\phi}{2}\right) \hat{\boldsymbol{y}} \right] . \end{aligned} \tag{7.6}$$

With this convention, $\Delta\phi = \pi$ creates at $z = 0$ a magnetic node, with a rotating transverse electric field. We hence choose this value of the phase $\Delta\phi = \pi$ in the following discussion, to have a rotating electric field at the magnetic nodes. The same conventions are used for the standing wave produced by the interaction of two LG beams. The main difference with respect to the PW case of Eqs.(7.5) and (7.6) corresponds to the field structure in the transverse plane

$$\begin{aligned}
\boldsymbol{E}_1 &= \frac{E_0}{\sqrt{1+\sigma_1^2}} U_{0\ell_1}(\rho,z)\,[\sin(\Phi_{0\ell_1}(z)+\omega t-kz)\hat{\boldsymbol{x}} \\
&+ \sigma_1\cos(\Phi_{0\ell_1}(z)+\omega t-kz)\hat{\boldsymbol{y}}]\ , \qquad (7.7)\\
\boldsymbol{E}_2 &= \frac{E_0}{\sqrt{1+\sigma_2^2}} U_{0\ell_2}(\rho,z)\,[-\sin(-\Phi_{0\ell_2}(z)+\omega t+kz+\pi)\hat{\boldsymbol{x}} \\
&+ \sigma_2\cos(-\Phi_{0\ell_2}(z)+\omega t+kz+\pi)\hat{\boldsymbol{y}}]\ , \qquad (7.8)\\
\boldsymbol{B}_1 &= \frac{E_0}{\sqrt{1+\sigma_1^2}\,c} U_{0\ell_1}(\rho,z)\,[-\sigma_1\cos(\Phi_{0\ell_1}(z)+\omega t-kz)\hat{\boldsymbol{x}} \\
&+ \sin(\Phi_{0\ell_1}(z)+\omega t-kz)\hat{\boldsymbol{y}}]\ , \qquad (7.9)\\
\boldsymbol{B}_2 &= \frac{E_0}{\sqrt{1+\sigma_2^2}\,c} U_{0\ell_2}(\rho,z)\,[\sigma_2\cos(-\Phi_{0\ell_2}(z)+\omega t+kz+\pi)\hat{\boldsymbol{x}} \\
&+ \sin(-\Phi_{0\ell_2}(z)+\omega t+kz+\pi)\hat{\boldsymbol{y}}]\ , \qquad (7.10)
\end{aligned}$$

where $\ell_{1,2}$ are the LG beam orders.

Using the above mentionned convention, with $\sigma = (1;-1)$ and $\ell = (0;0)$ we describe two colliding gaussian beams, which produce a rotating transverse electric field at the magnetic nodes. The only difference with the plane wave case is the amplitude distribution in the transverse plane. Note that for the LG beam order ℓ we choose a convention analogous to the one for sigma, i.e. ℓ is positive along the the axis of propagation of the beam. This means that $\ell_1 = 1$ gives positive orbital angular momentum along z and $\ell_2 = 1$ gives positive angular momentum along $-z$, so negative momentum along z.

The configurations discussed in the following are sorted into two groups. First what we call the *rotating cases*, for which $\sigma = (\pm 1; \mp 1)$, i.e. the beams have opposite circular polarisations. In this kind of configurations, at every given point in the focal plane, the transverse electric field is rotating with time. We refer to this as locally rotating field. The other group s referred to as *oscillating cases*. In these configurations $\sigma_1 = \sigma_2$ and, at every point of the focal plane, the transverse electric field oscillates, similar to what would happen in a linearly polarised wave.

Rotating cases

Here we discuss the rotating cases with $\sigma = (\pm 1; \mp 1)$. We actually present only the case with $\sigma = (1;-1)$ since the only difference with $\sigma = (-1;1)$ is the direction of the field rotation, and the sign of the spin component of the field angular momentum. Neither of these changes impact the physical results discussed in the following.

We first consider the cases with $\sigma = (1;-1)$ and $\ell = (\pm 1; \mp 1)$. Let us

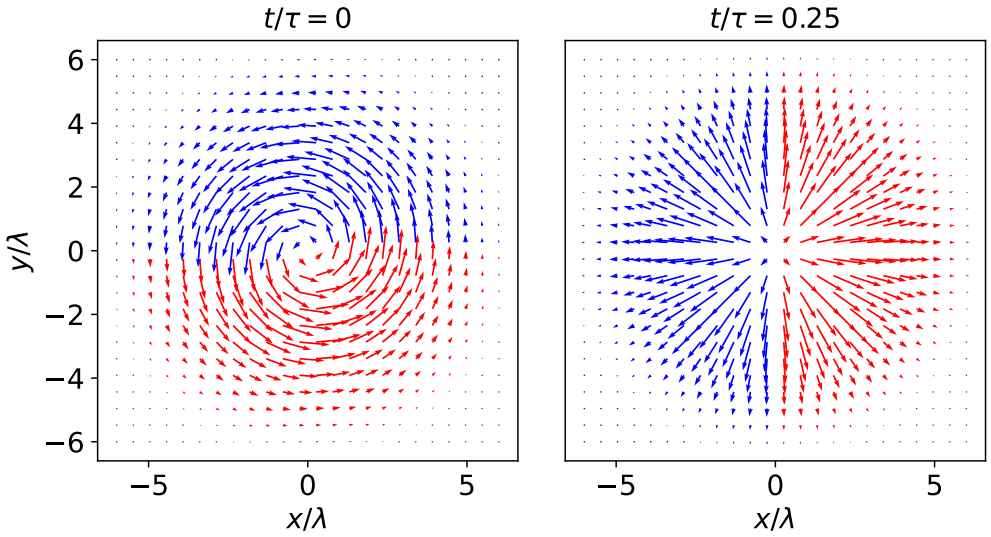

Figure 7.2: Transverse electric field at focus of two counter-streaming LG beams, with $\sigma = (1; -1)$ and $\ell = (1; -1)$. The two panels show the field at different times. The waist of the beams is $w_0 = 3\lambda$. The arrows are proportional to the electric field magnitude and are red when $E_x > 0$ and blue when $E_x \leq 0$. This configuration is called LG_{+1}(Rot) in table 7.1.

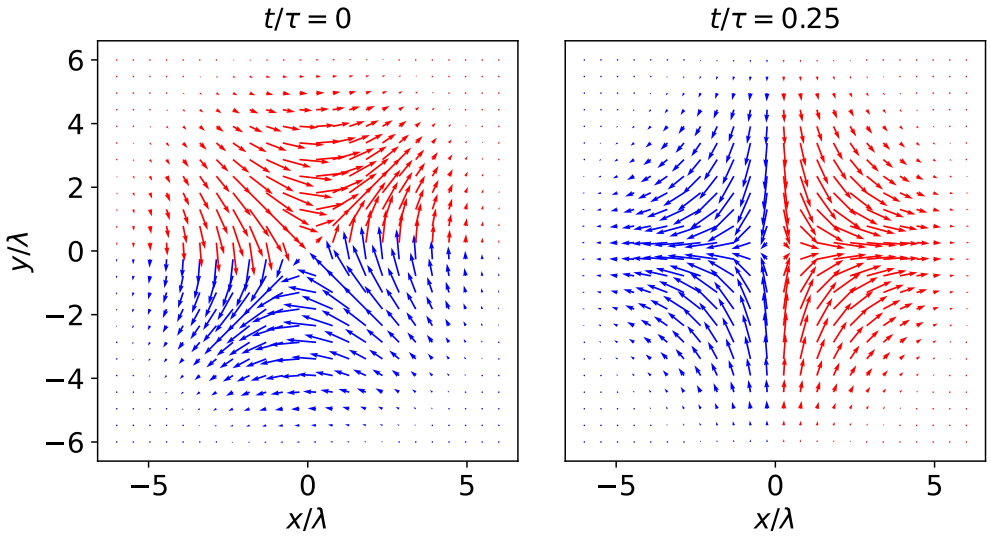

Figure 7.3: Transverse electric field at focus of two counter-streaming LG beams, with $\sigma = (1; -1)$ and $\ell = (-1; 1)$. The two panels show the field at different times. The waist of the beams is $w_0 = 3\lambda$. The arrows are proportional to the electric field magnitude and are red when $E_x > 0$ and blue when $E_x \leq 0$.This configuration is called LG_{-1}(Rot) in table 7.1.

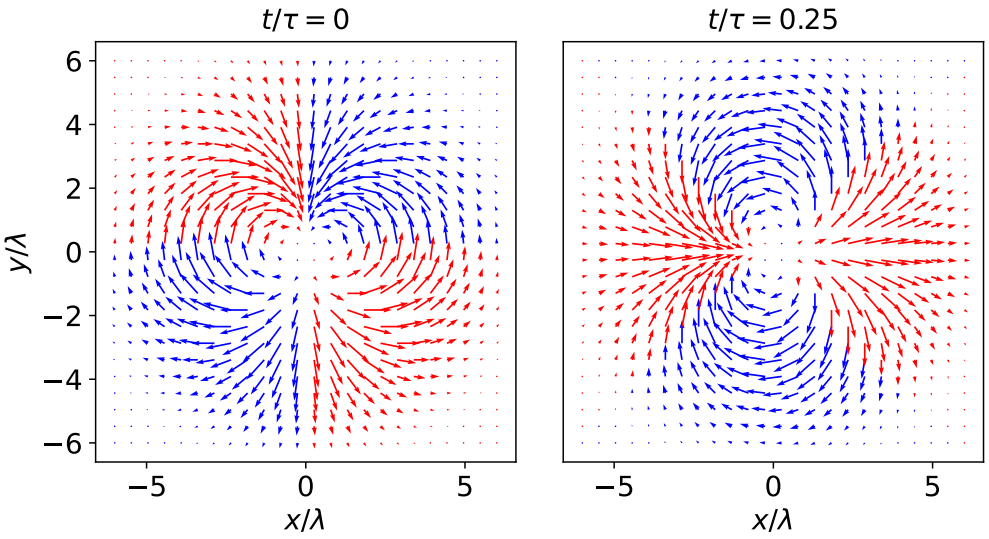

Figure 7.4: Transverse electric field at focus of two counter-streaming LG beams, with $\sigma = (1; -1)$ and $\ell = (2; -2)$. The two panels show the field at different times. The waist of the beams is $w_0 = 3\lambda$. The arrows are proportional to the electric field magnitude and are red when $E_x > 0$ and blue when $E_x \leq 0$.

look at the transverse electric field at focus for $\ell = (1; -1)$. In fig. 7.2 the field is displayed at two different times. A vortex-like structure, similar to the one beam case with $\sigma = 1\,;\, \ell = 1$ shown infig. 1.6 is present. Differently from the single beam configuration, there is no transverse magnetic field in fig. 7.2. As discussed in Chap. 1 regarding the single beam configuration, the LG beam phase structure leads to a rotation with time identified by the border between the red and blue arrows in fig. 7.2. This means that the beam carries a finite orbital angular momentum. This is consistent with the fact that the first beam has orbital momentum proportional to $\ell_1 = +1$ along the z axis and the second has $\ell_2 = -1$ along $-z$, which means a $+1$ contribution to the angular momentum along the z axis. So both beams have a positive orbital angular momentum along z.

The second case we would like to discuss is the one having $(\ell_1; \ell_2) = (-1; 1)$, where the sign of the LG beams orders have been swapped compared to the previous case. The field at focus in this case, shown in fig. 7.3, looks similar to the case of a single beam with $\sigma = 1\,;\, \ell = -1$ shown in fig. 1.7. The field has a saddle point structure which is rotating with time with the electric field coming parallel to the x and y axis. Here as well the phase structure rotates, but in the opposite direction with respect to the case shown in fig. 7.2, which indicates that the orbital angular momentum has the opposite sign.

If one wants to look at a more general situation, the absolute values of the LG beam orders can be increased. This is what is shown in figs. 7.4 and 7.5 for LG beams order $(2; -2)$ and $(-2; 2)$. The vortex case (fig. 7.4) is composed

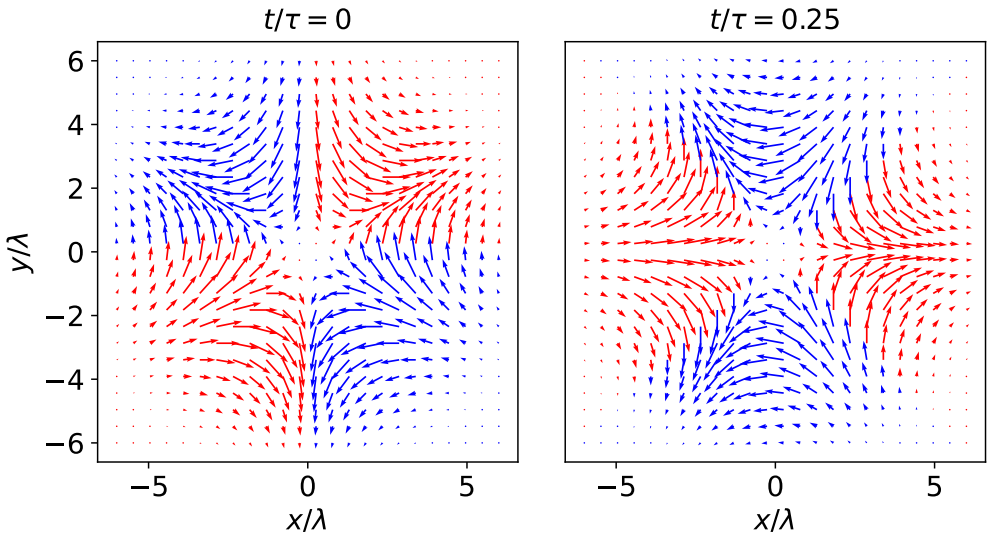

Figure 7.5: Transverse electric field at focus of two counter-streaming LG beams, with $\sigma = (1; -1)$ and $\ell = (-2; 2)$. The two panels show the field at different times. The waist of the beams is $w_0 = 3\lambda$. The arrows are proportional to the electric field magnitude and are red when $E_x > 0$ and blue when $E_x \leq 0$.

of two adjacent vortices. The saddle point case (fig. 7.5)has one more axis to which the field lines get parallel with respect to the case shown in fig. 7.3.

The previous cases considered LG beams having opposite ℓ orders. In the same way that opposite circular polarisations are needed to have locally rotating field, we can show that $\ell_1 - \ell_2 \neq 0$ is required to have a rotating phase structures. In the case of beam with the same absolute value of ℓ, this condition corresponds to having opposite sign for ℓ. Indeed, if we consider a configuration with the same ℓ for the two beams, for instance for $\ell = (1; 1)$, we obtain the field structure displayed in fig. 7.6. One can see that this has two lobes as a linearly polarised LG beam, and that they are not moving. However the electric field locally rotates as expected, given the choice of $\sigma = (1; -1)$. In general the configurations with $\sigma = (\pm 1; \mp 1)$ and $\ell = (\ell_1; \ell_1)$ have the number of lobes of a LP LG beam of order ℓ_1, but with the phase structure which does not rotate with time.

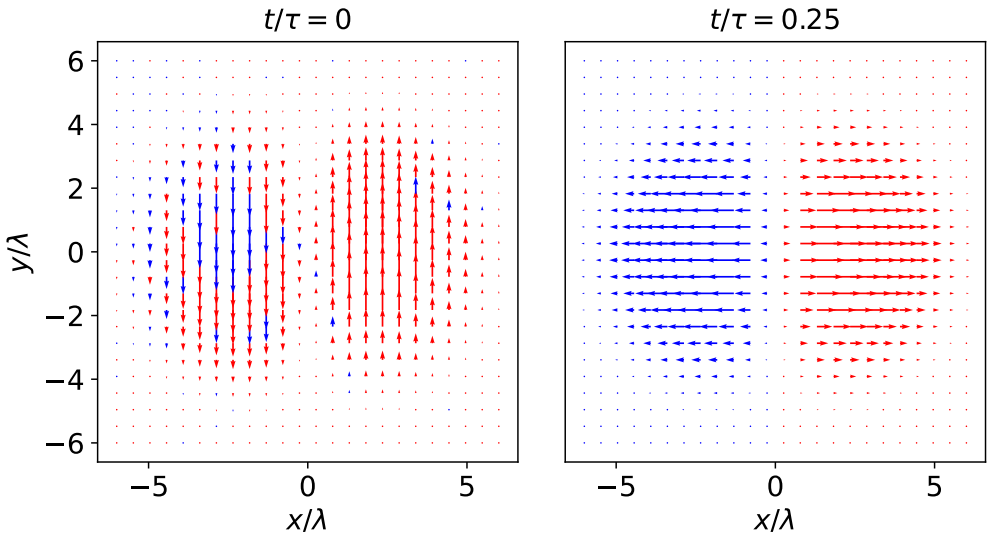

Figure 7.6: Transverse electric field at focus of two counter-streaming LG beams, with $\sigma = (1; -1)$ and $\ell = (1; 1)$. The two panels show the field at different times. The waist of the beams is $w_0 = 3\lambda$. The arrows are proportional to the electric field magnitude and are red when $E_x > 0$ and blue when $E_x \leq 0$.

Oscillating configurations

The oscillating configurations are obtained from the superposition of two counter-streaming beams, both with circular polarisation and same helicity.. Here we choose $\sigma = (1; 1)$ for simplicity and without loss of generality. It should be noted that for the oscillating configurations, there is a transverse magnetic field even in the focal plane. Since the electric field oscillates with time, the magnetic field reaches its maximum when the electric field vanishes and it has the same spatial structure as the electric one. Let us first start with cases with opposite ℓ. The configuration with $\ell = (1; -1)$, represented in fig. 7.7, has the same structure as the LP LG beams with $\ell = 1$ shown in fig. 1.1, composed of two rotating lobes and with the field locally oscillating. Moreover all the cases with $\sigma_{\pm 1;\pm 1}$ and $\ell = (\ell_1; -\ell_1)$ have the structure of the LP LG of order $\ell = \ell_1$.

More interesting configurations can be obtained with LG beams having the same order. In figs. 7.8 and 7.9 are represented the cases with $\ell = (1; 1)$ and $\ell = (-1; -1)$, respectively. The first one has a radially oscillating electric field, the second one has a saddle point phase structure. Both these structures differ from the corresponding rotating cases (figs. 7.2 and 7.3) as the field locally oscillates.

More general configurations than the ones presented here can be produced, for example by colliding LG beams of different order, using a gaussian and an LG beams, or LG beams with $p \neq 0$. However due to their complexity, these configurations have not been explored in this work, in particular with

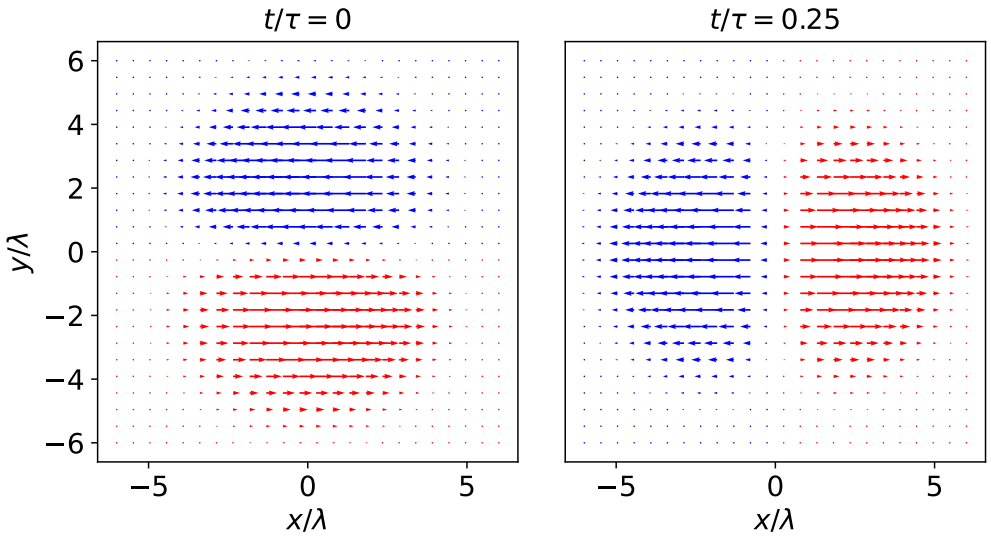

Figure 7.7: Transverse electric field at focus of two counter-streaming LG beams, with $\sigma = (1; 1)$ and $\ell = (1; -1)$. The two panels show the field at different times. The waist of the beams is $w_0 = 3\lambda$. The arrows are proportional to the electric field magnitude and are red when $E_x > 0$ and blue when $E_x \leq 0$.

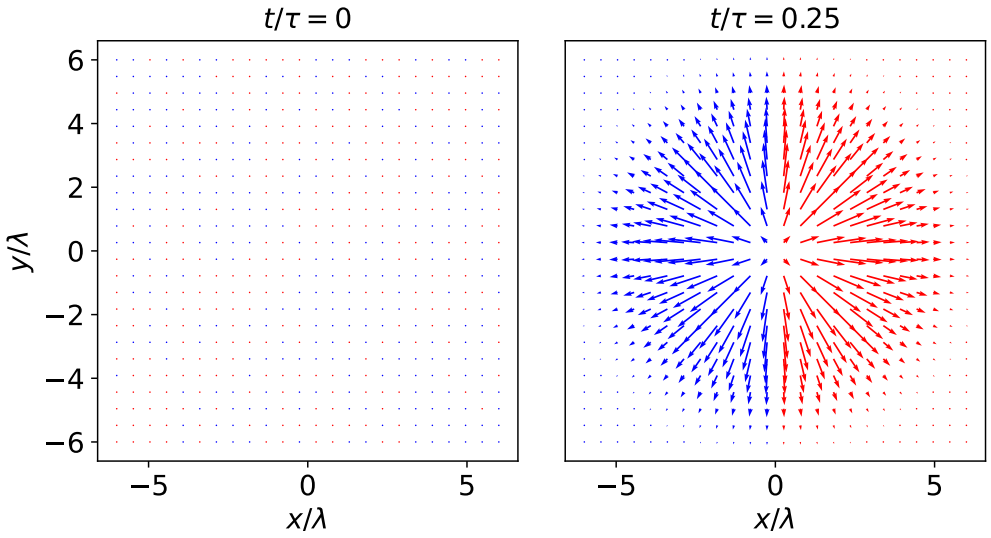

Figure 7.8: Transverse electric field at focus of two counter-streaming LG beams, with $\sigma = (1; 1)$ and $\ell = (1; 1)$. The two panels show the field at different times. The waist of the beams is $w_0 = 3\lambda$. The arrows are proportional to the electric field magnitude and are red when $E_x > 0$ and blue when $E_x \leq 0$. This configuration is called LG_{+1}(Osc) in table 7.1.

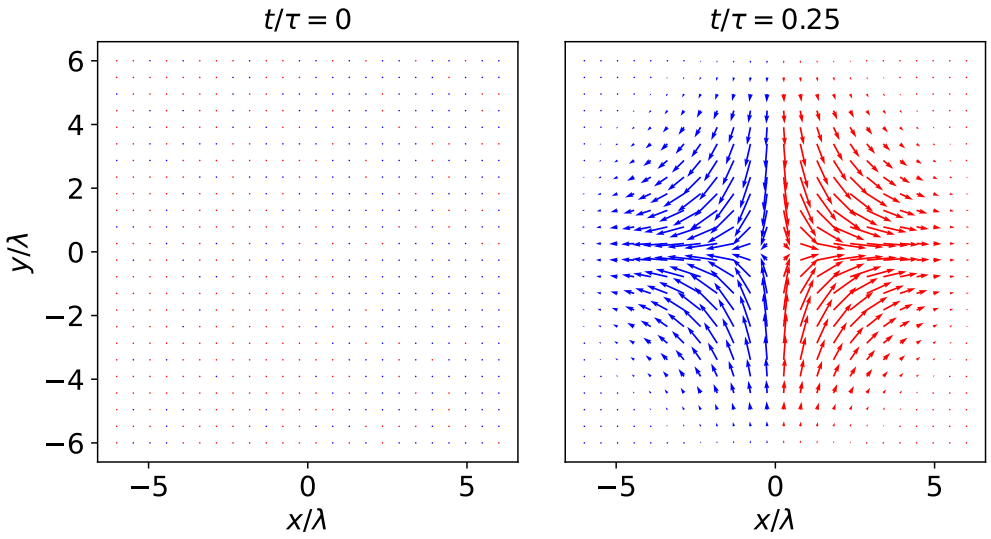

Figure 7.9: Transverse electric field at focus of two counter-streaming LG beams, with $\sigma = (1; 1)$ and $\ell = (-1; -1)$. The two panels show the field at different times. The waist of the beams is $w_0 = 3\lambda$. The arrows are proportional to the electric field magnitude and are red when $E_x > 0$ and blue when $E_x \leq 0$. This configuration is called LG_{-1}(Osc) in table 7.1.

the perspectives of future experiments in which the generation of such beams is still challenging at the high intensity required to produce electron-positron pairs.

Summary of the possible configurations

Summarizing the discussion about the different field configurations discussed in this section, we can classify the different configurations into categories that provide general guidance for the application of these configurations to pair production studies. This is the purpose of table 7.1, in which the first quantity is $\Sigma = \sigma_1 - \sigma_2$. One should remember that our convention is that σ_2 gives the polarisation along the axis of propagation of the second wave, i.e. $-z$. This is why Σ is defined as the difference and not the sum of the two components. As we have shown in figs. 7.7 to 7.9, if $\Sigma = 0$ the effects of each polarisation cancels with the other, and the field locally oscillates, meaning that at a fixed point in space the field arrow oscillates back and forth along a given direction. These are called the *oscillating* configurations in the *Field type* column of table 7.1. On the contrary, if $\Sigma \neq 0$ the field locally rotates, in a left handed way around z if $\Sigma > 0$ and the other way around if $\Sigma < 0$. Those cases belong to the *rotating* field type.

Analogously, another quantity of interest is the difference of the LG beams order $\Lambda = \ell_1 - \ell_2$. As we have seen, the quantities ℓ_1 and ℓ_2 are related to the orbital angular momentum of the respective beams. If $\ell_1 > 0$ the phase

structure of the first beam rotate in a right handed way around the z and the opposite for ℓ_2. The quantity Λ tells us if the phase structure is stationary (for $\Lambda = 0$), or rotating ($\Lambda \neq 0$), where the sign gives the rotation direction.

Note that not all the possible combinations are reported in table 7.1, as some are equivalent to already shown configurations. This is the case for configurations in which both polarisations change sign. For example the $(\sigma_1; \sigma_2) = (1; 1)$ case with two gaussians is equivalent to the $(-1; -1)$ case, put aside the sign of Σ and so the orientation of the local rotation of the field with time.

We named six different field configurations,(see the last column in table 7.1) distinguished by the rotating or oscillating nature of the beam, the beam type and in case the value of the first LG beam order. These six configurations will be the one explored with 3D PIC simulations and discussed in the following sections. One should notice that we will not discuss the configuration consisting of two gaussian beams with the same circular polarisations, because its field structure is similar to the two LP gaussian beams, which belong to the six different configurations we are going to study. Furthermore we will study two configurations of LG beams with the same circular polarisations, but none of the the two LG LP configurations. This is because the latter have field structures similar to a signle LP LG beam and are therefore of less interest. Finally, in the explored regime, the order of LG beams $l = \pm 1$ and $p = 0$ already allows to identify the effect of using configurations different from the standard Gaussian. We hence focus on these cases, as we do not expect a qualitative change on the results for higher LG beam orders.

Beam type	$(\sigma_1;\sigma_2)$	$(\ell_1;\ell_2)$	$\Sigma=\sigma_1-\sigma_2$	$\Lambda=\ell_1-\ell_2$	Field type	Structure type	Name
Gaussian (G)	$(0;0)$	$(0;0)$	0	0	Oscillating	Stationary	G(Osc)
	$(1;1)$		0		Oscillating	Stationary	
	$(1;-1)$		$+2$		Rotating	Stationary	G(Rot)
Laguerre-Gauss (LG)	$(0;0)$	$(1;-1)$	0	$+2$	Oscillating	Rotating	
		$(1;1)$		0		Stationary	
	$(1;1)$	$(1;-1)$		$+2$		Rotating	
		$(1;1)$		0		Stationary	LG_{+1}(Osc)
		$(-1;1)$		0		Stationary	LG_{-1}(Osc)
	$(1;-1)$	$(1;1)$	$+2$	0	Rotating	Stationary	
		$(1;-1)$		$+2$		Rotating	LG_{+1}(Rot)
		$(-1;1)$		-2		Rotating	LG_{-1}(Rot)

Table 7.1: Summary of the main characteristics of the considered achievable field configurations considering either two LG beams or two gaussian ones.

7.1.2 Physical simulations setup

Here we detail the simulations set-up. Which is schematically reproduced in fig. 7.1: two counter-streaming laser pulses collide and create a standing wave. Near the magnetic nodes, an electric type field is generated. As discussed in section 6.3 this corresponds to a region that can re-accelerate particles and hence regrow both their energy and their quantum parameter. This can happen in the interval of time between two emissions of hard gamma photons, leading to a self-sustained cascade.

Since the theoretical growth rate calculated in chapter 6, for the pure rotating electric field case, depends on the local field amplitude, we performed a study of the cascade by comparing different field configurations at the same maximum amplitude of the laser field. Please note that this contrasts with with the convention used in previous chapters, especially 4 5, where we considered pulses with the same energy. The choice for this chapter is made to isolate the influence of geometry of the field configuration from its amplitude.

In the simulations two counter-streaming gaussian or LG pulses collide in the presence of seeding electrons at their focus. Each pulse has a waist of 3λ (with λ the laser wavelength) and a $\sin^2$ temporal envelope in intensity with a full width at half maximum of 5τ (with τ the laser period). The total duration of a single pulse which also corresponds to the overlapping time between the two beams, is ten periods. The spatial resolution is $\lambda/24$ in the three directions and the temporal resolution is $\tau/1000$, that guarantees convergence of the numerical results. Since the LG beams have zero intensity on the laser axis, the seeding electrons are distributed along a diameter crossing the focal spot as represented on the right panel of fig. 7.1.

The maximum amplitude of a single beam is called here a_0, so that the peak of the field when the pulses cross is $a_{0,tot} = 2a_0$, that is our reference parameter. In an analogous way, the total electric field maximum amplitude, produced by the two beams is referred to in the following as $E_{0,\mathrm{tot}}$, while the maximum amplitude of the single beam is $E_{1\mathrm{B}}$. It can be useful to remind that if we were working at constant energy the amplitude of the maximum $\ell = 1$ LG circularly polarised beam a_0 would be reduced with respect to the maximum of the corresponding gaussian linear pulse a by the following factor $a_0 = e^{-1/2}a/\sqrt{2} \sim 0.4a$.

7.2 Cascade growth rate and spatial distribution of the resulting pairs

In this section we first discuss the growth rates obtained for different configurations and then look at the spatial distribution of the produced pairs.

7.2.1 Number of produced pairs and growth rates

In the case of two counter-streaming beams, as shown in section 7.1.1, we can sort our results depending on the value and local behaviour (rotating or oscillating) of the transverse electric field at focus. A first set of cases includes all the configurations in which the standing wave results in an electric field at the magnetic node that is very similar to the purely rotating electric field. Intuitively we expect this configuration to be more efficient. Indeed, in an analogous way to what has been shown for the quantum parameter of the gamma photon in chapter 4, a wider angle between the charges momenta and the electromagnetic field leads to a greater quantum parameter. The other set of configurations corresponds to a field that locally behaves like a linearly polarised wave. As most of the time the charges in this configuration have momentum parallel to the electric field, intuitively we expect this configuration to be less efficient. As mentioned in chapter 6, and pointed out by [Jirka et al., 2016], this intuition could be wrong, since the trajectory of the particles is not necessarily limited to the 2D plane at the magnetic nodes, because of three dimensional effects due to the presence of attractors (see Sec.6.4). Indeed, even if the seeding happens initially at a magnetic field node, where a rotating electric field can exist, the particles only stay for a finite time close to the magnetic node due to the effect of these attractors, and after roughly one period migrate towards electric nodes. This will impose an additional constraint on the efficiency of the avalanche generation. However, as we show in the following, we find for the values of the field intensity considered in our simulations that the cases close to a rotating field configuration are consistently more efficient. Another limiting factor could be due to the ponderomotive effects. However for the pulse duration and ultra-high fields considered in the simulations, the particle dynamics is governed at the lowest order by the local values of the field while ponderomotive effects seems to appear only towards the end of the simulation as it will be shown by the density distributions of the particles.

Let us now move to the results of the simulations. In a first set of reference simulations we consider $a_0 \simeq 643$ for one beam, that is $a_{0,tot} \simeq 1286$ when the

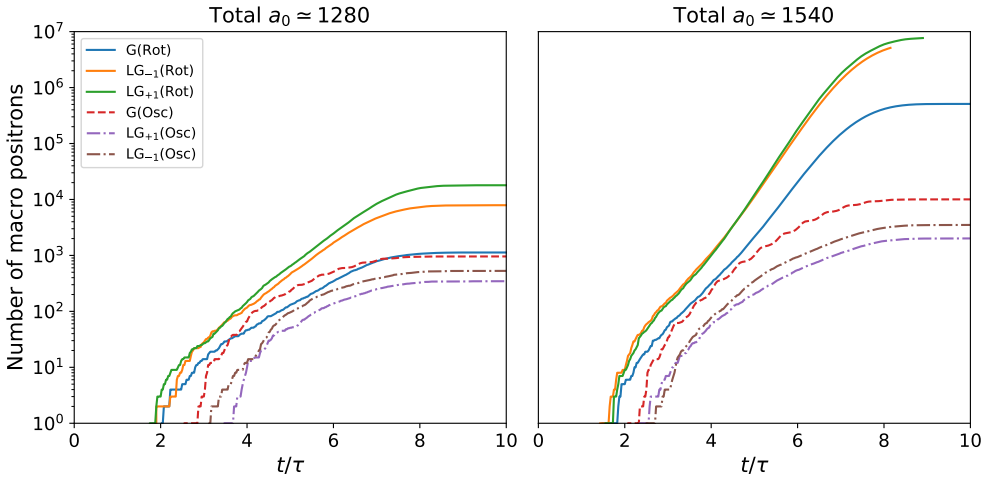

Figure 7.10: Number of positrons as a function of time in the simulations for the different field configurations with two LG beams, for two different total intensities at focus $a_{0,tot} \simeq 1280$ (left) and $a_{0,tot} \simeq 1540$ (right).

Case name	Growth rate ($a_{0,tot} = 1280$)	Growth rate ($a_{0,tot} = 1540$)
LG$_{-1}$(Rot)	$1.26\tau^{-1}$	$2.57\tau^{-1}$
LG$_{+1}$(Rot)	$1.34\tau^{-1}$	$2.73\tau^{-1}$
G(Rot)	$0.92\tau^{-1}$	$2.18\tau^{-1}$
G(Osc)	x	$1.19\tau^{-1}$
LG$_{-1}$(Osc)	x	$1.13\tau^{-1}$
LG$_{+1}$(Osc)	x	$1.06\tau^{-1}$

Table 7.2: Table of the growth rates extracted from the curves of the number of particles from figure 7.10. Due to the curve not being stable because the quasi steady state is not reached for the (Osc) cases with $a_{0,tot} = 1280$, no value is provided. For $a_{0,tot} = 1540$, the curves of the (Osc) cases being much more stable a value can be provided. It is given by the average slope of the number of the curve of the number of particles from $t/\tau = 5$ and $t/\tau = 5.5$, giving an average growth rate for the G(Osc) case.

two beams superimpose. This value is chosen based on existing literature [Jirka et al., 2016, Grismayer et al., 2016] where it was shown that one should expect a clear avalanche to develop, allowing to clearly identify the growth rate in the simulations.

The number of macro-positrons as a function of time for all the named configurations of table 7.1 with $a_{0,tot} = 1280$ is represented on the left panel of figure 7.10. The time $t = 0$ corresponds to the time at which the laser pulses start to overlap, and $t/\tau = 5$ corresponds to the time when the two pulses perfectly overlap. It is worth noticing that in figure 7.10 the relevant quantity is not the total number of particles that depends on the seeding and is affected by the spot size, but the growth rate, which can be deduced from the slope of the curves representing the number of pairs in logarithmic scale.

When an avalanche is triggered, the number of particles grows exponentially with time, resulting in straight line in figure 7.10. The saturation of this line corresponds to the finite laser time duration. As clearly visible in the figure, for this value of $a_{0,tot}$, the only cases which reach an avalanche are the locally rotating field cases, i.e. the two gaussians with opposite circular polarisation, and the two rotating LG cases with opposite circular polarisation and LG order. The respective values of the growth rate, reported in table 7.2 are $\Gamma\tau \simeq 0.9$ for the rotating gaussian and $\Gamma\tau \simeq 1.3$ for the LG $_{\pm 1}$(Rot) configuration: the latter performs better at the same maximum amplitude. Next, one has the two linearly polarised gaussians and the more exotic LG beams with locally oscillating field. We also notice that if we compare the Linear G case with respect to the Rotating G case the number of pairs created in the linearly polarised cases is larger in some intermediate time interval. However as we can see from the slope a quasi-steady state with exponential growth is not reached. This is why a value for the growth rate is not provided. The LG$_{\pm 1}$(Osc) cases result systematically in worst performances than the rotating ones.

In the second set of reference simulations we consider $a_0 \simeq 772$ for each beam, that is $a_{0,tot} \simeq 1544$ when the two beams superimpose. The resulting number of pairs is displayed on the right panel of fig. 7.10, and shows that the relative efficiency of the different configurations in term of pair production and growth rate is analogous to what found in the previous discussion of the cases with $a_{0,tot} = 1280$. The growth rates, reported in table 7.2 are larger than the values shown in the second column, $\Gamma\tau \simeq 2.2$ for the G(Rot) case and $\Gamma\tau \simeq 2.6$ and 2.7 for the LG$_{\pm 1}$(Rot), and result in a higher number of pairs. Contrary to the previous cases, the (Osc) cases have a more stable behaviour, which allows us to extract a value for the corresponding growth rate. We obtain it by taking the average slope between the maximum at $t/\tau = 5$ and the time t/τ. For the G(Osc) where the curve consists in steps, this provides an average growth rate. One can see that all of these oscillatory cases have comparable growth rates with $\Gamma\tau$ between 1 and 1.2.

7.2.2 Spatial density distributions of the pairs

As discussed earlier, the possibility of producing an avalanche can be affected by ponderomotive effects. In this respect LG beams have a very different behaviour form standard gaussians, since their intensity distribution results in a ponderomotive push of the particles both outside the pulse and toward its propagation axis where the intensity is zero. This feature can be interesting to trap the produced pairs, but it seems to play a role on time scales larger

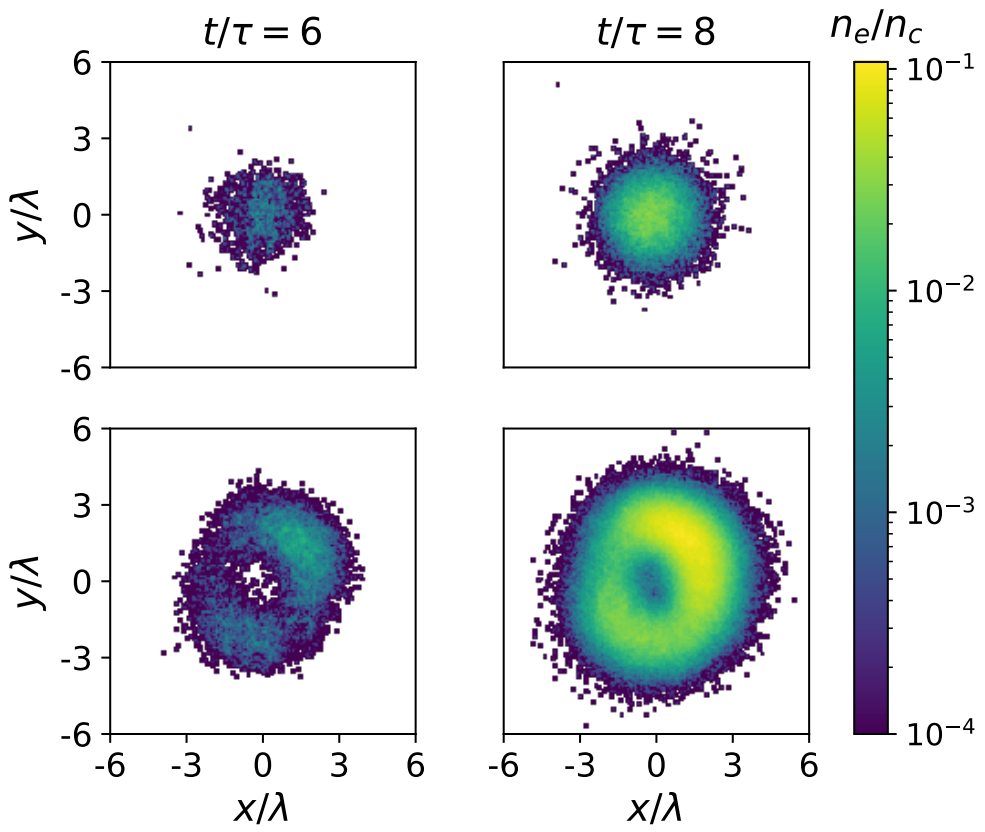

Figure 7.11: Density of the positrons at two different times in the focal plane, for the G(Rot) and LG_{-1}(Rot) cases, with $a_{0,tot} = 1540$.

than those considered here, as it will be shown by looking at the density distribution. In the following we thus present some preliminary results on the particle dynamics, even though a clear identification of the conditions for pair trapping deserves further studies. We here use the results of the $a_{0,tot} = 1540$ cases, since their higher number of pairs makes the visualisation of the density distribution easier.

The positron density in the focal plane is displayed for two different times, for the G(Rot) case on top of fig. 7.11, and for the LG_{-1}(Rot) case at the bottom of the same figure. Let us first consider the Gaussian case. The overlapping time where the fields reaches its peak value is $t = 5\tau$. On the top row of figure fig. 7.11, we reproduce the density of the pairs in the focal plane one period after the peak time, $t = 6\tau$, and at time $t = 8\tau$ just before the number of created pairs stops increasing exponentially. As we can see even for the later times only a few particles are outside the focal spot (3λ around the center here). As anticipated the ponderomotive push is weak, and only for pulses of longer duration or smaller transverse extension [Jirka et al., 2017] the growth rate of the cascade would be affected by particles that are leaving the focal spot in the transverse direction. At the same time, longer pulse duration

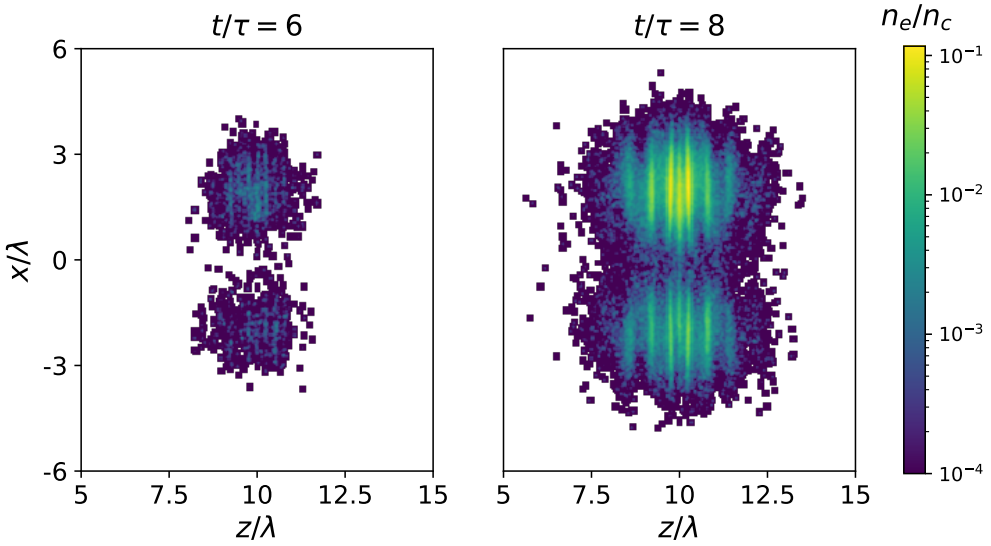

Figure 7.12: Density of the positrons at two different times in the longitudinal and transverse directions, for the LG_{-1}(Rot) case with $a_{0,tot} = 1540$.

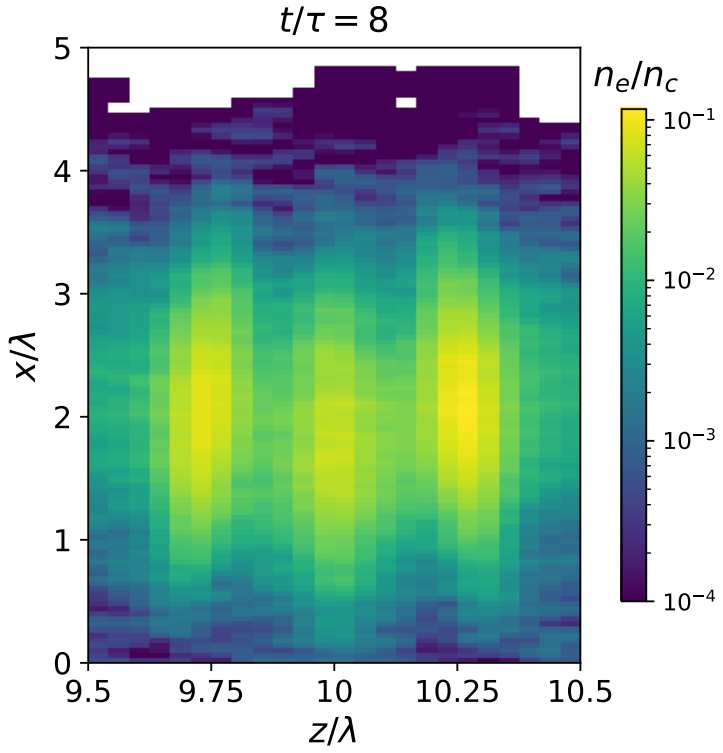

Figure 7.13: Zoom on the density of the positrons at $t/\tau = 8$ in the longitudinal and transverse directions, for the LG_{-1}(Rot) case $a_{0,tot} = 1540$.

likely results in more particles, due to a longer phase of exponential growth exponential growth, and so the collective back reaction of the pairs on the laser field can become important.

We next consider the rotating LG_{-1}(Rot) cases, in which a ring like distribution appears, where the density is also increasing with time up to the saturation of the pair production. Some particles are as expected going into the center, where the laser intensity vanishes, but at $t/\tau = 8$ the positron density at the center is one to two orders of magnitude lower than the maximum on the ring-like structure.

The same feature is observed by considering the particle distribution as a function of the laser propagation direction, represented in fig. 7.12. The stripes of higher and lower densities, correspond to the different region of the standing wave. A zoom of the density on those stripes is shown in figure fig. 7.13. We observe that the two stripes with the high densities lie at the electric field nodes ($z = 9.75\lambda$ and $z = 10.25\lambda$) before and after the focus (corresponding to $z = 10$). They both have slightly higher density than, but of the same order as, the stripe at the magnetic field node in the focal plane. This is the position where the cascade is predominantly developing. This analysis allows to say that the cascade develops fast enough to be self-sustained, but eventually particles migrate towards the attractors at the electric field nodes, as discussed in section 6.4.

7.3 Seeding particles and produced pairs distribution and moments

7.3.1 Seeding particles evolution

The trajectories of a selection of the initial seeding particles allow to visualize and interpret the particle dynamics. This is shown in the left panel of fig. 7.14 for the LG_{-1}(Rot) case. Most of the seeding particles, move to the spiral attractors on a one-to-two-periods timescale. Once they are around the electric nodes, they are trapped and keep spiraling in that region. We also notice that some particles are pushed towards the center of the LG beam, at $x/\lambda = 16$. To understand if the seeding particles are still participating to the cascade, one can draw the evolution in time of the average value of their quantum parameter and its dispersion, which are represented in fig. 7.15. The dispersion is defined as the ratio between the average value and the standard deviation σ_χ, which

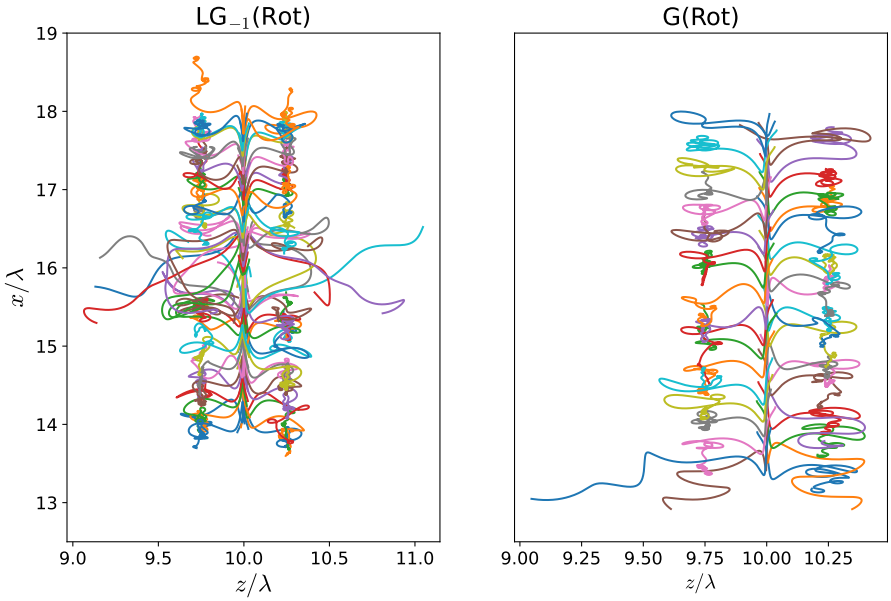

Figure 7.14: Trajectories of some seeding electrons from $t/\tau = 0$ to $t/\tau = 3$, for the cases LG$_{-1}$(Rot) on the left, and G(Rot) on the right, with $a_{0,tot} = 1540$ After a time of the order of the laser period, most of the particles are migrating to the attractors at the electric field nodes locations, in $x/\lambda = 9.75; 10.25$.

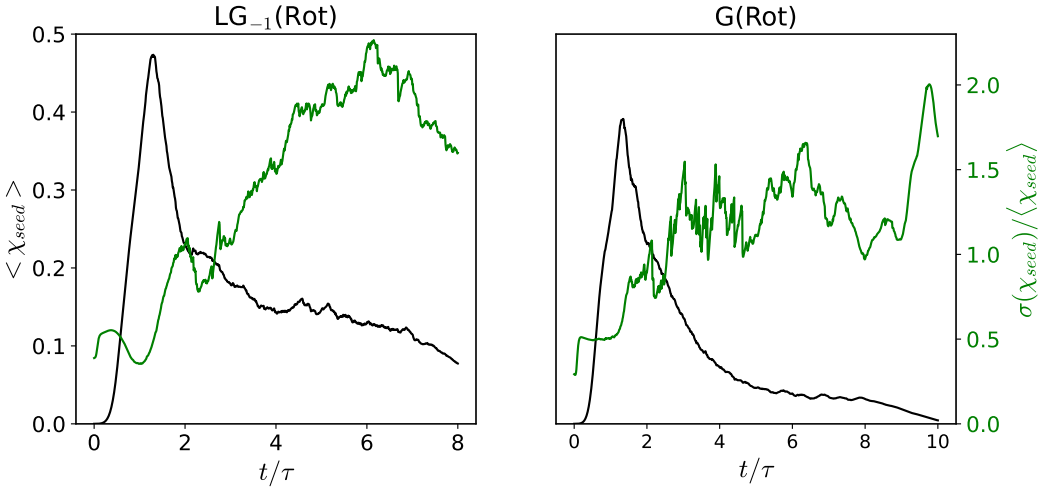

Figure 7.15: Average value (in black) and dispersion (in green) of the quantum parameter of the seeding particles $\frac{\sigma_{\chi_{seed}}}{\langle\chi_{seed}\rangle}$ as a function of time for the cases LG$_{-1}$(Rot) on the left, and G(Rot) on the right, with $a_{0,tot} = 1540$.

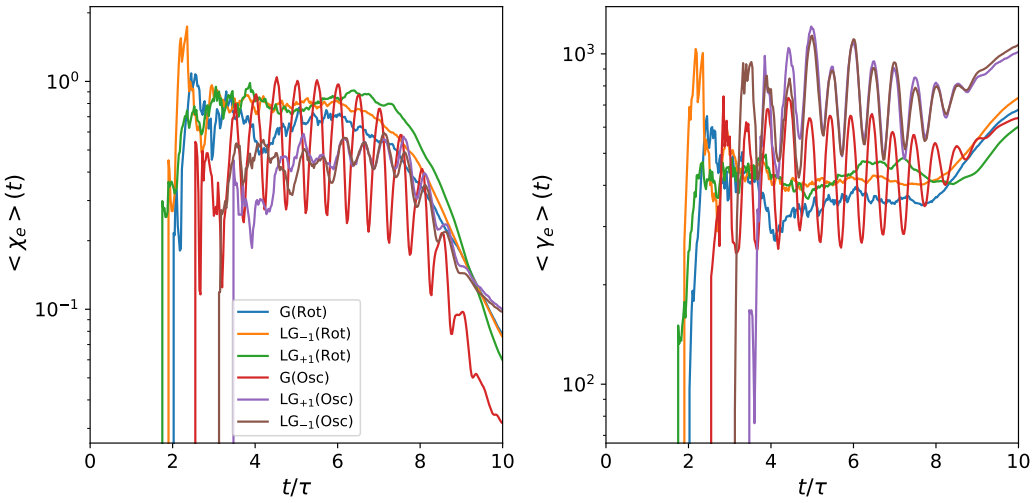

Figure 7.16: Average quantum parameter and Lorentz factor of the positrons as a function of time, for the different cases with two LG beams with $a_{0,tot} = 1280$.

is given by

$$\sigma_{\chi_{seed}} = \sqrt{\sum_{k=1}^{N_{seed}} \frac{(\chi_{seed} - \langle \chi_k \rangle)^2}{N_{seed}}}, \tag{7.11}$$

with N_{seed} being the number of seeding particles. It can bee seen that after the first peak in χ_{seed} at time$\sim 1.5t/\tau$, corresponding to the first acceleration and emission, the average quantum parameter decays slowly below 0.2. Nevertheless, its dispersion grows for most of the interaction time up to values around 2 at $t/\tau = 6$, and only after this time it decreases. This means that some of the seeding particles can still participate to the cascade for the majority of the interaction.

We now consider the rotating Gaussian case. The trajectories of a representative selection of the seeding particles, their average χ_{seed} and standard deviation are represented on the right panel of figs. 7.14 and 7.15. While the particles orbits appear similar to the LG case that we have just discussed, the average χ parameter and its dispersion have overall lower values. The average χ decreases faster, in particular the dispersion in χ is stagnating as opposed to the LG configuration, where it keeps a substantial value for much longer times. Understanding the reason of this different behaviour between the Gaussian and LG cases requires further studies.

7.3.2 Produced pairs moments

To have a better understanding of the physics at play and explain the relative efficiency of the different cases, we analyze the distribution of the quantum parameter and energy of the particles in the different configurations. The

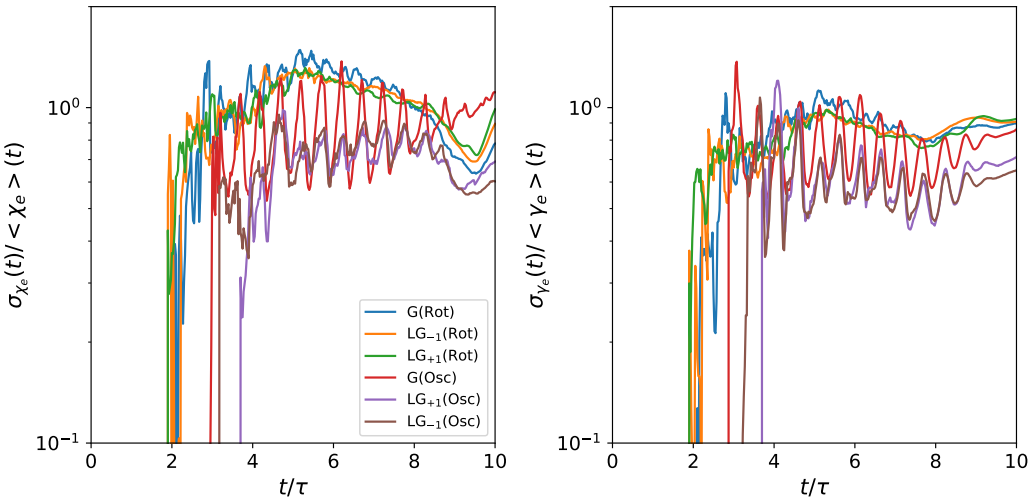

Figure 7.17: Dispersion of the quantum parameter $\frac{\sigma_{\chi_e}}{\langle\chi_e\rangle}$ and of the Lorentz factor of the positrons as a function of time, for the different cases with two LG beams with $a_{0,tot} = 1280$.

average values and the dispersion of the quantum parameter and energy of positrons as a function of time are reproduced in figs. 7.16 and 7.17. The dispersion is, as for the seeding particles given by the ration of the average and of the standard deviation. The average and standard deviation are given here by

$$\langle\chi_e\rangle = \frac{\int \mathrm{d}\chi_e w(\chi_e)\chi_e}{\int \mathrm{d}\chi_e w(\chi_e)}, \tag{7.12}$$

$$\sigma_{\chi_e} = \sqrt{\frac{\int \mathrm{d}\chi_e(\chi_e - \langle\chi_e\rangle)^2 w(\chi_e)}{\int \mathrm{d}\chi_e w(\chi_e)}}, \tag{7.13}$$

where $w(\chi_e)$ is the sum of the weights of positrons having the quantum parameter χ_e. Let us first look at the moments of the quantum parameter distribution. As expected, the rotating cases have the highest value of the average quantum parameter, that is almost one. The time evolution is smoother if compared to the oscillating cases, and a quasi steady state is reached. In the oscillating cases the average value of χ is lower than in the rotating ones and we can clearly see an oscillatory behaviour in time. All the rotating cases have an average quantum parameter that is of the same order, but the Gaussian case is the lowest, consistently with the growth rate results. The slow decrease after time $t/\tau = 5 - 6$ is due to the envelope of the pulses and the finite duration of the overlap. The abrupt increase at the beginning is due to the fact that only seeding particle exist at early time. The quasi steady state, for the (Rot) cases is manifested here in the fact that the average of the quantum parameter

around the pulses maximum is approximately flat. This suggests that for the current parameters the pulse duration is the main responsible for quenching of the regime of self-sustained cascade. However, to extrapolate this result to longer interaction, we have to carefully take into account competing effects, such as the ponderomotive force, that can play a more important role at longer times, and the back reaction on the laser from the pairs. This is left for further studies.

We now consider the dispersion of the quantum parameter, in fig. 7.17. The information provided by this quantity is consistent with the results on the average χ in the following way. In all cases the spread of χ is large, and comparable to the average value (the lowest value being around 0.6 for the LG(Osc) cases). However the (Rot) cases dispersions are higher and the rotating configurations reach a steady state, with a slowly varying dispersion, while the (Osc) cases do not. Moreover, taking into account that the oscillating setups have a lower average χ, we can also deduce from these curves that they have a lower number of positrons with high values of χ positrons, which are the key element for sustaining the cascade since they are responsible for the emission of hard photons.

The average value of the gamma factor, reproduced on the left panel of fig. 7.16, allows to highlight some important points. The configurations corresponding to most efficient pair production have smaller values of the average Lorentz factor than the less efficient ones, but still high, i.e. of the order of the order of $300-400$ in the rotating configurations. However, since the dispersions shown in fig. 7.17 are roughly the same for the different cases, we can conclude that the oscillating configurations have more positrons with higher energies. Moreover the probability of emission, according to Eq. (2.51), decreases for when the γ_e value increases at fixed χ_e since the emission rate decreases, which is consistent with the fact that the less efficient cases have a larger value of the average γ_e.

The χ_e factor, depending on γ_e, depends also on the angle that the particle momentum has with respect to the field, which is very different in the oscillating and rotating cases. This again favors the rotating cases, as the particles momentum may have a bigger angle with the field compared to the oscillating cases, where they oscillate along the electric field direction.

To summarize, the moments of the quantum parameter and Lorentz factor distributions of the positrons are consistent with the efficiency of the different setups and allow to understand why pair production is improved in the rotating cases.

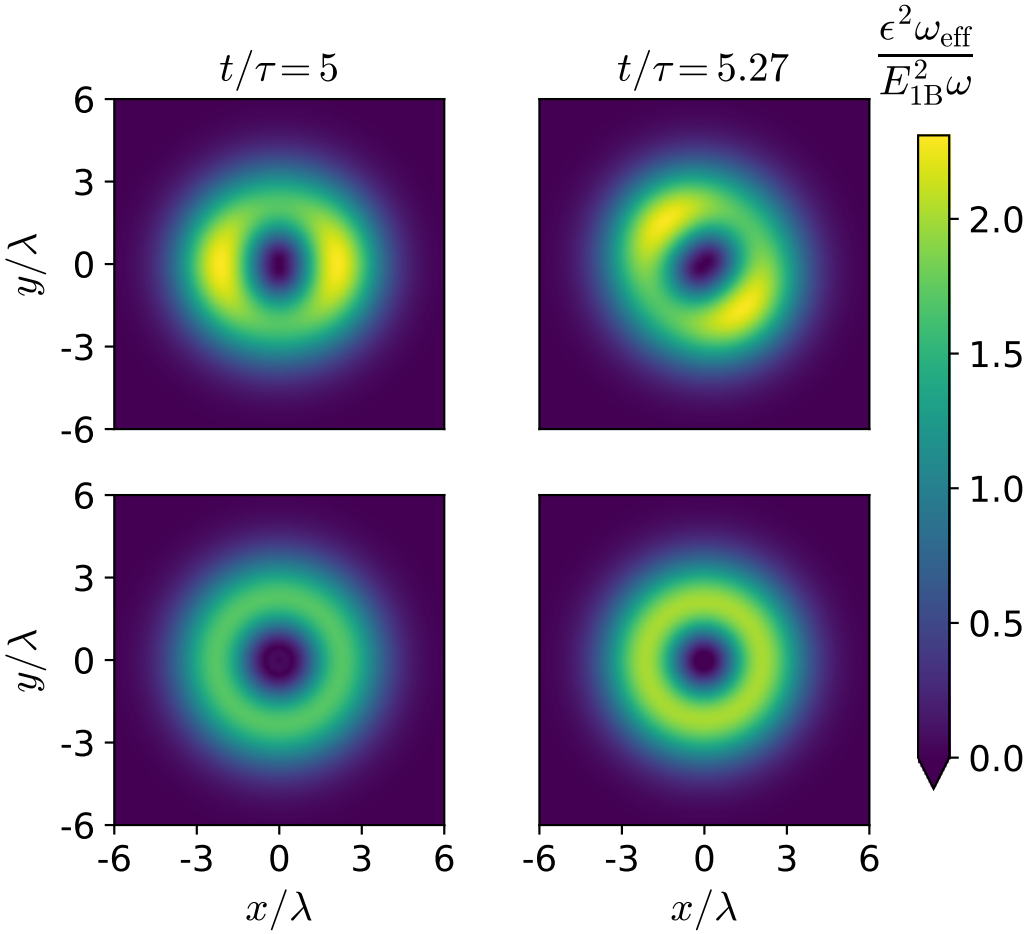

Figure 7.18: Value of $\frac{\epsilon^2\omega_{\rm eff}}{E_{\rm 1B}^2\omega}$ in the focal plane, at two different times for the LG_{-1}(Rot) case (top row) and the LG_{+1}(Rot) case (bottom row).

7.4 Reduced model for cascade

In this section we describe a simple analytical approach that allows to can predict that the relative efficiency of different field configurations, even if their maximum field amplitude is the same. We then verify that our predictions are consistent with the numerical simulations of the previous Secs. 7.2 and 7.3. Since particles migrate, the short time dynamics and the fact that the cascade can develop quickly is an essential ingredient. We can then use the model for the short time dynamics of a particle in a strong field presented in the previous chapter 6. This allows to calculate $\chi_e(t)$ for an electron or positron initially at rest, on timescales smaller than the laser frequency as given by Eq.(6.49)

$$\chi_e(t) \simeq \left(\frac{e^2\hbar\epsilon^2\omega_{\rm eff}}{m^3c^4}\right) t^2 \,. \tag{7.14}$$

The ω_{eff} quantity is given by (6.50)

$$\omega_{\text{eff}} = \sqrt{F_{\mu\nu,\sigma(0)} u_1^\mu u_1^\sigma (J^{-1})^\nu{}_\lambda F^\lambda{}_{\kappa,\rho(0)} u_1^\rho u_1^\kappa} \,. \tag{7.15}$$

The algorithm used to compute ω_{eff} from the given fields of the 3D PIC simulations is detailed in appendix B.1. Equation (6.49) suggests that the quantity $\epsilon^2\omega_{\text{eff}}$ is a key ingredient. In what follows we therefore discuss it in more details and us it to interpret our simulations results.

7.4.1 Model predictions for the different configurations

In the following we show the quantity $\epsilon^2\omega_{\text{eff}}$ extracted from 3D PIC simulations considering different cases. To have a proper picture of the field configuration, it is useful to represent this quantity at the focal plane, and for different times. Higher values of $\epsilon^2\omega_{\text{eff}}$ and a weaker time dependence correspond to the optimal configuration for pair creation. Its spatial extension in the focal plane plays also a role, since it takes large values only in a small region of space, particles may escape from the re-accelerating region limiting the pair production rate.

We first consider the most efficient cases $\text{LG}_{\pm1}(\text{Rot})$. The value of $\epsilon^2\omega_{\text{eff}}$ in the focal plane for the $\text{LG}_{-1}(\text{Rot})$ is shown in the top row of fig. 7.18 at two different times: 5τ (that corresponds to the peak of the pulses crossing) and roughly a quarter period later. We clearly see a ring-like shape rotating in time. The rotation can be identified that to the presence of two regions of higher amplitude where $\epsilon^2\omega_{\text{eff}} \simeq 2.30 E_{1\text{B}}^2\omega$, which is the highest maximum value of all cases, and two regions of lower amplitude with $\epsilon^2\omega_{\text{eff}} \simeq 1.7 E_{1\text{B}}^2\omega$. Moreover we observe that these values are constant in time (up to the slow variation of the envelope). Hence in this configuration there is always a region where particles renew their quantum parameter and keep emitting gamma photons.

The distribution of $\epsilon^2\omega_{\text{eff}}$ for the $\text{LG}_{+1}(\text{Rot})$ case is shown in the bottom row of fig. 7.18 and results as well in a ring. This case reaches one of the highest maximum value $\epsilon^2\omega_{\text{eff}} \simeq 2.25 E_{1\text{B}}^2\omega$ of all the simulations that we have performed, but its peak in the focal plane oscillates in time once in a laser period from a non-zero minimal value, equal to $\epsilon^2\omega_{\text{eff}} \simeq 1.7 E_{1\text{B}}^2\omega$, to its maximum. Despite the oscillation in time, this is one of the most favourable cases, thanks to the high value of $\epsilon 2\omega_{\text{eff}}$ and the fact that even the minimum is not zero, allowing to increase multiple times the quantum parameter of pairs.

The G(Rot) case distribution is shown in figure 7.19 and it consists in a single spot. Its maximum value at the center of the focal spot $\epsilon^2\omega_{\text{eff}} = 2E_{1\text{B}}^2\omega$ is constant in time (up to the slow variation of the envelope) but is lower than the previous LG cases. This was expected since at the center the field looks like

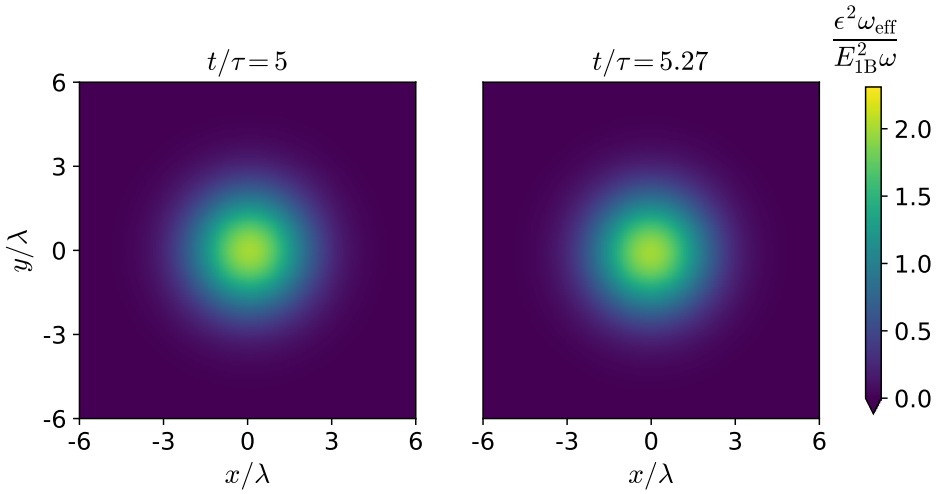

Figure 7.19: Value of $\frac{\epsilon^2\omega_{\text{eff}}}{E_{1B}^2\omega}$ in the focal plane, at two different times for the G(Rot) case.

a rotating electric field at a megntic node of two PW, with $\epsilon = 2E_{1B} = E_{0,\text{tot}}$ and $\omega_{\text{eff}} = 0.5\omega$. Moreover the maximum value of $\epsilon^2\omega_{\text{eff}}$ this case is consistent with the fact that this case is less efficient than the rotating LG configurations.

The distribution of the G(Osc) case on the left panel of 7.20 has a particular structure, composed of two lobes separated by a zero value axis. This line is at the center of the focal spot and is parallel to the polarisation direction of the electric field. The peak value of these lobes oscillates in time, with a maximum value $\frac{\epsilon^2\omega_{\text{eff}}}{E_{1B}^2\omega} \simeq 0.064$ lower than the previous case (Rot) cases. Since the electric field goes periodically to zero, there are times in which ϵ^2 vanishes everywhere. This happens in our configuration at the time $t = 5\tau$, reason why we do not show that figure. This is also true for all the other oscillating configurations.

Finally we consider the distribution of $\epsilon^2\omega_{\text{eff}}$ for the oscillating configurations $\text{LG}_{\pm1}$(Osc), shown on the right panel of 7.20 for LG_{-1}(Osc). The LG_{-1}(Osc) case shows a four-leaf clover-like pattern, which does not rotate and oscillates in time, going to zero at time 5τ (not shown here). This case has a higher maximum value than the previous G(Osc) configuration, with $\epsilon^2\omega_{\text{eff}} \simeq 0.126E_{1B}^2\omega$. However in this case this quantity does not only oscillate from zero to its maximum value, but $\epsilon^2\omega_{\text{eff}}$ is zero for half of the laser periods. This oscillating configuration has a non zero transverse magnetic field at focus at times when $\epsilon^2\omega_{\text{eff}}$ is close to its maximum. Since during half of the laser period, the field is of magnetic type, with $\epsilon = 0$, the particles quantum parameter cannot increase in this interval of time. This explains why this case is one with the lowest efficiency of pair production..

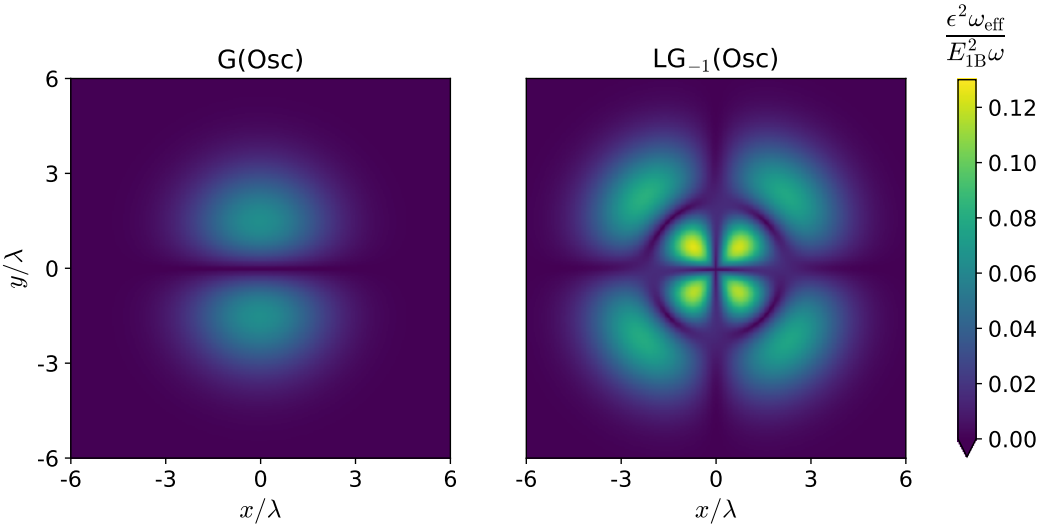

Figure 7.20: Value of $\frac{\epsilon^2\omega_{\text{eff}}}{E_{1B}^2\omega}$ in the focal plane, at time $t/\tau = 5.27$ for the G(Osc) case (left) and the LG$_{-1}$(Osc) case (right). The case LG$_{+1}$(Osc) is not represented here as its maximum value is less than 0.01. Please note that here the colour scale is different than from (Rot) case in figs. 7.18 and 7.19.

The last case hat we have investigate, is the LG$_{+1}$(Osc) configuration which has a very low maximum value $\epsilon^2\omega_{\text{eff}} \simeq 0.002 E_{1B}^2\omega$. Moreover the maximum of this quantity in the focal plane oscillates with time and is zero for half of the laser period, which is similar to the previous case. This means that the quantum parameter of the particles does not increase efficiently enough in comparison to the other cases and to drive a self-sustained cascade.

After putting together he analysis for all these cases, we can conclude that the insights given by the short time dynamics model are qualitatively coherent with the results of 3D PIC simulations. Indeed the rotating cases seem to be advantageous with respect to oscillating configurations with the same same amplitude. This can be understood because either the rotating cases have always a region with a substantial value of $\epsilon^2\omega_{\text{eff}}$ to regrow the produced particle quantum parameter, as the LG$_{-1}$(Rot) and G(Rot) cases, or because they have a high maximum value of $\epsilon^2\omega_{\text{eff}}$ quantity on a large portion of the focal plane, even though it is not constant with time, as the LG$_{+1}$(Rot) case. This qualitative agreement suggests a good direction to try to make a more quantitative estimation of the growth rate from the short time dynamics model.

7.4.2 Growth rate estimates

The numerical simulations presented in the previous sections together with theoretical insights gained from the model in [Mironov et al., 2021] (see also Sec. 6.3) lead us to propose a new model for predicting the growth rate of an electron-positron pair cascade. Indeed, our simulations clearly indicate that, in a realistic electromagnetic field configuration, particle migration out of the regions of strong field (where pair production is important) happens on a short timescale, at most of the order of the laser optical cycle. Hence, the cascade needs to develop on shorter timescales. One can thus consider the electron/positron dynamics over very short timescales as decribed by Mironov and collaborators. As it will be shown, this model allows to recover the correct cascade growth rate (within 40% from the value extracted from simulations) over a broad range of laser field strength (for $a_{0,tot}$ from 200 to 10^4), and for various field configurations.

The starting point of our model is the probability for an electron subject to a strong electromagnetic field to emit at least one photon during a time interval t (see, e.g. Sec. IV.C of [Niel et al., 2018a]):

$$P(t) = 1 - \exp\left(-\int_0^t W_\gamma(t')\mathrm{d}t'\right) , \tag{7.16}$$

where the integral term $s(t) \equiv \int_0^t W_\gamma(t')dt'$ is the optical depth at the basis of the Monte-Carlo procedure for inverse Compton scattering introduced in Sec. 3.3 and W_γ is the rate of high-energy photon emission given by Eq. (2.51). This depends on time through the emitting electron/positron Lorentz factor $\gamma(t)$ and quantum parameter $\chi(t)$ only

$$W_\gamma(t) = \frac{2\alpha^2}{3\tau_e}\,\frac{c_0\big(\chi(t)\big)}{\gamma(t)} . \tag{7.17}$$

As one focuses on short time scales, the model by Mironov et al. provides us with the time evolution of both quantities, $\gamma(t)$ and $\chi(t)$, as given by Eqs. (6.39) and (6.49), which we rewrite in the form

$$\gamma(t) \simeq \hat{\epsilon}\,\omega t\,, \tag{7.18}$$

$$\chi(t) \simeq \frac{\hbar\omega_{\mathrm{eff}}}{mc^2}\hat{\epsilon}^2\,(\omega t)^2 = \frac{\hbar\omega_{\mathrm{eff}}}{mc^2}\,\gamma^2(t)\,, \tag{7.19}$$

where times have been expressed in units of the inverse of the laser field frequency ω and $\hat{\epsilon} = e\epsilon/(mc\omega)$. From Eq. (7.16) one can define a characteristic

time $t_{\rm em}$ for high-energy photon emission in the form:

$$\int_0^{t_{\rm em}} W_\gamma(t')\mathrm{d}t' = 1\,. \tag{7.20}$$

Noting the bijection between time, energy and quantum parameter [Eqs. (7.18)-(7.19)], this integral can be rewritten in the form

$$\int_0^{\chi_{\rm em}} \frac{c_0(u)}{u}\mathrm{d}u = \frac{3\tau_e\omega}{\alpha^2}\,\hat{\epsilon} = \frac{\omega}{2W_0}\,\hat{\epsilon}\,. \tag{7.21}$$

This equation uniquely defines, for a given field invariant (ϵ, equivalently $\hat{\epsilon}$), the characteristic quantum parameter $\chi_{\rm em}$ that an electron/positron has reached when it emits a photon. Note that this characteristic quantum parameter is found to depend on ϵ only. Note also that the right hand side term $\propto \omega\,\hat{\epsilon}$ does not depend on ω as $\hat{\epsilon} \propto \epsilon/\omega$.

Once $\chi_{\rm em}$ is known for a given field invariant ϵ (equivalently $\hat{\epsilon}$), the characteristic photon energy at the moment of emission $\gamma_{\rm em}$ and the characteristic time of emission $t_{\rm em}$ can be computed as

$$\gamma_{\rm em} = \sqrt{\frac{mc^2}{\hbar\omega_{\rm eff}}\,\chi_{\rm em}}\,, \tag{7.22}$$

$$\omega t_{\rm em} = \frac{\gamma_{\rm em}}{\hat{\epsilon}}\,. \tag{7.23}$$

All three quantities, $\chi_{\rm em}$, $\gamma_{\rm em}$ and $t_{\rm em}$, are shown in Fig. 7.21 as a function of $\hat{\epsilon}$ considering $\omega_{\rm eff} = \omega/2$ and $\omega \simeq 2.35\times10^{15}\,\mathrm{s}^{-1}$ ($\lambda = 0.8\,\mu$m). We have considered here the particular case $\omega_{\rm eff} = \omega/2$ as it corresponds to what is expected for a purely rotating field, for which one also has $\hat{\epsilon} = a_{0,\rm tot}$.

For moderate values of $\hat{\epsilon} \lesssim 10^3$, the characteristic quantum parameter $\chi_{\rm em} < 1$, $c_0(\chi) \simeq (5/4)\sqrt{3}\chi$, and all quantities can be fairly well approximated using

$$\chi_{\rm em} \to \frac{4}{5\sqrt{3}}\frac{3\tau_e\omega}{\alpha^2}\hat{\epsilon} \;\simeq\; 0.461\left(\frac{1\,\mu\mathrm{m}}{\lambda}\right)\left(\frac{\hat{\epsilon}}{1000}\right)\,, \tag{7.24}$$

leading to $\gamma_{\rm em} \propto \sqrt{\hat{\epsilon}}$ and $\omega t_{\rm em} \propto 1/\sqrt{\hat{\epsilon}}$. For larger $\hat{\epsilon} < 10^3$, the characteristic quantum parameter $\chi_{\rm em}$ increases faster. Yet, even for very large values $\hat{\epsilon} \sim 10^4$, $\chi_{\rm em}$ does not reach very large values ($\chi_{\rm em} \sim 10$ for $\hat{\epsilon} \sim 10$). Taking the limit $c_0(\chi) \simeq (7/9)\,3^{2/3}\Gamma(2/3)\,\chi^{2/3}$ thus gives only a rough estimate for $\chi_{\rm em}$ in this range of large $\hat{\epsilon}$

$$\chi_{\rm em} \to \frac{2\sqrt{42}}{49\,\Gamma(2/3)^{3/2}}\left(\frac{3\tau_e\omega}{\alpha^2}\hat{\epsilon}\right)^{3/2} \;\simeq\; 0.167\left(\frac{1\,\mu\mathrm{m}}{\lambda}\right)^{3/2}\left(\frac{\hat{\epsilon}}{1000}\right)^{3/2}\,. \tag{7.25}$$

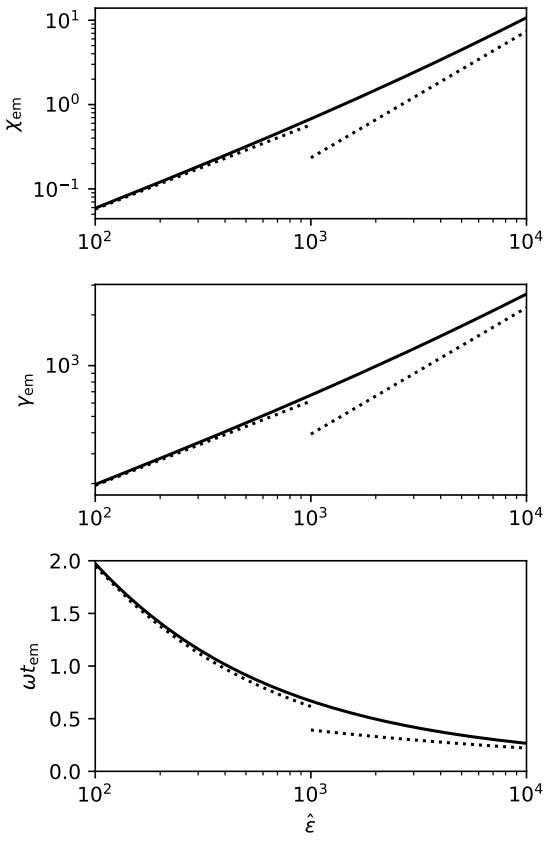

Figure 7.21: Cascade model predictions for (top) the characteristic electron quantum parameter $\chi_{\rm em}$ at the moment of emission, (middle) the characteristic electron Lorentz factor $\gamma_{\rm em}$ at the moment of emission, (bottom) the characteristic time of emission $t_{\rm em}$ (in units of ω^{-1}). All quantities are plotted as a function of the normalized Lorentz invariant $\hat{\epsilon} = e\epsilon/(mc\omega)$. Dotted lines show asymptotic behavior for which simple analytical expressions are obtained.

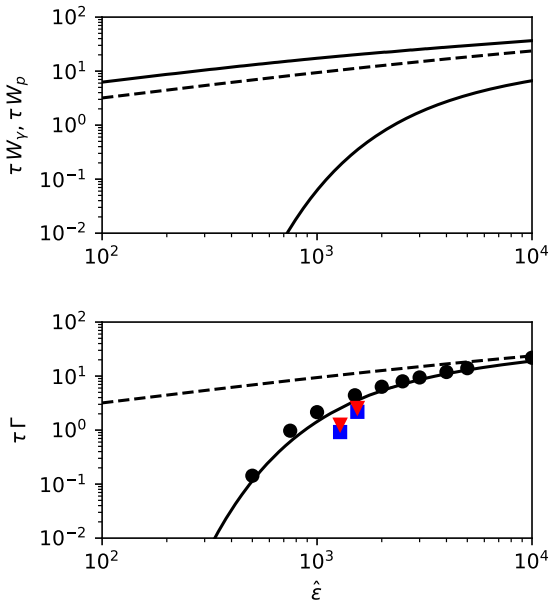

Figure 7.22: Cascade model predictions for (top) the high-energy photon emission rate W_γ and electron-positron pair production rate W_p, (bottom) the predicted cascade growth rate (in units of the inverse of the laser optical cycle $\tau = 2\pi/\omega$). All quantities are plotted as a function of the normalized Lorentz invariant $\hat{\epsilon} = e\epsilon/(mc\omega)$. Dashed lines show the inverse of the characteristic time of photon emission $\tau/t_{\rm em}$. The blue squares and red triangles in the bottom panel are the numerical growth rates for the G(Rot) and LG$_+$1(Rot) cases respectively.

To compute the growth rate Γ of the cascade, one then uses Eq. (6.11)

$$\Gamma = \frac{W_p}{2}\left(-1+\sqrt{1+\frac{8\,W_\gamma}{W_p}}\right), \tag{7.26}$$

where W_γ (Eq. (2.51) in Sec. 2.2.3) and W_p (the pair production rate, Eq. (2.43) in Sec. 2.2.2) are both evaluated using $\chi_{\rm em}$ and $\gamma_{\rm em}$. The corresponding predictions for W_γ, W_p and Γ are given in Fig. 7.22. The predicted growth rate for the purely rotating field ($\omega_{\rm eff} = \omega/2$, solid line in the bottom panel of Fig. 7.22) is found to be in very good agreement with the 1D3V Smilei simulation results presented in fig. 6.3 considering a purely rotating electric field. In that case indeed the discrepancy between our theoretical model and simulation does not exceed 40%.

We have also reported in the bottom panel of Fig. 7.22 the growth rates obtained for the case G(Rot) (blue squares) and LG$_{+1}$(Rot) (red triangles). We did not report the case LG$_{-1}$(Rot) as the corresponding growth rate is very close to (about 5% less than) the one obtained for LG$_{+1}$(Rot), while the growth rate for G(Rot) is about 30% lower. These values have however not been obtained extracting the maximum (local) growth rate of the simulations,

but examining the growth of the total number of electron-positron pairs. The resulting measure of the global growth rate cannot thus be directly compared to the predictions of our model. Yet, we want to point out that for the $LG_{\pm1}$(Rot) cases, the measured effective frequency $\omega_{\text{eff}} \sim 0.58\,\omega$ is larger by about 16% with respect to $\omega_{\text{eff}} \sim 0.5\,\omega$ obtained for the G(Rot) case. We believe this explains why the growth rate for the two LG beam cases is larger than that obtained with the Gaussian beam.

7.5 Conclusions

Let us summarize the results presented in this chapter. The rich variety of field configurations, which can be obtained from two counter-streaming LG beams, was presented. The different field structures allowed to discuss the main characteristics of the transverse electric field at focus. For a given polarisation and LG beam order, one can deduce if the transverse field is locally rotating (Rot) or oscillating (Osc) and if the phase structure is rotating or stationary, as summarised in table 7.1.

A set of 3D PIC simulations showing the development of pair avalanches were then performed for different field configurations. In all simulations the maximum intensity achieved at the crossing of the pulses in the focal spot was kept the same. Two different values of the total peak field were investigated, $a_{0,\text{tot}} \simeq 1280$ and $a_{0,\text{tot}} \simeq 1540$. The first value is not so far from the lower limit to induce an avalanche according to the pure rotating electric field case and the literature [Grismayer et al., 2016]. For these two values of the peak intensity, we showed that only the cases labelled as rotating (Rot) showed a clear slope with a well defined growth rate and in general a more efficient pair production than the cases labelled as oscillating (Osc), the difference being more pronounced for the highest intensity. This result is consistent with the values of the average pair quantum parameter, their Lorentz factor and their dispersion, as discussed in 7.3.2. Moreover the simulations showed that $LG_{\pm1}$(Rot) cases have larger growth rate than the G(Rot) case. This is coherent with the analysis performed by examining the seeding particle trajectories, and their quantum parameter average and dispersion. A different behaviour was observed in the gaussian and LG (Rot) cases. Indeed for the LG(Rot) cases pairs after being created participate more effectively and for a longer time to the growth of the avalanche than in the gaussian case.

We looked at the time evolution of the particles densities for the (Rot) cases to get some insights in the pair distribution. First of all an analysis of the trajectory of the seeding particles allowed to verify that the attractors

discussed in section 6.4 induce particles to migrate toward them over one or two periods. We also showed that even if the electric nodes behave as attractors, the magnetic node at focus corresponds to a region of high density. This means that even if particles migrate, pair production in this region is still fast enough to make the density grow substantially. In the parameter range and in particular for the pulse duration that we considered, the ponderomotive push of the pairs in the transverse direction was weak, and we can conclude that the main limiting effect for pair creation is the finite pulse duration.

In the last part of this chapter, we used the results for the short time dynamics developed in [Mironov et al., 2021] and we computed ϵ and ω_{eff} for the various configurations to explain the improvement in pair production for the rotating set-up with respect to the oscillatory one. We also showed that $\text{LG}_{\pm 1}(\text{Rot})$ cases have a higher maximum value of the product $\epsilon^2 \omega_{\text{eff}}$ than the gaussian case, which is consistent with their higher growth rate. Finally we derived a simple analytical model to predict the growth rate based on the short time dynamics. The estimated growth rate showed very good agreement with simulations for the ideal rotating electric field case for a wide range of parameters.

Future perspectives include the extension of this model to obtain the growth rate for more realistic configurations such as two counter-streaming LG beams.

Conclusion

In order to conclude the present work, let us summarise all the results which have been presented, and discuss the perspectives and upcoming studies.

The main purpose of this work was to study nonlinear Breit-Wheeler pair creation driven by intense lasers with a focus on how the various laser parameters affect the pair creation process. In order to extend the already existing work, and due to the recent interest of the community in Laguerre-Gauss beams which have a vortex structure and other interesting properties, our work focused on this type of laser pulses. The common thread was to see how to improve pair production, as one of the ultimate goal of future ultra intense laser facilities is to create enough pairs to produce a pair plasma. In this quest for creating more pairs we looked at two different types of configurations, which are either promising or might be available in a near future.

Soft shower regime

The first configuration was the soft-shower discussed in part two. It is one of the simplest configuration, involving the head-on collision of the laser pulses with seeding particles (gamma photons in this study) and will likely be the first configuration in future facilities. In order to generalise previous work, we performed a study at fixed laser pulse energy, looking at how the spatio-temporal profile of the laser pulse influences pair production. However this work was not only comparisons of the results of simulations with different parameters for laser pulses. To do this study we have built our own reduced semi-analytical model from scratch. Starting from the SFQED probability rates of a gamma photons interacting with a strong field, we could derive the probability for the photon to be converted into a pair when interacting with a plane wave. Taking the plane wave case as an elementary block we were able to generalise our model to arbitrary laser pulses with non-trivial phase structures such as LG beams, and with spatio-temporal envelope. Applying the model to regimes of high probabilities of conversion, we insisted on some counter intuitive results, such as the fact that in some cases increasing the seeding particles energy is lowering the probability of pair creation, or that tight focusing, while in-

creasing the laser peak intensity does not necessarily allows to produce more pairs. The soft-shower model is successful as it is predicting with a very good precision the number of pairs obtained from 3D PIC simulations. Equipped with this new model, we performed 3D PIC simulations at constant laser pulse energy and verified how the transverse and temporal shape of laser pulses was influencing the pair creation in different intensity regimes. We arrived at one of the main results of this work which is that in the shower configuration, focusing the laser to the maximum is not always the best option to maximise pair creation. After the publication of this study [Mercuri-Baron et al., 2021], this result was confirmed by other teams arriving at the same conclusions independently [Salgado et al., 2021, Óscar Amaro and Vranic, 2021], which confirms the relevance and validity of the present work for the community.

In the same work we derived guidelines for future experiments based on their expected specifications. In particular facilities like Apollon, ELI or CORELS should not focus too much the laser in order to maximise pair production, whereas other facilities with lower intensities should do the opposite. Looking in particular at the Apollon facility case, since it is developed in the laboratory this thesis was made, we showed the counter-intuitive result that it is not worth it to increase too much the seeding particles energy after a few GeV for the field intensities that will be achieved, in order to maximise pair production. Finally we tried to describe how our model could be adapted to various situations, with longer laser-pulses, or with seeding particles which have more general spatial distribution and a wide energy spectrum.

Perspectives of this first configuration are diverse. First we should note that some current facilities are planning to realise the head-on collision experiment with gamma photons, like in [Salgado et al., 2021]. Another point is that the present work used gamma photons as seeding for the shower configuration. For a seeding high energy electron beam instead of a gamma flash, the pair production may be different in some laser configurations. In particular, it could happen that high energy electrons never see the maximum amplitude of the pulse, leading to different results in term of pair production. As we presented in part two, some previous works like [Blackburn et al., 2014] considered electrons, but not in LG beams, however recently [Óscar Amaro and Vranic, 2021] studied the effect of the laser and electron beam shapes on pair production in the soft-shower configuration.

Another point is the long term dynamics of the produced particles, and their evolution in the laser pulse. Indeed our study and simulations stopped relatively soon, right after pair creation has stopped. However as it was shown in the phase space of the pairs presented in Sec. 5.3, even for LG beams, some

pairs remain in the middle of the pulse, with positive momentum along the propagation direction of the pulse. It would be interesting to study if this could be used to trap and guide pairs or to produce a quasi neutral beam of pairs using LG beams.

Finally, our work was focusing on the soft regime of the shower configuration, neglecting secondary pairs. As laser intensities and seeding particles energy are increasing, the study of the hard shower regime, where the number of secondary pairs is greater than the number of primary could become relevant. In the context the hard shower, a key aspect which needs to be understood is how many steps can exist in the shower, before pair production stops. This should depend on seeding particles energy and laser intensities off course, but maybe also on the field configuration.

Avalanche study

The second configuration studied in this work was the avalanche driven by two counter-streaming laser pulses, and was the main topic of part three. In this part, we studied how, at a fixed maximum field amplitude, the electromagnetic field configuration could influence the onset of the avalanche. The LG beams are a very good tool to probe many different configurations, and we tried several LG beams order combined with different polarisations. In the begening of chapter 7 we presented the diversity of field configurations which can be obtained by combining two counter-streaming LG beams. We discussed the transverse electric field configurations of the main combinations of LG beams order and polarisation. Finally practical rules to infer local field behaviour and dynamics of the phase structures were given. They simply rely on the sign of the differences LG beam order and polarisation numbers.

The results of the study, done with 3D PIC simulations at the same peak intensity, show that configurations with locally rotating transverse field are better than oscillating configurations. Moreover rotating LG beams configurations are the best configurations at fixed peak intensity, as they allow to reach the largest cascade growth rates. In particular they are better better than the usual configurations with two circularly polarised gaussian beams with opposite polarisations. Checking the average value and dispersion of the quantum parameter and Lorentz factor of pairs for the different cases confirms that the relative difference of efficiency from rotating cases compared to the oscillating configurations is consistent. As a final aspect on the simulations results, we discussed the pairs distribution in space, showing the existence of the expected attractors presented in 6.4. We also discussed briefly the transverse ponderomotive push of the particles, which is not dominant in our case.

The simulations shows that in the studied cases, what stops the cascade is the separation of the pulses over time, and is not the back reaction of the produced pairs on the laser field or the ponderomotive effects. This results off course is expected to change for longer pulses or tinier focal spots.

In the last part of chapter 7 is presented a semi analytical model regarding the avalanche. First we compare the relative efficiencies obtained from the simulation, to the qualitative predictions provided by a model of the literature presented in Sec. 6.3 which describes the short time dynamics of particles in strong field. This model provides the quantum parameter and energy evolution of charges with time for an arbitrary configuration. By comparing the quantities $\epsilon^{\omega}_{\text{eff}}$ and ϵ, driving the evolution of the quantum parameter over the different cases, we see that the model qualitatively agrees with the simulations. This suggests that even without making a quantitative prediction, this could be used in order to make an educated guess about the ability of a configuration to start a cascade.

In the end of chapter 7 we finally present a model which predicts the growth rate of a cascade for the ideal rotating electric field case. In order to do so, we use the short time dynamics results mentioned previously to compute the time t_{em} after which the probability of emission of a charge in a strong field is of order one. We used this time to estimate the rate of emission of radiation by charges. This time depends on the ω_{eff} quantity (6.50) and the ϵ invariant (6.33) described in Sec. 6.3 and can be computed numerically. Still using the short time dynamics model, the quantum parameter of the charge at this time χ_{em} can be estimated, and is shown to depend only on the ϵ Lorentz invariant. Knowing χ_{em}, we can then compute the Lorentz factor of the charge at the time of emission as well as the characteristic time t_{em} of emission. Having these quantities, one can estimate the gamma emission rate W_γ as the NCS rate (2.51) evaluated at the time t_{em}. In the same way, the pair production rate W_p is estimated as the NBW rate (2.43) evaluated at χ_{em} and γ_{em}. These two rates are then plugged into the steady state avalanche growth rate expression (6.11). This allows us to compute the growth rate for the ideal rotating electric field case, which is in good agreement with the 1D3V PIC simulations presented in fig. 6.3.

These results open new perspectives in the possibility of estimating the growth rate of avalanches in more realistic 3D counter-streaming configuration. Indeed, to the knowledge of the author, no model performed this well on the estimate of the growth rate of the pure rotating electric field case, for the range of parameter probed here between the high intensity and low intensity limits, from a_0 of a few hundred to 10^4. However due to the non-trivial

field configuration of the counter-streaming configuration, the extension of the estimate to more realistic field configuration should be made carefully.

Finally as for the shower case, the possibility to trap the produced pairs with LG beams should be investigated further. The study of the density of the particles in space showed that some particles are indeed in the center of LG beams where the field is low, but the behaviour of those particles after the pulses separation was not the main concern of this work and should be addressed into more details.

Due to all the results and perspectives presented above, the present work allowed the make a step forward in the optimisation of pair production in ultra intense laser and in the understanding of the behaviour of two promising configuration to achieve this goal. Moreover multi-PW laser facilities like the Apollon Research Infrastructure, will give the possibility to either test the predictions made here or to use them to perform experiments.

Acknowledgements

First I would like to thank my parents, as without them non of this would have been possible. this manuscript is the final proof of all of the support they gave me for my studies over the years. They allowed me to be free to realise my dream to do physics and were always interested in what I did. I want to especially thank my mother, who is the best one in the observable universe!

I would like to thank my two supervisors Caterina Riconda and Mickael Grech for all of what they did for me during these (a bit more than) three years of the thesis. They deserve even more credit as this adventure started a few months before the covid-19 pandemic, and it is evident that if supervising well a student is hard, doing so under health crisis conditions is orders of magnitude more difficult. Caterina, I would like to specifically thank you as even though you had an overwhelming timetable, and what appears to me as an infinite amount of things to address you always had time to talk with me about my subject. Mickael I would like to thank you on that side too, and also for paying attention to every detail in my work, as I believed a real understanding of physics mainly comes from this. I hope both of you don't hate me too much for always being late and in a rush with the writing of the manuscript of the thesis!

I would also like to thank all of the members of the jury, Pr Richard Taieb, Pr Ben King, Dr Felix Karbstein, Dr Rachel Nuter and Dr Thomas Grysmayer, first for accepting to be a part of the jury, but also for all their reviewing work, and their interesting suggestions. I hope you found this thesis interesting.

Next, I would like to thank Anna Grassi. I believe that without Anna, I will still be writing my first paper, and struggling with its organisation, its figures, and the English. It is also thanks to you that this manuscript is readable, and in correct English, so thank you again for everything!

I would like to thank Paula Kleij, who is one of the best personal encounters I ever had during those three years, and in general. We both started this PhD journey at the same time, enduring the difficult pandemic times and we overcame it! Paula I congratulate you on your thesis, you did a great job, and it was really difficult! I would also like to thank you for all the times you help

me. I wish you the best in whatever way you may pursue, I am sure you will be successful. I hope I was able to help you a few times in this adventure.

I would also like to thank Arseny Mironov who joined the team at the beginning of the last year of my PhD and is now a friend. The final chapter with the model for the growth rates of the cascade is possible because of your previous work, as it's based on it. I would like to thank you for all the work we did together and all the times you helped me. I think you are a great physicist and I hope we will continue to do some math and physics together.

I want also to thank Samuel Marini for all of the exciting physics discussions we had. I wish you the best in your new lab!

I would like to thank Tommaso Vinci and Frédéric Pérez for their help, especially on the numerical side. I hope that I wasn't too annoying with Frédéric, asking about weird stuff in Smilei that almost nobody uses. I would also like to thank every person in LULI and elsewhere with whom I worked or who helped me.

Finally, I would like to wish good luck to the two new students of the TIPS group, Giuseppe Nicotera and Mattys Pouyez, I hope you will enjoy your thesis here.

I think the TIPS group in which this thesis was made is an exception in the sense that all members have very good human qualities. I was very lucky to do my thesis here and I think it is one of the best places you can think of to do so. I probably forgot some important aspects, but I hope that I showed everyone mentioned above that I am grateful.

Appendices

Appendix A

Gamma photon conversion

A.1 Approximation of the pair production rate integral

In this Appendix, we detail how the integral $\mathcal{I}_\varepsilon(\chi_0) = \int_0^\pi b_0(\chi_0 \Psi_\varepsilon(\varphi))\, d\varphi$ [Eq. (4.16)] can be efficiently approximated by Eq. (4.17). To do so, let us start by stressing that, in general, and in particular at small χ, $b_0(\chi)$ is a steep function of χ. One thus expects the principal contribution to the integral to come from the phase φ around $\varphi_m = \pi/2$, for which $\chi_0\, \Psi_\varepsilon(\varphi) \simeq \chi_m$ with $\chi_m = \chi_0/\sqrt{1+\varepsilon^2}$. To compute the contribution of this maximum analytically, we approximate the integrand in Eq. (4.16) around ϕ_m as

$$b_0(\chi_0 \Psi_\varepsilon(\varphi)) \simeq b_0(\chi_m)\, \exp\left(-\frac{(\varphi-\varphi_m)^2}{2 s_\varepsilon^2(\chi_m)}\right), \tag{A.1}$$

where $s_\varepsilon(\chi_m)$ is chosen so that the exact and approximated integrand have the same second derivative at $\varphi = \varphi_m$, which gives

$$s_\varepsilon(\chi_m) = \sqrt{\frac{3}{2}}\, \frac{c(\chi_m)}{\sqrt{1-\varepsilon^2}} \quad \text{with} \quad c(\chi) = \sqrt{\frac{2 b_0(\chi)}{3\chi b_0'(\chi)}}\,. \tag{A.2}$$

With the ansatz Eq. (A.1), the integral can be performed analytically, leading to

$$\mathcal{I}_\varepsilon(\chi_0) \simeq \pi\, b_0\left(\chi_m\right)\, F(s_\varepsilon(\chi_m)) \quad \text{with} \quad F(s) = \sqrt{2/\pi}\, s\, \mathrm{erf}\big(\pi\sqrt{2}/(4s)\big)\,. \tag{A.3}$$

The ansatz Eq. (A.1) gives a good approximation of the integrand for arbitrary values of ε as long as χ_m is small enough. It is also exact (for all χ_0) in the cases $\varepsilon = \pm 1$ for which $s_{\pm1}(\chi_m) \to +\infty$. Hence, Eq. (A.3) provides a very good, fully analytical approximation of Eq. (4.16) for a wide range of ε and

χ_0.

The approximation however needs to be corrected for $\chi_0 \gg 1$ and $|\varepsilon| < 1$. In this limit, the integrand in Eq. (4.16) can be approximated using Eq. (2.45) leading to

$$\mathcal{I}_\varepsilon(\chi_0) \simeq \pi\, b_0\,(\chi_m)\; f(\varepsilon) \quad \text{with} \quad f(\varepsilon) = \frac{1}{\pi}\int_0^\pi \left[\sin^2\varphi + \varepsilon^2\cos^2\varphi\right]^{1/3} d\varphi\,. \tag{A.4}$$

Equations (A.3) and (A.4) can be combined in Eq. (4.17). This form ensures the correct asymptotic behaviour of the integral Eq. (4.16) in both small and large χ_0 limits. It departs from the exact expression (integrated numerically) by less than 20%, the error being maximum for intermediate values of $\chi_0 \sim 1$. This was tested over a broad range of $\chi_0 \in [0.1\,,\,1000]$ for various polarization parameter $\varepsilon \in \{0, 0.25, 0.5, 0.75, 1\}$.

A.2 1D Pic simulations parameters

Here are described the simulations parameters leading to panel (c) of fig. 4.2. A series of 1D3V (1 dimensional in space and 3 dimensional in velocity) PIC simulations, considering a plane wave colliding head-on with a flash of gamma photons, have been performed to produce Fig. 4.2c. We simulated a box of length $2.5\,\lambda$ with spatial resolution $\lambda/256$, for a simulation time of $1.75\,\tau$, with temporal resolution $\tau/512$. This is a long enough time to study the full interaction of the plane wave with a flash of gamma photons of extension $\lambda/2$ and extract the probability from the number of surviving photons. The probability map in Fig. 4.2c is obtained from the results of 4096 (64×64) simulations performed over a the logarithmically spaced range of $a_0 \in [10, 4000]$ and $\gamma_\gamma \in [100, 40000]$.

Appendix B

Short times dynamics of charges

B.1 Algorithm for the computation of ω_{eff}

Here is detailed how the ω_{eff} quantity from equation (6.50) computed from the fields of 3D PIC simulations.

First of all we ran simulations with only the laser beams, and with the same parameters as the cascade simulations presented in chapter 7, with a spatial resolution $\Delta x = \lambda/32$ (the convergence of the computation was checked by increasing the spatial resolution). Then the field components are extracted from simulations to build the electromagnetic field strength tensor

$$F^{\mu}_{\ \nu} = \begin{pmatrix} 0 & E_x/c & E_y/c & E_z/c \\ E_x/c & 0 & B_z & -B_y \\ E_y/c & -B_z & 0 & B_x \\ E_z/c & B_y & -B_x & 0 \end{pmatrix} . \tag{B.1}$$

Then we use it to compute the value of the following Lorentz invariants

$$\mathcal{F} = -\frac{c^2}{4} F^{\mu\nu} F_{\mu\nu} = (\boldsymbol{E}^2 - c^2 \boldsymbol{B}^2)/2 \tag{B.2}$$

$$\mathcal{G} = -\frac{c}{4} F^{*\mu\nu} F_{\mu\nu} = c \boldsymbol{B}.\boldsymbol{E} \,, \tag{B.3}$$

in order to compute ϵ

$$\epsilon = \sqrt{\sqrt{\mathcal{F}^2 + \mathcal{G}^2} + \mathcal{F}} \,. \tag{B.4}$$

We will then in following compute ω_{eff} for all the points where $\epsilon > 0$, as it has one of the hypothesis of the derivation presented in 6.3.

The second step is to compute the fields time and space derivatives of the field components. The spatial derivative of the components of the fields are computed as follows. For example, the derivative along x of the components i

of the electric field E_i is given by

$$\frac{\partial E_i}{\partial x}(x,y,z,t) \simeq \frac{E_i(x+\Delta x,y,z,t) - E_i(x-\Delta x,y,z,t)}{\Delta x}\,, \tag{B.5}$$

with Δx being the spatial resolution of the simulation along x. In an analogous way the derivatives are computed along the other spatial directions. Regarding time derivatives, we get them from spatial derivatives using the Maxwell's equations

$$\boldsymbol{\nabla}\times\boldsymbol{E} = -\frac{\partial \boldsymbol{B}}{\partial t} \tag{B.6}$$

$$,\boldsymbol{\nabla}\times\boldsymbol{B} = \frac{\partial \boldsymbol{E}}{\partial t}\,. \tag{B.7}$$

Then the ω_{eff} quantity can be compute using the relation (6.50)

$$\omega_{\text{eff}}^2 = F_{\mu\nu,\sigma(0)}u_1^\mu u_1^\sigma (J^{-1})^\nu{}_\lambda F^\lambda{}_{\kappa,\rho(0)} u_1^\rho u_1^\kappa\,. \tag{B.8}$$

Where the J matrix is given by

$$J = \left(2\frac{\epsilon}{c}\mathbb{I} - F_{(0)}\right)^2\,, \tag{B.9}$$

and the u_1 vector is the eigen vector of $F_{(0)}$ associated to the eigen value ϵ/c. Its expression is given by

$$u_1 = \begin{pmatrix} 1 \\ \frac{B_x^2E_x+B_x(B_yE_y+B_zE_z)+\epsilon(-B_yE_z+B_zE_y+E_x\epsilon)}{\epsilon\left(B_x^2+B_y^2+B_z^2+\epsilon^2\right)} \\ \frac{B_xB_yE_x+B_xE_z\epsilon+B_y^2E_y+B_yB_zE_z-B_zE_x\epsilon+E_y\epsilon^2}{\epsilon\left(B_x^2+B_y^2+B_z^2+\epsilon^2\right)} \\ \frac{B_xB_zE_x-B_xE_y\epsilon+B_yB_zE_y+B_yE_x\epsilon+B_z^2E_z+E_z\epsilon^2}{\epsilon\left(B_x^2+B_y^2+B_z^2+\epsilon^2\right)} \end{pmatrix}\,. \tag{B.10}$$

Bibliography

[Abramowicz et al., 2021] Abramowicz, H., Acosta, U., Altarelli, M., Assmann, R., Bai, Z., Behnke, T., Benhammou, Y., Blackburn, T., Boogert, S., Borysov, O., et al. (2021). Conceptual design report for the luxe experiment. *The European Physical Journal Special Topics*, 230(11):2445–2560.

[Abramowicz et al., 2019] Abramowicz, H., Altarelli, M., Aßmann, R., Behnke, T., Benhammou, Y., Borysov, O., Borysova, M., Brinkmann, R., Burkart, F., Büßer, K., Davidi, O., Decking, W., Elkina, N., Harsh, H., Hartin, A., Hartl, I., Heinemann, B., Heinzl, T., TalHod, N., Hoffmann, M., Ilderton, A., King, B., Levy, A., List, J., Maier, A. R., Negodin, E., Perez, G., Pomerantz, I., Ringwald, A., Rödel, C., Saimpert, M., Salgado, F., Sarri, G., Savoray, I., Teter, T., Wing, M., and Zepf, M. (2019). Letter of intent for the luxe experiment. arXiv:1909.00860.

[Allen, 1992] Allen, L. (1992). Orbital angular momentum of light and the transformation of laguerre-gaussian laser modes. *Phys. Rev. A*, 45(11).

[Arber et al., 2015] Arber, T. D., Bennett, K., Brady, C. S., Lawrence-Douglas, A., Ramsay, M. G., Sircombe, N. J., Gillies, P., Evans, R. G., Schmitz, H., Bell, A. R., and Ridgers, C. P. (2015). Contemporary particle-in-cell approach to laser-plasma modelling. *Plasma Physics and Controlled Fusion*, 57:113001.

[Baier and Katkov, 1968] Baier, V. and Katkov, V. (1968). Processes involved in the motion of high energy particles in a magnetic field. *Sov. Phys. JETP*, 26:854.

[Baier et al., 1998] Baier, V. N., Katkov, V. M., and Strakhovenko, V. M. (1998). *Electromagnetic Processes at High Energies in Oriented Single Crystals*. World Scientific, Singapore.

[Barnett, 2010] Barnett, S. M. (2010). Rotation of electromagnetic fields and the nature of optical angular momentum. *Journal of Modern Optics*, 57(14-15):1339–1343. PMID: 24808629.

[Barnett and Allen, 1994] Barnett, S. M. and Allen, L. (1994). Orbital angular momentum and nonparaxial light beams. *Optics Communications*, 110(5):670 – 678.

[Bashmakov et al., 2014] Bashmakov, V. F., Nerush, E. N., Kostyukov, I. Y., Fedotov, A. M., and Narozhny, N. B. (2014). Effect of laser polarization on quantum electrodynamical cascading. *Physics of Plasmas*, 21(1):013105.

[Bell and Kirk, 2008] Bell, A. R. and Kirk, J. G. (2008). Possibility of prolific pair production with high-power lasers. *Phys. Rev. Lett.*, 101:200403.

[Berestetskii et al., 1982] Berestetskii, V. B., Lifshitz, E. M., and Pitaevskii, L. P. (1982). *Quantum Electrodynamics: Volume 4*, volume 4. Butterworth-Heinemann.

[Blackburn et al., 2017] Blackburn, T. G., Ilderton, A., Murphy, C. D., and Marklund, M. (2017). Scaling laws for positron production in laser-electron-beam collisions. *Phys. Rev. A*, 96:022128.

[Blackburn and Marklund, 2018] Blackburn, T. G. and Marklund, M. (2018). Nonlinear breit–wheeler pair creation with bremsstrahlung γ rays. *Plasma Physics and Controlled Fusion*, 60(5):054009.

[Blackburn et al., 2014] Blackburn, T. G., Ridgers, C. P., Kirk, J. G., and Bell, A. R. (2014). Quantum Radiation Reaction in Laser–Electron-Beam Collisions. *Phys. Rev. Lett.*, 112:015001.

[Bliokh et al., 2014] Bliokh, K. Y., Dressel, J., and Nori, F. (2014). Conservation of the spin and orbital angular momenta in electromagnetism. *New Journal of Physics*, 16(9):093037.

[Boris, 1970] Boris, J. P. (1970). *Plasma Physics Laboratory.*

[Breit and Wheeler, 1934] Breit, G. and Wheeler, J. A. (1934). Collision of Two Light Quanta. *Phys. Rev.*, 46.

[Bromage et al., 2019] Bromage, J., Bahk, S.-W., Begishev, I. A., Dorrer, C., Guardalben, M. J., Hoffman, B. N., Oliver, J. B., Roides, R. G., Schiesser, E. M., Shoup III, M. J., Spilatro, M., Webb, B., Weiner, D., and Zuegel, J. D. (2019). *High Power Laser Sci. Eng.*, 7:e4.

[Burke et al., 1997] Burke, D. L., Field, R. C., Horton-Smith, G., Spencer, J. E., Walz, D., Berridge, S. C., Bugg, W. M., Shmakov, K., Weidemann, A. W., Bula, C., McDonald, K. T., Prebys, E. J., Bamber, C., Boege, S. J.,

Koffas, T., Kotseroglou, T., Melissinos, A. C., Meyerhofer, D. D., Reis, D. A., and Ragg, W. (1997). Positron production in multiphoton light-by-light scattering. *Phys. Rev. Lett.*, 79:1626–1629.

[Capdessus et al., 2018] Capdessus, R., King, M., Del Sorbo, D., Duff, M., Ridgers, C. P., and McKenna, P. (2018). Relativistic Doppler-boosted γ-rays in High Fields. *Scientific Reports*, 8:9155.

[Chen et al., 2018] Chen, Y., Li, J., Hatsagortsyan, K., and Keitel, C. (2018). γ -ray beams with large orbital angular momentum via nonlinear compton scattering with radiation reaction. *Physical Review Letters*, 121:074801.

[Chen et al., 2019] Chen, Y.-Y., He, P.-L., Shaisultanov, R., Hatsagortsyan, K. Z., and Keitel, C. H. (2019). Polarized positron beams via intense two-color laser pulses. *Phys. Rev. Lett.*, 123:174801.

[Cros et al., 2014] Cros, B., Paradkar, B., Davoine, X., Chancé, A., Desforges, F., Dobosz-Dufrénoy, S., Delerue, N., Ju, J., Audet, T., Maynard, G., Lobet, M., Gremillet, L., Mora, P., Schwindling, J., Delferrière, O., Bruni, C., Rimbault, C., Vinatier, T., Piazza, A. D., Grech, M., Riconda, C., Marquès, J., Beck, A., Specka, A., Martin, P., Monot, P., Normand, D., Mathieu, F., Audebert, P., and Amiranoff, F. (2014). Laser plasma acceleration of electrons with multi-PW laser beams in the frame of CILEX. *Nuclear Instruments and Methods in Physics Research Section A: Accelerators, Spectrometers, Detectors and Associated Equipment*, 740:27 – 33. Proceedings of the first European Advanced Accelerator Concepts Workshop 2013.

[Davis, 1979] Davis, L. (1979). Theory of electromagnetic beams. *Phys. Rev. A*, 19(1177–1179).

[Derouillat et al., 2018] Derouillat, J., Beck, A., Pérez, F., Vinci, T., Chiaramello, M., Grassi, A., Flé, M., Bouchard, G., Plotnikov, I., Aunai, N., Dargent, J., Riconda, C., and Grech, M. (2018). Smilei : A collaborative, open-source, multi-purpose particle-in-cell code for plasma simulation. *Computer Physics Communications*, 222(Supplement C):351 – 373.

[Di Piazza, 2018] Di Piazza, A. (2018). Implementing nonlinear compton scattering beyond the local-constant-field approximation. *Phys. Rev. A*, 98(012134).

[Di Piazza et al., 2010] Di Piazza, A., Hatsagortsyan, K. Z., and Keitel, C. H. (2010). Quantum radiation reaction effects in multiphoton compton scattering. *Phys. Rev. Lett.*, 105:220403.

[Di Piazza et al., 2012] Di Piazza, A., Müller, C., Hatsagortsyan, K. Z., and Keitel, C. H. (2012). Extremely high-intensity laser interactions with fundamental quantum systems. *Rev. Mod. Phys.*, 84:1177–1228.

[Di Piazza et al., 2011] Di Piazza, A., Müller, C., Hatsagortsyan, K., and Keitel, C. (2011). Extremely high-intensity laser interactions with fundamental quantum systems. *Reviews of Modern Physics*, 84.

[Dirac, 1938] Dirac, P. A. M. (1938). Classical theory of radiating electrons. *Proceedings of The Royal Society A: Mathematical, Physical and Engineering Sciences*, 167:148–169.

[Duclous et al., 2010a] Duclous, R., Kirk, J., and Bell, A. (2010a). Monte carlo calculations of pair production in high-intensity laser-plasma interactions. *Plasma Physics and Controlled Fusion*, 53.

[Duclous et al., 2010b] Duclous, R., Kirk, J. G., and Bell, A. R. (2010b). Monte carlo calculations of pair production in high-intensity laser–plasma interactions. *Plasma Physics and Controlled Fusion*, 53(1):015009.

[Duff et al., 2020] Duff, M., Wilson, R., King, M., Gonzalez-Izquierdo, B., Higginson, A., Williamson, S., Davidson, Z., Capdessus, R., Booth, N., Hawkes, S., Neely, D., Gray, R., and Mckenna, P. (2020). High order mode structure of intense light fields generated via a laser-driven relativistic plasma aperture. *Scientific Reports*, 10.

[Elkina et al., 2011] Elkina, N. V., Fedotov, A. M., Kostyukov, I. Y., Legkov, M. V., Narozhny, N. B., Nerush, E. N., and Ruhl, H. (2011). Qed cascades induced by circularly polarized laser fields. *Phys. Rev. ST Accel. Beams*, 14:054401.

[Enk and Nienhuis, 1994] Enk, S. V. and Nienhuis, G. (1994). Commutation rules and eigenvalues of spin and orbital angular momentum of radiation fields. *Journal of Modern Optics*, 41(5):963–977.

[Esirkepov, 2001] Esirkepov, T. (2001). Exact charge conservation scheme for particle-in-cell simulation with an arbitrary form-factor. *Computer Physics Communications*, 135(2):144–153.

[Esirkepov et al., 2014] Esirkepov, T. Z., Bulanov, S. S., Koga, J. K., Kando, M., Kondo, K., Rosanov, N. N., Korn, G., and Bulanov, S. V. (2014). Attractors and chaos of electron dynamics in electromagnetic standing wave. *arXiv preprint arXiv:1412.6028*.

[Faure et al., 2004] Faure, J., Glinec, Y., Pukhov, A., Kiselev, S., Gordienko, S., Lefebvre, E., Rousseau, J.-P., Burgy, F., and Malka, V. (2004). A laser–plasma accelerator producing monoenergetic electron beams. *Nature*, 431(7008):541–544.

[Fedotov et al., 2022] Fedotov, A., Ilderton, A., Karbstein, F., King, B., Seipt, D., Taya, H., and Torgrimsson, G. (2022). Advances in qed with intense background fields. *arXiv preprint arXiv:2203.00019*.

[Fedotov et al., 2010] Fedotov, A., Narozhny, N., and Korn, G. (2010). Limitations on the attainable intensity of high power lasers. *Physical review letters*, 105:080402.

[Fernandez-Corbaton et al., 2014] Fernandez-Corbaton, I., Zambrana-Puyalto, X., and Molina-Terriza, G. (2014). On the transformations generated by the electromagnetic spin and orbital angular momentum operators. *J. Opt. Soc. Am. B*, 31(9):2136–2141.

[Feynman et al., 2010] Feynman, R. P., Leighton, R. B., and Sands, M. (2010). The feynman lectures on physics: the new millennium edition. *Reading: Addison-Wesley Publishing Company*.

[Fradkin et al., 1991] Fradkin, E. S., Gitman, D. M., Shvartsman, S. M., and Gitman, D. M. (1991). *Quantum electrodynamics: with unstable vacuum*. Springer.

[Geddes et al., 2004] Geddes, C., Toth, C., Van Tilborg, J., Esarey, E., Schroeder, C., Bruhwiler, D., Nieter, C., Cary, J., and Leemans, W. (2004). High-quality electron beams from a laser wakefield accelerator using plasma-channel guiding. *Nature*, 431(7008):538–541.

[Gelfer et al., 2022] Gelfer, E., Fedotov, A., Mironov, A., and Weber, S. (2022). Nonlinear compton scattering in time-dependent electric fields beyond the locally constant crossed field approximation. *Physical Review D*, 106(5):056013.

[Gelfer et al., 2015] Gelfer, E., Mironov, A., Fedotov, A., Bashmakov, V., Nerush, E., Kostyukov, I., and Narozhny, N. (2015). Optimized multibeam configuration for observation of qed cascades. *Physical Review A*, 92.

[Glauber, 1963] Glauber, R. J. (1963). Coherent and incoherent states of the radiation field. *Physical Review*, 131(6):2766.

[Gong et al., 2017] Gong, Z., Hu, R., Shou, Y., Qiao, B., Chen, C., He, X., Bulanov, S., Esirkepov, T., Bulanov, S. V., and Yan, X. (2017). High-efficiency γ-ray flash generation via multiple-laser scattering in ponderomotive potential well. *Physical Review E*, 95.

[Gong et al., 2016] Gong, Z., Hu, R., Shou, Y., Qiao, B., Chen, C., Xu, F., He, X., and Yan, X. (2016). Radiation reaction induced spiral attractors in ultra-intense colliding laser beams. *Matter and Radiation at Extremes*, 1(6):308–315.

[Gonoskov et al., 2017] Gonoskov, A., Bashinov, A., Bastrakov, S., Efimenko, E., Ilderton, A., Kim, A., Marklund, M., Meyerov, I., Muraviev, A., and Sergeev, A. (2017). Ultrabright gev photon source via controlled electromagnetic cascades in laser-dipole waves. *Phys. Rev. X*, 7:041003.

[Gonoskov et al., 2014] Gonoskov, A., Bashinov, A., Gonoskov, I., Harvey, C., Ilderton, A., Kim, A., Marklund, M., Mourou, G., and Sergeev, A. (2014). Anomalous radiative trapping in laser fields of extreme intensity. *Physical review letters*, 113(1):014801.

[Gonoskov et al., 2015] Gonoskov, A., Bastrakov, S., Efimenko, E., Ilderton, A., Marklund, M., Meyerov, I., Muraviev, A., Sergeev, A., Surmin, I., and Wallin, E. (2015). Extended particle-in-cell schemes for physics in ultrastrong laser fields: Review and developments. *Phys. Rev. E*, 92:023305.

[Gonsalves et al., 2019] Gonsalves, A., Nakamura, K., Daniels, J., Benedetti, C., Pieronek, C., De Raadt, T., Steinke, S., Bin, J., Bulanov, S., Van Tilborg, J., et al. (2019). Petawatt laser guiding and electron beam acceleration to 8 gev in a laser-heated capillary discharge waveguide. *Physical review letters*, 122(8):084801.

[Grech et al., 2021] Grech, M., Lancia, L., Andriyash, I. A., Audebert, P., Beck, A., Corde, S., Davoine, X., Frotin, M., Grassi, A., Gremillet, L., Le Pape, S., Lobet, M., Leblanc, A., Mathieu, F., Massimo, F., Mercuri-Baron, A., Papadopoulos, D., Pérez, F., Prudent, J., Riconda, C., Romagnani, L., Specka, A., Thaury, C., Phuoc, K. T., and Vinci, T. (2021). Investigating strong-field QED processes in laser-electron beam collisions at Apollon. MP3 White Paper, https://hal.archives-ouvertes.fr/hal-03229914.

[Grismayer et al., 2016] Grismayer, T., Vranic, M., Martins, J. L., Fonseca, R. A., and Silva, L. O. (2016). Laser absorption via quantum electrody-

namics cascades in counter propagating laser pulses. *Physics of Plasmas*, 23(5):056706.

[Grismayer et al., 2017] Grismayer, T., Vranic, M., Martins, J. L., Fonseca, R. A., and Silva, L. O. (2017). Seeded qed cascades in counterpropagating laser pulses. *Phys. Rev. E*, 95:023210.

[Harlow, 1955] Harlow, F. (1955). A machine calculation method for hydrodynamic problems. technical report lams-1956.

[Harvey et al., 2009] Harvey, C., Heinzl, T., and Ilderton, A. (2009). Signatures of high-intensity compton scattering. *Physical Review A*, 79(6):063407.

[Haus, 1984] Haus, H. A. (1984). *Waves and Fields in Optoelectronics*. Prentice-Hall, Englewood Cliffs, NJ.

[Hirsch et al., 2012] Hirsch, M. W., Smale, S., and Devaney, R. L. (2012). *Differential equations, dynamical systems, and an introduction to chaos*. Academic press.

[Ilderton et al., 2018] Ilderton, A., King, B., and Seipt, D. (2018). High-intensity qed beyond the locally constant field approximation. *arXiv*, 1808(10339v1).

[Ilderton et al., 2019] Ilderton, A., King, B., and Seipt, D. (2019). Extended locally constant field approximation for nonlinear compton scattering. *Physical Review A*, 99(4):042121.

[Jackson, 1999] Jackson, J. D. (1999). *Classical Electrodynamics*. John Wiley and Sons, third edition edition.

[Jirka et al., 2016] Jirka, M., Klimo, O., Bulanov, S. V., Esirkepov, T. Z., Gelfer, E., Bulanov, S. S., Weber, S., and Korn, G. (2016). Electron dynamics and γ and $e^{-}e^{+}$ production by colliding laser pulses. *Phys. Rev. E*, 93:023207.

[Jirka et al., 2017] Jirka, M., Klimo, O., Vranic, M., Weber, S., and Korn, G. (2017). Qed cascade with 10 pw-class lasers. *Scientific Reports*, 7.

[Jordan and Smith, 2007] Jordan, D. and Smith, P. (2007). *Nonlinear ordinary differential equations: an introduction for scientists and engineers*. OUP Oxford.

[Keller, 2003] Keller, U. (2003). Recent developments in compact ultrafast lasers. *nature*, 424(6950):831–838.

[King and Hu, 2016] King, B. and Hu, H. (2016). Classical and quantum dynamics of a charged scalar particle in a background of two counterpropagating plane waves. *Physical Review D*, 94(12):125010.

[Kirk, 2016] Kirk, J. (2016). Radiative trapping in intense laser beams. *Plasma Physics and Controlled Fusion*, 58(8):085005.

[Kirk et al., 2009] Kirk, J. G., Bell, A. R., and Arka, I. (2009). Pair production in counter-propagating laser beams. *Plasma Physics and Controlled Fusion*, 51(8):085008.

[Kostyukov and Nerush, 2016] Kostyukov, I. and Nerush, E. (2016). Production and dynamics of positrons in ultrahigh intensity laser-foil interactions. *Physics of Plasmas*, 23:093119.

[Landau and Lifshitz, 1980] Landau, L. D. and Lifshitz, E. M. (1980). *The classical theory of fields*. Butterworth Heinemann, 4th edition.

[Leader, 2018] Leader, E. (2018). A proposed measurement of optical orbital and spin angular momentum and its implications for photon angular momentum. *Physics Letters B*, 779:385–387.

[Leader and Lorcé, 2014] Leader, E. and Lorcé, C. (2014). The angular momentum controversy: What's it all about and does it matter? *Physics Reports*, 541(3):163–248. The angular momentum controversy: What's it all about and does it matter?

[Lee et al., 2018] Lee, S., Kim, H., Choi, I., Kim, C., and Nam, C. (2018). Exploration of strong field physics with multi-pw lasers. *J. Korean Phys. Soc.*, 73:179–189.

[Lehmann and Spatschek, 2012] Lehmann, G. and Spatschek, K. H. (2012). Phase-space contraction and attractors for ultrarelativistic electrons. *Phys. Rev. E*, 85:056412.

[Lobet, 2015] Lobet, M. (2015). *Radiative and QED effects in ultra-relativistic laser-matter interaction*. PhD thesis, Université de Bordeaux.

[Lobet et al., 2016] Lobet, M., d'Humières, E., Grech, M., Ruyer, C., Davoine, X., and Gremillet, L. (2016). Modeling of radiative and quantum electrodynamics effects in PIC simulations of ultra-relativistic laser-plasma interaction. *Journal of Physics: Conference Series*, 688(1):012058.

[Longman et al., 2020] Longman, A., Salgado, C., Zeraouli, G., naniz, J. I. A., Pérez-Hernández, J. A., Eltahlawy, M. K., Volpe, L., and Fedosejevs, R. (2020). Off-axis spiral phase mirrors for generating high-intensity optical vortices. *Opt. Lett.*, 45(8):2187–2190.

[Lv et al., 2021] Lv, Q., Raicher, E., Keitel, C., and Hatsagortsyan, K. (2021). Anomalous violation of the local constant field approximation in colliding laser beams. *Physical Review Research*, 3(1):013214.

[M. Abramowitz, 1964] M. Abramowitz, I. A. S. (1964). *Handbook of Mathematical Functions with Formulas, Graphs and Mathematical Tables*. National BUreau of Standards.

[M. Lax, 1975] M. Lax, WH. Louisell, W. M. (1975). From maxwell to paraxial wave optics. *Phys. Rev. A*, 11(1365–1370).

[Mackenroth, 2014] Mackenroth, K. F. (2014). *Quantum radiation in ultra-intense laser pulses*. Springer.

[Magnusson et al., 2019] Magnusson, J., Gonoskov, A., Marklund, M., Esirkepov, T., Koga, J., Kondo, K., Kando, M., Bulanov, S., Korn, G., and Bulanov, S. (2019). Laser-particle collider for multi-gev photon production. *Physical Review Letters*, 122.

[Mangles et al., 2004] Mangles, S. P., Murphy, C., Najmudin, Z., Thomas, A. G. R., Collier, J., Dangor, A. E., Divall, E., Foster, P., Gallacher, J., Hooker, C., et al. (2004). Monoenergetic beams of relativistic electrons from intense laser–plasma interactions. *Nature*, 431(7008):535–538.

[Marini et al., 2021] Marini, S., Kleij, P., Pisani, F., Amiranoff, F., Grech, M., Macchi, A., Raynaud, M., and Riconda, C. (2021). Ultrashort high energy electron bunches from tunable surface plasma waves driven with laser wavefront rotation. *Physical Review E*, 103(2):L021201.

[Mendonça and Vieira, 2014] Mendonça, J. T. and Vieira, J. (2014). Donut wakefields generated by intense laser pulses with orbital angular momentum. *Physics of Plasmas*, 21(3):033107.

[Mercuri-Baron et al., 2021] Mercuri-Baron, A., Grech, M., Niel, F., Grassi, A., Lobet, M., Piazza, A. D., and Riconda, C. (2021). Impact of the laser spatio-temporal shape on breit–wheeler pair production. *New Journal of Physics*, 23(8):085006.

[Meuren et al., 2020] Meuren, S., Bucksbaum, P. H., Fisch, N. J., Fiúza, F., Glenzer, S., Hogan, M. J., Qu, K., Reis, D. A., White, G., and Yakimenko, V. (2020). On seminal hedp research opportunities enabled by colocating multi-petawatt laser with high-density electron beams.

[Meuren et al., 2015] Meuren, S., Hatsagortsyan, K. Z., Keitel, C. H., and Di Piazza, A. (2015). Polarization-operator approach to pair creation in short laser pulses. *Phys. Rev. D*, 91:013009.

[Mironov et al., 2021] Mironov, A. A., Gelfer, E. G., and Fedotov, A. M. (2021). Onset of electron-seeded cascades in generic electromagnetic fields. *Phys. Rev. A*, 104:012221.

[Mitter, 1975] Mitter, H. (1975). Quantum electrodynamics in laser fields. *Acta Phys. Austriaca*, XIV(397).

[Mora, 2021] Mora, P. (2021). *Plasmas créés par laser*. EDP Sciences.

[Nam et al., 2018] Nam, C. H., Sung, J. H., Lee, H. W., Youn, J. W., and Lee, S. K. (2018). Performance of the 20 fs, 4 pw ti:sapphire laser at corels. In *Conference on Lasers and Electro-Optics*, page STu4O.3. Optical Society of America.

[Nerush et al., 2011a] Nerush, E. N., Bashmakov, V. F., and Kostyukov, I. Y. (2011a). Analytical model for electromagnetic cascades in rotating electric field. *Physics of Plasmas*, 18(8):083107. Publisher: American Institute of Physics.

[Nerush et al., 2011b] Nerush, E. N., Kostyukov, I. Y., Fedotov, A. M., Narozhny, N. B., Elkina, N. V., and Ruhl, H. (2011b). Laser Field Absorption in Self-Generated Electron-Positron Pair Plasma. *Phys. Rev. Lett.*, 106:035001.

[Niel, 2021] Niel, F. (2021). *Classical and quantum description of plasma and radiation in strong fields*. Springer Nature.

[Niel et al., 2018a] Niel, F., Riconda, C., Amiranoff, F., Duclous, R., and Grech, M. (2018a). From quantum to classical modeling of radiation reaction: A focus on stochasticity effects. *Phys. Rev. E*, 97:043209.

[Niel et al., 2018b] Niel, F., Riconda, C., Amiranoff, F., Lobet, M., Derouillat, J., Pérez, F., Vinci, T., and Grech, M. (2018b). From quantum to classical modeling of radiation reaction: a focus on the radiation spectrum. *Plasma Physics and Controlled Fusion*, 60(9):094002.

[Nuter et al., 2014] Nuter, R., Grech, M., González de Alaiza Martínez, P., Bonnaud, G., and D'Humières, E. (2014). Maxwell solvers for the simulations of the laser-matter interaction. *The European Physical Journal D*, 68.

[Nuter et al., 2020] Nuter, R., Korneev, P., Dmitriev, E., Thiele, I., and Tikhonchuk, V. T. (2020). Gain of electron orbital angular momentum in a direct laser acceleration process. *Phys. Rev. E*, 101:053202.

[Ornigotti and Aiello, 2014] Ornigotti, M. and Aiello, A. (2014). Surface angular momentum of light beams. *Opt. Express*, 22(6):6586–6596.

[Papadopoulos et al., 2016] Papadopoulos, D. N., Zou, J. P., Le Blanc, C., Cheriaux, G., Georges, P., Druon, F., Mennerat, G., Ramirez, P., Martin, L., Fréneaux, A., Beluze, A., Lebas, N., Monot, P., Mathieu, F., and Audebert, P. (2016). The apollon 10 pw laser: Experimental and theoretical investigation of the temporal characteristics. *High Power Laser Science and Engineering*, 4.

[Pérez and Grech, 2019] Pérez, F. and Grech, M. (2019). Oblique-incidence, arbitrary-profile wave injection for electromagnetic simulations. *Phys. Rev. E*, 99:033307.

[Phuoc et al., 2012] Phuoc, K., Corde, S., Thaury, C., Malka, V., Tafzi, A., Goddet, J.-P., Shah, R., Sebban, S., and Rousse, A. (2012). All-optical compton gamma-ray source. *Nature Photonics*, 6:308–311.

[Pike et al., 2014] Pike, O., Mackenroth, F., Hill, E., and Rose, S. (2014). A photon–photon collider in a vacuum hohlraum. *Nature Photonics*, 8(6):434–436.

[Podszus and Di Piazza, 2021] Podszus, T. and Di Piazza, A. (2021). First-order strong-field qed processes including the damping of particle states. *Phys. Rev. D*, 104:016014.

[Press et al., 2007] Press, W. H., Teukolsky, S. A., Vetterling, W. T., and Flannery, B. P. (2007). *Numerical recipes 3rd edition: The art of scientific computing*. Cambridge university press.

[Ribeyre et al., 2016] Ribeyre, X., d'Humières, E., Jansen, O., Jequier, S., Tikhonchuk, V., and Lobet, M. (2016). Pair creation in collision of γ-ray beams produced with high-intensity lasers. *Physical Review E*, 93(1):013201.

[Ridgers et al., 2012] Ridgers, C. P., Brady, C. S., Duclous, R., Kirk, J. G., Bennett, K., Arber, T. D., Robinson, A. P. L., and Bell, A. R. (2012). Dense Electron-Positron Plasmas and Ultraintense γ rays from Laser-Irradiated Solids. *Phys. Rev. Lett.*, 108:165006.

[Ritus, 1979] Ritus, V. I. (1979). *Quantum effects of the interaction of elementary particles with an intense electromagnetic field.* PhD thesis.

[Rohrlich, 2008] Rohrlich, F. (2008). Dynamics of a charged particle. *Phys. Rev. E*, 77:046609.

[Salgado et al., 2021] Salgado, F. C., Grafenstein, K., Golub, A., Döpp, A., Eckey, A., Hollatz, D., Müller, C., Seidel, A., Seipt, D., Karsch, S., and Zepf, M. (2021). Towards pair production in the non-perturbative regime. *New Journal of Physics*, 23(10):105002.

[Sampath et al., 2021] Sampath, A., Davoine, X., Corde, S., Gremillet, L., Gilljohann, M., Sangal, M., Keitel, C. H., Ariniello, R., Cary, J., Ekerfelt, H., Emma, C., Fiuza, F., Fujii, H., Hogan, M., Joshi, C., Knetsch, A., Kononenko, O., Lee, V., Litos, M., Marsh, K., Nie, Z., O'Shea, B., Peterson, J. R., Claveria, P., Storey, D., Wu, Y., Xu, X., Zhang, C., and Tamburini, M. (2021). Extremely dense gamma-ray pulses in electron beam-multifoil collisions. *Phys. Rev. Lett.*, 126:064801.

[Sauter, 1931] Sauter, F. (1931). Uber das Verhalten eines Elektrons im homogenen elektrischen Feld nach der relativistischen Theorie Diracs. *Z. Phys.*, 69(742).

[Schwartz, 2014] Schwartz, M. D. (2014). *Quantum field theory and the standard model.* Cambridge University Press.

[Schwinger, 1951] Schwinger, J. (June 1, 1951). On Gauge Invariance and Vacuuwn Polarization. *Phys. Rev.*, 82(5).

[Seipt, 2012] Seipt, D. (2012). *Strong-field qed processes in short laser pulses.* PhD thesis.

[Seipt and King, 2020] Seipt, D. and King, B. (2020). Spin- and polarization-dependent locally-constant-field-approximation rates for nonlinear compton and breit-wheeler processes. *Phys. Rev. A*, 102:052805.

[Siegman, 1986] Siegman, A. E. (1986). *Lasers.* Univ Science Books; Revised ed. edition.

[Slade-Lowther et al., 2019] Slade-Lowther, C., Sorbo, D. D., and Ridgers, C. P. (2019). Identifying the electron–positron cascade regimes in high-intensity laser-matter interactions. *New Journal of Physics*, 21(1):013028.

[Strickland and Mourou, 1985] Strickland, D. and Mourou, G. (1985). Compression of amplified chirped optical pulses. *Optics Communications*, 22(6):447–449.

[Taflove et al., 2005] Taflove, A., Hagness, S. C., and Piket-May, M. (2005). 9 - computational electromagnetics: The finite-difference time-domain method. In CHEN, W.-K., editor, *The Electrical Engineering Handbook*, pages 629–670. Academic Press, Burlington.

[Tajima and Dawson, 1979] Tajima, T. and Dawson, J. M. (1979). Laser electron accelerator. *Physical Review Letters*, 43(4):267.

[Tamburini et al., 2017] Tamburini, M., Di Piazza, A., and Keitel, C. H. (2017). Laser-pulse-shape control of seeded qed cascades. *Scientific Reports*, 7(1).

[Tamburini and Meuren, 2021] Tamburini, M. and Meuren, S. (2021). Efficient high-energy photon production in the supercritical qed regime. *Phys. Rev. D*, 104:L091903.

[Taub, 1948] Taub, A. H. (1948). Orbits of charged particles in constant fields. *Phys. Rev.*, 73:786–798.

[Thomas, 2014] Thomas, A. (2014). Antimatter creation in an x-ray bath. *Nature Photonics*, 8(6):429–431.

[Vallone, 2015] Vallone, G. (2015). On the properties of circular beams: normalization, laguerre–gauss expansion, and free-space divergence. *Opt. Lett.*, 40(8):1717–1720.

[Vay, 2008] Vay, J.-L. (2008). Simulation of beams or plasmas crossing at relativistic velocity. *Physics of Plasmas*, 15(5).

[Vranic et al., 2016] Vranic, M., Grismayer, T., Fonseca, R., and Silva, L. (2016). Electron - positron cascades in multiple-laser optical traps. *Plasma Physics and Controlled Fusion*, 59.

[Vranic et al., 2019] Vranic, M., Grismayer, T., Meuren, S., Fonseca, R. A., and Silva, L. O. (2019). Are we ready to transfer optical light to gamma-rays? *Physics of Plasmas*, 26(5):053103.

[Vranic et al., 2018] Vranic, M., Klimo, O., Korn, G., and Weber, S. (2018). Multi-gev electron-positron beam generation from laser-electron scattering. *Scientific Reports*, 8.

[Yakimenko et al., 2019] Yakimenko, V., Alsberg, L., Bong, E., Bouchard, G., Clarke, C., Emma, C., Green, S., Hast, C., Hogan, M. J., Seabury, J., Lipkowitz, N., O'Shea, B., Storey, D., White, G., and Yocky, G. (2019). Facet-ii facility for advanced accelerator experimental tests. *Phys. Rev. Accel. Beams*, 22:101301.

[Zhang et al., 2020] Zhang, P., Bulanov, S. S., Seipt, D., Arefiev, A. V., and Thomas, A. G. R. (2020). Relativistic plasma physics in supercritical fields. *Physics of Plasmas*, 27(5):050601.

[Zhu et al., 2019] Zhu, X., Chen, M., Tong-Pu, Y., Weng, S., He, F., and Sheng, Z. (2019). Collimated gev attosecond electron–positron bunches from a plasma channel driven by 10 pw lasers. *Matter and Radiation at Extremes*, 4:014401.

[Zhu et al., 2020] Zhu, X., Chen, M., Weng, S., Tong-Pu, Y., Wang, W., He, F., Sheng, Z., Mckenna, P., Jaroszynski, D., and Zhang, J. (2020). Extremely brilliant gev γ-rays from a two-stage laser-plasma accelerator. *Science Advances*, 6:eaaz7240.

[Óscar Amaro and Vranic, 2021] Óscar Amaro and Vranic, M. (2021). Optimal laser focusing for positron production in laser–electron scattering. *New Journal of Physics*, 23(11):115001.